ANALYSIS OF TWO-DIMENSIONAL FLOWS IN MAGNETO-DYNAMIC PLASMA ACCELERATORS

by

Jean-Marc G. Chanty

Ingénieur de l'Ecole Supérieure d'Electricité, 1983
S.M. Aeronautics and Astronautics, Massachusetts Institute of Technology, 1986

Submitted to the Department of Aeronautics and Astronautics
in partial fulfillment of the requirements for the degree of

Doctor of Philosophy

at the

MASSACHUSETTS INSTITUTE OF TECHNOLOGY

June 1992

Signature of Author ....
Department of Aeronautics and Astronautics
May 21, 1992

Certified by ....
Manuel Martinez-Sanchez
Thesis Supervisor, Associate Professor of Aeronautics and Astronautics

Certified by ....
Earll Murman
Member of the Thesis Committee, Professor of Aeronautics and Astronautics

Certified by ....
Jeffrey Freidberg
Member of the Thesis Committee. Professor of Nuclear Engineering

Accepted by ....
Professor Harold Y. Wachman
Chairman, Department Graduate Committee

ANALYSIS OF TWO-DIMENSIONAL FLOWS IN MAGNETO-DYNAMIC PLASMA ACCELERATORS

by

Jean-Marc G. Chanty

Submitted to the Department of Aeronautics and Astronautics
on May 21, 1992, in partial fulfillment of the
requirements for the degree of
Doctor of Philosophy

Abstract

The main focus of this dissertation is the study of ionized gas flows through magneto-dynamic accelerators, also called *MPD thrusters*. The analysis is based on a one-fluid magneto-hydrodynamic model. The fundamental parameters considered here are the magnetic Reynolds number and the Hall parameter. This dissertation is focused on the regime of large magnetic Reynolds number. Two methods of analysis are considered in this study. First, a singular perturbation based on the small parameter $\epsilon = 1/R_m$. This singular perturbation leads to the formal separation of the problem into several sub-problems defined in different regions, and linked by a suitable asymptotic matching process. The outer problem is solved using a numerical simulation based on a Galerkin finite element method. Several inner-regions are also considered: the inlet acceleration layer, the magnetic boundary layer over an insulator, and the flow around a weak corner.

The second method of analysis is a regular perturbation method based on the perturbation of a uniform flow by a small deformation of the boundaries, leading to a linear problem of fourth order. This problem can be solved by Fourier transformation. This method is used to find the inner solution near an isolated corner and to calculate the flow inside a weakly divergent thruster.

These methods give qualitative results for the structure of the flow in the thrusters. The results underscore the importance of the Hall effect which is responsible for the existence of strong transverse gradients within the thruster. The analysis shows that the quasi one-dimensional model is inadequate when the inter-electrode distance is not large compared to the magnetic interaction length. In addition, it is shown that expansion fans obeying classical gas-dynamic laws on a small length scale, originate at the tip of the electrodes, and that the current lines refract across the expansion fan. In particular, near the anode tip, current lines refract away from the electrode surface.

Thesis Supervisor: Manuel Martinez-Sanchez
Title: Associate Professor of Aeronautics and Astronautics

Acknowledgments

I gratefully thank Professor Manuel Martinez-Sanchez, for his friendship, his patience, and his willingness to go out of his way in order to help his students. I dedicate this dissertation to my family who has patiently supported me throughout these years. I would like to acknowledge the help and encouragements of the members of my doctoral committee, my coworkers and my friends. In particular I would like to acknowledge: Judson R. Baron, Rodger J. Biasca, Nada N. Boustany, Jeremiah U. Brackbill, Isaac M. Colbert, Hubert Curien, Svevolod Dmitrieff, Marc Drela, Hélène Felici, Alissa M. Fizgerald, Jeffrey P. Freidberg, Stephanie A. Gajar, Nikolaos A. Gatsonis, Mike B. Giles, Sarah T. Gille, Alexandros Gioulekas, Aga Goodsell, Daniel E. Hastings, Karl D. Handelsman, Lindsay Haugland, Daniel J. Heimerdinger, Francisco J. Higuera, Vernon M. Ingram, Mårten Landhal, Dana R. Lindquist, Maris A. Mantenieks, James R. Melcher, Scott A. Miller, Knox T. Millsaps Jr., Dave L. Modiano, Kim Molvig, Earll M. Murman, Eliahu H. Niewood, Max Pervaiz, Ken Powell, David R. Rivas, Tom Roberts, André P. Saxer, Richard A. Shapiro, Eric J. Sheppard, James S. Sovey, Peter J. Turchi, Harold Y. Wachman and Kathleen Wienhold.

Contents

NOMENCLATURE

b, B	Magnetic field
$C_1, .., C_4$	Integration constants
c_a	Acoustic velocity
c_v	Magneto-acoustic velocity
E	Electric field
H_a	Hall number
h, H	Thruster height
J	Current density
k	Wave number
L_{ref}	Thruster length
M_a	Mach number $= \frac{u}{c_a}$
M_v	Mach-Alfven number $= \frac{u}{c_v}$
n	Normal coordinate
p, P	Pressure
P_e	Electron pressure
R	Density
R_m	Magnetic Reynolds number
s	Streamwise coordinate
T	Temperature
u, U	Velocity
v, V	Velocity
x, X	x-coordinate
y, Y	y-coordinate

β_o	$\frac{p_o}{b_o^2}$ plasma-β
β_a	$\beta_a^2 = M_a^2 - 1$
β_e	$\beta_e = H_a \frac{B}{B_{ref}}$ Hall coefficient
β_v	$\beta_v^2 = M_v^2 - 1$
γ	Ratio of specific heat
δ	$\frac{M_v^2}{M_a^2}$
ϵ	Expansion parameter
η	Characteristic coordinate or similarity coordinate
θ	Angle
Λ_m	Magnetic interaction length (dimensional)
μ	Mach, Mach-Alfven angle
μ_o	Vacuum permeability
μ_j	Coefficient in the Fourier transform of v_1
ν_1, ν_2	Solutions of the fourth order characteristic equation
ξ	Characteristic coordinate
ρ	Density
σ	Electric conductivity
$\Upsilon(X)$	Step function
ϕ	Angle
χ	Angle
ω	Vorticity or frequency

Chapter 1

Introduction

1.1 General Description of the Magneto Dynamic Accelerator

1.1.1 Electric Propulsion

In classical rocket engines, the exhaust velocity (and therefore the specific impulse) is limited by the chemical energy stored in the propellants and released by the combustion reaction within the engine. By using an alternative source of energy, namely an external electric generator, one can accelerate the propellant gas to higher velocities and also lower the fuel consumption needed to produce a given impulse.

However, increasing the exhaust velocity also means increasing the energy consumption. The choice of an optimal exhaust velocity thus depends on the specific power of the electric generator, on the mission duration, and on the total impulse needed for the mission. The higher the specific power of the generator (W/kg), the higher the optimal exhaust velocity will be.

Several electric propulsion engines have been investigated. The most commonly known is the ion engine. In this system the ions are accelerated by an electric field present between two electrodes. They leave the thruster with an energy corresponding to the potential difference between the electrodes. This system can accelerate the ions to very high velocities, but it is inefficient at lower exhaust velocities.

A second class of propulsion devices is known as the arcjet. In this system the propellant is heated by an electric discharge. The electric energy is converted into thermal energy by Ohmic dissipation. The thermal energy is then recovered by expanding the gas through a supersonic nozzle. This device is the closest to a traditional rocket engine, both in performance and in physical construction.

A third class of devices can be identified: the electro-magnetic accelerators. In these systems a magnetic field plays a significant role in the acceleration of the plasma. This dissertation is focused on a particular device, the magneto-dynamic accelerator, also known as the Magneto-Plasma-Dynamic Thruster (MPD), or as the Magneto-Plasma-Dynamic Arcjet. This system is a good candidate for electric propulsion since it is able to generate exit velocities of the order of 50 km/s.

In such a system there are two modes of acceleration: the electro-thermal mode and the magneto-dynamic (also known as the electromagnetic) mode. The electro-thermal mode is similar to the mode of operation of an arcjet. The magneto-dynamic mode corresponds to the mode of operation of an ordinary D.C. electric motor, and is characterized by a potentially higher efficiency. This suggests that the efficiency of the thruster might be increased if the magneto dynamic mode were made dominant. A simple analysis based on dimensional considerations shows that the ratio between the electro-magnetic and the electro-thermal powers is proportional to a non-dimensional number called the magnetic Reynolds number.[1] This suggests that there is a practical benefit to studying the theory of the magneto-dynamic thruster for large magnetic Reynolds numbers: the more efficient magneto-dynamic mode becomes dominant when the magnetic Reynolds number is large.

The main focus of this thesis is to study the relative effects of the electromagnetic and the electro-thermal forces on the flow of the plasma within an idealized self-field accelerator in the framework of a resistive magneto-hydrodynamic model.

---

[1] For a more detailed discussion, see the appendices at the end of the dissertation, in particular appendix B.

1.2 Experimental Background: Phenomenological Description

1.2.1 Typical Devices

Experimental magneto-dynamic accelerators have been tested since the 60's. The major programs were canceled in the early 70's, but related research continued on a small scale in the USA, the USSR, Japan and Europe. A cutaway view of an idealized thruster is shown in figure 1-1, and some thruster geometries are shown in figures 1-2, 1-3, and 1-4. They consist of a combination of two coaxial electrodes, the outer electrode being the anode (the positive electrode), and the inner electrode being the cathode (negative electrode). The electrodes also play the role of the nozzle, and their geometry contributes to the shaping of the flow. The current flowing from the anode to the cathode through the plasma creates a magnetic field which is in the azimuthal direction, i.e. $\mathbf{B} = B_\phi \mathbf{e}_\phi$. This field is called self-field, because it is a consequence of the current flowing through the device. The magnetic field is confined between the two electrodes. It has a maximum at the inlet of the plasma chamber near the root of the cathode, and decreases downstream (with increasing z), as well as radially (with increasing r). In addition some designs have incorporated an external coil generating an axial magnetic field, whose purpose is to stabilize the flow and to act as a magnetic nozzle. This improves the thrust and the system efficiency. Since the current drawn by these devices can be considerable, many experiments are done with short current pulses, with an instantaneous current of several tens of kiloamperes, and powers of several megawatts.

A review of the performance of magneto-dynamic accelerators has been recently published by Sovey and Mantenieks [58]. The experimental results indicate a general increase of propulsive efficiency as the current is increased. However there exists a threshold above which the discharge becomes highly unstable. This unstable regime is characterized by high frequency oscillations of the interelectrode voltage. Kurtz, Auweter-Kurtz *et al.* [31] found the oscillations to be in the $200 - 300$ kHz range.

The maximum efficiency is about 20-25% when argon is used as propellant, and seems to increase for lower atomic mass propellants. The onset of instabilities can be experimentally correlated with a critical value of the ratio $\frac{I^2}{\dot{m}}$ (where I is the current and $\dot{m}$ is the mass flow rate,) which depends on the type of gas used as propellant and is higher for the lower atomic masses as reported by Lien and Garrison [36].

The next section will concentrate on some important phenomena which have been observed experimentally.

1.2.2 Current Distribution

An example of current patterns observed experimentally is shown in figure 5-9. It can be seen that as the current flows from the anode to the cathode, it concentrates at both ends of the electrodes. Notice that the current lines do not strike the surface of the electrodes at right angles. On the cathode, the current lines concentrate at the upstream end, and on the anode they concentrate at the downstream end. In the exit region the current lines converge towards the corner at the end of the anode, some of them attach on the corner's downstream side.

1.2.3 Anode Depletion

A decrease of particle density (neutral particles, ions and electrons) in the vicinity of the anode has been observed at high current. Due to the high thermal fluxes and the short response time needed for the sensor, the actual measurement of particle densities within the thruster is a difficult task. The experimental evidence is mostly related to the measurement of the charged particle densities (n_e and n_i) by indirect methods.

Vainberg *et al.* [63] have reported estimates of the electron density obtained by using an electrostatic probe and by measuring the anode potential drop. The electrostatic probe measures the relation between the probe potential drop (U) and probe current flow (I). Combining these (U,I) characteristics with some assumptions about the thermodynamical state of the plasma, one can estimate the electron density and temperature in the neighborhood of the probe. In the second method, they measured the anode potential drop which is the potential drop in the non-neutral layer which covers the anode surface. Normally this layer is electron-repelling due to an excess of negative charges in the layer, and the potential drop is therefore negative. They have measured the change of this potential drop as a function of the mass flow rate and of the total current. They observed that for high values of the $I^2/\dot{m}$ ratio, the potential-drop across the non-neutral electrode layer changes sign and becomes positive. This observation can be interpreted as an indication of a decrease in electron density within the plasma at the edge of the non-neutral layer.[2]

Another evidence of low electronic density near the anode was provided by the experiment described by Kilfoyle *et al.* [26]. They observed the spectroscopic emission in the gas near the exit plane of a self field magneto-dynamic thruster working near the threshold of instabilities. They measured the line broadening of the H_α and H_β lines of hydrogen. From these measurements, they were able to estimate the electron density in the region near the exit plane. They observed a maximum density near the cathode and a minimum near the anode. The minimum appears to be very low, and the point where the density is half of the maximum value is located halfway between the electrodes.

These observations of low ionic and electronic density near the anode have two consequences. One is the suggestion that one-dimensional models may be inadequate to describe the thruster behavior since the transverse gradients may be more important than the longitudinal.

Another consequence of this depletion has to do with the stability of the thruster. Although there is no general consensus on the theory or on the actual mechanism of this instability, many authors like Baksht *et al.* [4] have suggested that the mass-

---

[2] This is briefly explained below. The anode current-density can be estimated as $j_a = j_e e^{\frac{e\Delta V_a}{kT_e}}$ where ΔV_a is the anode drop, $j_e = \frac{1}{4}\bar{c}_e n_e$ is the electron thermal flux in the plasma, T_e is the electron temperature and $\bar{c}_e \sim \sqrt{T_e}$ is the mean thermal velocity for the electrons. If T_e is constant, a decrease of n_e can only be compensated by an increase of ΔV_a. If the density becomes very low, ΔV_a can become positive. In addition, this saturation ($j_a \geq j_e$) can only occur in highly ionized plasmas. In weakly ionized plasma, the necessary current can be provided by additional ionization of the plasma.

depletion near the anode is the cause of high current instabilities. This question will be addressed again below.

1.2.4 Effect of the Tank Pressure

There has been some controversy about the extent to which test measurements made on the ground reflected the true performance of the thrusters in vacuum. Some researchers have postulated that thrust level and efficiency were often overestimated in ground tests because the thrusters were fired in tanks which could not reach the low pressure level likely to be encountered in outer space.

The effect of ambient tank pressure on the thrust and arc voltage of a 70 kW continuously fired *self-field thruster* was studied by Kurtz, Auweter-Kurtz *et al.* [30]. They considered tank pressures in the 10^{-1} to 1.3 Pascal range. Although they did not notice measurable changes in the 10^{-1} Pa to 2.6×10^{-1} Pa range, they observed a small increase (~ 2.5 %) in arc voltage and a small decrease (~ 5 %) in the thrust as the pressure was increased to its maximum value of 1.3 Pascals.

The effect of ambient pressure on the performance of the applied field thruster was studied in a series of experiments at NASA's Lewis Research Center by Connolly *et al.* [15]. They observed that the performance varied with the background pressure; at high pressure (13 Pa) the thrust to pressure ratio could be increased by a factor of two over the low pressure ratio. At intermediate pressure, this ratio could go as low as half of the reference ratio. They attributed these effects to the entrainment of background gases into the arc discharge. Using spectroscopic methods, Connolly *et al.* measured the species' axial velocity in the plume. They observed that a significant part of the acceleration occurred as far as 10 cm from the exit plane. This observation suggests that some of the electromagnetic interactions may happen outside the thruster, which would be consistent with the presence of a significant amount of magnetic field and currents downstream of the exit plane. This also suggests that the analysis of a thruster could be incomplete when the condition beyond the exit plane is not considered.

1.2.5 Onset of Instabilities

Experiments have shown that the overall efficiency and the exhaust velocity increase with the current. Unfortunately the flow becomes highly unstable above a certain current. This unstable regime is characterized by large fluctuations in the arc voltage and a simultaneous increase of the electrode erosion rate on the cathode and on the anode. The threshold of these instabilities is a function of mass flow rate and total current. It has been correlated with a critical value of the parameter: $\frac{I^2}{\dot{m}}$.

The phenomenon is poorly understood and several theories have been proposed to explain these instabilities. Baksht *et al.* [4] suggested that it may be related to the disappearance of charge carriers near the anode. These carriers are removed by the action of the magnetic field on the plasma near the anode. When the carrier density becomes too small, a diffusive discharge is no longer possible and experiments have shown that the discharge breaks up into a number of concentrated conductive channels which are animated with rapid motion over the anode surface. This mode is called the anode spot mode. However it is not clear how the transition from a diffuse discharge to a multiple anode spot discharge can affect the stability of the bulk of the discharge away from the anode.

Some researchers have also attempted to correlate the onset of instabilities to cathode and bulk processes. Kilfoyle *et al.* [26] looked at the spectroscopic emission of Ar and Ar^+ near the exit. Through a measurement of the anode potential drop they observed a charge carrier depletion near the anode at high currents. However, this depletion was observed at a current level (35 kA) for which the flow remained stable. They also observed that the emission of Ar becomes very weak near the threshold of instabilities around 60 kA at 4 g/s. These observations suggest that a mechanism other than anode depletion may be the source of the unstable behavior.

1.3 Magneto-Hydrodynamic Theories

In order to understand the behavior of the thruster it is convenient to use a magneto-hydrodynamic model, which assumes that the plasma can be described as a fluid. This assumption is considered satisfactory when the collision frequency is large enough to maintain local thermodynamic equilibrium, at least for each species considered. In the case of most magneto-dynamic thrusters, the local thermodynamic equilibrium is usually valid, assuming different equilibrium temperatures for the electrons and the heavy species.

1.3.1 One-dimensional Models

Kuriki *et al.* [29] have presented a justification of the current distribution based on a one-dimensional, one-fluid, magneto-hydrodynamic model. They consider a narrow channel, assume that the quantities vary only in the streamwise direction, and neglect the Hall effect and the pressure. The authors show that the current tends to concentrate at both ends of the channel. They identify the magnetic Reynolds number as a parameter which controls the shape of the discharge. This parameter represents the relative strengths of the diffusive and convective effects on the magnetic field, and it is defined by

$$R_m = \mu_0 \; \sigma_0 \; u_{ref} \; L_{ref} \tag{1.1}$$

where μ_0 is the magnetic permeability of vacuum, σ_0 is the electrical conductivity, u_{ref} is the reference velocity, and L_{ref} is the reference length, in this case the thruster length.

As the same time it is possible to define a scale length Λ_m for which the diffusive and convective effects are of the same order. This scale length will be called the magnetic interaction length in the rest of this thesis and is defined by the following expression:

$$\Lambda_m = \frac{1}{\mu_0 \sigma u_{ref}} = \frac{L_{ref}}{R_m}. \tag{1.2}$$

With this definition the magnetic Reynolds number becomes:

$$R_m = \frac{L_{ref}}{\Lambda_m}. \tag{1.3}$$

As the magnetic Reynolds number increases, the concentration at the ends of the channel becomes more pronounced. They distinguish between three regions: the inlet concentration where there is a strong dissipation, the core of the channel where there is little current and little dissipation, and the exit concentration region, again with strong dissipation. The current concentration regions have a thickness of the order of the magnetic interaction length Λ_m As the magnetic Reynolds number decreases, the end-regions eventually overlap each other, creating a rather homogeneous discharge over the whole length of the channel. The authors considered the effect of the electrode geometry on the solution of their one-dimensional model. They predicted that the best efficiency is given by the convergent-divergent geometry, which allows a smooth passage from sub-alfvenic to super-alfvenic flow.[3]

In a later article Kunii *et al.* [28] compared the results of their theory with experiments. They confirmed the tendency for the current to concentrate near the electrode ends with increasing total current. However they were unable to match the experimental shape of the current distribution along the electrodes with the predicted values. They observed that the most efficient geometry was the divergent geometry, and not the convergent-divergent geometry predicted by the theory.

Martinez-Sanchez [39],[40] has extended the above theory to include the effect of the pressure on the flow. By adding an energy equation he was able to confirm the theoretical results of Kuriki *et al.* in particular in the regime of high magnetic Reynolds number ($R_m \gg 1$), where the flow is everywhere supersonic. In addition he predicted the existence of a mixed supersonic/subsonic regime which appears when the magnetic Reynolds number falls below a threshold value. In this regime the supersonic and subsonic regions are separated by a shock, which introduces additional losses and decreases the efficiency. This shock is imposed by the constraint that the flow be choked at the exit, or that the exit Mach number cannot become less than one,

---

[3] The alfvenic velocity is the velocity at which small amplitude waves propagate transverse to the magnetic field in a cold magnetized plasma. The equivalent to the Mach number for these waves is called the Alfven number and is defined by,

$$A_v = \frac{u}{\sqrt{2b^2/\rho}}, \tag{1.4}$$

where the variables are written in non-dimensional form.

since the thruster flow exits into the vacuum. If one reduces the magnetic Reynolds number still further the channel eventually becomes completely subsonic, and the shock disappears. Martinez-Sanchez has studied the effect of the electrode gap variation on the properties of the discharge, and confirmed the theoretical results of Kuriki *et al.*, suggesting use of a converging-diverging geometry in order to increase the overall efficiency. Martinez-Sanchez also presented a perturbation method which solves the equations by separating the inlet and exit regions from the non-dissipative core of the discharge. An analytic solution based on this perturbation method was given for the case where the pressure is neglected, and a numerical solution was presented for the case of an ideal gas and for the case of an ionized gas in thermodynamical equilibrium. This analysis introduces two important non-dimensional numbers: the Mach number

$$M_a = \frac{u}{\sqrt{\gamma p/\rho}} \tag{1.5}$$

which indicates the ratio between the fluid velocity and the classical speed of sound, and the Mach-Alfven number

$$M_v = \frac{u}{\sqrt{\gamma p/\rho + 2b^2/\rho}} \tag{1.6}$$

which indicates the ratio between the fluid velocity and the magneto-acoustic speed of sound. It was found that the Mach-Alfven number appears in the large-scale flow behavior in the outer solution whereas the Mach number appears in the inner solution, namely the resistive inlet layer, and controls the shock behavior.

Subsequently Heimerdinger [24] undertook an experimental validation of the theoretical predictions. He studied a quasi one-dimensional thruster with several cathode geometries: a constant area channel, a divergent channel, and a convergent-divergent channel. He measured the current density in the channel and estimated the thruster efficiency. He reported that the divergent and convergent-divergent channels had a higher efficiencies than the constant area channel.

In an effort to analyse the effect of the non-ideal character of the plasma, Martinez-

Sanchez and Niewood [47] have extended the one-dimensional model by including some of the physical effects which are potentially important, in particular the distinction between electron and heavy-particle properties. The underlying idea was to describe the plasma by a two-fluid hydrodynamic model with separate properties (density, temperature, velocity) for the electrons and the heavy particles (ions and neutrals). Each fluid is considered to be in local thermal equilibrium. The authors allowed for different electron and heavy particle temperatures, different velocities, non-equilibrium ionization, viscous friction, and the ambipolar charge diffusion to the walls. Experiments show that this description is required when the plasma density is low and the collisions are not frequent enough to maintain a unique temperature for the whole plasma.

They presented the results of numerical simulations which included various combinations of these phenomena. Most of these simulations were done for a magnetic Reynolds number of approximately 5, which can be considered to be the lower end of the magneto-dynamic regime. Their results showed that the current distribution is not significantly modified by the presence of these effects, but that the efficiency is lowered by ionization and viscous losses. The viscosity of the fluid had the largest effect both on the distribution of the current along the electrodes and on the efficiency. Its effect was to distribute the current more uniformly on the surface of the electrodes. They concluded that the plasma was not fully ionized even near the thruster exit plane, and they noticed large temperature differences between electrons and heavy particles.

In conclusion it appears that one-dimensional resistive magneto-hydrodynamic models of the plasma flow can quantitatively explain the current concentration at the ends of the electrodes, and predict the thrust with a good accuracy. But magneto-hydrodynamic models do not accurately predict the voltage, which is equivalent to overestimating the efficiency. Nor do they explain the mechanism by which the thrusters become unstable at high current.

1.3.2 Shortcomings of One-Dimensional Models

Since real flows are two- or three-dimensional, a study based on a one-dimensional model raises the question of its applicability. The argument which leads from an original two-dimensional model to a one-dimensional approximation is usually the following: The quantities can be averaged over the cross section of the thruster, for instance

$$< a >= \frac{1}{\Sigma} \int a \, d\Sigma$$

and the original set of partial differential equations reduces to a set of ordinary differential equations. In order to relate these averaged quantities to each other, it is necessary to assume that the average of a product can be approximated by the product of the averages:

$$< ab >=< a > < b > .$$

This last operation may not be valid, in particular when the quantities are very inhomogeneous. Although it can be seen that this approximation becomes nearly exact when the variables are nearly uniform on the integration surfaces, in general there is no guarantee that the results of a particular problem will be meaningful, and it is difficult to estimate the order of magnitude of the error introduced by the averaging method.

Kevorkian and Cole [25] offer another argument to justify the applicability of a one-dimensional model. This argument is based on a limiting process where the thickness of the channel is a small parameter which goes to zero. The solution is then sought as an asymptotic expansion in terms of the small parameter. This method incorporates the influence of the boundary conditions directly. An analysis of the magneto-hydrodynamic model shows that according to Kevorkian and Cole's definition, the one-dimensional model does not apply to the magneto-dynamic thruster, because some of the quantities (namely ρ, u, T) do not assume a one-dimensional distribution in the limit of narrow channels. Therefore it seems that the one-dimensional model is built on shaky mathematical grounds.

In addition there are two important issues which have not been addressed by the one-dimensional models described above, namely the effect of the Hall conductivity on the channel flow, and the analysis of the exit region where the flow expands into vacuum. The Hall parameter reflects the relative level of the electron collisions frequency $1/\tau_e$ and the electron cyclotron frequency ω_{ce}, and is defined by:

$$H_a = \omega_{ce}\ \tau_e. \tag{1.7}$$

Even in narrow channel geometries where the one-dimensional model is *a priori* likely to be accurate, the effect of the Hall conductivity introduces constraints on the solutions which imply the presence of very strong gradients in the transverse direction.

Finally the analysis of the exit region of narrow channels poses another difficulty as the problem changes from a channel-flow to an expansion into the vacuum. In the one-dimensional models considered above, the calculation is ended somewhat arbitrary at the end of the electrodes where the boundary condition $B = 0$ is usually applied. However experimental plots of the current lines show that a significant fraction (10 to 20%) of the current flows outside the channel.

Consequently it appears that the one-dimensional model may not be adequate in order to understand the thruster behavior, and it seems logical to look at two-dimensional flows.

1.3.3 Two-Dimensional Models

Two approaches can be employed to study two-dimensional models of magneto-dynamic flows. One approach is to simplify the model to the point where it can be solved analytically, or can be reduced to a quadrature. Another approach is to rely on numerical simulations.

As for the first approach one should mention the work done in the Soviet Union during the 1960s. The review presented by Morozov and Solovev in [35] summarizes their research. In [44] Morozov and Solovev considered ideal magneto-hydrodynamic flows in axisymmetrical nozzles. They obtained analytic solutions for narrow channels and for flows with slowly varying parameters along the axis of symmetry. In [45] they extended their analysis to include the Hall effect. In these analyses, the resistivity is ignored, and consequently the inlet acceleration layer (see chapter 2) is not taken into account.

Baksht *et al.* proposed a method to reduce the two-dimensional analysis to a one-dimensional problem by averaging the quantities across the channel. By taking into account the local behavior of the low density layer along the anode surface they predicted the impossibility to pass more than a certain amount of current through the accelerator. This maximum current corresponds to the value for which the entire anode surface becomes electron-attracting. They show that the saturation occurs when the parameter $I^{7/4}/\dot{m}\sqrt{M}$ reaches a critical value. (Here I is the total current, $\dot{m}$ is the mass-flow rate and M is the atomic mass of the accelerated species.) This theory fits well with the parameter $I^2/\dot{m}\sqrt{M}$ used by experimentalists to predict the onset of instabilities.

Soviet work based on numerical simulations dating from the same period is reviewed by Brushlinskii and Morozov in [35]. Most simulations are based on one-fluid MHD models, and consider simple (idealized) geometries, including a convergent-divergent nozzle and an axisymmetrical accelerator with a short central electrode. The authors rely on a time-marching algorithm. They consider three classes of problems: the non-resistive plasma, the resistive plasma without the Hall effect, and the resistive plasma with the Hall effect. Numerical results were easily obtained in the first two cases, but the simulation of resistive plasmas with the Hall effect could only be obtained within a narrow range of parameters. They report that their calculation becomes unstable when the Hall effect exceeds a critical value which is a function of the plasma-β (defined by $\beta = \frac{p}{b^2}$) and of the magnetic Reynolds number. They obtain the following correlation: $H_a^* = \beta^{1/4}R_m^{1/2}$. If one assumes that the plasma-β is independent of of the geometry (which is supported by the results of the one-dimensional model,) and is also independent of the Hall parameter, and if one accepts the authors' suggestion that the calculation's unstable behavior corresponds to a physical instability, this correlation suggests that the stability of the device can be improved by increasing the Reynolds number, that is by increasing the thruster length. The authors also presented a series of results for an axisymmetric thruster with a short central electrode. They noticed the presence of a compression region along the axis of symmetry, starting at the tip of the central electrode. This compression region was characterized by very high temperatures and densities. Subsequently they extended their model by including ionization processes. Under certain conditions they observed sharp temperature oscillations and periodic changes in the the position of the ionization front. All their calculations start with a flow which has its origin at $-\infty$. In this situation the dissipative effects which would normally appear within the inlet acceleration layer are ignored, and it is not possible to predict the effect of this dissipative region on the flow.

Kimura *et al.* [27] presented a two-dimensional simulation of a self-field magnetodynamic thruster in the limit of very *small* magnetic Reynolds Number. In this limit the thruster works in the electrothermal regime, the convective term can be neglected in the magnetic field equation, and the magnetic field can be solved independently from the flow of the plasma. The authors did not attempt to calculate the plasma flow, but limited their analysis to the magnetic field. This magnetic field is controlled by an elliptic equation which was solved by a finite difference method. The Hall effect which appears both in the equation and in the boundary conditions was included in the analysis. They calculated the current distribution on the electrodes for several values of the Hall parameter, and concluded that the Hall phenomenon displaced the current distribution toward the exit along the anode surface, and toward the inlet along the cathode surface. They compared their calculation to experimental results and concluded that there was a good correlation as long as the Hall effect was included.

Tanaka *et al.* [59] extended this model to systems working with an external focusing magnetic field. From their numerical simulation they concluded that the external magnetic field changed the current flow and the current distribution along the electrodes. In particular, they observed that the applied magnetic field compensated some of the effects of the Hall conductivity along the cathode by reducing the concentration of current on the upstream part of the electrode and by increasing the current concentration on the downstream part of the anode. Finally they noticed that the flow pattern moved progressively outside of the thruster as the applied magnetic field was increased, despite the complete absence of any convective effect in their model.

In a subsequent paper Tanaka and Kimura [60] have included the convection term in the magnetic equation and estimated the plasma flow using a quasi one-dimensional model which was coupled to the magnetic field. The effects of the magnetic field on the plasma are averaged in the direction normal to the streamwise coordinate and then applied to the one-dimensional variable-area model. Similarly the results of the model are applied to the magnetic field equation assuming that the flow quantities are constant in the direction normal to the streamlines. This coupling method raises a question which was left unanswered: what indication do the authors have that the averaging-coupling process will not erase some significant two-dimensional features of the flow?

In a previous study [12] the author of this dissertation developed a two-dimensional numerical simulation based on a one-fluid, isothermal, magneto-hydrodynamic model of the plasma. The system of partial differential equations was discretized using a finite volume technique and the steady state was solved using a Newton-Raphson method. This simulation was limited to small magnetic Reynolds numbers corresponding to the electrothermal regime.

In addition Sleziona, Kurtz, Auweter-Kurtz and Schrade [57], [3] have presented several numerical simulations corresponding to small and medium R_m, characteristic of the type of experimental thrusters studied at the University of Stuttgart.

More recently, Niewood [48] presented axisymmetrical two fluid simulations with magnetic Reynolds number below 5. He studied the Hall effect as well as non-equilibrium effects. He confirmed the existence of a strong mass-depletion along the anode.

In conclusion, several two-dimensional numerical simulations of magneto-dynamic thrusters have been presented in the literature. However none of these models covers the regime of high magnetic Reynolds numbers. This limitation is essentially due to the presence of numerical problems at high currents, namely unstable codes and non-physical results like negative temperature, entropy decrease, *etc.*

1.4 Other Aspects of Magneto-Dynamic Accelerator Flows

So far the discussion was centered on theories and simulations based on resistive magneto-hydrodynamic equations. At this point it seems necessary to widen the object of the discussion and to pay some attention to several physical phenomena not considered before.

1.4.1 Transport Phenomena

In addition to electric conductivity other transport phenomena have an impact on the flow inside a magneto-dynamic thruster. Classical transport coefficients based on the Boltzmann theory of atomic and electronic collisions, will be considered first.

The most important of these phenomena, in addition to the electric resistivity, is most likely the viscosity. The viscous friction within the fluid creates additional losses which increase the plasma temperature and entropy and decrease the maximum efficiency. Viscous boundary layers exist near the electrode surfaces. An estimate of the size of these boundary layers is given in appendix D. It shows that the viscous scale length is smaller than the magnetic scale length, so that viscous boundary layers will be smaller than magnetic boundary layers. However, for flows in narrow channels (when the width is not large compared to the magnetic interaction length) viscous boundary layers are expected to merge, and a parabolic velocity profile should appear in the channel. Niewood and Martinez-Sanchez [47] have considered the effect of viscosity on the flow in a slender magneto-dynamic thruster. They concluded that the addition of viscosity drastically lowers the overall thruster efficiency.

Along with the viscosity, the thermal conductivity is responsible for some additional decrease in the overall thruster efficiency. Since the plasma is composed of different species, an additional transport phenomenon exists which has no equivalent in the one-fluid MHD model, namely the diffusion of species as a response to density gradients. The ambipolar diffusion mechanism transports energy from the core of the discharge to the walls, where a fraction of the ionization energy is lost to the wall when the ions and electrons recombine on the electrode surface. In addition experimental data indicate that the electron temperature is very nearly constant. A high electron thermal conductivity contributes to maintaining the electron temperature within narrow bounds. An accurate evaluation of thermal conductivity, of the electron diffusion rate and of the electron density is important in order to predict the heat transfer to the electrodes. These effects were studied by Niewood and Martinez-Sanchez using a one-dimensional model described in [47].

One must also pay attention to the so-called anomalous transport coefficients. When the plasma becomes turbulent the effective transport coefficients increase because of the mixing induced by the turbulence.

Gallimore *et al.* [19] have estimated the conductivity near the anode of a Princeton "benchmark" thruster by using measurement of current density near the anode and by assuming *ad hoc* expressions for the other unknowns. They concluded that the electrical resistivity near the anode is lower than the classical expression derived from kinetic theory (Spitzer-Härm formula), and that the discrepancy increases with higher current levels. The authors considered two mechanisms which could explain the discrepancy: one related to a boundary layer of nearly collisionless and highly magnetized electrons near the anode surface; and another related to the "anomalous transport" due to small scale instabilities.

Hastings and Niewood [23] considered a modified two-stream instability and estimated its effect on the electric conductivity, as well as on the ion heating rate. They concluded that the instability could increase the resistivity by at least an order of magnitude. Choueiri [13] also attributes the increase of resistivity to the onset of small scale turbulence due to a two-stream instability. Tilley *et al.* [61] considered two types of instabilities: the electron-cyclotron drift instability and the generalized lower hybrid drift instability. These last two articles do not give quantitative predictions for the anomalous plasma resistivity, however Choueiri has proposed correlations between the anomalous resistivity and the local Hall effect derived from experimental measurements.

The plasma fusion community has done a considerable amount of work on anomalous resistivity in the context of tokamaks and other fusion machines. However many of these results are derived for conditions which are very different from that of magneto-dynamic thrusters, and therefore not directly applicable.

In order to be consistent, any consideration of "anomalous transport" should be done systematically for all transport phenomenona including the Hall effect. This means that a new Ohm's law must be derived in a consistent way. An additional effect should also be expected on the plasma viscosity, considering the sensitivity of the viscosity to the ionization fraction.

1.4.2 Onset of Macroscopic Instabilities

Experimental observations have shown that the thruster regime of operation becomes unstable for large currents. The onset of macroscopic instabilities has important practical consequences since these instabilities are often destructive in nature. Several theories have been proposed in order to explain the physics of these instabilities, and to predict the limit of the unstable regime.

A first theory suggests that the onset of instability appears when the whole surface of the anode is depleted of charge carriers by the Hall effect. A criterion for anode starvation was derived by Baksht, Moishes, and Rybakov [4]. Although the authors did not claim that starvation was a cause of instability their theory is often considered a theory of onset of macroscopic instabilities because they were able to predict the scaling law observed experimentally.

Lawless and Subramanian [34] have suggested that the onset of instability was due to a limitation on the value of the "electromotive force": $\mathbf{E}_{EMF} = \mathbf{u} \times \mathbf{B}$. However this theory is not satisfactory because it is based on a misunderstanding of the free parameters in the one-dimensional problem. The authors' argument can be summarized as follows: the one-dimensional model cannot have solutions when the ratio $\frac{I^2}{\dot{m}}$ is larger than a certain critical value. But it can be shown (see chapter 2 for the details) that the one-dimensional model always has a unique solution for any value of $\frac{I^2}{\dot{m}}$, and therefore the mechanism proposed by Lawless and Subramanian cannot be a possible explanation for the onset of instabilities.

Schrade *et al.* [53] have suggested that the onset is due to a loss of axial symmetry in the discharge. Their theory relies only on magneto-hydrodynamic effects, and predicts a localized current concentration at the anode surface which is consistent with the increase of erosion rate observed in experiments. However the theory does not predict the unsteadiness of the phenomenon.

Niewood, Preble *et al.* [49] have investigated two mechanisms: the electrothermal and the modified two-stream instabilities. They concluded that both of these mechanisms were likely to be present in experimental systems. Moreover, the electrothermal mechanism correlates well with experimental observations of the unstable regime.

The modified two-stream instability mechanism was also investigated by Hastings and Niewood [23] and by Choueiri [13]. The goal of this last author was to find an explanation for the onset of instabilities. A combination of theory and experiments lead him to believe that a two-stream instability was consistent with the experimental result and that the instability was strongest in the regions of large Hall parameter.

1.4.3 Other Aspects of Plasma Simulations

In parallel to the additional complexity of the physics of the flow one should also consider more general numerical methods and comment on their relevance to the simulation of magneto-dynamic flows. A logical approach is to consider what has been done in the various branches of plasma physics. Since the physics of plasmas varies considerably from one problem to the next, the numerical methods used in practice are fairly specialized, and depend on each application. A sampling of the numerical methods used in the various branches of plasma physics can be found in [17].

Most plasma simulation methods fall in two categories: particle simulations and finite difference methods applied to magneto-hydrodynamic models. Particle simulations are well-adapted to analyzing local phenomena, wave propagation, plasma stability, particle-wave interaction, and transient phenomena. Large scale phenomena are best studied with finite difference codes based on magneto-hydrodynamic models.

Ideal magneto-hydrodynamics dominates the simulation of astrophysical problems involving plasma interactions with magnetospheres. In the absence of collisions, transport processes are essentially anomalous. The principles of magneto-hydrodynamic simulation in space plasma are described by Sato in [51]. Specific problems associated with local interactions are treated by particle methods. The principles of particle simulations for space plasma are described by Matsumoto and Omura in [41].

The same distinction between particle and finite-difference models can be found in thermonuclear plasma simulations. Most small-scale problems are treated by the *Particle-In-Cell* method, reflecting the original interest in simulating high-temperature, unsteady, and collisionless plasmas. In this type of algorithm the plasma is simulated by a large number of particles while the electromagnetic field is described by its nodal values on a grid. An example of such program is described by Brackbill in [8]. Although particle codes are well suited to study transient phenomena they do not handle steady-state problems very efficiently. On the other hand fluid codes based on magneto-hydrodynamic models can be used to study the global plasma equilibrium and its stability problems. An example of magneto-hydrodynamic stability analysis using a finite element method can be found in [21].

In addition several methods were developed in order to simulate devices with rather different physics, like particle accelerators, free-electron lasers or millimeter-wave generators, most of them based of particle codes.

The methods most applicable to the analysis of space propulsion devices are those developed for the analysis of plasma switches. These devices often work in low-temperature, collisional regimes, with significant plasma velocities.

A program called MACH2 was developed for the purpose of simulating transient, collisional flows. The program can currently simulate the evolution of a plasma based on a one-fluid magneto-hydrodynamic model. It can model transport phenomena like electric conductivity and viscosity. It uses both Lagrangian and Eulerian meshes, and the transition from one to the other can be controlled so as to cluster a large number of grid points near a moving front. The model can also simulate the onset of anomalous transport at low density by using the appropriate model for the resistivity as a function of the plasma density.

This program has been used in the simulation of plasma switches by Buff *et al.* in [10] and [11]. It was designed to follow the dynamics of the transient regime appearing in pulsed discharges. However it is less practical when the steady-state regime is sought. The program assumes a predetermined distribution of magnetic field along the boundaries. In order to reach a steady state consistent with the behavior of the plasma, these boundary conditions must be updated taking into account the current flowing inside the plasma. This requires a careful analysis of the coupling, as well as some additional programming. When these problems are solved, this program can become a very efficient tool for studying magneto-dynamic flows.

1.5 Focus of the Thesis

1.5.1 General Philosophy

A large number of theories can be found in the literature, which attempt to explain the physics of the flow and onset of the unstable regime. Many of these theories are based on *ad hoc* hypotheses, often based on experimental correlations. This leads to a situation where each experimental phenomenon is explained by a different set of physical laws, some of them introduced without a logical reason, except for the fact that the results will match some particular experiment.

In reaction to this tendency of introducing *ad hoc* hypotheses, the author has attempted to formulate the simplest model which incorporates the minimum number of physical phenomena necessary to capture the following effects: the compressibility of the fluid (necessary since the the flows expands into the vacuum), the electric resistivity (necessary to describe the Ohmic heating of the gas), the Hall effect (which appears as the main performance limiting factor), the effect of convection on the magnetic field (the essence of the magneto-dynamic regime) and a simple thermodynamic model for the gas in order to have an indication of the energetic balance and temperature variations.

The author believes that a systematic progression from the simplest to the most complicated analytic model is more logical and easier to assimilate than a direct numerical simulation of a complete model including all the possible effects, whose results can be difficult to interpret.

1.5.2 What Will be Addressed by this Thesis

This thesis considers some of the two-dimensional effects which are not covered by the one-dimensional magneto-hydrodynamic model of Martinez-Sanchez. The main questions which are considered are, on one hand, the influence of the Hall effect on the flow through the accelerator, and on the other hand, the structure of the flow in the region of the exit plane where the plasma leaves the channel and expands into the vacuum.

It is believed that the plasma flow can be significantly modified by the Hall effect. The most direct consequence of this effect is to polarize the electrodes, canceling the symmetry between the anode and the cathode. Experimental data suggest that the Hall effect promotes the excursion of the current outside the thruster, and is responsible for mass depletion near the anode.

1.5.3 Method of Approach

The underlying idea in this thesis is to find approximate two-dimensional solutions, valid in the regime of high magnetic Reynolds numbers, which can be solved by a mixture of analytic an numerical methods. Two approaches are used in this thesis. The first approach is a singular perturbation method based on a small parameter which is taken as $\epsilon = \frac{1}{R_m}$. Using this approach the two-dimensional non-linear problem can be solved approximately by reducing the entire problem to several simpler ones. These problems are of two types, the outer and the inner problems.

The outer problems are valid away from the singular regions. The solution to an outer problem typically does not satisfy some of the boundary conditions. These boundary conditions must be satisfied by the appropriate inner solutions, and the relevant inner and outer solutions must then be matched in order to construct a solution which is valid over the whole domain. In this case the outer problem is the non-resistive problem, governed by the equations of ideal magneto-hydrodynamics. The inner problems are valid near the boundaries. They are typically of higher order than the outer problems. Their solutions satisfy the boundary conditions (or internal conditions) relevant to their domain of definition, and must match asymptotically the appropriate outer solution(s). In this case the inner solutions contain the effect of resistivity. They are typically non-linear, and harder to solve than the outer solutions, but can sometimes be approximated by a one-dimensional or a self-similar solution

A second approach is a small disturbance linearization method. This method is a regular perturbation method. One considers a uniform flow, which is perturbed by a small change in the boundary shape. This method will be used to analyse the structure of the flow near the exit of an idealized thruster, first by looking at an isolated corner, and subsequently by analyzing the channel flow inside a weakly divergent thruster.

These two methods should provide qualitative results on the flow structure within the thruster and near the exit, including the scale of the phenomena, shape of the current lines, their attachment point.

1.5.4 Range of the Parameters R_m and H_a in Experimental Devices

Eventually the results of these models are compared with experimental designs chosen for their quasi one-dimensional geometries and their operating mode in the high magnetic Reynolds number. These designs are: a flared thruster studied by Wolff *et al.* [65] at Princeton University, shown in figure 1-2; a plasma gun studied by Schoenberg *et al.* [52] at Los-Alamos, shown in figure 1-3; and a constant area,

	Flared	Gun	Parallel
Gas	Ar	H, Ar	Ar
r_a [cm]	5	28	N.A.
r_c [cm]	0.9	18.5	N.A.
h (gap) [cm]	4.1	9.5	5.1
L (length) [cm]	22	112	13.3
I [kA]	21.3	100	104
$\dot{m}$ [g/s]	3	5	24
u_{ref} [km/s]	(25.1)	(82.9)	(94.)
σ [Si/m]	(3000.)	(3000.)	(3000.)
Λ_m [cm]	(1.1)	(0.32)	(0.28)
$R_m(L)$	(20.8)	(350)	(47.3)
$R_m(h)$	(3.8)	(29.7)	(18)
H_a	(2.)	?	?

Table 1.1: Operating characteristics of several thrusters. The first thruster is a quasi-one-dimensional thruster with a flared anode, studied by Wolff, Kelly and Jahn at Princeton. The second thruster is a large plasma gun studied by Schoenberg *et al.* at Los Alamos. The third thruster is a parallel plate thruster studied by Di Capua, Kelly, and Jahn at Princeton. The parameters which are in parenthesis have been estimated.

thruster studied by Di Capua *et al.* [16] at Princeton University, shown in figure 1-4. The characteristic parameters of these devices are described in table 1.1. In addition some qualitative comparisons will be made with other experimental results.

1.5.5 Formulation of the Problem

The plasma is described by a two-dimensional magneto-hydrodynamic model of the discharge, where the gas is assumed to be ideal, with constant γ and constant conductivity σ. The geometry is cartesian with the flow in the (x, y) plane and the magnetic field is in the z-direction. The magnetic field is the self-induced field created by the current flow within the plasma. The details of the process leading to these equations is described in appendix A. After a suitable non-dimensionalization (which is described in detail in appendix B and which introduces the magnetic Reynolds number $R_m = \mu_0 \sigma u_{ref} L_{ref}$ and the Hall number H_a) the equations take the non-dimensional form:

$$\nabla(\rho\ \mathbf{u}) = 0 \tag{1.8}$$

$$\rho(\mathbf{u}\cdot\nabla)\mathbf{u} + \nabla p + \nabla\ b^2 = 0 \tag{1.9}$$

$$\rho^{\gamma}(\mathbf{u}\cdot\nabla)\left(\frac{p}{\rho^{\gamma}}\right) = \frac{2(\gamma-1)}{R_m}(\nabla b)^2 \tag{1.10}$$

$$\rho(\mathbf{u}\cdot\nabla)\left(\frac{b}{\rho}\right) = \frac{1}{R_m}\nabla^2 b \tag{1.11}$$

$$\mathbf{e} = -\mathbf{u}\times\mathbf{b} + \frac{1}{R_m}\nabla\times\mathbf{b} + \frac{H_a}{R_m}(\nabla\times\mathbf{b})\times\mathbf{b} \tag{1.12}$$

1.5.6 Justification of the Choice of the Model

In order to analyze the flow in a magneto-dynamic thruster some simplifications must be made. As a first step one can assume that the problem can be described by a one-fluid model. This simplification relies on the assumption that the fluid is very near thermal equilibrium. The consequence of this assumption will be most severe in the energy balance equation. However the longitudinal momentum balance will not be affected as much since the pressure term is small compared either to the gas momentum or to the magnetic pressure. For the same reason it seems reasonable to neglect the ionization, despite its considerable impact of the gas temperature, the thermal conductivity as well as the variation of the plasma enthalpy with the temperature.

The effect of the viscosity will depend on the relative size of the viscous boundary layer and of the channel height. In addition one can compare the relative effects of the viscosity and of the resistivity. For the thrusters considered in this analysis the viscous scale length is smaller than the magnetic scale length. This indicates that the main features of the discharge will be determined by the resistive transport, and that the viscosity will most likely bring smaller corrections to the main features of the flow.

Thus the most important transport phenomenon appear to be the resistivity of plasma, including the Hall term. This Hall term is responsible for a significant departure from the one-dimensionality in the flow in narrow channels, as will be shown in this dissertation. On the other hand the role of viscosity seems more benign in the sense that its most important effect will be some additional entropy losses. This will be confirmed in a particular case: in the analysis of the magnetic boundary layer which appears when the magnetized plasma flows along an insulator. This problem is treated in chapter 6. The results show that the plasma viscosity and thermal conductivity do not introduce significant modifications in the structure of the flow.

1.5.7 Structure of the Thesis

The dissertation will be structured in the following way: The first chapter contains the general introduction. It includes a review of the relevant experimental observations, and of the theories and models published in the literature. It introduces the formulation of the magneto-hydrodynamic model, and the goals of the thesis.

The second chapter contains, in a first section, a review of the one-dimensional theory of the magneto-dynamic accelerator in the case of a constant area channel. This should provide the reader, who may not be familiar with this theory, with the knowledge which will facilitate the understanding of the rest of the dissertation. The inlet inner-layer is then discussed in a second section. It will be shown that the inlet inner-layer, coupled to the outer solution by the asymptotic matching process, determines the flow properties in the channel except in the region near the exit. Finally this chapter introduces the properties of one-dimensional wave propagation in the plasma. The existence of two different length scales is put in evidence, and should be useful to understand the properties of the two-dimensional solutions.

The outer problem is discussed in the third chapter. The chapter starts with a general introduction of the flow properties in the absence of resistivity (ideal MHD), and introduces a finite-element numerical method which can be used to compute the outer flow. In addition the chapter contains a presentation of a method of characteristics and a qualitative analysis of the exit region

The fourth chapter contains the analysis of the flow in the region of the exit. This analysis contains elements of both the inner-outer singular perturbation method based on the parameter $\frac{1}{R_m}$, and of the regular perturbation method based on the boundary perturbations (small deflection angle). The chapter includes the discussion of the effects of these phenomena on the flow, and the prediction for the thruster performance.

The fifth chapter extends the linear analysis to the case of a weakly divergent channel. The influence of the channel height will be considered.

The sixth chapter contains an analysis of the flow along an insulating surface. This chapter introduces a self-similar method which gives the asymptotic solution of the magnetic boundary layer growing along an insulator. In the absence of momentum and heat transfer the model predicts an infinite temperature at the surface of the insulator. This singularity disappears when the momentum and heat transport are included in the model.

The seventh chapter summarizes the results and achievements of this research, as well as suggesting future work based on what was learned in this research.

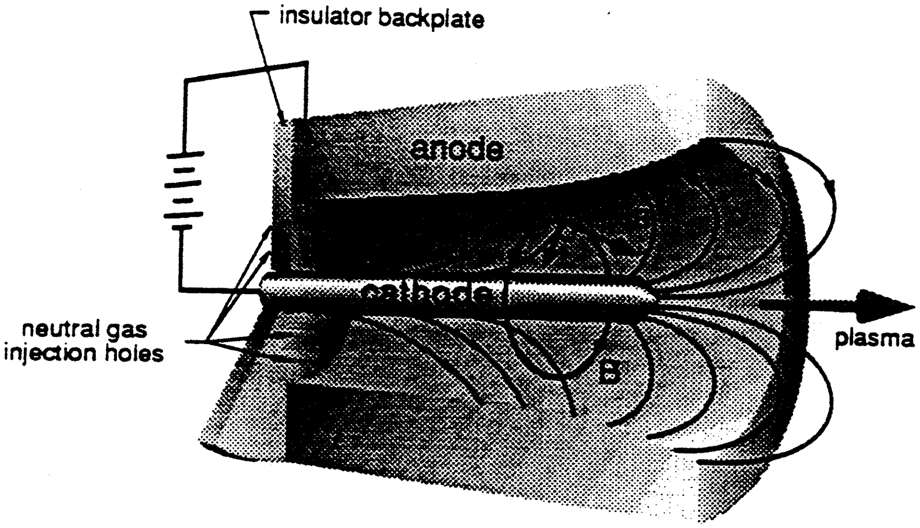

Figure 1-1: Cutaway view of an idealized thruster.

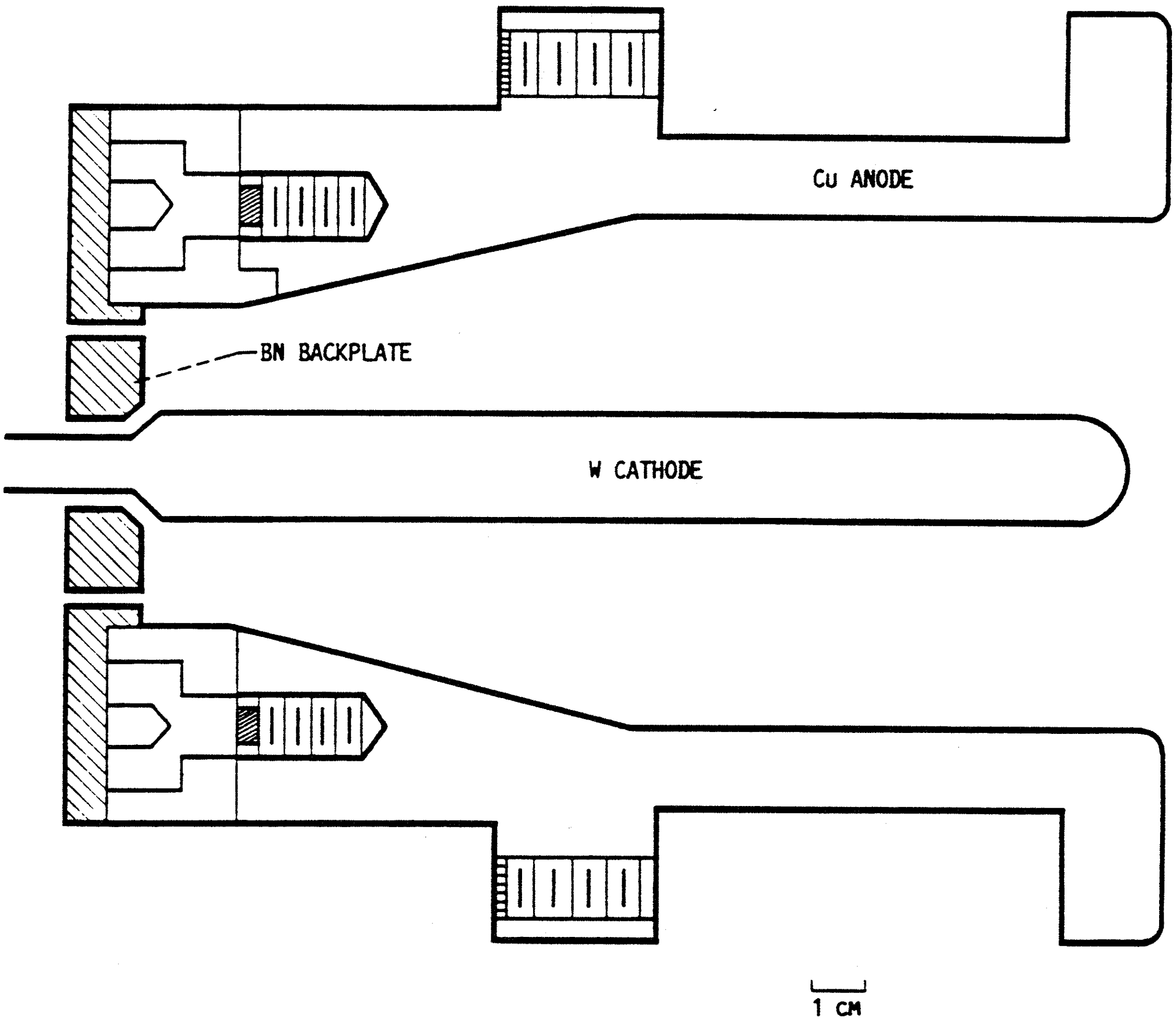

Figure 1-2: Example of an experimental device: a quasi one-dimensional self-field thruster from [Wolff, Kelly and Jahn, 1984]

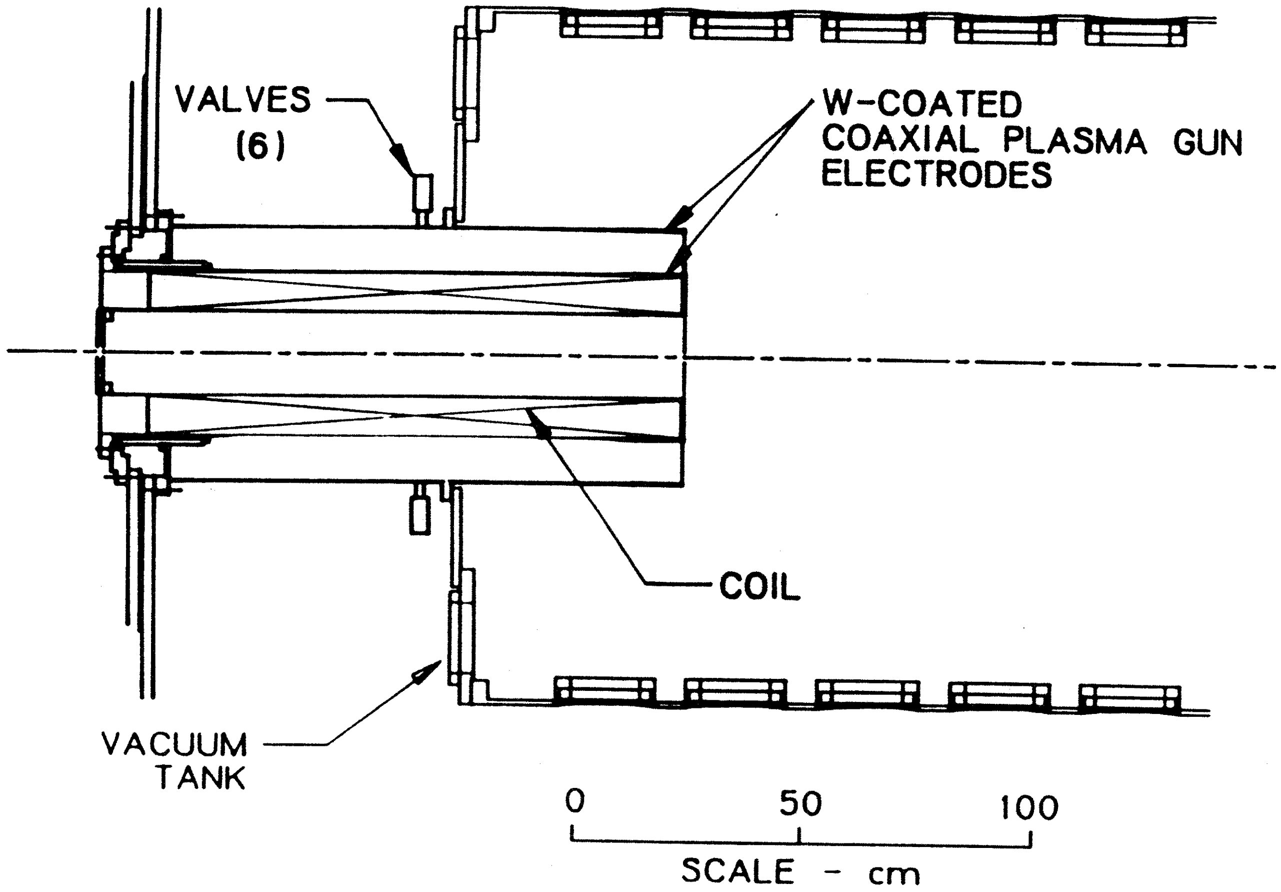

Figure 1-3: Example of an experimental device: a large plasma gun from [Schoenberg *et al.*]

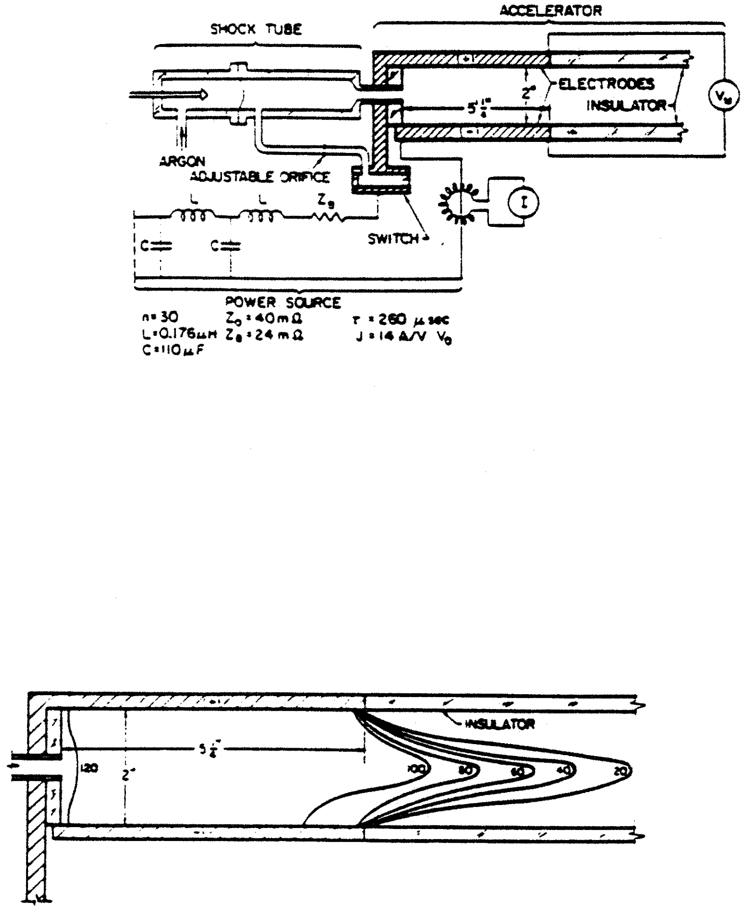

Figure 1-4: Example of an experimental device: a parallel plate thruster studied by [Di Capua and Jahn, 1971]. The lower drawing (b) shows the electrode geometry and an example of enclosed current contours.

Chapter 2

Review of the One-Dimensional Model

2.1 Solution to the One-Dimensional Constant Area Channel

This section reviews the analysis of the one-dimensional model for the constant-area channel. The model formulation is derived from the equations in conservative form described in the appendix A. After the appropriate non-dimensionalization, and dropping the derivatives with respect to y, one obtains the following system describing the flow of gas in a narrow one-dimensional channel. The unknowns are ρ, u, p, and b.

$$\frac{\partial}{\partial x}(\rho u) = 0 \tag{2.1}$$

$$\frac{\partial}{\partial x}(\rho u^2 + p + b^2) = 0 \tag{2.2}$$

$$\frac{\partial}{\partial x}(\frac{\rho u^3}{2} + \frac{\gamma}{\gamma - 1}up + 2ub^2) = \frac{1}{R_m}\frac{\partial^2 b^2}{\partial x^2} \tag{2.3}$$

$$\frac{\partial}{\partial x}(ub) = \frac{1}{R_m}\frac{\partial^2 b}{\partial x^2} \tag{2.4}$$

Since in most experimental devices, the three easily controllable parameters are the total current, the inlet mass flow rate, and the gas inlet enthalpy, those will be chosen as the inlet (boundary) conditions for this model as well. In addition there is a one-to-one relation between the total current and the inlet magnetic field. As a result one can specify the inlet magnetic field instead of the total current in the thruster. At the outlet the boundary conditions on ρ, u, and p are unknown, but the magnetic field b is assumed to go to zero.

It is possible to find a closed-form solution of this system of equations. The solution was derived by Martinez-Sanchez in [39]. After integrating the set of equations with respect to the distance x one obtains,

$$C_1 = \rho u \tag{2.5}$$

$$C_2 = \rho u^2 + b^2 + p \tag{2.6}$$

$$C_3 = \frac{\rho u^3}{2} + \frac{\gamma}{\gamma - 1} up + 2ub^2 - \frac{1}{R_m}\frac{d}{dx}b^2 \tag{2.7}$$

$$C_4 = ub - \frac{1}{R_m}\frac{db}{dx} \tag{2.8}$$

Eliminating p and ρ gives a quadratic equation for u:

$$0 = u^2\{\frac{\gamma+1}{2(1-\gamma)}C_1\} + u\{\frac{\gamma}{(\gamma-1)}(C_2 - b^2)\} + \{2C_4 b - C_3\} \tag{2.9}$$

with solutions:

$$u_+ = \frac{\gamma}{\gamma+1}\frac{C_2 - b^2}{C_1}(1 + \sqrt{\Delta}) \tag{2.10}$$

$$u_- = \frac{\gamma}{\gamma+1}\frac{C_2 - b^2}{C_1}(1 - \sqrt{\Delta}) \tag{2.11}$$

$$\Delta = 1 + 2\frac{\gamma^2 - 1}{\gamma^2}\frac{2C_4 b - C_3}{(C_2 - b^2)^2}C_1. \tag{2.12}$$

The solution u_- corresponds to the subsonic branch (near the inlet) and the solution u_+ corresponds to the supersonic branch. The equation (2.9) has solutions if and only if the discriminant Δ is positive. This discriminant equals zero when the velocity u equals the speed of sound $\sqrt{\frac{\gamma p}{\rho}}$. Since the gas should accelerate past the sonic point, one must impose the condition that the discriminant reaches zero at the sonic point, but never goes below zero around this point, and verifies simultaneously the equations:

$$\Delta = 0, \tag{2.13}$$

$$\frac{d\Delta}{db} = 0, \tag{2.14}$$

that is respectively:

$$b_s^3 - C_2\, b_s + \frac{\gamma^2 - 1}{\gamma^2}\, C_1\, C_4 = 0, \tag{2.15}$$

$$3\, C_4\, b_s^2 - 2\, C_3\, b_s + C_2\, C_4 = 0. \tag{2.16}$$

The second equation is a quadratic equation in b, and the root which guarantees that $\Delta \geq 0$ around the sonic point should be chosen. This condition imposes a constraint on the values of (C_1, C_2, C_3, C_4) which satisfy the two equations:

$$b_s^3 - b_s C_2 + \frac{\gamma^2 - 1}{\gamma^2} C_4 C_1 = 0 \tag{2.17}$$

$$b_s = \frac{C_3}{3\, C_4} + \frac{1}{3}\sqrt{\left(\frac{C_3}{C_4}\right)^2 - C_2}. \tag{2.18}$$

The magnetic convection equation,

$$C_4 = ub - \frac{1}{R_m}\frac{db}{dx} \tag{2.19}$$

can be integrated a second time, giving x as a function of b:

$$x\ R_m = \int_{b(x)}^{b(0)} \frac{db'}{C_4 - u_{(b')} b'}, \tag{2.20}$$

with boundary conditions:

$$b(1) = 0 \tag{2.21}$$

$$b(0) = 1. \tag{2.22}$$

The constant $C_4 = E_y$ is given by the boundary conditions:

$$R_m = \int_0^1 \frac{db'}{C_4 - u_{(b')} b'}, \tag{2.23}$$

and the relation between b and x is obtained by inverting the function:[1]

$$x\ R_m = F(b; C_1, C_2, C_3, C_4).$$

An example of a solution is given in figure 2-1. One can identify 3 regions: (1) The inlet acceleration region where the plasma goes from a negligible velocity to a velocity on the order of the magneto-acoustic speed of sound, in a distance on the order of the magnetic interaction length ($\frac{\Lambda_m}{L_o} \sim 1/R_m$ in reduced variables); (2) a central region where the electric field is approximately equal to the Electro-Motive Field: $E \sim u\,b$; (3) an exit region with a length on the order of the magnetic interaction length where the diffusive aspect of the magnetic field is important. This region is characterized by the competing effects of the magneto-dynamic acceleration and of the resistive heating, resulting in a pressure increase and a succession of acceleration and deceleration near the outlet. At high magnetic Reynolds numbers the following ordering for the Mach and Mach-Alfven Numbers is valid:

---

[1] The integral 2.20 gives x as a function of b. In practice one may be more interested to find b as a function of x. This can be calculated by discretizing the system of ordinary differential equations, and solving it numerically, either by a shooting method like Runge-Kutta, or by an iterative method like the Newton-Raphson method. Another approach that can be taken in this particular case is to convert the system into an integral equation and solve it by a Picard iteration method. This can be done because the singularity at the sonic point can be regularized beforehand by a consistent choice of the constants C_1, C_2, C_3, C_4. The integral equation can be written:

$$b(x) = b(0) + R_m \int_0^x (u(b)\ b - C_4) dx.$$

The Picard iteration method consists in a repeated calculation of $b(x)$ based on the integration, which can be summarized by the recurrence relation between two successive estimates of $b(x)$:

$$b_{n+1}(x) = b(0) + R_m \int_0^x (u(b_n(\xi))\ b_n(\xi) - C_4) d\xi.$$

Region	Mach Number	Mach-Alfven Number	Region Type and Properties
(1)	M_a increases from ~ 0 to ~ 3	M_v increases from ~ 0 to ~ 1	resistive acceleration; sonic passage at $M_a = 1$.
(2)	$M_a \sim 3$	$M_v \sim 1$	Magneto-Dynamic Region; small magnetic diffusion.
(3)	M_a decreases from ~ 3 to ~ 1	$M_v \sim 1$	exit region; resistive heating.

When the magnetic Reynolds number is decreased a shock appears near the exit through which the solution jumps from the supersonic to the subsonic branch. As the value of R_m is decreased the shock moves upstream until it reaches the sonic point (close to the inlet), then disappears, as the whole channel becomes completely subsonic.

2.2 Analysis of the Inlet Inner-Layer in the Absence of the Hall Effect

Consider the case of an inlet with a cartesian geometry. The inlet is parallel to the y direction (see figure 2-2). It is assumed that the quantities (ρ, u, v, p, b) are independent of y.

First, the coordinate x is rescaled according to $X = \frac{x}{\epsilon}$ (with $\epsilon = 1/R_m$) which eliminates the parameter R_m from the equations. The inner expansion is then :

$$(\rho, u_x, u_y, p, b) = (R_x, U_x, \epsilon V_x, P_x, B_x) + ...$$

The transverse velocity is neglected. The expansions are then substituted in the main equations. The system is then a system of ordinary differential equations similar to the equations of the one-dimensional constant area channel. However the boundary conditions for the first term of the expansions are different from those of the finite length channel. They are defined as follows. At the inlet: $B(0)$ and the inlet total

H_{T0}	0.01	0.001	0.0001
ρ_0	38.432	375.03	3742.3
u_0	$2.60\ 10^{-2}$	$2.667\ 10^{-3}$	$2.672\ 10^{-4}$
P_0	0.1485	0.1494	0.1496
B_0	1.	1.	1.
T_0	$3.8641\ 10^{-3}$	$3.985\ 10^{-4}$	$3.9969\ 10^{-5}$
Ma_0	0.3242	0.1034	0.03274
Mv_0	$1.076\ 10^{-1}$	$3.443\ 10^{-2}$	$1.090\ 10^{-2}$
ρ_∞	1.2848	1.3098	1.3124
u_∞	0.7783	0.7634	0.7620
P_∞	$4.226\ 10^{-2}$	$4.1456\ 10^{-2}$	$4.1372\ 10^{-2}$
B_∞	0.5949	0.5892	0.5886
T_∞	$3.289\ 10^{-2}$	$3.1651\ 10^{-2}$	$3.1525\ 10^{-2}$
Ma_∞	3.3241	3.3241	3.3242
Mv_∞	1.00000	1.00000	1.00000

Table 2.1: Values taken by the variables at the beginning of the inlet (subscripts zero), and at the edge of the layer, where it matches the outer flow (subscripts infinity).

enthalpy $H_T(0) = \frac{1}{2}U(0)^2 + \frac{\gamma}{\gamma-1}\frac{P(0)}{R(0)}$ are given. There is an "internal condition" imposed by the smooth passage through the singularity at the sonic point. This fixes one parameter. There is one free parameter, the transverse electric field in the inlet layer, which is adjusted in order to match the outer solution, according to:

$$\lim_{X\to\infty}(R, U, P, B) = \lim_{x\to 0}(\rho, u, p, b) \tag{2.24}$$

The results for the case ($M_v = 1$) are shown in figure 2-3, for a particular choice of $H_{T0} = 0.001$. The values at $X = 0$ and $X \to \infty$ of $\rho, u, P, B, T, M_a, M_v$ for different values of H_{T0} are also listed in table 2.2.

2.3 Discussion of the Results

This analysis shows that, in the limit of high magnetic Reynolds number and in the absence of the Hall effect, there exists an inner-layer near the inlet which accelerates the gas from its small initial velocity to a high velocity. This layer can be calculated by the equations of the one-dimensional model described in the previous section. The thickness of this layer is proportional to the magnetic interaction length Λ_m. At the end of this acceleration layer the velocity is high, and the local magnetic field is large. The energy needed to accelerate the gas through this layer is essentially derived from the electro-magnetic field. The pressure and the temperature within the gas are relatively small, reflecting the fact that most of the magnetic energy (proportional to b^2) is transformed into kinetic energy (proportional to $\frac{1}{2}\rho u^2$, and since the product ρu is constant, also proportional to u).

In order to insure a consistent solution it is necessary to match the inner solution with the outer solution. It appears that this matching process is not always possible. There is a limited range of outer-solutions which can be matched to the inlet solution, namely those which are sub-magneto-sonic at the inlet (see figure 2-4). The limiting case is that of an inner solution matching an outer flow with a Mach-Alfven number equal to one. Consequently, if there is a throat downstream of the inlet (convergent-divergent thruster), the inlet layer will accelerate the flow to the point where it matches the outer solution, and that will be at a Mach-Alfven number strictly less than one. If however there is no throat downstream of the inlet, the inlet layer will accelerate the gas to a maximum velocity for which the Mach-Alfven number equals one, but cannot accelerate it further.

Contrary to the case of a finite length thruster (see above) the inlet inner-solution cannot include a shock. Such a shock typically appears in the one-dimensional model, when the magnetic Reynolds number is below 4. Since the expansion procedure matches only the first terms of the inner acceleration layer with the outer solution, the conditions at the outlet cannot be felt at this order in the expansion in the inlet inner-solution.

The mathematical singularity associated with the "sonic passage", is located within the inlet acceleration layer. At this point the mathematical nature of the equations changes from elliptic to partially hyperbolic. This singularity acts as an inner boundary condition. This fact should be taken in consideration when writing a two-dimensional numerical code, and care should be exercised in order to avoid overspecifying the inlet boundary conditions.

2.4 One-Dimensional Wave Propagation through the Plasma

The one-dimensional propagation of small amplitude waves through the plasma gives the reader another insight into the different behaviors of the resistive plasma at small and large scale lengths. Since there may be some confusion about the speed at which waves propagate in the plasma, it will be shown below that one can define two speeds of propagation, one being relevant at high frequency: the sonic velocity; the other being relevant at low frequency: the magneto-sonic velocity. This last velocity is only relevant when the thruster dimensions are large in front of the magnetic interaction length.

2.4.1 Dispersion Relation

The presence of dissipation in the equations introduces two effects on wave propagation through the medium. The first effect is the presence of damping. The dissipation due to the resistivity tends to damp out the waves, in particular those which have a wavelength close to the magnetic interaction length Λ_m. The second effect is the dispersion of the waves according to their wavelength or frequency. Two limiting cases, where the wavelength goes either to 0 or to ∞, are considered. Long waves propagate at the magneto-acoustic velocity while short waves propagate at the acoustic velocity, which is typically two to four times slower than the magneto-acoustic velocity.

In this section the one-dimensional equations are used to derive a dispersion equation for small amplitude harmonic waves. This dispersion equation relates the frequency of an elementary Fourier mode to its wave-number. Later the wave behavior in the two limiting case of low and high frequency will be considered.

Notice that this analysis does not include the effect of the field boundary conditions, and the ideal low frequency behavior is necessarily perturbed by the size of the thruster so that any wave with a wavelength larger than the length of the channel will not follow the dispersion relation found below. Similarly there exists another limit to the applicability of this model at the higher end of the spectrum. This limit corresponds to the onset of other physical phenomena which are neglected in this analysis. In the framework of a magneto-hydro-dynamic model, the viscous friction and the heat diffusion both cause an attenuation of the acoustic waves at the high end of the spectrum. An order of magnitude analysis shows that these effects scale as $1/R_e$ where R_e is the classical Reynolds number. In practice $R_e/R_m \sim 100$, so these effects can be legitimately neglected in this analysis.

The one-dimensional equations for the propagation of the small perturbations $(\tilde{\rho}, \tilde{u}, \tilde{p}, \tilde{b})$ are obtained by linearizing the equations (B.36-B.39). This system can be written in the matrix form:

$$\frac{\partial}{\partial t}\begin{pmatrix} \tilde{\rho} \\ \tilde{u} \\ \tilde{p} \\ \tilde{b} \end{pmatrix} + \mathbf{L}\frac{\partial}{\partial x}\begin{pmatrix} \tilde{\rho} \\ \tilde{u} \\ \tilde{p} \\ \tilde{b} \end{pmatrix} + \mathbf{M}\frac{\partial^2}{\partial x^2}\begin{pmatrix} \tilde{\rho} \\ \tilde{u} \\ \tilde{p} \\ \tilde{b} \end{pmatrix} = 0, \tag{2.25}$$

with:

$$\mathbf{L} = \begin{pmatrix} u & \rho & 0 & 0 \\ 0 & u & \frac{1}{\rho} & 2\frac{b}{\rho} \\ 0 & \gamma p & u & 0 \\ 0 & b & 0 & u \end{pmatrix} \tag{2.26}$$

$$\mathbf{M} = \begin{pmatrix} 0 & 0 & 0 & 0 \\ 0 & 0 & 0 & 0 \\ 0 & 0 & 0 & 0 \\ 0 & 0 & 0 & -\frac{1}{R_m} \end{pmatrix} \tag{2.27}$$

The Hall effect will be neglected in this analysis, and the wavefronts are assumed to be planes, normal to the direction of propagation. After substitution of the Fourier modes of the form $W = W_0 e^{i(kx-\omega t)}$ in the above equation one obtains a homogeneous linear system:

$$-i\omega W + ik\mathbf{L}W - k^2\mathbf{M}W = 0$$

This can be viewed as an eigenvalue problem in either ω or k, provided the other variable is specified. The system admits non-zero solutions if the matrix is singular, *i.e.*:

$$\det(-i\omega\mathbf{I} + ik\mathbf{L} - k^2\mathbf{M}) = 0 \tag{2.28}$$

After substitutions, this equation can be written as:

$$0 = (ku-\omega)\left\{(ku-\omega)^2\left(ku-\omega-i\frac{k^2}{R_m}\right) - k^2\frac{\gamma p}{\rho}\left(ku-\omega-i\frac{k^2}{R_m}\right) - 2\frac{k^2b^2}{\rho}(ku-\omega)\right\}. \tag{2.29}$$

This is a polynomial of 4th order in ω, and of 5th order in k. In general this equation can be solved for ω as a function of k, or for k as a function of ω, but the analysis is simpler for the first case, since the polynomial is of lower order. In this case the frequency $\omega = \omega_r + i\omega_i$, is sought as a function of the wave vector k. When k is real this is equivalent to assuming that a perturbation is present everywhere in space at time zero, and to observing its evolution in time.

The term $ku - \omega$, which corresponds to an undamped convected mode, can be factored, as shown in (2.29), leaving a complex polynomial of third order in ω. Rather than writing the general solution which is rather complicated, it is sufficient for the purpose of this discussion to consider two limiting cases: the case of low wave-number/frequency (ideal MHD), and the case of high wave-number/frequency where the magnetic diffusion dominates the behavior of the magnetic field and the fluid decouples from the magnetic field.

2.4.2 Low Wave Numbers

For low wave numbers ($1/k \gg 1$) the dispersion relation reduces to:

$$0 = (ku-\omega)^2\left\{(ku-\omega)^2 - k^2\left(\frac{\gamma p}{\rho} + \frac{2b^2}{\rho}\right)\right\}, \tag{2.30}$$

which gives the following solutions to first order:

$$\begin{cases} \omega = ku & \text{convected modes} \\ \frac{\omega}{k} = u \pm \sqrt{\frac{\gamma p}{\rho} + \frac{2b^2}{\rho}} & \text{magneto-acoustic modes} \end{cases}$$

At low wave numbers (to the first order), the solutions $\omega(k)$ are all real. This situation corresponds to high magnetic Reynolds numbers: $R_m \gg 1$ where the convection dominates the behavior of the magnetic field. The waves that propagate through the fluid correspond to the hybrid between the transverse Alfven waves and the sonic waves. They are usually called magneto-sonic or magneto-acoustic waves, propagating with a velocity:

$$c = \sqrt{\frac{\gamma p}{\rho} + \frac{2b^2}{\rho}} \tag{2.31}$$

The other two modes are convected at the speed of the fluid.

The other terms of the solution expansion in powers of k are:

$$\omega_1 = ku \tag{2.32}$$

$$\omega_2 = ku - \frac{ik^2}{2R_m}\left(\frac{2b^2}{\gamma p + 2b^2}\right) + O(k^3) \tag{2.33}$$

$$\omega_3 = k\left(u + \sqrt{\gamma\frac{p}{\rho} + 2\frac{b^2}{\rho}}\right) - \frac{ik^2}{2R_m}\left(\frac{2b^2}{\gamma p + 2b^2}\right) + O(k^3) \tag{2.34}$$

$$\omega_4 = k\left(u - \sqrt{\gamma\frac{p}{\rho} + 2\frac{b^2}{\rho}}\right) - \frac{ik^2}{2R_m}\left(\frac{2b^2}{\gamma p + 2b^2}\right) + O(k^3) \tag{2.35}$$

A damping term (negative imaginary part), appears in the second order correction in three of the four modes. This damping term corresponds to the influence of the electric resistivity. Its absence in one of the modes corresponds to the existence of an undamped mode which is not directly coupled to the magnetic field. This mode is convected by the fluid.

2.4.3 High Wave Numbers

At high wave numbers the dispersion relation reduces (to leading order in k) to:

$$0 = (ku - \omega)\left((ku - \omega)^2 - k^2\gamma\frac{p}{\rho}\right)\left(\omega + i\frac{k^2}{R_m}\right) \tag{2.36}$$

whose solutions are: $\omega = ku$, $\frac{\omega}{k} = u \pm \sqrt{\gamma\frac{p}{\rho}}$, $\omega = -i\frac{k^2}{R_m}$. At high wave numbers the fluid and the magnetic field decouple. This situation corresponds to low magnetic Reynolds numbers $R_m \ll 1$, where the diffusion dominates the behavior of the magnetic field. The complex root:

$$\omega = k^2(-\frac{i}{R_m}) + ku + O(k^0) \tag{2.37}$$

represents the diffusive behavior of the magnetic field. The other roots,

$$\omega = k\left(u \pm \sqrt{\gamma\frac{p}{\rho}}\right) - i\frac{R_m b^2}{\rho} + O(k^{-1}), \tag{2.38}$$

represent damped waves[2] propagating at the sonic speed of sound $c_s = \sqrt{\gamma RT}$. The undamped mode, convected by the fluid, is also present in the high frequency limit.

2.4.4 Intermediate Domain

Between these two limiting cases there is a region where the waves are strongly damped by the medium, and cannot propagate very far, particularly when the magnetic Reynolds number based on the wavelength is of order one. Thus the plasma behaves like a very diffusive system except for the entropy-mode which is convected

---

[2] In dimensional variables the dispersion relation for the acoustic waves can be written

$$\omega = k\left(u \pm \sqrt{\gamma\frac{p}{\rho}}\right) - i\frac{\sigma B^2}{2\rho} = v\,k - i\Omega \tag{2.39}$$

The Fourier mode is then $e^{ikx - i\omega t} = e^{ik(x - vt)}e^{-\Omega t}$. The expression for the time-constant in dimensional variables is:

$$\tau = 1/\Omega = \frac{2\rho}{\sigma B^2}$$

With the following values: $\rho = 10^{-5}$ kg m^{-3}; $\sigma = 3000$ Si m^{-1}; $B = 0.1$ T, typical of magnetodynamic thruster flows, the time constant is then, $\tau = 0.66\ 10^{-6}$ s, which corresponds to a relatively fast decay.

without attenuation. In the presence of viscosity or heat diffusion this entropy-mode would be damped as well.

2.4.5 Effects of Finite Thruster Length

As was mentioned earlier, this analysis is ill-suited to the situation where the length of the thruster is of the same order as the wavelength. In this case it is necessary to take the boundary conditions and the non-uniformity of the steady-state solution into account. The problem becomes more complicated since one must now solve a linear eigenvalue problem whose solutions are the eigenvalues (allowed frequencies) and the eigenvectors (waveforms). Since the problem is bounded, the eigenvectors are no longer simple exponentials but they must meet the homogeneous boundary conditions.

This eigenvalue problem was solved by discretizing the one-dimensional equations over a grid with a finite number of points and solving the resulting matrix-eigenvalue problem by a standard eigenvalue solver (EISPACK). The eigenvectors and eigenvalues give an indication of the behavior of the continuous system. If the background variables are uniform the results are stable. Four modes can be identified: a strongly damped mode associated with the decay of magnetic perturbations, a weakly damped convected mode, and two modes corresponding to the propagation of short waves near the acoustic velocity. If the background variables have the spatial distribution corresponding to the solution of the one-dimensional constant-area channel, including some strong gradients at the inlet and at the outlet, some of the modes are now unstable. Four modes can still be identified: a strongly damped mode associated with the decay of magnetic perturbations, two stable modes corresponding to the propagation of short waves near the acoustic velocity, and an unstable mode propagating at a velocity lower than the convective velocity. This unstable mode appears at short wavelength and grows quickly. A numerical simulation was attempted in order to verify the results of the numerical eigenmode analysis. The simulation involved the discretization of the one-dimensional equations on a regular one-dimensional grid. The dynamics of the solution were simulated by a second order time-accurate im-

Low Spatial Frequency Magneto-Acoustic Regime $k \ll 1$	High Spatial Frequency Acoustic Regime $k \gg 1$
$\omega_1 = ku$	$\omega_1 = ku$
$\omega_2 = ku + O(k^2)$	$\omega_2 = -i\frac{k^2}{R_m} + ku + O(k^0)$
$\omega_3 = k\left(u + \sqrt{\gamma\frac{p}{\rho} + \frac{2b^2}{\rho}}\right) + O(k^2)$	$\omega_3 = k\left(u + \sqrt{\gamma\frac{p}{\rho}}\right) - i\frac{R_m b^2}{\rho} + O(k^{-1})$
$\omega_4 = k\left(u - \sqrt{\gamma\frac{p}{\rho} + \frac{2b^2}{\rho}}\right) + O(k^2)$	$\omega_4 = k\left(u - \sqrt{\gamma\frac{p}{\rho}}\right) - i\frac{R_m b^2}{\rho} + O(k^{-1})$

Table 2.2: Summary of asymptotic dispersion relations. Note that in order to be consistent with the notations in the rest of the dissertation all the quantities are non-dimensionalized according to the relations introduced in the Appendix B.

plicit method (Crank-Nicolson). The same unstable modes were observed and they are likely to be an intrinsic feature of the flow. In addition these results suggest that, in the regime of high magnetic Reynolds numbers, a numerical simulation based on a time marching algorithm is unlikely to reach a steady state. The addition of artificial viscosity can cure the problem of instabilities, but this raises the question of the relevance of the answer. If the level of artificial dissipation is too high, the calculation no longer simulates a flow in the regime of high magnetic Reynolds number.

2.4.6 Conclusion

Table 2.2 summarizes the asymptotic forms of the results.

At high frequency a damped acoustic wave propagates through the plasma at a velocity of $\sqrt{\gamma p/\rho}$. At low frequency a slightly damped magneto-acoustic wave propagates through the plasma at a velocity of $\sqrt{\gamma p/\rho + 2b^2/\rho}$ in non-dimensional units or $\sqrt{\gamma P/\rho + B^2/\mu_o\rho}$ in *SI* units. In the intermediate domain where the wavelength is of the same order as the magnetic interaction length, the perturbation is strongly damped, and the concept of wave no longer applies to the situation.

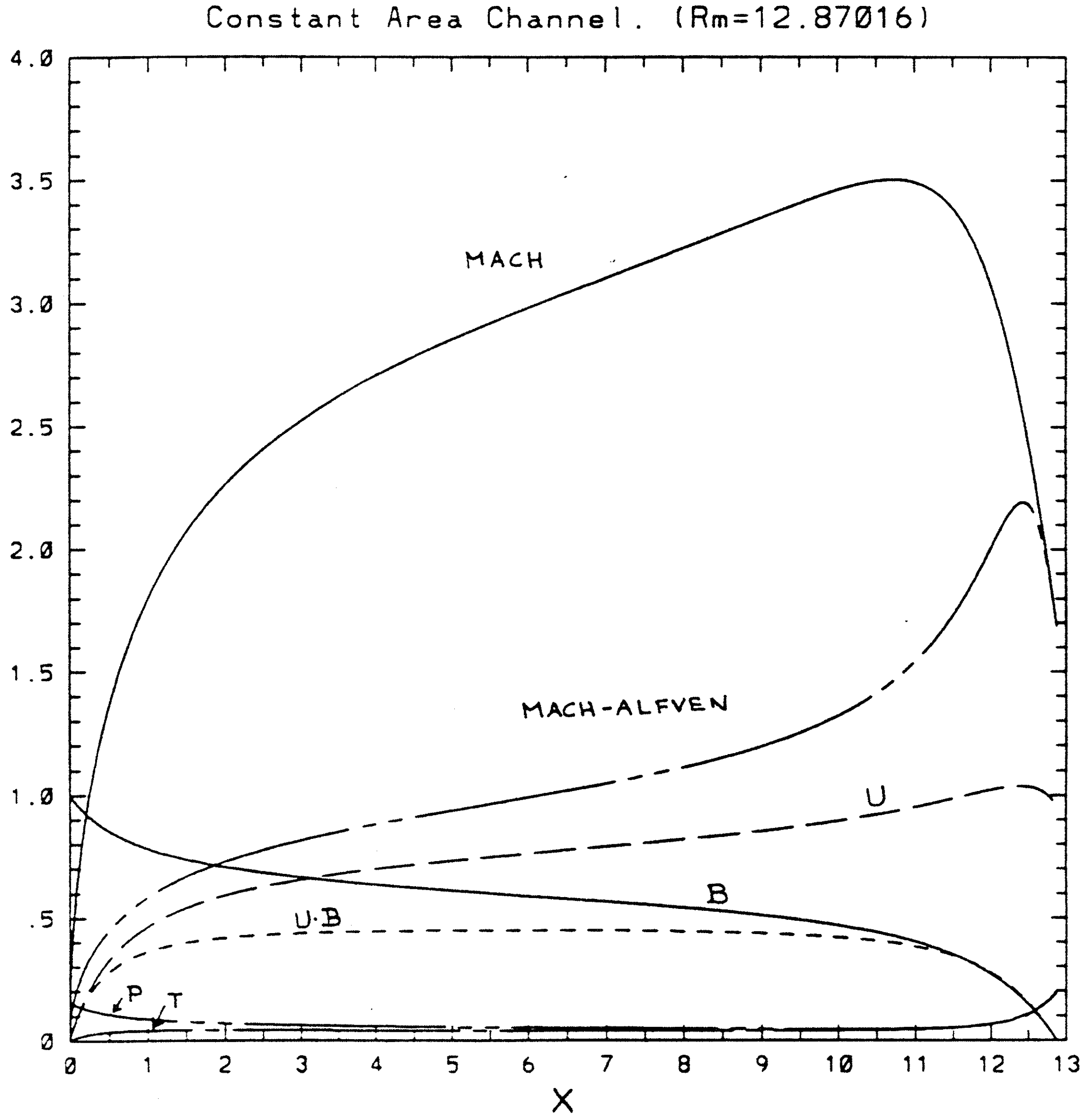

Figure 2-1: This shows an example of the solution for the constant-area channel, using the one-dimensional model. The inlet total-enthalpy is $H_T = 0.001$, the electric field is $E = 0.47$

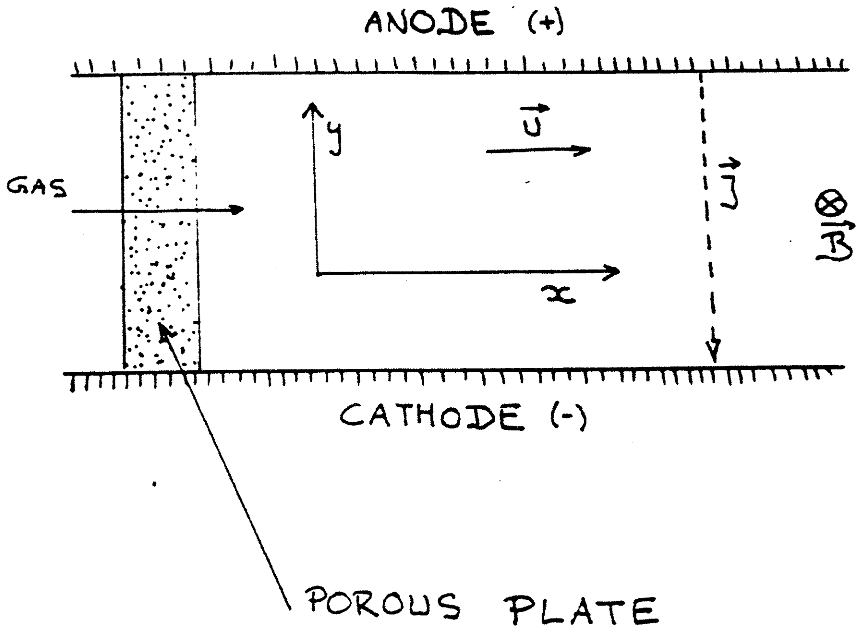

Figure 2-2: Geometry of the inlet. The fluid enters from a porous plate with a very small velocity.

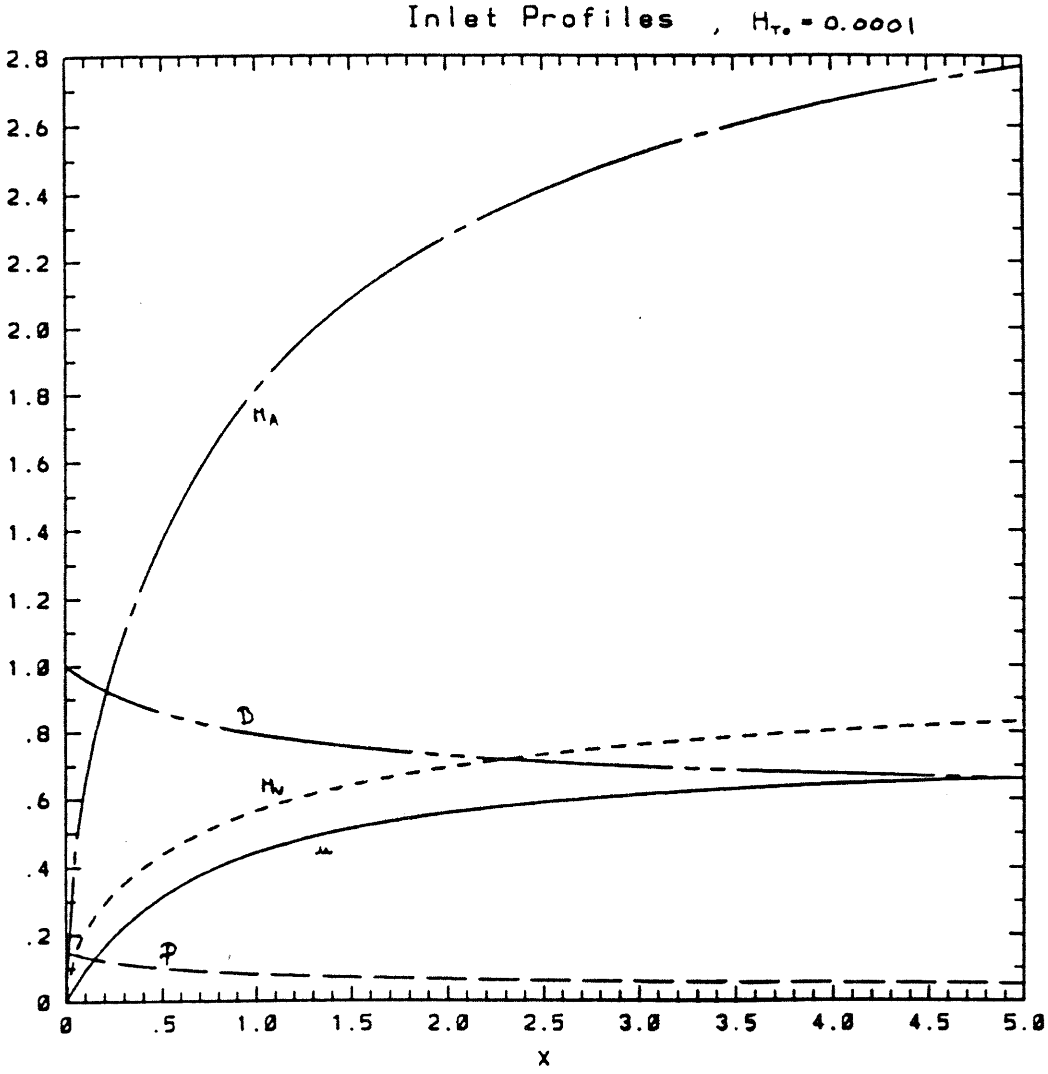

Figure 2-3: Inlet layer profiles. The horizontal coordinate corresponds to the distance from the back plate, measured in units of magnetic interaction length (Λ_m). The vertical coordinate indicates the value taken by the non-dimensionalized variables: (a) M_a, the Mach number; (b) b, the magnetic field; (c) M_v, the Mach-Alfven number; (d) u, the velocity; (e) p, the pressure. The parameters for this calculation are: $H_{T_o} = 0.0001, b = 1.$, and the flow is chosen to reach a Magneto-sonic number of 1 at ∞, which corresponds to the case of a thruster with no throat downstream of the inlet layer.

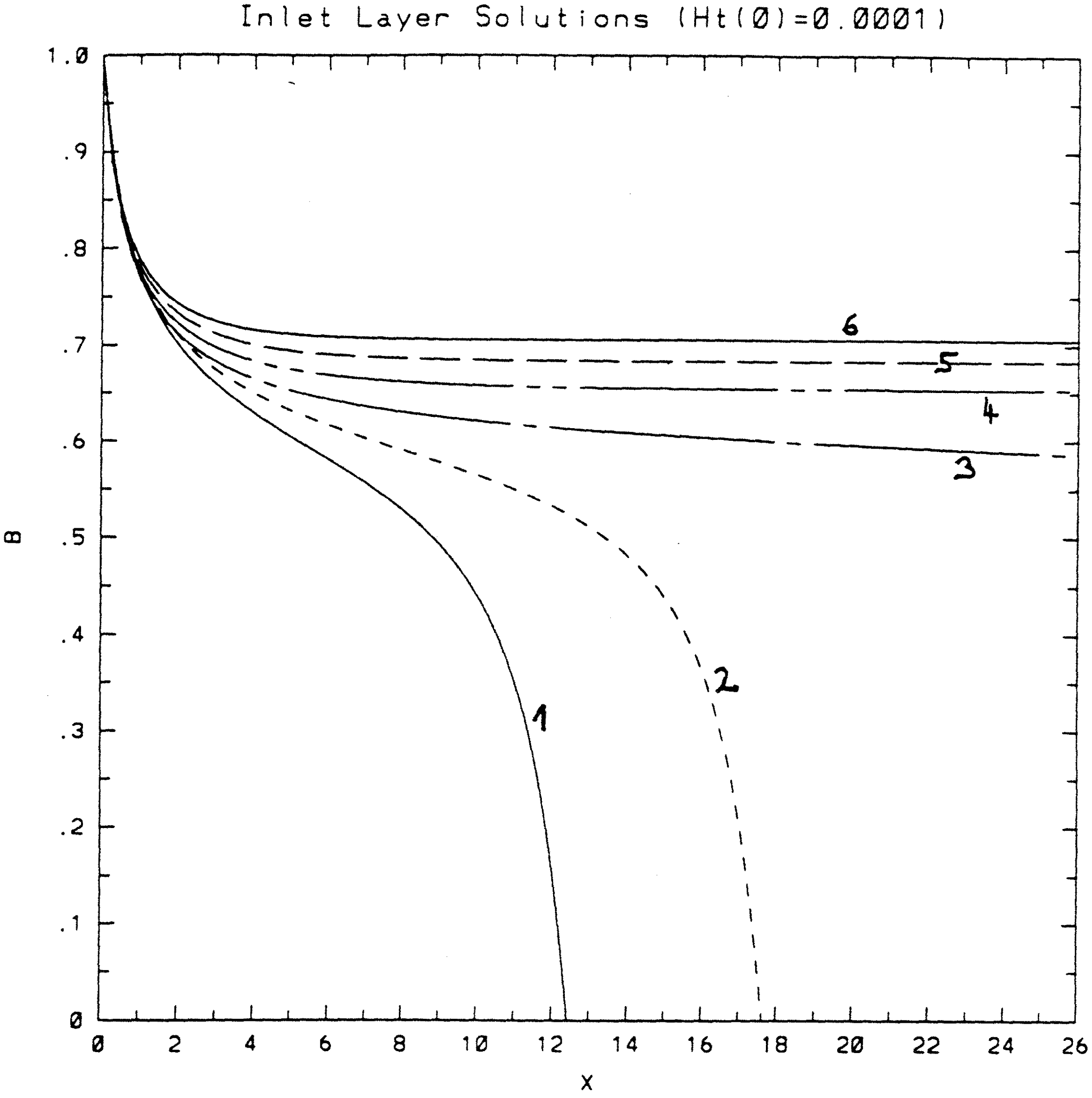

Figure 2-4: Inlet layer profiles. The horizontal coordinate corresponds to the distance from the back plate, measured in units of magnetic interaction length (Λ_m). The vertical coordinate indicates the value taken by the non-dimensionalized magnetic field b for different values of the constant $C_4 = e_y - ub$. The curves 1,2,3 are divergent; b tends to $-\infty$ at large distance. They cannot be matched to an outer solution. The curves 4,5,6 are convergent at ∞ and therefore can be matched to an outer solution. Curve number 4 corresponds to the limit case of a Mach-Alfven number of one at infinity, which is the highest Mach-Alfven number that can be matched by the inlet acceleration layer. The curves 5,6 correspond to cases of lower matching velocity. The parameters for this calculation are $H_{T_o} = 0.0001$ and $b = 1$.

Chapter 3

Non-Resistive Approximation

The non-resistive approximation represents the ideal limit where the gas gains very little entropy through Ohmic heating. Its first appeal is in the mathematical simplification associated with the dropping of the diffusive and dissipative terms. In this case the fluid entropy is conserved. The magnetized plasma behaves in a way which is very similar to that of an ordinary compressible gas, with the exception that the Mach number is replaced by a Mach-Alfven number which includes the effect of the magnetic field. In this case the magnetic field plays a role similar to that of the pressure, and varies along the streamlines according to its own conservation equation.

Although the mathematical simplicity of this method is a clear advantage, its shortcomings should also be considered. The method will overestimate the efficiency of the thruster. It cannot take into account the Hall effect. It overlooks the regular gas-dynamic effects which occur at small scale lengths, *i.e.* when the plasma decouples from the magnetic field. On the other hand, the conclusions of the following chapters indicate that this approximation is valid when all the thruster dimensions, and in particular the inter-electrode gap, are large compared to the magnetic interaction length.

3.1 Background on Ideal Magneto-Hydrodynamic Flows

In [35] and [44] Morozov and Solov'ev studied ideal magneto-hydrodynamic flows in the context of magneto-dynamic accelerators. In their analysis the authors neglected the pressure term in the momentum equation and ignored the energy equation. They showed that as the flow passes through a throat, the plasma undergoes a transition from sub-alfvenic to super-alfvenic. They derived analytic solutions for the two-dimensional flow through a variable-area thruster with slowly varying cross-section. Their analysis was later extended in order to account for some aspects of the Hall effect in idealized thruster geometries, while still keeping a system of first order equations. In this case however streamlines are no longer equipotentials, and the boundary conditions of the ideal MHD problem are not compatible with the equipotential conditions at the electrode surfaces.

Numerical simulations of ideal magneto-hydrodynamic flows in idealized thruster geometries were presented by Brushlinskii and Solov'ev in [9]. These simulations do not account for the thermodynamic pressure and are limited to very simple geometries. From their numerical simulations, they concluded that high speed flows of a non-resistive plasma in a magneto-dynamic thruster are stable.

3.2 Formulation and Properties of the Solution

The outer problem represents the limiting case where the resistivity of the medium is negligible. The model reduces to an ideal MHD problem. Its formulation is obtained by setting the term $\frac{1}{R_m}$ to zero in the model equations (1.8), giving the system:

$$\nabla(\rho \ \mathbf{u}) = 0 \tag{3.1}$$

$$\rho(\mathbf{u} \cdot \nabla)\mathbf{u} + \nabla p + \nabla \ b^2 = 0 \tag{3.2}$$

$$(\mathbf{u} \cdot \nabla)\left(\frac{p}{\rho^{\gamma}}\right) = 0 \tag{3.3}$$

$$(\mathbf{u} \cdot \nabla)\left(\frac{b}{\rho}\right) = 0 \tag{3.4}$$

$$\mathbf{E} = \mathbf{u} \times \mathbf{b} \tag{3.5}$$

This simplification brings out many conservation relations. Here are some of these properties.

First, the streamlines are equipotentials. This can be established by noting that the Ohm's law for infinite conductivity can be written as: $\mathbf{E} = \mathbf{u} \times \mathbf{b}$, therefore, $\mathbf{E} \cdot \mathbf{u} = (\mathbf{u} \times \mathbf{b}) \cdot \mathbf{u} = \mathbf{0}$. Consequently the walls, being streamlines, are also equipotentials, independent of their actual resistivity. (In other words, the walls will be equipotentials even if they are insulators. If this is the case there will be currents flowing within the plasma in a thin boundary layer along the wall surface. This situation will be considered in more detail in the chapter dedicated to the magnetic boundary layer. In any case these currents are not part of the outer solution.) From equation (3.4) it can be seen that the ratio $\frac{b}{\rho}$ is constant along a streamline. From equation (3.3) it can be seen that the entropy is also constant along a streamline. A modified Bernoulli relation can be established for this problem: the sum $\frac{u^2}{2} + \frac{\gamma}{\gamma-1}p/\rho + 2\frac{b^2}{\rho}$ is constant along a streamline. This can be established by observing that the flow is barotropic, and by combining the momentum equation with the mass, entropy and magnetic conservation equations.

From the momentum equation it can be shown that, with some additional uniformity assumptions, the ratio of the vorticity over the density is constant along a streamline. The vorticity is defined as $\vec{\omega} = \nabla \times \mathbf{u}$. The momentum equation can be transformed into:

$$\nabla \times (\vec{\omega} \times \mathbf{u}) + \nabla \times \left(\frac{1}{\rho}\nabla(b^2 + p)\right) = 0. \tag{3.6}$$

Assuming that the vorticity is normal to the plane of the flow and that p/ρ^{γ} and b/ρ are constant everywhere, then, the ratio of the vorticity over the density is constant along a streamline:

$$\mathbf{u} \cdot \nabla \left(\frac{\omega}{\rho} \right) = 0. \tag{3.7}$$

Finally, the Hall effect disappears from both the main equations and from the boundary conditions.

3.2.1 Dynamic Effects

Although this dissertation is mostly concerned with steady-state phenomena it seems useful to remind the reader of the dynamics of small wave propagation. By including in the model the terms which contain the time derivatives, and by looking at the dynamics of small perturbations, one concludes that infinitesimal waves propagate with a velocity which is a hybrid between the transverse (magnetic) Alfven wave and the acoustic wave. This magneto-acoustic (also called magneto-sonic or Mach-Alfven) velocity is given by,

$$c_v^2 = \frac{\gamma p + 2b^2}{\rho}. \tag{3.8}$$

For more details the reader should look at the end of chapter 2 where this analysis was done for the general case of a resistive plasma. The non-resistive approximation is the limit of the resistive solution for large wavelengths. Since the velocity of wave propagation is higher than for a regular gas, it is logical to redefine the Mach number in order to take into account the change in the wave velocity. This new number can be defined as:

$$M_v = \frac{u}{c_v} = \frac{u}{\sqrt{\frac{\gamma p + 2b^2}{\rho}}}. \tag{3.9}$$

This number appears naturally as a critical parameter in the analysis of the non-resistive problem. For instance it appears as the critical parameter for the transition from elliptic ($M_v < 1$) to hyperbolic ($M_v > 1$) behavior of the coupled system (3.1)-(3.4).

3.3 Numerical Method

3.3.1 Introduction to the Galerkin Finite Element method

A Galerkin finite element method has been developed to solve the non-resistive outer problem. The computational domain is decomposed into elementary triangles. The partial differential equations are expressed in conservative form and discretized using the method of Galerkin.

Assuming a two-dimensional problem governed by a linear partial differential equation: $L(u) = 0$, in a domain Ω, with boundary conditions: $S(u) = 0$ on $\partial\Omega$. The Galerkin method approximates the solution $u(x,y)$ by the sum: $u_a = \sum_{j=1}^{N} a_j \phi_j(x,y)$, where the coefficients a_j are to be determined, and the functions $\phi_j(x,y)$ are defined in advance. Substituting the approximation in the partial differential equation gives a residual R which is a function of the independent variables x and y, and of the unknown coefficients a_j: $R(a_0, a_1, ..., a_N, x, y) = L(u_a) = \sum_{j=1}^{N} a_j L(\phi_j)$. Defining the inner product: $(f,g) = \iint_\Omega f\ g\ dx\ dy$, the Galerkin method chooses the a_j by imposing: $(R, \phi_k) = 0$ for $k = 1, N$. This means that the coefficients a_j are chosen such that the projections of the residual onto the functions ϕ_j used in the approximation are zero. This gives a system of N equations where the a_j are unknowns.

3.3.2 Formulation of the Problem

Recall the equations for the first term of the outer solution, in 2-dimensional cartesian coordinates, in conservative form.

$$\frac{\partial}{\partial t}(\rho) + \frac{\partial}{\partial x}(\rho\, u) + \frac{\partial}{\partial y}(\rho\, v) = 0, \tag{3.10}$$

$$\frac{\partial}{\partial t}(\rho\, u) + \frac{\partial}{\partial x}(\rho\, u^2 + p + b^2) + \frac{\partial}{\partial y}(\rho\, u\, v) = 0, \tag{3.11}$$

$$\frac{\partial}{\partial t}(\rho\, v) + \frac{\partial}{\partial x}(\rho\, u\, v) + \frac{\partial}{\partial y}(\rho\, v^2 + p + b^2) = 0, \tag{3.12}$$

$$\begin{aligned}
&\frac{\partial}{\partial t}(\frac{1}{2}\rho(u^2+v^2)+\frac{p}{\gamma-1}+b^2)\\
+\ &\frac{\partial}{\partial x}(u(\frac{1}{2}\rho(u^2+v^2)+\frac{\gamma}{\gamma-1}p+2b^2))\\
+\ &\frac{\partial}{\partial y}(v(\frac{1}{2}\rho(u^2+v^2)+\frac{\gamma}{\gamma-1}p+2b^2))=0,
\end{aligned}\tag{3.13}$$

$$\frac{\partial}{\partial t}(b)+\frac{\partial}{\partial x}(u\,b)+\frac{\partial}{\partial y}(v\,b)=0.\tag{3.14}$$

The following boundary conditions apply: On the walls the normal velocity is zero (i.e. the velocity is tangent to the wall). At the inlet the conditions are imposed by matching the inlet inner-solution. At the outlet the conditions depend on whether the flow is locally super-magneto-sonic (and the system of partial differential equations is hyperbolic), or locally sub-magneto-sonic (and the system of partial differential equations is elliptic). The one-dimensional model suggests that the flow is locally super-magneto-sonic near the outlet. When the flow is sub-magneto-sonic, the boundary conditions are determined from conditions both inside and outside the computational domain. When the flow is super-magneto-sonic, one can use the method of characteristics to establish the proper boundary conditions. In practice a time-marching algorithm is employed, where the boundary conditions and the computational domain are relaxed simultaneously.

3.3.3 Description of the Finite Element Discretization

The functions ρ, u, v, p, b are approximated by : $\rho_a = \sum_j \rho_j N_j(x,y)$, $u_a = \sum_j \rho_j N_j(x,y)$, $v_a = \sum_j v_j N_j(x,y)$, $p_a = \sum_j p_j N_j(x,y)$, $b_a = \sum_j b_j N_j(x,y)$, where the $N_j(x,y)$ are continuous functions based on the discretized mesh, and such that $N_j(x_j,y_j)=1$ and $N_j(x_i,y_i)=0$ for $i \neq j$. The base functions are taken as piecewise linear functions, which are zero almost everywhere, except near the node j, where they are equal to one. (N_j looks like a pyramid with its summit above the point with coordinates (x_j,y_j), and its base on the triangles adjacent to the node j. See figure 3-1.)

The projection of the partial differential equations on the trial functions N_k gives the following set of equations:

$$\begin{aligned}&\iint_{\Omega} N_k(x,y)\frac{\partial}{\partial t}(\rho)dx\,dy+\\&\quad\iint_{\Omega} N_k(x,y)\frac{\partial}{\partial x}(\rho\,u)dx\,dy+\iint_{\Omega} N_k(x,y)\frac{\partial}{\partial y}(\rho\,v)dx\,dy=0,\end{aligned}\tag{3.15}$$

$$\begin{aligned}&\iint_{\Omega} N_k(x,y)\frac{\partial}{\partial t}(\rho\,u)dx\,dy+\\&\quad\iint_{\Omega} N_k(x,y)\frac{\partial}{\partial x}(\rho\,u^2+p+b^2)dx\,dy+\\&\quad\iint_{\Omega} N_k(x,y)\frac{\partial}{\partial y}(\rho\,u\,v)dx\,dy=0,\end{aligned}\tag{3.16}$$

$$\begin{aligned}&\iint_{\Omega} N_k(x,y)\frac{\partial}{\partial t}(\rho\,v)dx\,dy+\\&\quad\iint_{\Omega} N_k(x,y)\frac{\partial}{\partial x}(\rho\,u\,v)dx\,dy+\\&\quad\iint_{\Omega} N_k(x,y)\frac{\partial}{\partial y}(\rho\,v^2+p+b^2)dx\,dy=0,\end{aligned}\tag{3.17}$$

$$\begin{aligned}&\iint_{\Omega} N_k(x,y)\frac{\partial}{\partial t}(\frac{1}{2}\rho(u^2+v^2)+\frac{p}{\gamma-1}+b^2)\,dx\,dy+\\&\quad\iint_{\Omega} N_k(x,y)\frac{\partial}{\partial x}(u(\frac{1}{2}\rho(u^2+v^2)+\frac{\gamma}{\gamma-1}p+2b^2))\,dx\,dy+\\&\quad\iint_{\Omega} N_k(x,y)\frac{\partial}{\partial y}(v(\frac{1}{2}\rho(u^2+v^2)+\frac{\gamma}{\gamma-1}p+2b^2))\,dx\,dy=0,\end{aligned}\tag{3.18}$$

$$\begin{aligned}&\iint_{\Omega} N_k(x,y)\frac{\partial}{\partial t}(b)\,dx\,dy+\\&\quad\iint_{\Omega} N_k(x,y)\frac{\partial}{\partial x}(u\,b)\,dx\,dy+\iint_{\Omega} N_k(x,y)\frac{\partial}{\partial y}(v\,b)\,dx\,dy=0,\end{aligned}\tag{3.19}$$

where Ω is the whole domain of computation. This is a non-linear system, and it would be difficult to substitute the approximations directly into each variable. Instead it is possible to use the method of **group finite element** (see for instance Fletcher[18]), and to approximate directly the flux vectors: $\mathbf{F}^t=(\rho\,u,\rho\,u^2+p+b^2,\ \rho\,u\,v,u\{\frac{1}{2}\rho(u^2+$

$v^2) + \frac{\gamma}{\gamma-1}p + 2b^2\}, b)$, and $\mathbf{G}^t = (\rho v, \rho uv, \rho v^2 + p + b^2, v\{\frac{1}{2}\rho(u^2 + v^2) + \frac{\gamma}{\gamma-1}p + 2b^2\}, b)$. For instance the x-momentum equation becomes:

$$\begin{aligned}
&\iint_\Omega \frac{\partial}{\partial t}\sum_j (\rho\, u)_j N_k\, N_j dx\, dy + \\
&\quad \iint_\Omega N_k(x,y)\frac{\partial}{\partial x}\{\sum_j(\rho\, u^2 + p + b^2)_j N_j(x,y)\} dx\, dy + \\
&\quad \iint_\Omega N_k(x,y)\frac{\partial}{\partial y}\{\sum_j(\rho\, u\, v)_j N_j(x,y)\} dx\, dy = 0
\end{aligned} \tag{3.20}$$

or also:

$$\begin{aligned}
&\frac{\partial}{\partial t}\{\sum_j(\rho\, u)_j\} \iint_\Omega N_k\, N_j dx\, dy + \\
&\quad \sum_j(\rho\, u^2 + p + b^2)_j \iint_\Omega N_k(x,y)\frac{\partial}{\partial x}N_j(x,y) dx\, dy + \\
&\quad \sum_j(\rho\, u\, v)_j \iint_\Omega N_k(x,y)\frac{\partial}{\partial y}N_j(x,y) dx\, dy = 0.
\end{aligned} \tag{3.21}$$

This gives a set of $5N$ equations with unknowns $(\rho_j, u_j, v_j, p_j, b_j)$ for $j = 1, N$. A time-marching scheme, based on an approximate integration in time, is used to iterate the solution towards the steady-state. The time integration is based on the 4-step Runge-Kutta method used by Shapiro [55]. The time-step is allowed to vary locally in order to accelerate the convergence. Its value is fixed by the local constraint imposed by the Courant-Friedrichs-Lewy condition. The CFL number is determined from the local mesh size, the value of the magneto-sonic speed of sound, and the the gas velocity.

In this method the primitive variables (ρ, u, v, p, b). are replaced by the set:

$$\mathbf{Q}^t = (\rho, \rho u, \rho v, \{\frac{1}{2}\rho(u^2 + v^2) + \frac{p}{\gamma - 1} + b^2\}, b),$$

and the these variables are updated directly from the evaluation of the residuals. For instance, for the momentum equation the residual is by definition:

$$\mathrm{Res}^{\alpha=2}(N_k) = \sum_j (\rho\, u^2 + p + b^2)_j \iint_\Omega N_k(x,y) \frac{\partial}{\partial x} N_j(x,y) dx\, dy \tag{3.22}$$

$$+ \sum_j (\rho\, u\, v)_j \iint_\Omega N_k(x,y) \frac{\partial}{\partial y} N_j(x,y) dx\, dy. \tag{3.23}$$

The momentum equation is then:

$$\sum_j \{\frac{\partial}{\partial t}(\rho u)_j\} \iint_\Omega N_j\ N_k\ dx\ dy + \mathrm{Res}(N_k) = 0, \tag{3.24}$$

which can be written in the matrix form:

$$M_{jk} \frac{\partial}{\partial t} Q_j^{\alpha'} = -R_k^\alpha. \tag{3.25}$$

Where $M_{jk} = (N_j, N_k) = \iint_\Omega N_j\ N_k\ dx\ dy$ is the element of the mass matrix, $R_k^\alpha = \mathrm{Res}^\alpha(N_k)$ is the residual of the α-equation, and Q_j^α is the unknown vector: $Q_j^{\alpha=1,\dots 5} = (\rho_j, (\rho u)_j, (\rho v)_j, \dots)$

Following Shapiro [55] the mass-matrix is replaced by a lumped mass-matrix. This matrix is obtained by lumping the different M_{jk} onto the diagonal, so that the diagonal value becomes: $M^*_{kk} = \sum_j M_{jk}$, and $\mathbf{M}^* = \mathrm{diag}(\dots M_{kk} \dots)$. For instance the momentum equation becomes:

$$\{\frac{\partial}{\partial t}(\rho u)_k\}\{\sum_j \iint_\Omega N_j\ N_k\ dx\ dy\ \} = \mathrm{Res}^{\alpha=2}(N_k), \tag{3.26}$$

or

$$\frac{\partial}{\partial t}\mathbf{Q}^\alpha = -(\mathbf{M}^*)^{-1}\ \mathbf{R}^\alpha = -(\mathrm{diag}(\dots, M^*_{kk}, \dots))^{-1}\ \mathbf{R}^\alpha = -\mathrm{diag}(\dots, \frac{1}{M^*_{kk}}, \dots)\ \mathbf{R}^\alpha, \tag{3.27}$$

$$\frac{\partial}{\partial t} Q_k^\alpha = -\frac{R_k}{\sum_j M_{jk}}. \tag{3.28}$$

Finally the equations can be written as

$$\begin{aligned}\frac{\partial}{\partial t}(\rho)_k \;&=\; -\frac{1}{\sum_j < N_j, N_k >}\left\{\sum_j (\rho\, u)_j < N_k, \frac{\partial}{\partial x}N_j > \right. \\ &\left. + \sum_j (\rho\, v)_j < N_k, \frac{\partial}{\partial y}N_j > \right\},\end{aligned} \tag{3.29}$$

$$\begin{aligned}\frac{\partial}{\partial t}(\rho\, u)_k \;&=\; -\frac{1}{\sum_j < N_j, N_k >}\left\{\sum_j (\rho\, u^2 + p + b^2)_j < N_k, \frac{\partial}{\partial x}N_j > \right. \\ &\left. + \sum_j (\rho\, u\, v)_j < N_k, \frac{\partial}{\partial y}N_j > \right\},\end{aligned} \tag{3.30}$$

$$\begin{aligned}\frac{\partial}{\partial t}(\rho\, v)_k \;&=\; -\frac{1}{\sum_j < N_j, N_k >}\left\{\sum_j (\rho\, u\, v)_j < N_k, \frac{\partial}{\partial x}N_j > \right. \\ &\left. + \sum_j (\rho\, v^2 + p + b^2)_j < N_k, \frac{\partial}{\partial y}N_j > \right\},\end{aligned} \tag{3.31}$$

$$\begin{aligned}&\frac{\partial}{\partial t}(\frac{1}{2}\rho(u^2+v^2) + \frac{p}{\gamma-1} + b^2)_k = -\frac{1}{\sum_j < N_j, N_k >} \\ &\left\{\sum_j (u(\frac{1}{2}\rho(u^2+v^2) + \frac{\gamma p}{\gamma-1} + 2b^2))_j < N_k, \frac{\partial}{\partial x}N_j > \right. \\ &\left. + \sum_j (v(\frac{1}{2}\rho(u^2+v^2) + \frac{\gamma p}{\gamma-1} + 2b^2))_j < N_k, \frac{\partial}{\partial y}N_j > \right\},\end{aligned} \tag{3.32}$$

$$\begin{aligned}&\frac{\partial}{\partial t}(b)_k = -\frac{1}{\sum_j < N_j, N_k >} \\ &\left\{\sum_j (ub)_j < N_k, \frac{\partial}{\partial x}N_j > + \sum_j (vb)_j < N_k, \frac{\partial}{\partial y}N_j > \right\}.\end{aligned} \tag{3.33}$$

The various integrals, like $< N_k, \frac{\partial}{\partial x}N_j > = \iint_\Omega N_k \frac{\partial N_j}{\partial x}\, dxdy$, are in turn broken into their elemental constituents. In order to maintain stability the algorithm uses a second order artificial damping. The damping algorithm is a modified version of the one used by R. Shapiro in [55]. The modification concerns the switch used to turn on the damping in the regions of strong gradients. In the present algorithm the switch is always on. As a result the damping is constant throughout the computational domain, which makes the solution first-order accurate. This implies that the error terms will decrease proportionally to the element's size. In classical computational fluid dynamics it is customary to turn-off the second-order artificial viscosity in regions where it is not needed and to rely on a constant level of fourth-order artificial viscosity in order to maintain the stability. The second-order artificial viscosity is designed to be turned on in regions where shocks are located, which are detected by looking at the local pressure gradients. In this calculation the situation is slightly different. First, the stability problem arises because of the gas expansion near a corner, not because of a shock. Second, the rationale for the use of the thermodynamic pressure rather than the magnetic pressure or any other variable is not clear. After several heuristic attempts at choosing an adequate variable for the switch it was found that the most reliable behavior was obtained when the switch was eliminated. This does not mean that the code cannot benefit from a more appropriate type of artificial damping.

In the method described so far, the trial functions are not differentiated and the "flux vectors" are differentiated once with respect to the spatial variables x and y. It is however possible to formulate the problem in a different way. If one integrates by parts the integrals of equations (3.30) to (3.34) one obtains a new set of equations where the trial functions are now differentiated with respect to x and y, and the "flux vectors" are not. This method offers the advantage of incorporating directly the boundary conditions in the formulation of the problem.[1] However the algorithm based on this formulation seemed less robust than the algorithm based on the direct

---

[1] This is done by integrating by part the integrals of the form: $\iint \frac{\partial N_j}{\partial x} N_k \, dx \, dy$. For the momentum equation this gives:

$$\mathrm{Res}(N_k) = \sum_j (\rho u^2 + p + b^2)_j \{ - \iint_\Omega N_j \frac{\partial N_k}{\partial x} \, dx \, dy + \oint_{\partial\Omega} N_j \, N_k \, dy \}$$

$$+ \sum_j (\rho u \, v)_j \{ - \iint_\Omega N_j \frac{\partial N_k}{\partial y} \, dx \, dy - \oint_{\partial\Omega} N_j \, N_k \, dy \}, \tag{3.34}$$

method. Consequently the results of the direct method are displayed below.

$$\begin{aligned}\mathrm{Res}(N_k) = &-\sum_j(\rho u^2+p+b^2)_j \iint_\Omega N_j \frac{\partial N_k}{\partial x}\,dx\,dy\\ &+\sum_j(\rho u^2+p+b^2)_j \oint_{\partial\Omega} N_j\,N_k\,dy\\ &-\sum_j(\rho u\,v)_j \iint_\Omega N_j\frac{\partial N_k}{\partial y}\,dx\,dy - \sum_j(\rho u\,v)_j\oint_{\partial\Omega} N_j\,N_k\,dx.\end{aligned} \tag{3.35}$$

The two line integrals of (3.35) are zero everywhere except when either j or k is on the boundary. In addition the terms in ρu^2 and ρuv disappear in the line integrals along the walls, since the normal component of the velocity is zero there:

$$\mathbf{u}\cdot\mathbf{n} = u\,dy - v\,dx = 0, \tag{3.36}$$

and

$$u_j \oint_{\partial\Omega} N_j\,N_k\,dy - v_j \oint_{\partial\Omega} N_j\,N_k\,dx = \oint_{\partial\Omega} N_j\,N_k(u_j dy - v_j dx) = 0. \tag{3.37}$$

Along the walls the contribution of the line integrals disappears from the equations, except in the momentum equations where there are terms due to the effect of the pressure and of the magnetic pressure. Finally:

$$\frac{\partial}{\partial t}(\rho)_k = \frac{\sum_j(\rho\,u)_j < N_j, \frac{\partial}{\partial x}N_k > + \sum_j(\rho\,v)_j < N_j, \frac{\partial}{\partial y}N_k >}{\sum_j < N_j, N_k >}, \tag{3.38}$$

$$\begin{aligned}\frac{\partial}{\partial t}(\rho\,u)_k \quad = \quad & \frac{1}{\sum_j < N_j, N_k >}\left\{\sum_j(\rho\,u^2+p+b^2)_j < N_j, \frac{\partial}{\partial x}N_k >\right.\\ &\left. + \sum_j(\rho\,u\,v)_j < N_j, \frac{\partial}{\partial y}N_k > - \sum_j(p+b^2)_j \oint_{\partial\Omega} N_j\,N_k\,dy\right\},\end{aligned} \tag{3.39}$$

$$\begin{aligned}\frac{\partial}{\partial t}(\rho\,v)_k \quad = \quad & \frac{1}{\sum_j < N_j, N_k >}\left\{\sum_j(\rho\,u\,v)_j < N_j, \frac{\partial}{\partial x}N_k >\right.\\ &\left. + \sum_j(\rho\,v^2+p+b^2)_j < N_j, \frac{\partial}{\partial y}N_k > + \sum_j(p+b^2)_j \oint_{\partial\Omega} N_j\,N_k\,dx\right\},\end{aligned} \tag{3.40}$$

$$\frac{\partial}{\partial t}(\mathcal{E})_k = \frac{\sum_j(\mathcal{H}\,u)_j < N_j, \frac{\partial}{\partial x}N_k > + \sum_j(\mathcal{H}\,v)_j < N_j, \frac{\partial}{\partial y}N_k >}{\sum_j < N_j, N_k >}, \tag{3.41}$$

with $\mathcal{H} = \frac{\rho}{2}(u^2+v^2) + \frac{\gamma}{\gamma-1}p + 2b^2$ and $\mathcal{E} = \frac{\rho}{2}(u^2+v^2) + \frac{1}{\gamma-1}p + b^2$.

3.3.4 Discussion

The algorithm was tested for simple configurations like straight and flared channels for super-magneto-sonic conditions, and for a test case which can be calculated analytically: the self-similar solution described below. The Figures 3-3 to 3-5 show the solution for the self similar flow in the channel whose geometry appears in figure 3-2. The comparison with the analytic solution is shown in figure 3-6. The curve represents the analytic solution and the isolated points represent the numerical solution in the the center of the computational domain.

Figures 3-8 to 3-14 show the results for two divergent thrusters whose geometries appear in figures 3-7 and 3-11, with an incoming flow which is super-magneto-acoustic. The calculations presented here were done on two similar unstructured grids composed of 928 finite elements, linking 510 nodes. The calculations were interrupted after 500 iterations, which took about 12 minutes of computer time on a DECstation 5000. The rate of convergence for the last calculation is shown in figure 3-15. The horizontal coordinate indicates the iteration number, whereas the vertical coordinates shows the logarithm of the residuals for the first and the last equations (density and magnetic field). The algorithm reaches machine accuracy in about 450 iterations. The Courant-Friedrichs-Lewy number for these iterations was $CFL = 0.5$. The second-order viscosity coefficient (See Shapiro's thesis [55] for details) was $\nu_2 = 0.09$. The fourth-order artificial viscosity coefficient was set to zero.

The magneto-acoustic expansion fans are visible near the corners. In theory these fans should converge towards the corners, which are singular points for all variables. In practice the artificial viscosity, which is necessary to maintain stability, imposes a certain amount of smearing near the corners. The asymmetry between the upper and the lower parts of the channel is attributed to the different orientations of the triangular finite elements. It appears that the shape and orientation of the elements has an effect on the accuracy of the results. The errors can be traced to the fact that the internal energy equation is ill-conditioned. Since the internal energy is small compared to the kinetic and magnetic energy, any error in either one of the two dominant terms will decrease the accuracy of the internal energy considerably. Since the temperature is proportional to the internal energy, an error in the internal energy may result in the appearance of negative temperatures and infinite Mach numbers. An attempt to regularize the problem by eliminating the dominant balance from the equations failed. The resulting equation could not be put in conservative form, and only conservative forms can be handled by the finite element method considered.

However it must be kept in mind that at high magnetic Reynolds numbers, the effect of the internal energy on the general flow is small compared to those of the dominant terms. Consequently the density, the velocity and the magnetic field are not strongly affected by the errors in the energy equation.

3.4 Method of Characteristics

The one-dimensional model predicts that the outer flow in a divergent or a convergent-divergent thruster channel will be super-magneto-sonic downstream of the section of minimal area (the throat). When this is the case, the system of equations becomes hyperbolic and the method of characteristics can be used to solve the outer problem in the super-magneto-sonic region. For many types of thrusters working in the magneto-dynamic regime, this region constitutes most of the volume of the channel, as well as the exit region where the flow expands into the vacuum. The method of characteristics, applied to magneto-dynamic flows, is derived in the following section. Although it has many similarities with the method of characteristics for normal gases, it must be noted that the details of the expressions are slightly different, reflecting the additional interaction of fluid with the magnetic field.

3.4.1 Derivation

After some reorganization the non-resistive equations can be written in the following form:

$$\frac{\partial}{\partial x}(\rho u_x) + \frac{\partial}{\partial y}(\rho u_y) = 0, \qquad (3.42)$$

$$\rho u_x \frac{\partial u_x}{\partial x} + \rho u_y \frac{\partial u_x}{\partial y} + \frac{\partial}{\partial x}(p + b^2) = 0, \qquad (3.43)$$

$$\rho u_x \frac{\partial u_y}{\partial x} + \rho u_y \frac{\partial u_y}{\partial y} + \frac{\partial}{\partial y}(p + b^2) = 0, \tag{3.44}$$

$$\rho^\gamma u_x \frac{\partial}{\partial x}(\frac{p}{\rho^\gamma}) + \rho^\gamma u_y \frac{\partial}{\partial y}(\frac{p}{\rho^\gamma}) = 0, \tag{3.45}$$

$$\rho u_x \frac{\partial}{\partial x}(\frac{b}{\rho}) + \rho u_y \frac{\partial}{\partial y}(\frac{b}{\rho}) = 0. \tag{3.46}$$

Changing the coordinates to (s, n), where s is aligned with the the streamlines and n is normal to s, one obtains the following system,

$$\frac{1}{\rho}\frac{\partial \rho}{\partial s} + \frac{1}{w}\frac{\partial w}{\partial s} + \frac{\partial \theta}{\partial n} = 0, \tag{3.47}$$

$$\frac{\partial}{\partial s}(\frac{1}{2}w^2 + \frac{\gamma}{\gamma - 1}\frac{p}{\rho} + \frac{2b^2}{\rho}) = 0, \tag{3.48}$$

$$w^2 \frac{\partial \theta}{\partial s} + \frac{1}{\rho}\frac{\partial}{\partial n}(p + b^2) = 0, \tag{3.49}$$

$$\frac{\partial}{\partial s}(\ln \frac{p}{\rho^\gamma}) = 0, \tag{3.50}$$

$$\frac{\partial}{\partial s}(\frac{b}{\rho}) = 0. \tag{3.51}$$

where $u_x = w\cos\theta, u_y = w\sin\theta$. Notice that equations 3.48, 3.50, 3.51, are in characteristic form and that the streamline is a characteristic line for these three equations.

The remaining two characteristic lines are actually the Mach-Alfven lines defined by the angle $\pm\mu$ with,

$$\tan \mu = \frac{1}{\sqrt{M_v^2 - 1}}. \tag{3.52}$$

Defining the distance along the characteristics as (ξ,η) , respectively, the equations can be written in characteristic form. Along the $(+\mu)$ characteristic, the equation is:

$$\frac{1}{\sin \mu}\ \frac{\partial}{\partial \eta}(p + b^2) + \frac{\rho\, w^2}{\cos \mu}\ \frac{\partial \theta}{\partial \eta} = 0, \tag{3.53}$$

Along the $(-\mu)$ characteristic, it is:

$$\frac{1}{\sin\mu}\,\frac{\partial}{\partial\xi}(p+b^2)-\frac{\rho\,w^2}{\cos\mu}\,\frac{\partial\theta}{\partial\xi}=0, \tag{3.54}$$

with

$$M_v=\frac{w}{\sqrt{\frac{\gamma p}{\rho}+\frac{2b^2}{\rho}}}, \tag{3.55}$$

$$\xi=\frac{s}{\cos\mu}-\frac{n}{\sin\mu}, \tag{3.56}$$

$$\eta=\frac{s}{\cos\mu}+\frac{n}{\sin\mu}. \tag{3.57}$$

When b/ρ, p/ρ^γ and h_T are constant everywhere p and b are functions of ρ only. It is then possible to express $p+b^2$ and w as functions of ρ only, and to turn the characteristic equations into:

$$\frac{\sqrt{M_v^2-1}}{M_v^2}\,\frac{1}{\rho}\,\frac{\partial\rho}{\partial\eta}+\frac{\partial\theta}{\partial\eta}=0, \tag{3.58}$$

$$\frac{\sqrt{M_v^2-1}}{M_v^2}\,\frac{1}{\rho}\,\frac{\partial\rho}{\partial\xi}-\frac{\partial\theta}{\partial\xi}=0. \tag{3.59}$$

It is now convenient to introduce the function ν such that:

$$-\,d\nu=\frac{\sqrt{M_v^2-1}}{M_v^2}\,\frac{d\rho}{\rho}. \tag{3.60}$$

This function ν depends on ρ and on two parameters. Here these parameters are chosen as $\beta_0=\frac{p_o}{b_o^2}$ and $M_{v0}^2=\frac{w_0^2\rho_0}{\gamma p_0+2b_0^2}$, where the subscript $_0$ refers to the upstream values. An expression for $d\nu$ as a function of $\bar\rho=\rho/\rho_0$ can be obtained by replacing M_v^2 by its expression as a function of ρ,

$$d\nu=-\frac{\sqrt{\gamma\beta_0\bar\rho^{\gamma-1}+2\bar\rho}\sqrt{[M_{v0}^2(2+\gamma\beta_0)+\frac{2\gamma\beta_0}{\gamma-1}+4]-\frac{\gamma(\gamma+1)}{\gamma-1}\beta_0\bar\rho^{\gamma-1}-6\bar\rho}}{\bar\rho\left(M_{v0}^2(2+\gamma\beta_0)+\frac{2\gamma\beta_0}{\gamma-1}(1-\bar\rho^{\gamma-1})+4(1-\bar\rho)\right)}d\bar\rho. \tag{3.61}$$

This can be integrated to give

$$\nu = -\int^{\bar{\rho}} \frac{\sqrt{\gamma\beta_0\bar{\rho}^{\gamma-1} + 2\bar{\rho}}\sqrt{[M_{v0}^2(2+\gamma\beta_0) + \frac{2\gamma\beta_0}{\gamma-1} + 4] - \frac{\gamma(\gamma+1)}{\gamma-1}\beta_0\bar{\rho}^{\gamma-1} - 6\bar{\rho}}}{\bar{\rho}\left(M_{v0}^2(2+\gamma\beta_0) + \frac{2\gamma\beta_0}{\gamma-1}(1-\bar{\rho}^{\gamma-1}) + 4(1-\bar{\rho})\right)} d\bar{\rho}. \quad (3.62)$$

This function reduces to the classical Prandtl-Meyer function in the limit when β_0 goes to ∞.

The last two characteristic equations can now be written as:

$$\frac{\partial}{\partial\eta}(\nu - \theta) = 0, \quad (3.63)$$

$$\frac{\partial}{\partial\xi}(\nu + \theta) = 0, \quad (3.64)$$

where ν is a function of ρ only.

In conclusion, if b/ρ, p/ρ^γ and h_T are constant everywhere, a function ν similar to the Prandtl-Meyer function can be defined, and the problem reduces to a system of characteristic equations similar to that of ordinary supersonic gas dynamics. If the quantities are not constant everywhere, all the characteristic equations (3.48, 3.50, 3.51, 3.53, 3.54) must be kept and must be integrated along the three characteristic directions.

3.4.2 Self-Similar Solution

A self-similar solution, analogous to the Prandtl-Meyer expansion fan for a perfect gas can be found for the corner flow in the simplified case of an infinite corner and negligible magnetic diffusion ($R_m = \infty$).

Changing to a system of cylindrical coordinates (r, ϕ, z) centered on the corner vertex one finds:

$$\frac{\partial}{\partial r}(r\rho u_r) + \frac{\partial}{\partial\phi}(\rho u_\phi) = 0, \quad (3.65)$$

$$\rho u_r \frac{\partial u_r}{\partial r} + \rho u_\phi \frac{1}{r}\frac{\partial u_r}{\partial\phi} - \frac{1}{r}\rho u_\phi^2 + \frac{\partial}{\partial r}(b^2 + p) = 0, \quad (3.66)$$

$$\rho u_r \frac{\partial u_\phi}{\partial r} + \rho u_\phi \frac{1}{r}\frac{\partial u_\phi}{\partial \phi} + \frac{1}{r}\rho u_r u_\phi + \frac{1}{r}\frac{\partial}{\partial \phi}(b^2 + p) = 0, \tag{3.67}$$

$$(\rho^\gamma u_r \frac{\partial}{\partial r} + \rho^\gamma u_\phi \frac{1}{r}\frac{\partial}{\partial \phi})(\frac{p}{\rho^\gamma}) = 0, \tag{3.68}$$

$$(\rho u_r \frac{\partial}{\partial r} + \rho u_\phi \frac{1}{r}\frac{\partial}{\partial \phi})(\frac{b}{\rho}) = 0. \tag{3.69}$$

Since there is no scale-length in either the equations or in the boundary conditions, the solution will be independent of the distance r. Following the method discussed by Landau and Lifshitz [32], it is possible to find an integral which relates the angular coordinate ϕ to the variable ρ in the expansion fan. Dropping the dependence on r and integrating the system gives three conservation equations:

$$\frac{u_r^2 + u_\phi^2}{2} + \frac{\gamma}{\gamma - 1}\frac{p}{\rho} + 2\frac{b^2}{\rho} = \text{const.} = H_o, \tag{3.70}$$

$$\frac{p}{\rho^\gamma} = \text{const.} \tag{3.71}$$

$$\frac{b}{\rho} = \text{const.} \tag{3.72}$$

Some manipulations of the equations of continuity and momentum lead the following equation:

$$(\frac{\partial u_\phi}{\partial \phi} - u_r)(1 - \frac{c^2}{u_\phi^2}) = 0, \tag{3.73}$$

with $c^2 = \gamma\frac{p}{\rho} + 2\frac{b^2}{\rho}$, which shows the two types of solutions to this system. Either $1 - \frac{c^2}{u_\phi^2} = 0$, that is $u_\phi^2 = c^2$, corresponding to the fan solution, or $\frac{\partial u_\phi}{\partial \phi} = u_r$, which implies that $u_r^2 + u_\phi^2 =$ constant, and eventually that ρ, p and b are constant, leading to a uniform flow. The equation $\rho u_r + \frac{\partial}{\partial \phi}(\rho u_\phi) = 0$, can be integrated, giving

$$d\phi = -\frac{d(\rho u_\phi)}{\rho u_r}. \tag{3.74}$$

Next, u_r, u_ϕ, p and b can be eliminated using $u_\phi^2 = c^2 = \gamma\frac{p}{\rho} + 2\frac{b^2}{\rho}$, and the three integrals above, leaving an expression where $d\phi$ can be written as a function of ρ

only. Finally:

$$\phi = -\int_{\rho_o}^{\rho} \frac{\gamma(\gamma+1)(p_o/\rho_o^{\gamma})\rho^{\gamma-1} + 6(\frac{p_o^2}{\rho_o^2})\rho}{2\sqrt{\{\gamma(\frac{p_o}{\rho_o^{\gamma}})\rho^{\gamma+1} + 2(\frac{b_o^2}{\rho_o^2})\rho^3\}\{2H_o - 2(\frac{p_o}{\rho_o^{\gamma}})\frac{\gamma+1}{\gamma-1}\rho^{\gamma-1} - 6(\frac{b_o^2}{\rho_o^2})\rho\}}} d\rho, \qquad (3.75)$$

with the reference variables, ρ_o, p_o, b_o, H_o, taken equal to the values at the origin of the fan.

The solution depends on two parameters. Those can be chosen as $\beta_0 = \frac{p_o}{b_o^2}$ and $M_{v0} = \sqrt{\frac{u_{r0}^2 + u_{\phi 0}^2}{c_0^2}}$, where the index 0 refers to the beginning of the fan. Changing the integration variable to $\bar{\rho} = \frac{\rho}{\rho_o}$, leads to:

$$\phi(\bar{\rho}) = -\int_{1}^{\bar{\rho}} \frac{\gamma(\gamma+1)\beta_0\bar{\rho}^{\gamma-1} + 6\bar{\rho}}{2\sqrt{\gamma\beta_0\bar{\rho}^{\gamma+1} + 2\bar{\rho}^3}\sqrt{[2M_{v0}^2(1 + \frac{\gamma\beta_0}{2}) + 2\beta_0\frac{\gamma}{\gamma-1} + 4] - \frac{\gamma(\gamma+1)}{\gamma-1}\beta_0\bar{\rho}^{\gamma-1} - 6\bar{\rho}}} d\bar{\rho}. \qquad (3.76)$$

Let χ be the angle between the streamline and the reference direction. Then:

$$\cot(\chi - \phi) = \frac{u_r}{u_\phi}. \qquad (3.77)$$

After substitutions one finds,

$$\cot^2(\chi - \phi) = \frac{2(M_{v0}^2(1 + \frac{\gamma\beta_0}{2}) + \frac{\gamma\beta_0}{\gamma-1} + 2) - \frac{\beta_0(\gamma+1)\gamma}{\gamma-1}\bar{\rho}^{\gamma-1} - 6\bar{\rho}}{\gamma\beta_0\bar{\rho}^{\gamma-1} + 2\bar{\rho}}, \qquad (3.78)$$

which uniquely determines all the variables in the fan. Finally, ϕ and χ are related to the Prandtl function ν defined above by:

$$\chi - \frac{\pi}{2} = \nu.$$

Some results for a particular choice of $M_{v0} = 1$ and $\beta_0 = 0.1$ are listed in table 3.1. The maximum turning angle for such a flow (69.38°), is less than for a classical gas of identical compressibility (90°). In the limit where the pressure forces become negligible, the plasma behaves like a gas with $\gamma = 2$, and has a maximum turning angle of 65.88°.

ϕ°	ν°	$\bar{\rho}$	M_v	M_a	β
0.000	0.000	1.000	1.000	2.646	0.1000
9.902	0.069	0.990	1.015	2.681	0.1003
14.02	0.181	0.980	1.030	2.717	0.1007
22.28	0.707	0.950	1.060	2.789	0.1017
31.80	1.924	0.900	1.153	3.006	0.1036
45.83	5.107	0.800	1.320	3.382	0.1077
57.31	8.921	0.700	1.506	3.788	0.1126
67.72	13.21	0.600	1.722	4.240	0.1186
77.70	17.96	0.500	1.985	4.764	0.1260
87.70	23.22	0.400	2.321	5.403	0.1357
98.15	29.18	0.300	2.788	6.243	0.1494
109.7	36.19	0.200	3.530	7.496	0.1710
124.0	45.30	0.100	5.110	9.941	0.2154
133.8	51.77	0.050	7.224	12.94	0.2714
146.9	60.63	0.010	15.43	23.36	0.4642
159.4	69.38	0.000	∞	∞	∞

Table 3.1: Expansion fan for a transversely magnetized plasma with zero conductivity, for $M_{v0} = 1$ and $\beta_0 = 0.1$

3.4.3 Discussion: Structure of the Idealized Flow Near the Exit

Consider a (somewhat idealized) region located at a distance from the corner which is large compared to the magnetic interaction length Λ_m (so that the non-resistive approximation is valid), but small compared to the inter-electrode gap H, (so that the presence of the other corner can be ignored), *i.e.* $\Lambda_m \ll x, y \ll H$.

Two cases can be distinguished. If the corner deflection angle is small, the expansion is incomplete. The expansion has the structure indicated in figure 3-16, with three zones: (i) ahead of the corner the values are constant; (ii) downstream of the characteristic line coming from the corner where the expansion fan begins, this fan is the self-similar solution described above; (iii) finally when the velocity becomes parallel to the downstream boundary, the flow becomes constant again. The three zones are separated from each other by a weak discontinuity.

If the deflection angle is increased, the plasma will expand up to the point where it reaches the maximum turning angle, at which point the expansion is complete. Beyond this point the plasma will not be able to turn any further. If the plasma expands into a vacuum there will be a limiting angle, beyond which the density, the pressure and the magnetic field are zero. Zone (iii) disappears and is replaced by an empty cavity separated from the self-similar fan (ii) by a tangential discontinuity, as shown in figure 3-17.

If the plasma expands into a medium with finite residual pressure, the solution is slightly different; there is an additional stagnation region, separated from the constant flow region (zone iii) by a tangential discontinuity. Across this tangential discontinuity there is no mass flow, and there is a jump in both the tangential velocity and the magnetic field. The residual pressure in zone (iv), p_e, is equal to the sum of the pressure and the magnetic pressure from zone (iii): $p_e = p_{iii} + b_{iii}^2$. (See figure 3-18.) A tangential discontinuity (shear flow) is generally a source of Kelvin-Helmholtz instabilities and such instabilities can be expected in the exhaust plume as well.The line of tangential discontinuity is also a current line (since the magnetic field jumps from b_{iii} to zero across the discontinuity) and the current density along this line is large (infinite in the limit of zero resistivity).

Consider now the two-dimensional expansion of the plasma through a slit. In this case the presence of the other channel wall introduces a scale length, and destroys the self-similarity of the solution. However some of the properties of the solution are preserved. Figure 3-19 shows a complete two-dimensional expansion in the absence of back-pressure. The constant flow zone (I) still exists in the domain delimited by the two walls and the characteristic lines leaving from the corners. The self-similar fan is replaced by two expansion fans which originate at each corner and which merge in the center of the plume. The current lines leave from one corner, extend downstream into the plume, then turn around, come back on the other side of the jet, and reattach on the other corner. If the gas expands into a stagnant medium with some residual pressure the flow becomes more complicated. The background pressure prevents a complete expansion from taking place. The jet is separated from the stagnation region by a tangential discontinuity which is a surface of discontinuity for the magnetic field, and therefore is also a current sheet. A series of successive expansion and recompression zones (similar to that of figure 3-20) is likely to exist, making the analysis rather complicated. The recompression of the plasma is accompanied by a simultaneous increase in the magnetic field. Consequently there will be current flowing along the lines defining contours of constant pressure. There the current flows in the opposite direction from that corresponding to an expansion and consequently current loops will appear in the plume. In addition the tangential discontinuity which defines the jet boundary is also a current sheet.

All of these phenomena are reminiscent of the behavior of a classical gas expansion. However this analogy is not complete because of the presence of the magnetic field.

3.5 Conclusion

In conclusion it has been shown that the outer-solution behavior is similar to that of a gas. However the presence of the magnetic field introduces some quantitative differences, in particular a self-similar solution shows that the maximum turning angle is smaller than that of a normal gas.

Numerical and analytic results show that currents extend downstream into the plume. If the jet of ionized gas is injected into a medium with a finite pressure instead of into a vacuum, a pattern of successive expansion and compression regions appears in the plume, implying the existence of current loops.

As a practical implication of this analysis, it appears that the plasma should be expanded within the thruster in order to recover as much of the electro-magnetic energy as possible.

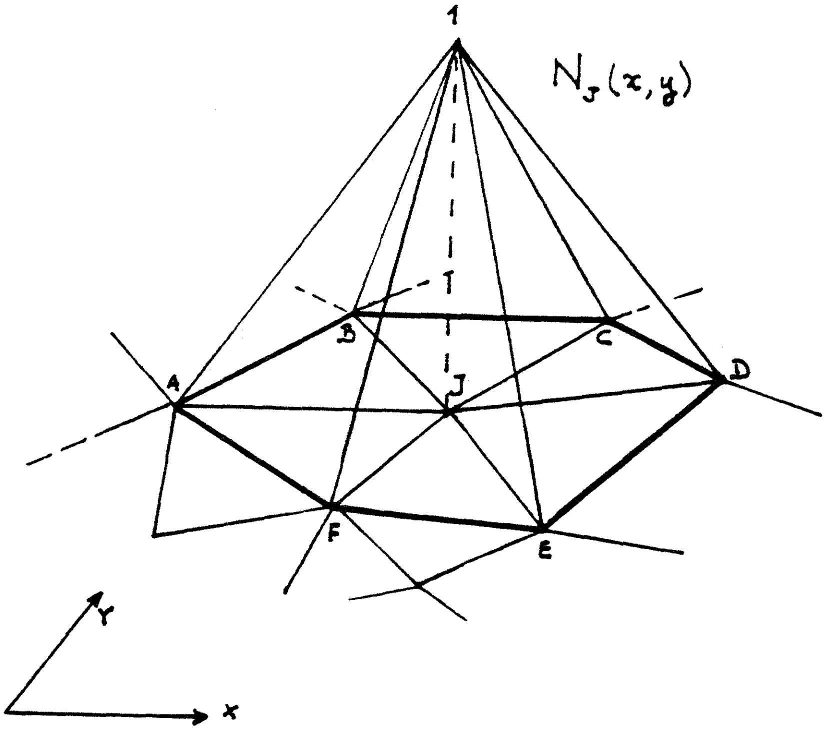

Figure 3-1: Example of a piecewise linear interpolation function N_j associated with the node j.

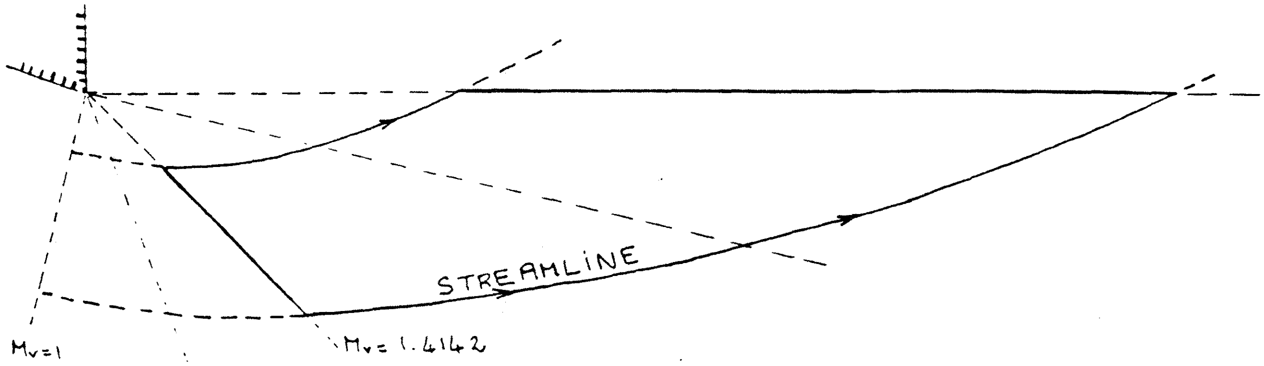

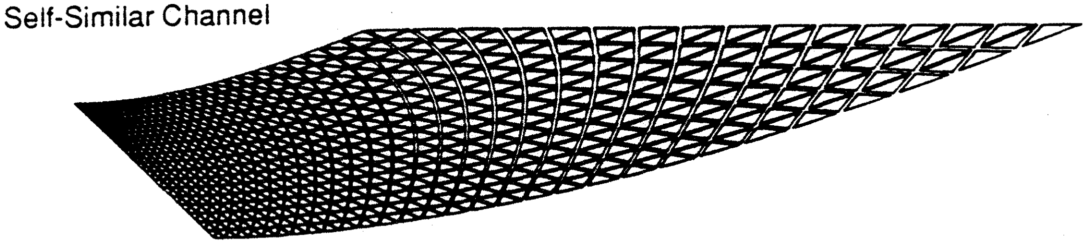

Figure 3-2: Plot of the geometry used as a test case for the algorithm. The results can be compared with an exact solution, namely the self-similar expansion around a corner. The top drawing shows the relationship between the corner and the computational domain. The lower drawing shows the finite element grid.

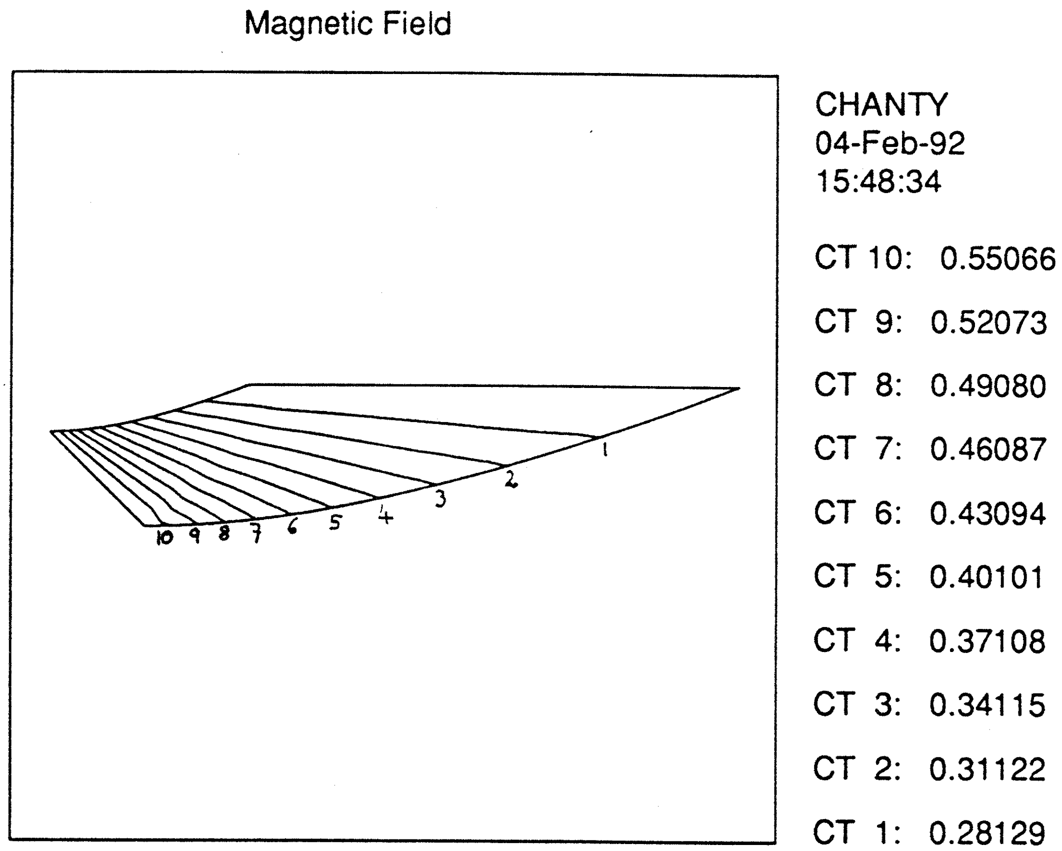

Figure 3-3: Result of the calculation for the test case. The plot shows the magnetic field. The inlet conditions are $M_v = 1.4142$, $\beta_0 = 0.1$. and $b_0 = 0.5886$

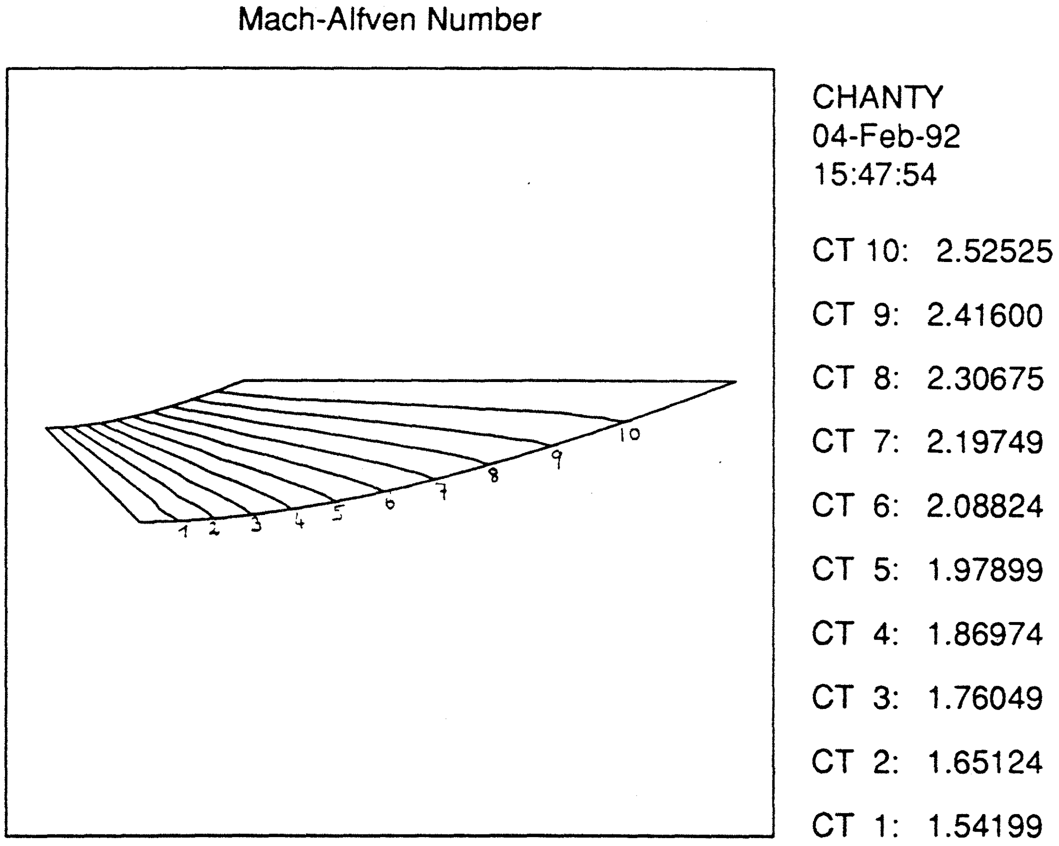

Figure 3-4: Result of the calculation for the test case. The plot shows the Mach-Alfven number. The inlet conditions are $M_v = 1.4142$, $\beta_0 = 0.1$. and $b_0 = 0.5886$

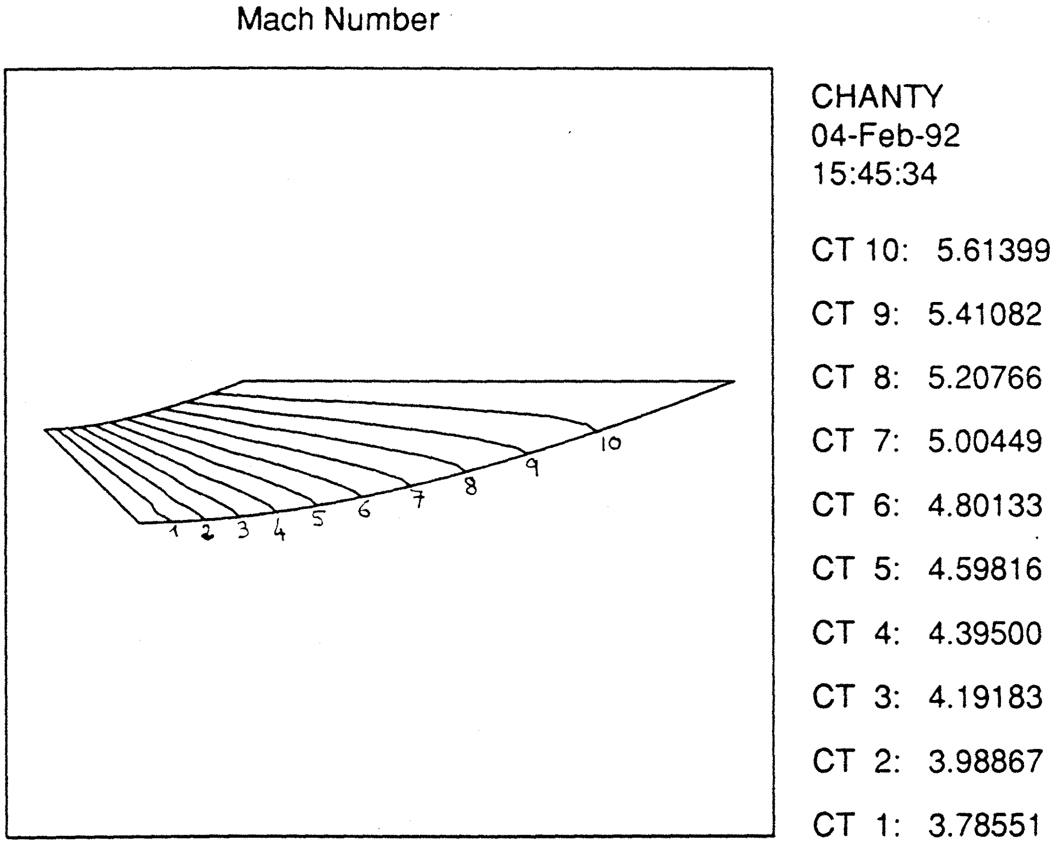

Figure 3-5: Result of the calculation for the test case. The plot shows the Mach number. The inlet conditions are $M_v = 1.4142$, $\beta_0 = 0.1.$ and $b_0 = 0.5886$

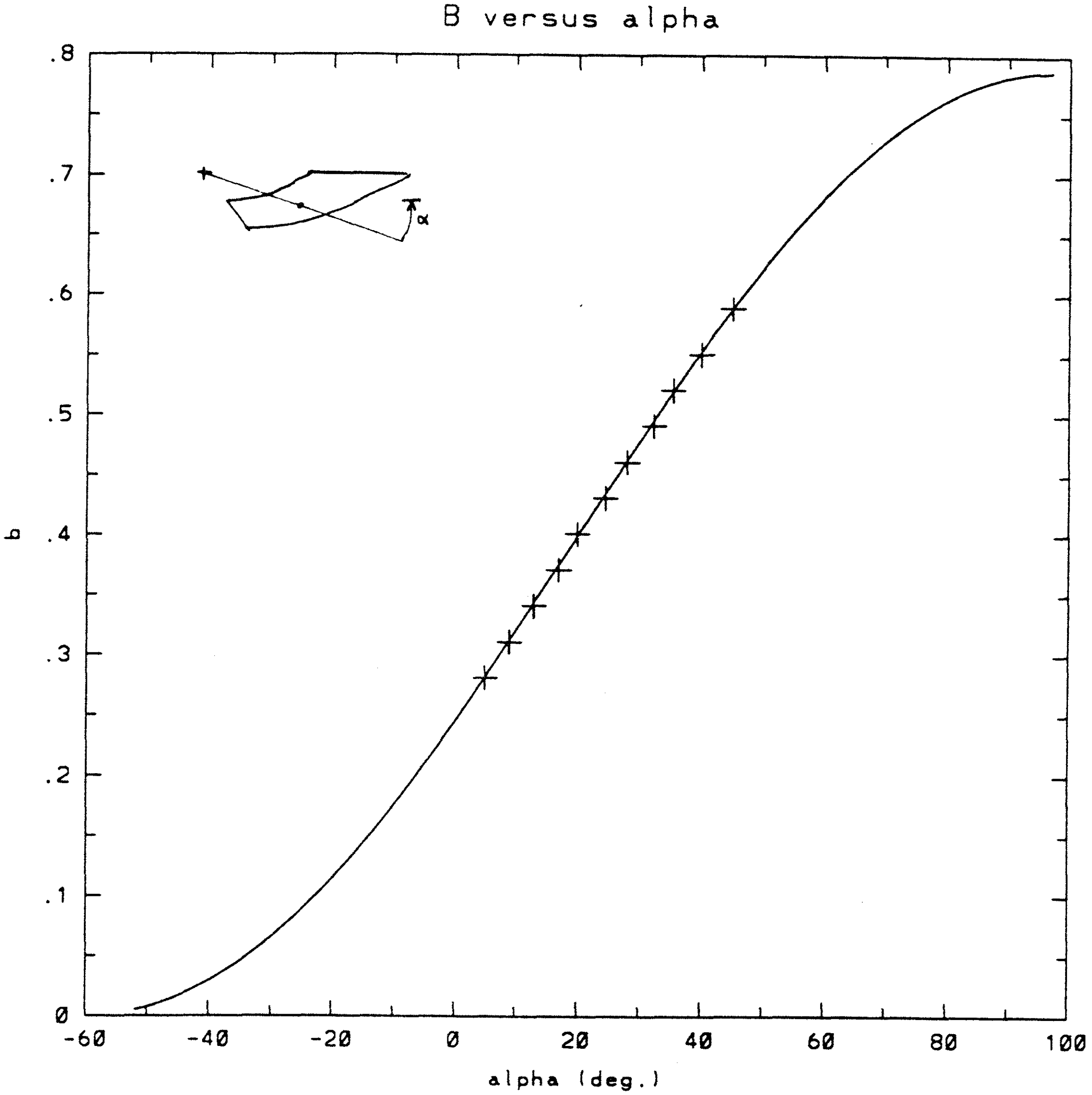

Figure 3-6: Comparison between the finite-element calculations for the test case, and the analytic self-similar solution. The plot shows the magnetic field as a function of the angle with respect to the horizontal line.The inlet conditions are $M_v = 1.4142$, $\beta_0 = 0.1$. and $b_0 = 0.5886$

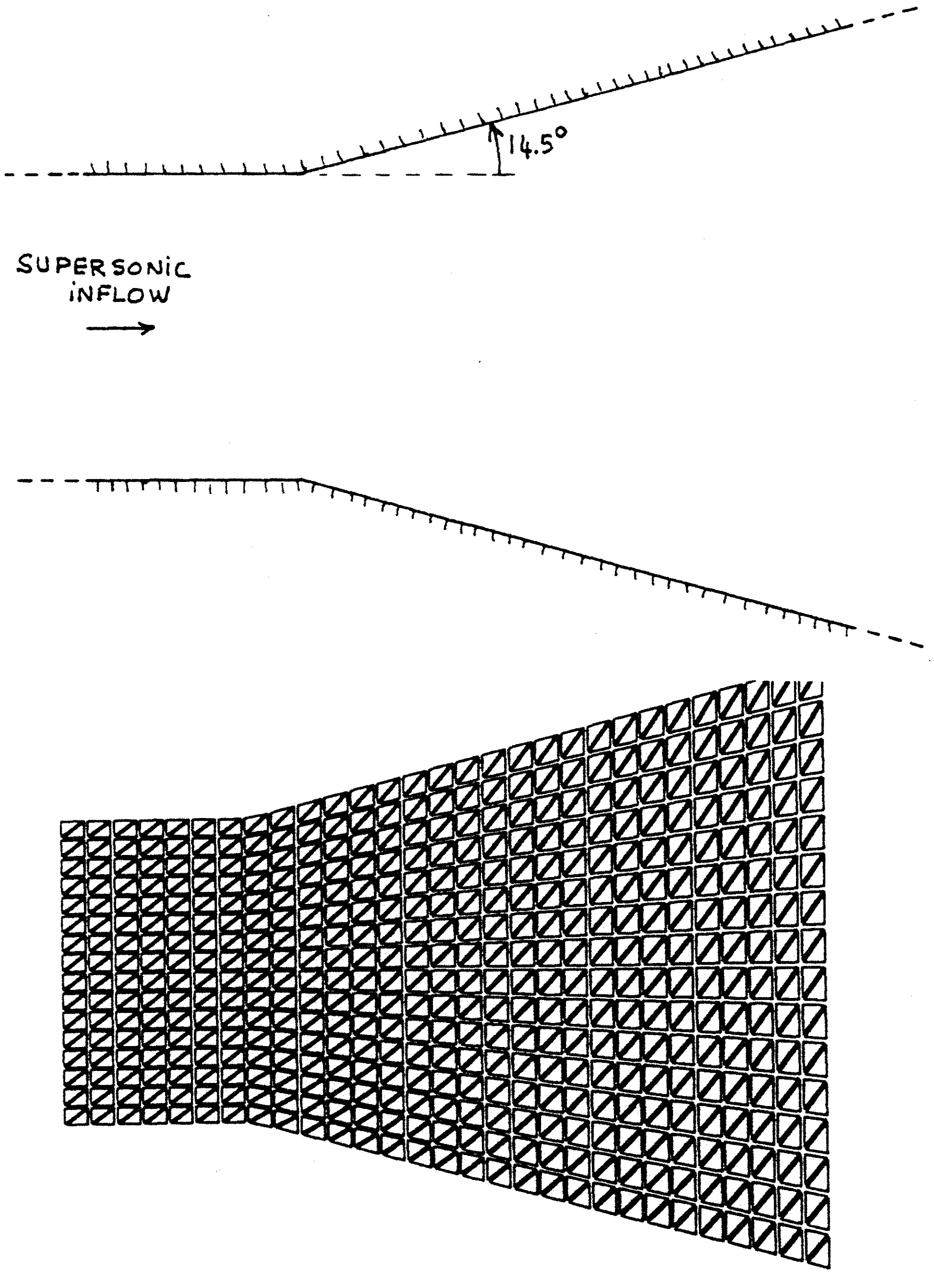

Figure 3-7: Geometry and finite element grid for a divergent channel. The angle between the divergent section and the horizontal axis is 14.5°. The initial conditions are $M_v = 1.4142$, $\beta_0 = 0.1$ and $b_0 = 0.5886$.

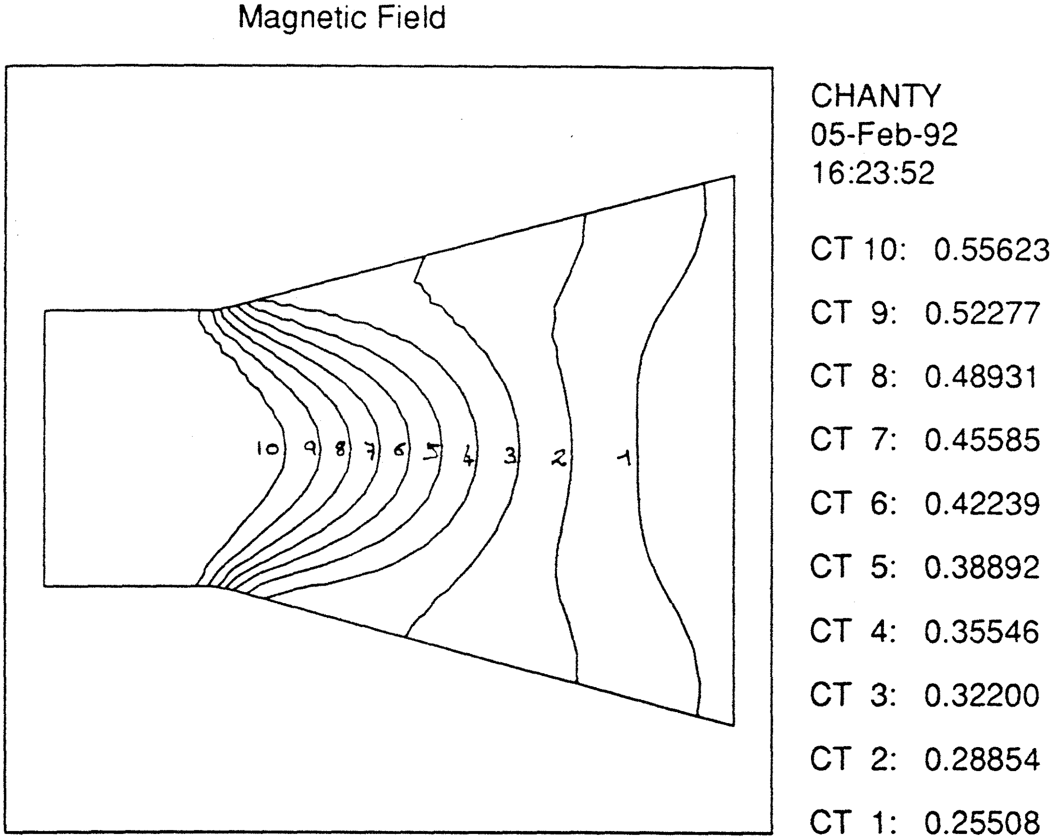

Figure 3-8: Magnetic field obtained by the finite element algorithm for the non-resistive plasma flowing in a diverging channel. The angle between the divergent section and the horizontal axis is 14.5°. The initial conditions are $M_v = 1.4142$, $\beta_0 = 0.1$ and $b_0 = 0.5886$.

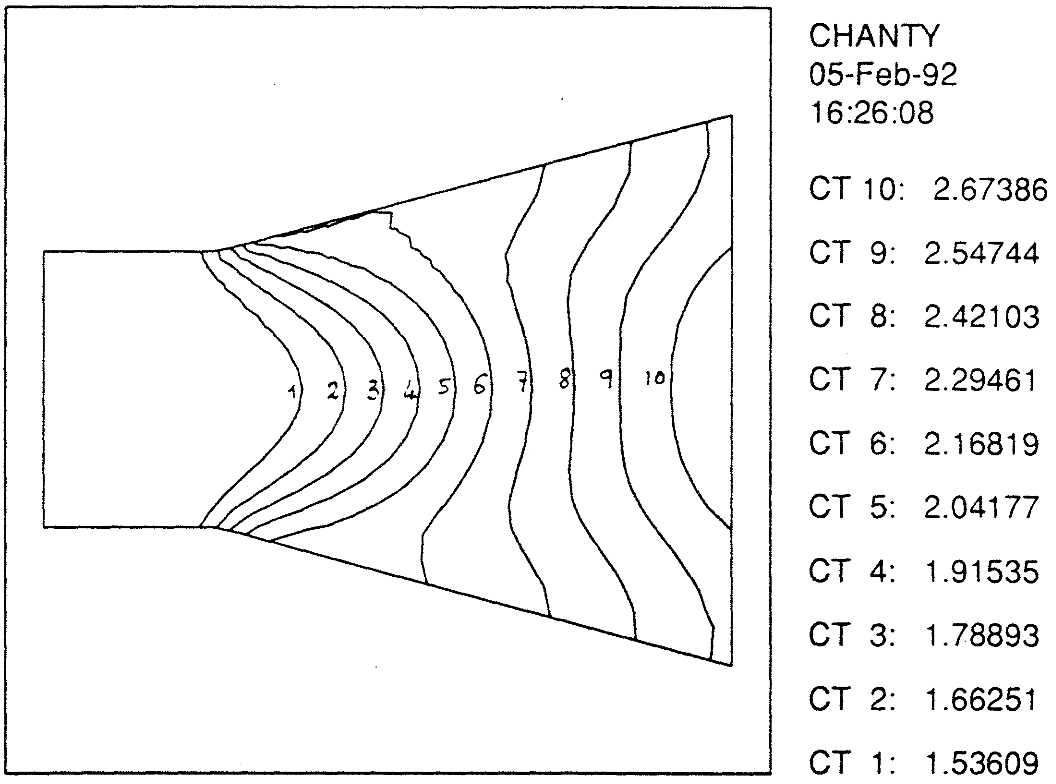

Mach-Alfven Number

Figure 3-9: Mach-Alfven number obtained by the finite element algorithm for the non-resistive plasma flowing in a diverging channel. The angle between the divergent section and the horizontal axis is 14.5°. The initial conditions are $M_v = 1.4142$, $\beta_0 = 0.1$ and $b_0 = 0.5886$.

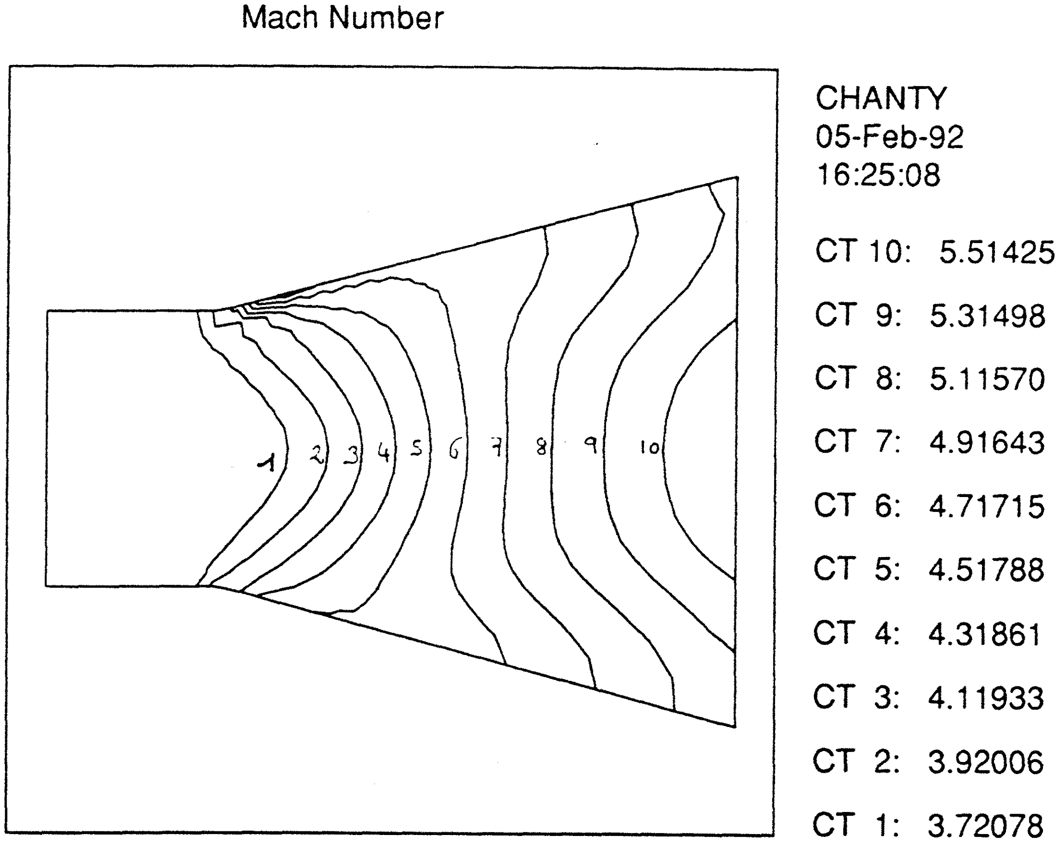

Figure 3-10: Mach number obtained by the finite element algorithm for the non-resistive plasma flowing in a diverging channel. The angle between the divergent section and the horizontal axis is 14.5°. The initial conditions are $M_v = 1.4142$, $\beta_0 = 0.1$ and $b_0 = 0.5886$.

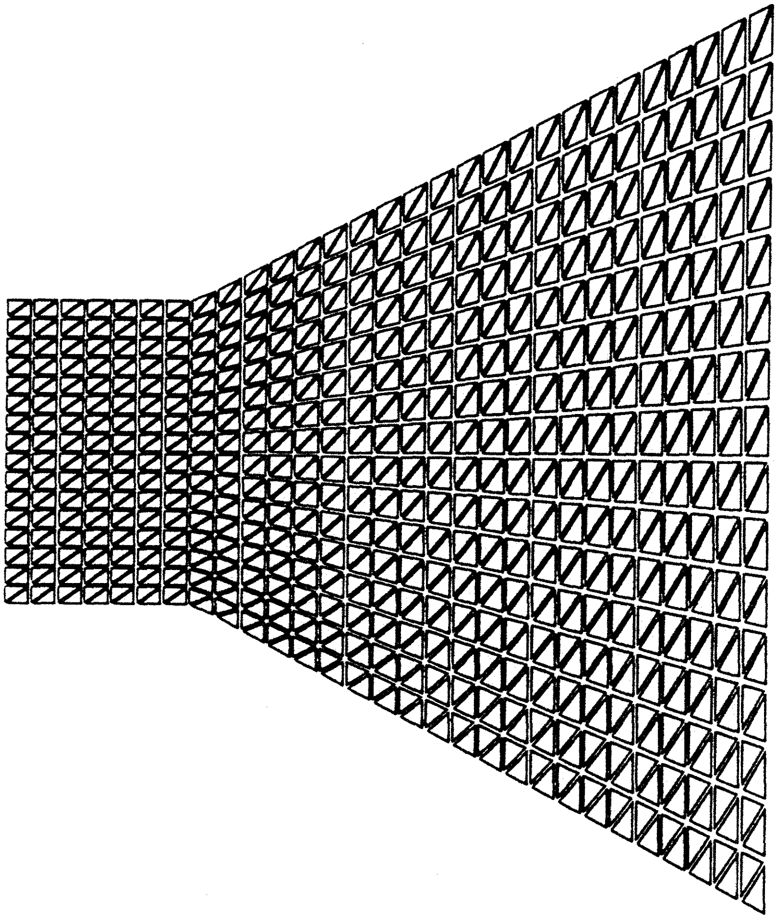

Figure 3-11: Finite element grid for a divergent channel. The angle of the divergent section is 28°. The initial conditions are $M_v = 1.4142$, $\beta_0 = 0.1$ and $b_0 = 0.5886$

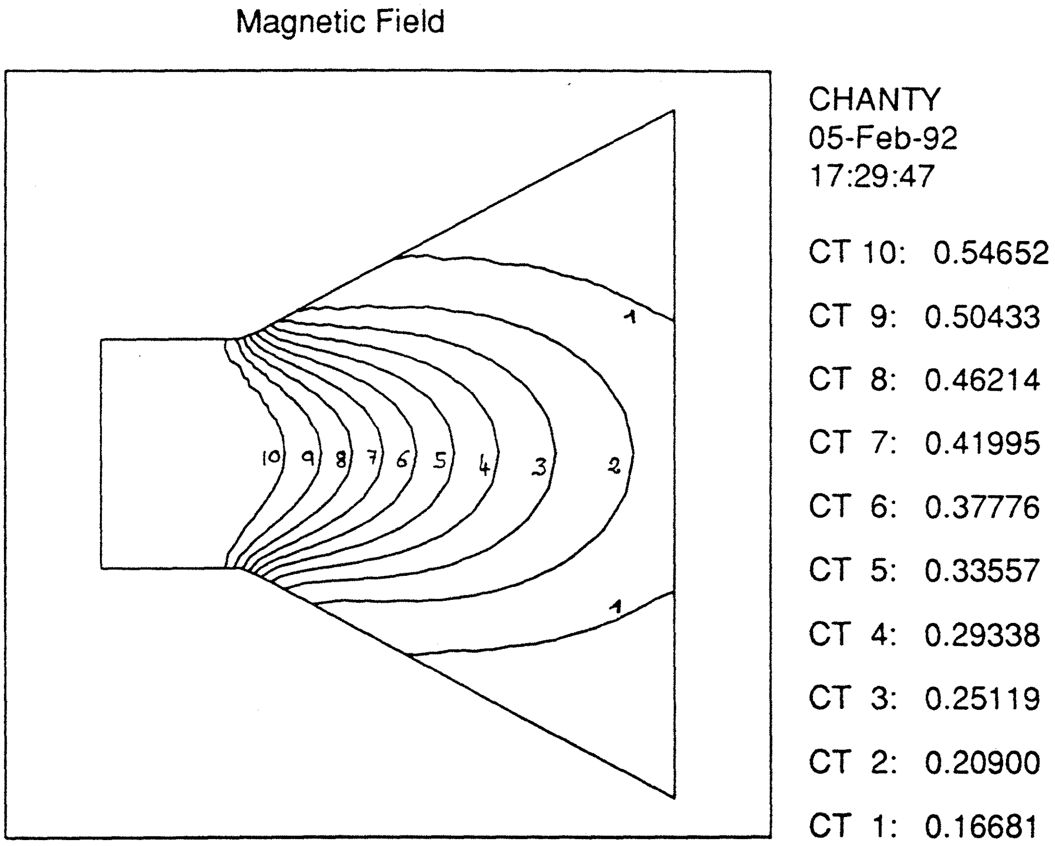

Figure 3-12: Magnetic field obtained by the finite element algorithm for the non-resistive plasma flowing in a diverging channel. The angle of the divergent section is 28°. The initial conditions are $M_v = 1.4142$, $\beta_0 = 0.1$ and $b_0 = 0.5886$

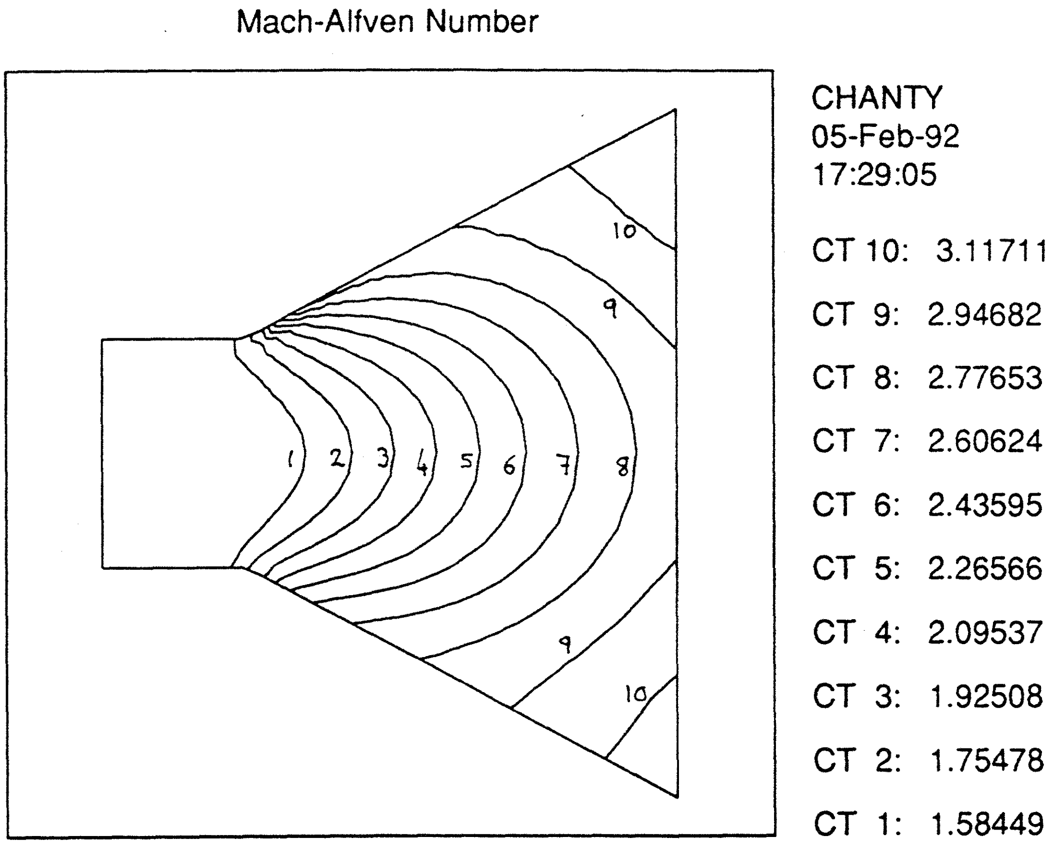

Figure 3-13: Mach-Alfven number obtained by the finite element algorithm for the non-resistive plasma flowing in a diverging channel. The angle of the divergent section is 28°. The initial conditions are $M_v = 1.4142$, $\beta_0 = 0.1$ and $b_0 = 0.5886$

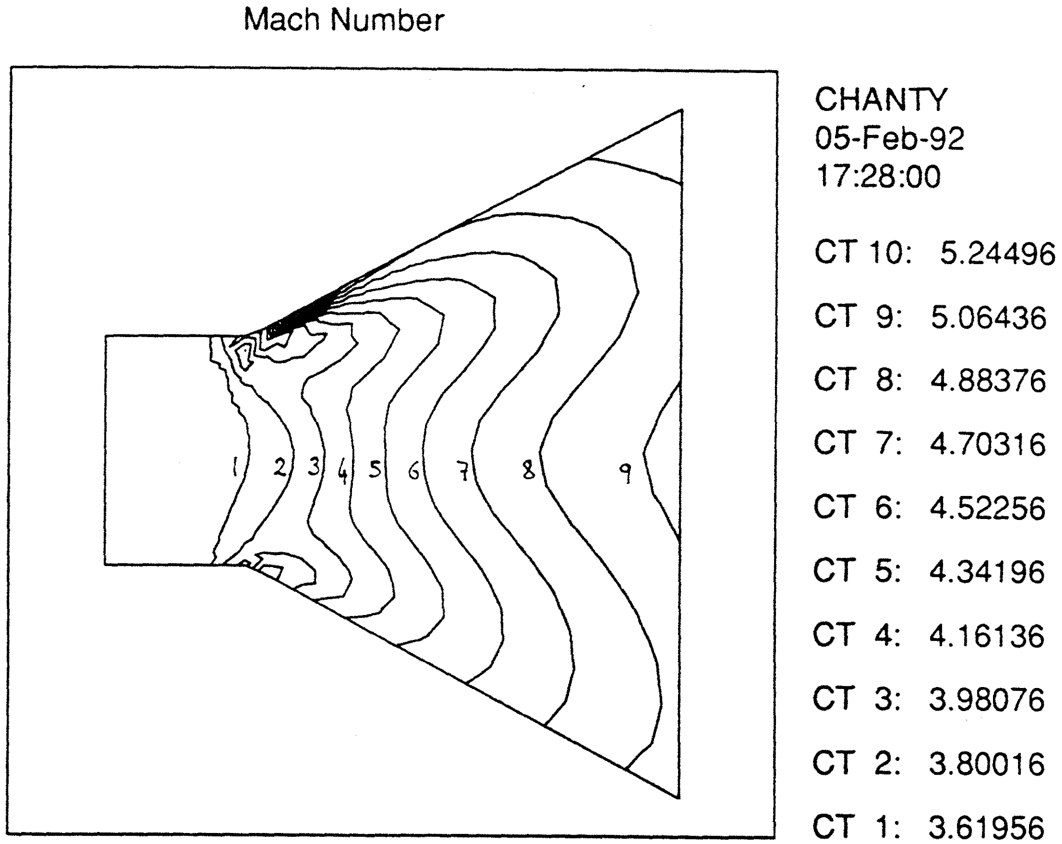

Figure 3-14: Mach number obtained by the finite element algorithm for the non-resistive plasma flowing in a diverging channel. The angle of the divergent section is 28°. The initial conditions are $M_v = 1.4142$, $\beta_0 = 0.1$ and $b_0 = 0.5886$

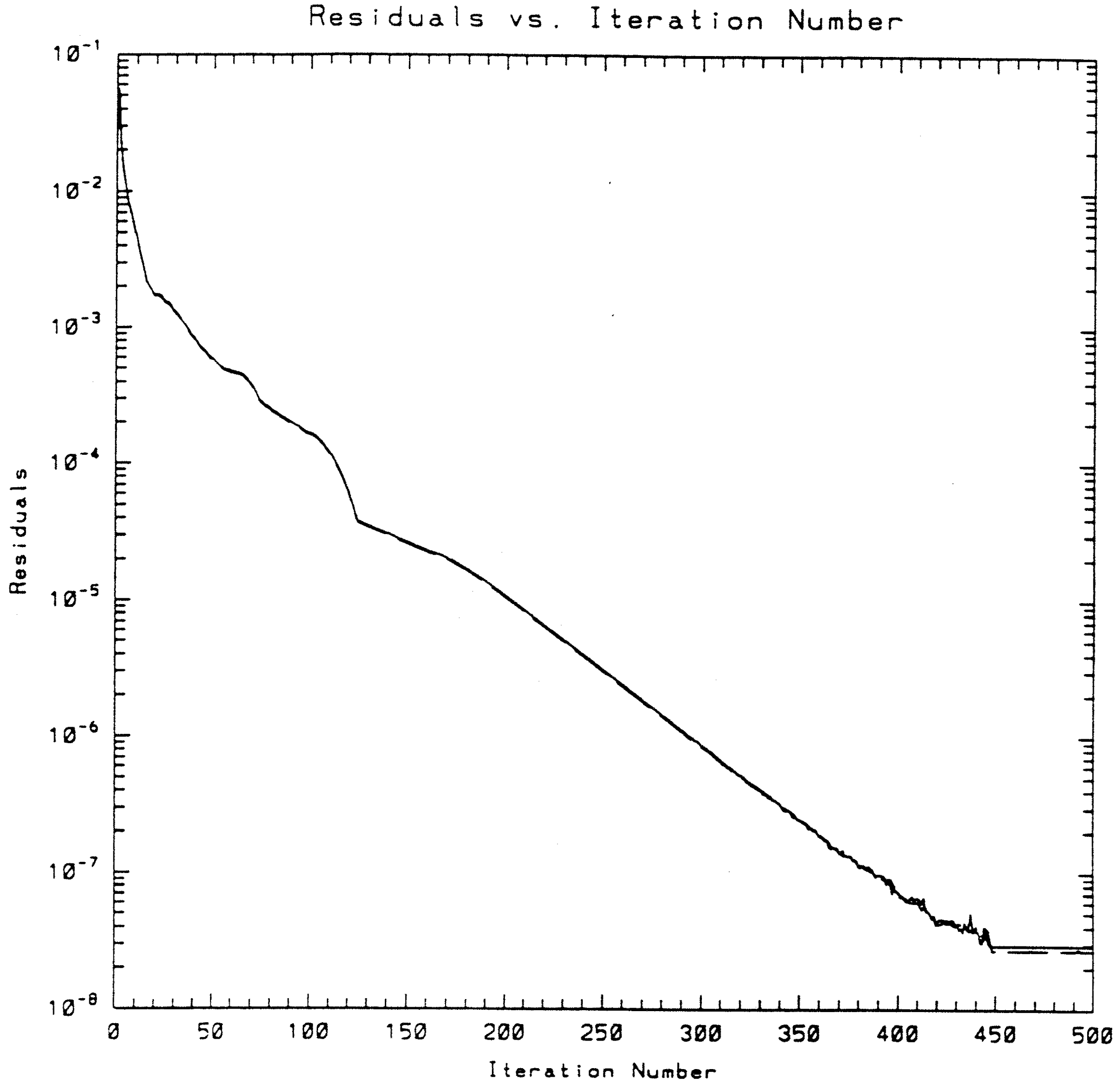

Figure 3-15: Evolution of the maximum residual for the density and the magnetic field as a function of the number of iterations during the calculation corresponding to the last three figures.

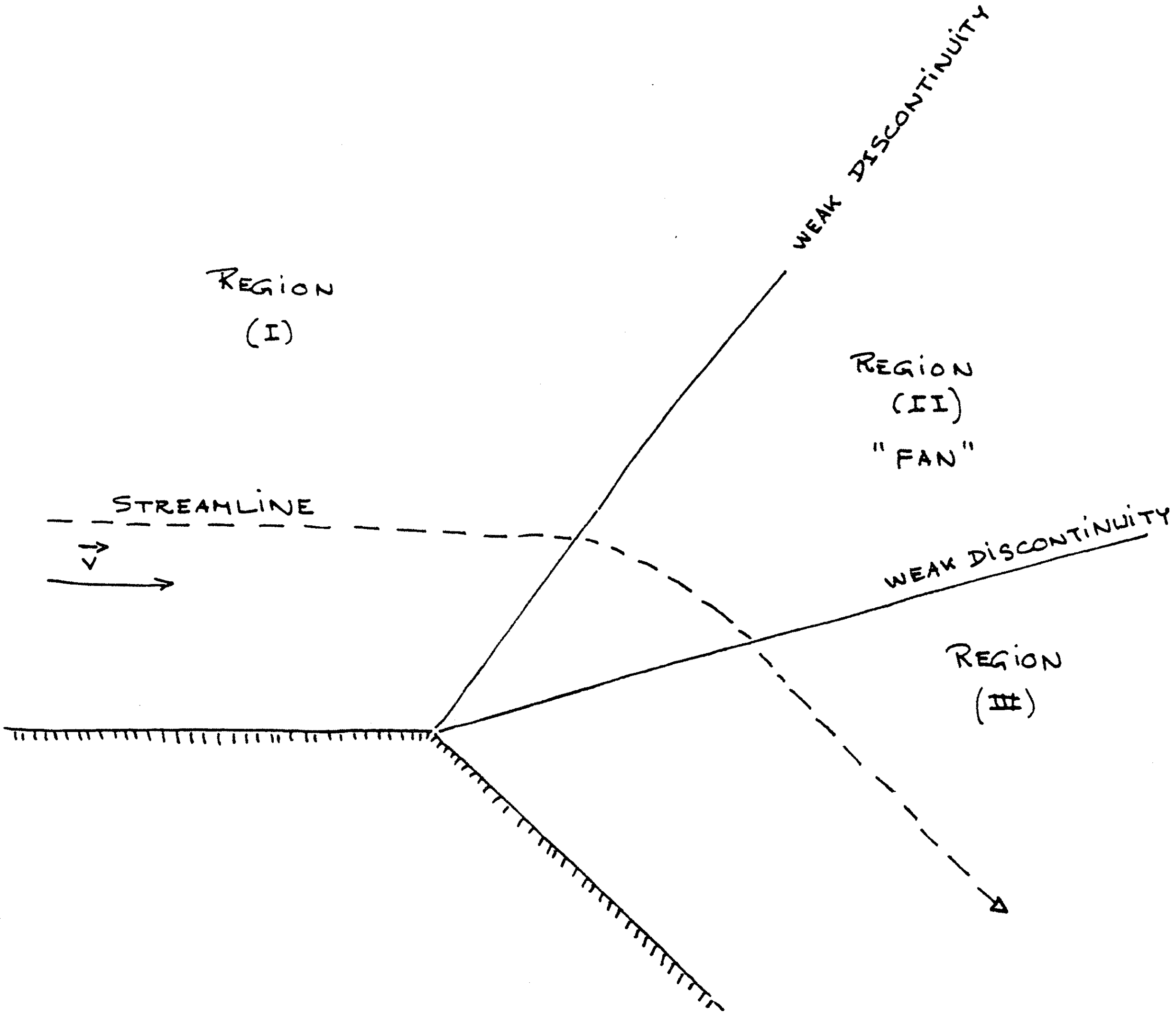

Figure 3-16: Magneto-Plasma expansion around a corner, in the limit when the resistivity goes to zero. The flow is super-magneto-sonic. We distinguish three zones: (I) and (III) are constant flow zones, zone (II) is the self similar expansion fan.

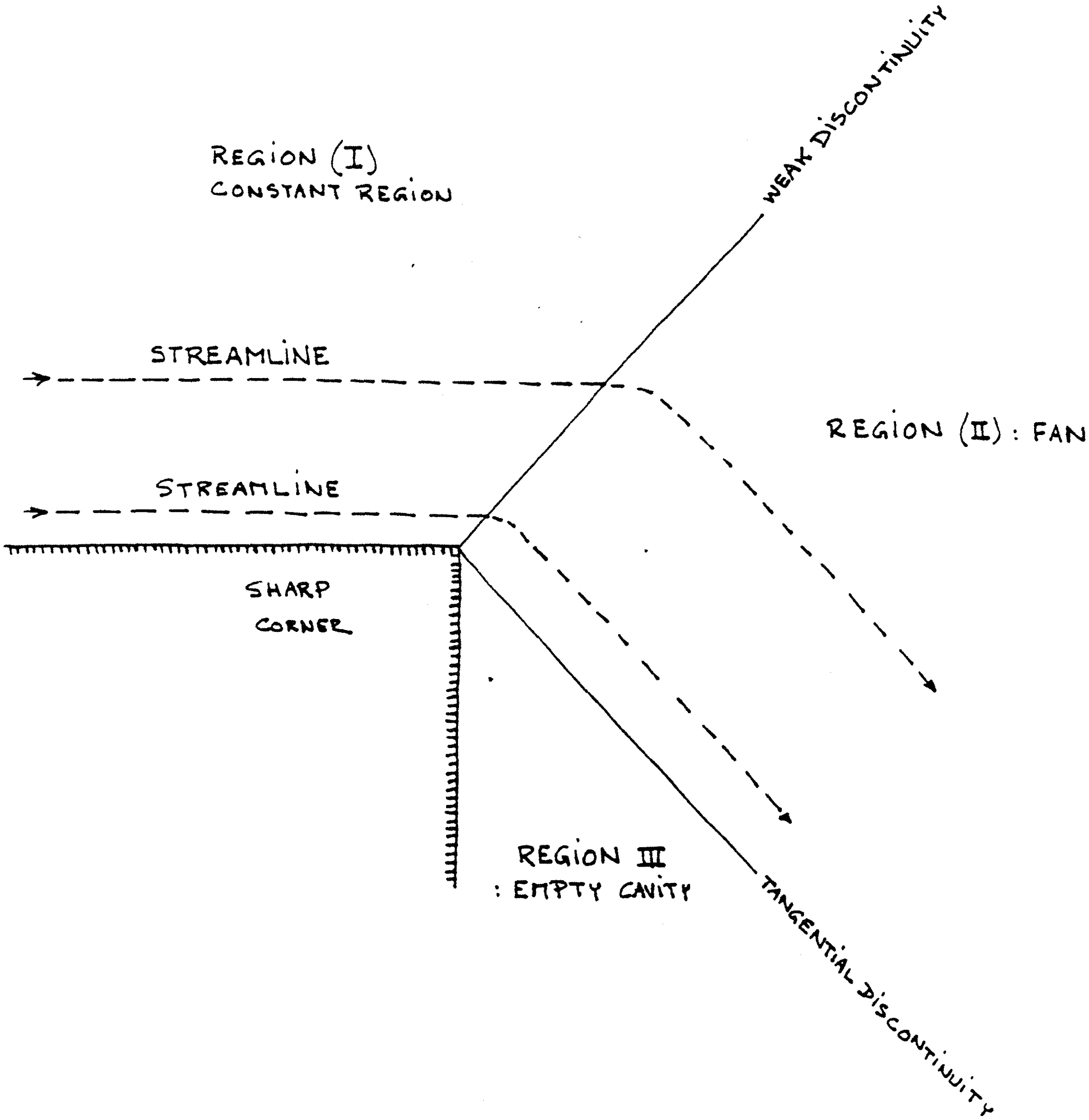

Figure 3-17: Magneto-Plasma expansion around a corner in the limit when the resistivity goes to zero. The flow is super-magneto-sonic. The expansion is complete. Zone (I) is a constant flow region. Zone (II) is the self similar expansion fan. Zone (III) is an empty cavity.

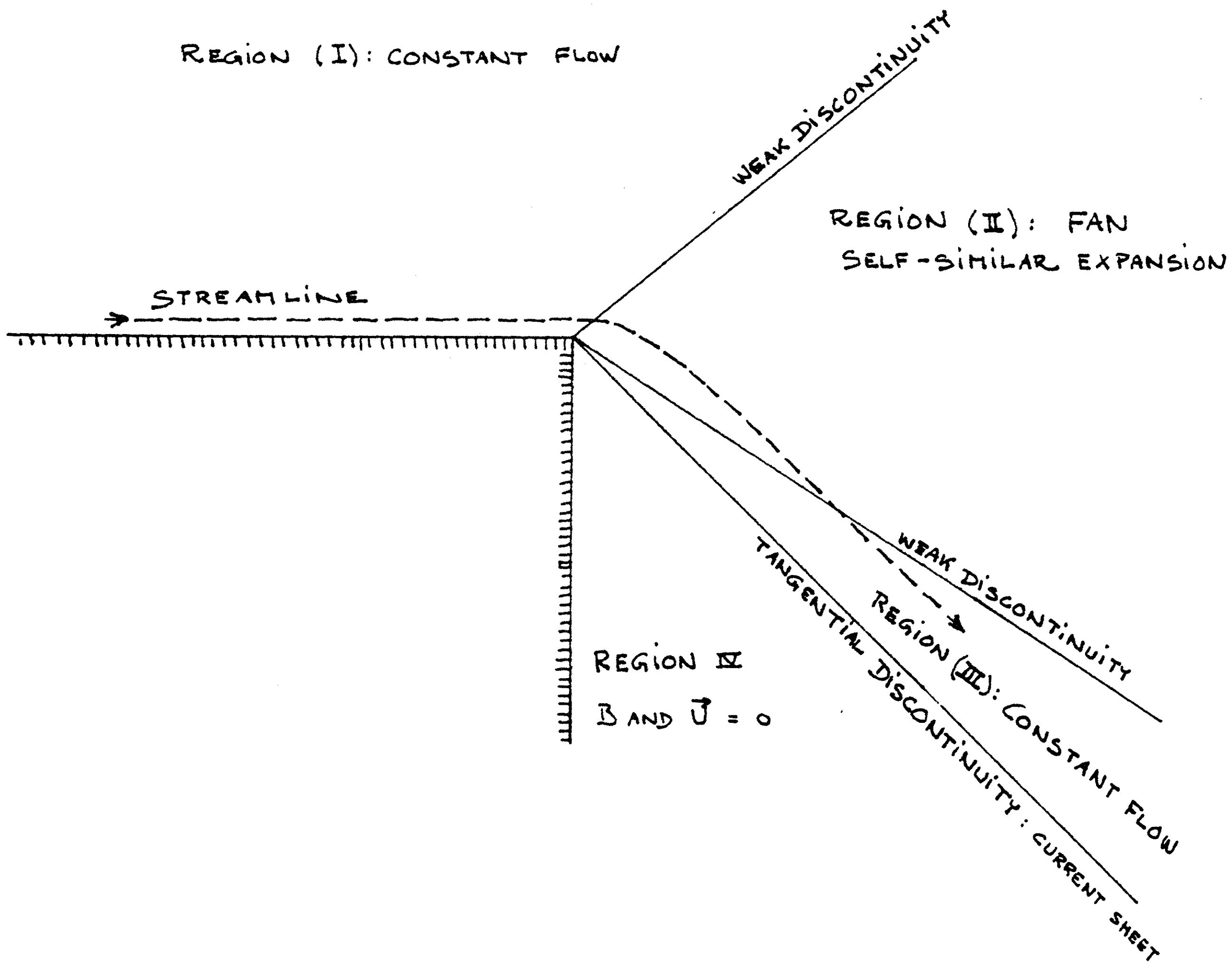

Figure 3-18: Magneto-Plasma expansion around a corner in the limit when the resistivity goes to zero. The flow is super-magneto-sonic. The expansion is incomplete. The jet expands into a medium with final residual pressure and separates from the wall. There are four zones: (I) is a constant flow zone, (II) is the self similar expansion fan, (III) is a narrow constant flow zone, (IV) is a zone where the velocity and the magnetic field are zero, but the pressure and density have constant non-zero value. The interface between zones (III) and (IV) is a tangential discontinuity.

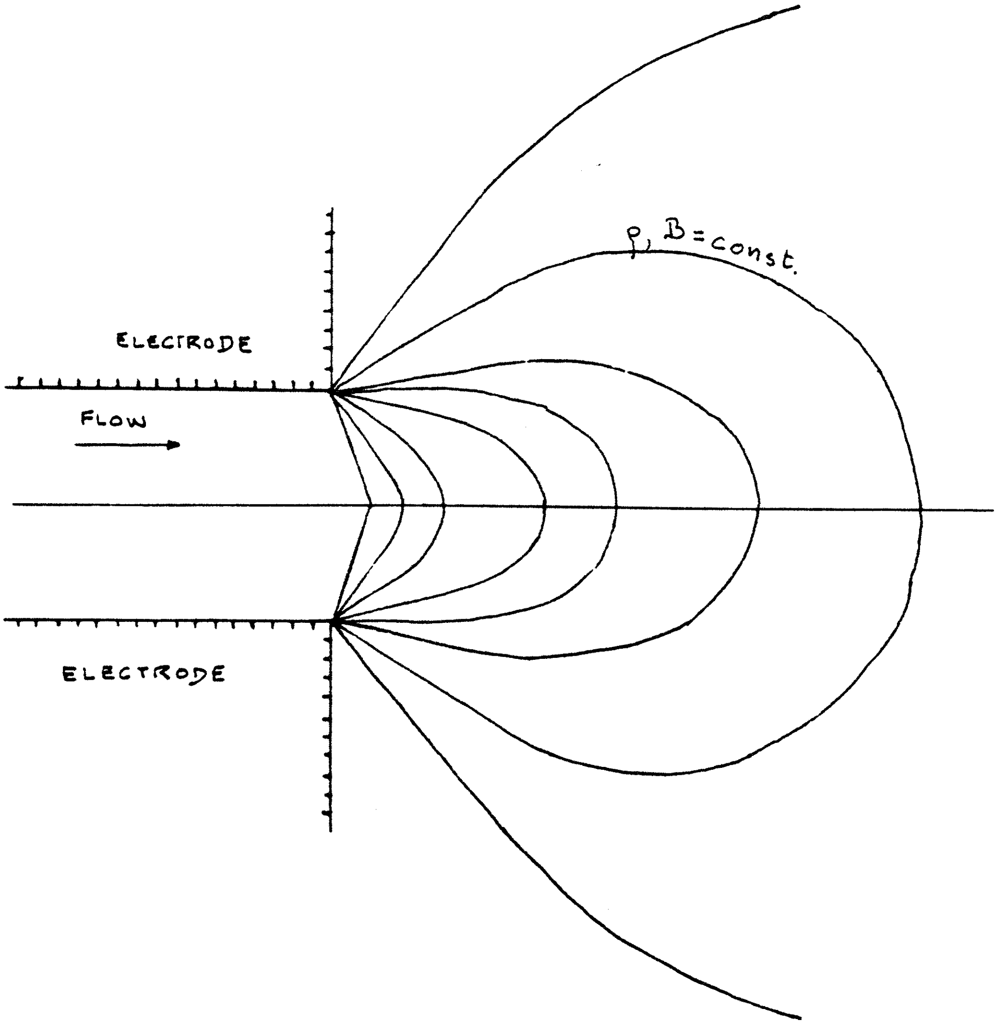

Figure 3-19: Magneto-Plasma expansion from a two-dimensional orifice in the limit when the resistivity goes to zero. The expansion takes place into a vacuum.

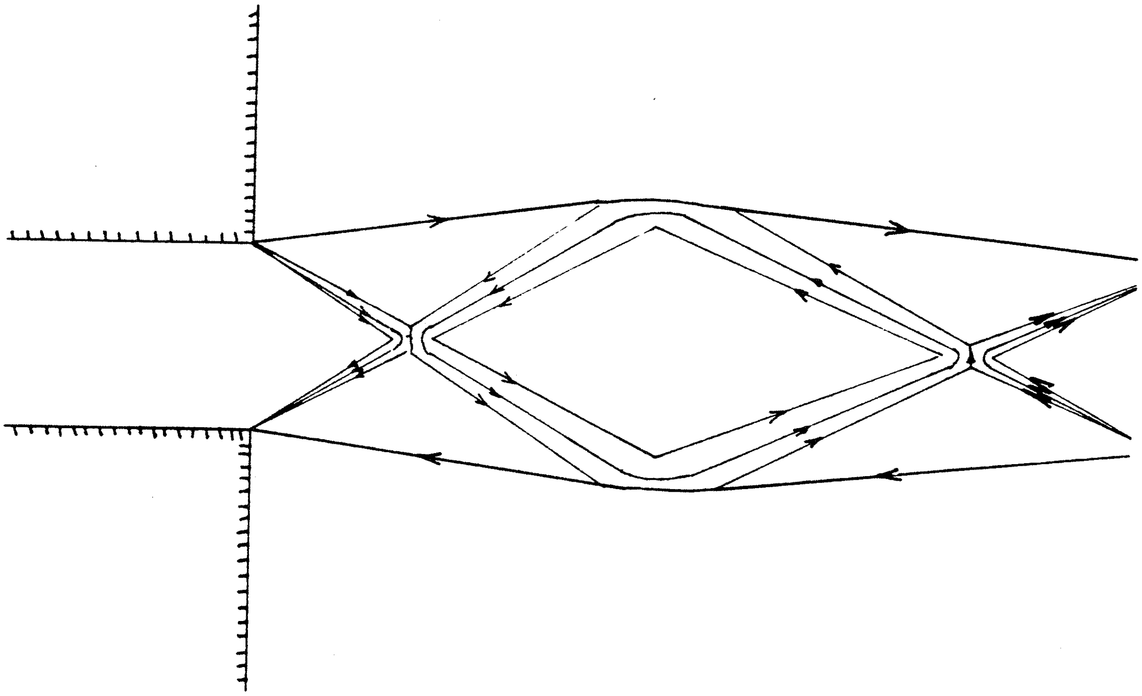

Figure 3-20: Magneto-Plasma expansion from a two-dimensional orifice in the limit when the resistivity goes to zero. The expansion takes place into a medium with residual pressure. The initial expansion is followed by a recompression region where the magnetic field increases, leading to the creation of current loops.

Chapter 4

Resistive Analysis Near a Weak Corner

As indicated above, the next step in the perturbation analysis is to study the various inner-solutions. The inner-solution located near the inlet can easily be solved in the absence of the Hall effect. The solution is a variation of the one-dimensional model, and is discussed above. (See section 2.2.) In the presence of the Hall effect the problem is more complicated and will not be treated here.

Another inner-region is that which is adjacent to the sharp corners of the exit. The study of the flow around the exit has some important justifications. In the general case it is a poorly understood region; despite its relative accessibility there have been few investigations of the plasma density, velocity and temperature. The magnetic field and the current have been more thoroughly studied, but few investigators have looked at the field leakage along the surface of the anode beyond the point where the jet detaches itself from the electrode. In the quasi-one-dimensional theories discussed in the introduction, the researchers assume that the magnetic field reaches zero at the end of the channel. But there is no reason to dismiss the possibility that some of the current can leak out of the main channel and attach itself along other surfaces of the electrodes, away from the plasma jet. Along the anode this effect is probably reinforced by the Hall conduction.

This non-linear problem is difficult to solve. It is possible to solve a closely related problem using a semi-analytical method by considering the limiting case of a corner with a small deflection angle. In this case the problem becomes linear. This type of approximation is often called a small disturbance approximation, and will be considered next.

4.1 Background on the Small-Disturbance Approximation

The small disturbance approximation has been used to solve several problems in aerodynamics. Some of the earliest applications were the lifting line theory of Prandtl; the thin airfoil theory of Munk [46]; the analysis of supersonic flows by Ackeret [1]; and the analysis of compressible flows by Glauert [20].

The transonic regime, where the linear theory is not valid, was treated by Oswatitsch and Berndt [50]. The resulting equation, called the small disturbance transonic equation, reduces to the linear equations both in the subsonic and in the supersonic regime. The viscous flow through a convergent-divergent nozzle was analyzed by Sichel [56] using an extension of the transonic equation which incorporates an additional term describing the viscous effects, first derived by Liepmann, Ashkenas, and Cole [37]. These works could conceivably be used as a starting point for the analysis of a plasma flowing through a convergent-divergent channel, where the outer flow changes from sub-magnetosonic to super-magnetosonic at the throat.

Unsteady problems can also be treated by the small disturbance method. The diffraction of a weak shock wave by a small corner was treated by Bargman [5] and later extended by Lighthill [38] to the case of strong normal shocks. The flow around an oscillating airfoil was treated by Timman, van de Vooren and Greidanus [62]. These works could be a starting point for a study of the stability of the thruster with respect to small amplitude perturbations.

The flow of an ideal dissociating gas around a sharp corner was treated by Clarke and McChesney [14] by the small disturbance approximation. This problem has many similarities with the flow of a resistive plasma, including the presence of two different expansion fans, namely a frozen flow expansion fan located near the corner and an equilibrium flow expansion fan located at large distances. In their analysis Clarke and McChesney use a Laplace transformation in the x direction which they were able to invert analytically. In the flow of a resistive plasma, the diffusive effects propagate upstream from the corner, so the solution requires the use of a Fourier transformation instead of a Laplace transformation.

The flow of ionized gases over thin airfoils and slender bodies was studied by Lary [33], by Sears and Resler [54] in the limit of high magnetic Reynolds numbers. Compressible effects were studied by McCune and Resler [42]. However the geometry considered by these authors differed from the geometry considered in this dissertation by the orientation of the magnetic field. In addition the Hall effect was not considered.

4.2 Formulation of the Linear Problem

Consider the regular perturbation whose small parameter is a measure of the deformation of the boundary, and the zero-order term of the expansion is a uniform flow.[1] The solution is sought as a perturbation expansion of the form:

$$(\rho, u, v, p, b) = (\rho_0, u_0, 0, p_0, b_0) + \epsilon /, (\rho_1, u_1, v_1, p_1, b_1) + \cdots \tag{4.1}$$

with the small parameter being the corner deflection angle:

$$0 < \epsilon \rightarrow 0. \tag{4.2}$$

---

[1] The constant background solution satisfies the differential equations, as well as the boundary conditions. In particular it satisfies the boundary condition for the magnetic field which is: $\frac{\partial b}{\partial n} = 0$.

The original system of partial differential equations can be written in cartesian coordinates in the following way:[2]

$$\frac{\partial}{\partial X}(\rho u) + \frac{\partial}{\partial Y}(\rho v) = 0, \tag{4.3}$$

$$\rho u \frac{\partial u}{\partial X} + \rho v \frac{\partial u}{\partial Y} + \frac{\partial}{\partial X}(p + b^2) = 0, \tag{4.4}$$

$$\rho u \frac{\partial v}{\partial X} + \rho v \frac{\partial v}{\partial Y} + \frac{\partial}{\partial Y}(p + b^2) = 0, \tag{4.5}$$

$$\frac{1}{\gamma - 1}\left(\rho^\gamma u \frac{\partial}{\partial X} + \rho^\gamma v \frac{\partial}{\partial Y}\right)\left(\frac{p}{\rho^\gamma}\right) = 2\left(\left(\frac{\partial b}{\partial X}\right)^2 + \left(\frac{\partial b}{\partial Y}\right)^2\right), \tag{4.6}$$

$$\left(\rho u \frac{\partial}{\partial X} + \rho v \frac{\partial}{\partial Y}\right)\left(\frac{b}{\rho}\right) = \left(\frac{\partial^2 b}{\partial X^2} + \frac{\partial^2 b}{\partial Y^2}\right). \tag{4.7}$$

After substitution of the perturbation expansions the following system of linear equations is obtained:

$$\rho_0 \frac{\partial u_1}{\partial X} + u_0 \frac{\partial \rho_1}{\partial X} + \rho_0 \frac{\partial v_1}{\partial Y} = 0, \tag{4.8}$$

$$\rho_0 u_0 \frac{\partial u_1}{\partial X} + \frac{\partial p_1}{\partial X} + 2b_0 \frac{\partial b_1}{\partial X} = 0, \tag{4.9}$$

$$\rho_0 u_0 \frac{\partial v_1}{\partial X} + \frac{\partial p_1}{\partial Y} + 2b_0 \frac{\partial b_1}{\partial Y} = 0, \tag{4.10}$$

$$\frac{1}{p_0}\frac{\partial p_1}{\partial X} - \gamma \frac{1}{\rho_0}\frac{\partial \rho_1}{\partial X} = 0, \tag{4.11}$$

$$u_0 \frac{\partial b_1}{\partial X} - \frac{u_0 b_0}{\rho_0}\frac{\partial \rho_1}{\partial X} = \left(\frac{\partial^2 b_1}{\partial X^2} + \frac{\partial^2 b_1}{\partial Y^2}\right). \tag{4.12}$$

This system is completed by several boundary conditions. The *causality condition*, implies that the perturbations vanish at ∞ upstream of the corner, giving the condi-

---

[2] In these equations, the magnetic Reynolds number is absorbed into the coordinates, which amounts to measuring the distance in units of the magnetic interaction length. The new coordinates X, Y are defined by:

$$X = \frac{\bar{x}}{\Lambda_m}$$

$$Y = \frac{\bar{y}}{\Lambda_m}$$

where $\bar{x}, \bar{y}, \Lambda_m$ are the dimensional coordinates and magnetic interaction length.

tions:

$$(\rho_1, u_1, v_1, p_1, b_1)(-\infty, Y) = 0, \tag{4.13}$$

$$(\rho_1, u_1, v_1, p_1, b_1)(X, \infty) = 0. \tag{4.14}$$

The *tangency condition* states that the velocity is tangent to the boundary surface. It can be written

$$v_1(X, 0) = u_0 \frac{1}{\epsilon} \frac{dY}{dX}. \tag{4.15}$$

In this case $\frac{1}{\epsilon}\frac{dY}{dX} = -\Upsilon(X)$, where $\Upsilon(X)$ is the step function, so that:

$$v_1(X, 0) = -u_0 \Upsilon(X). \tag{4.16}$$

The equipotential condition imposes that the current be normal to the electrode in the absence of the Hall effect, that is:

$$\frac{\partial b_1}{\partial Y}(X, 0) = 0, \quad \text{for} \quad X \in \mathbf{R}. \tag{4.17}$$

From equation 4.11 it can be seen that the Joule heating does not appear in this system of equations and that, to the order of this approximation, the solution is isentropic.

4.3 Transformation into a Hyper-Elliptic Operator

It is possible to rearrange the system of equations into one unique equation of fourth order, as follows: Equations (4.9) and (4.11) can be integrated to give conservative quantities: the momentum perturbation and the entropy perturbation. In addition, the combination of the two momentum equations gives

$$\frac{\partial u_1}{\partial Y} = \frac{\partial v_1}{\partial X}. \tag{4.18}$$

It is possible to eliminate all but one variable. The result defines a linear partial differential operator of fourth order. For instance one can write the problem in terms of the normal velocity perturbation v_1 with the following equation and boundary conditions:

$$u_0\frac{\partial}{\partial X}\left((1-M_v^2)\frac{\partial^2}{\partial X^2}+\frac{\partial^2}{\partial Y^2}\right)v_1=\frac{M_v^2}{M_a^2}\nabla^2\left((1-M_a^2)\frac{\partial^2}{\partial X^2}+\frac{\partial^2}{\partial Y^2}\right)v_1, \tag{4.19}$$

$$v_1(X,0)=-u_0\Upsilon(X), \tag{4.20}$$

$$(1-M_a^2)\frac{\partial^2 v_1}{\partial X^2}+\frac{\partial^2 v_1}{\partial Y^2}=0, \qquad \text{for } Y=0, \tag{4.21}$$

where $\Upsilon(X)$ is the step function, $M_a^2=\frac{\rho_0 u_0^2}{\gamma p_0}$, and $M_v^2=\frac{\rho_0 u_0^2}{\gamma p_0+2b_0^2}$. Notice that the operator is identical no matter which variable is chosen, though the boundary conditions depend on the actual variable $(\rho_1, u_1, v_1, p_1, b_1, \ldots)$.

4.3.1 Analysis of the Equation

Equation 4.19 is of fourth order. The left hand side is the convective part; the right-hand side is the convective-diffusive part. An analysis of the characteristics of the operator gives a way to classify the nature of this operator. Following Ames [2], it can be shown that the operator has four characteristic roots: two real roots,

$$z_\pm=\tan\mu_\pm=\pm\frac{1}{\sqrt{M_a^2-1}}, \tag{4.22}$$

which define the Mach lines and which correspond to the hyperbolic behavior; and two complex characteristic roots. Since the operator has real characteristics, it is partially hyperbolic and one can expect the existence of discontinuities in the solution across the characteristic lines. These discontinuities can appear either in the variables themselves (strong discontinuities) or in their derivatives (weak discontinuities). It appears that ρ_1, p_1, u_1 and v_1 have strong discontinuities and b_1 has weak discontinuities across the characteristic lines.

Care must be taken to define a well-posed problem by choosing a set of boundary conditions which are compatible. In the following sections the cases of an isolated corner and an infinite channel are considered, and four independent boundary conditions are specified in each case.

4.4 Solutions at Large Distances

It is logical to start the analysis of the small disturbance problem by looking at the solution behavior at large distance from the corner. In a first step one can identify the *far field solution* which is obtained by neglecting the effects of resistivity in the equations. This *far field solution* is simply a magneto-sonic fan similar to that which is shown in figure 4-1. The effect of the linearization is to collapse the width of the expansion fan into a discontinuity, therefore the far field solution corresponds to an abrupt change of the variables along the characteristic line leaving from the corner.

The second step is to improve the *far field solution* by taking the resistivity into account. Since the order of the partial differential equation increases when the resistivity is taken into consideration, the problem is a singular perturbation problem in terms of $\frac{1}{R_m}$, which can be analyzed considering inner and outer expansions. The *far field solution* is simply the first term of the outer expansion. An inner expansion must be constructed in each region where the outer expansion is singular and it is possible to construct from these expansions a uniformly valid solution which is called the *asymptotic solution.* The analysis will be limited to the calculation of two inner regions: the transition layer along the characteristic line, and the magnetic wake along the wall.

In principle another way to calculate asymptotic solutions would be to find asymptotic expansions of the Fourier integral considered in the next section. However this is complicated by the presence of fourth order roots.

4.4.1 Far Field Solution

At large distance from the corner, the right hand side of the equation (4.19) becomes negligible. After integration the equation reduces to:

$$\left((1 - M_v^2)\frac{\partial^2}{\partial X^2} + \frac{\partial^2}{\partial Y^2}\right) v_1^{(o)} = 0. \tag{4.23}$$

with the boundary conditions, $v_1^{(o)}(-\infty, Y) = 0$, $v_1^{(o)}(X, \infty) = 0$, $v_1^{(0)}(X, 0) = \Upsilon(X)$. Since the flow near the exit is most likely to be super-magneto-sonic, this analysis is limited to the case where $M_v^2 \geq 1$, and thus the operator is hyperbolic. The solution is similar to that of a supersonic flow around a corner with a Mach number equal to M_v. The solution of this problem is then: $v_1^{(o)}(X, Y) = -u_0\Upsilon(X - Y\sqrt{M_v^2 - 1})$. It has a discontinuity along the characteristic line defined by: $\tan\mu_v = \frac{1}{\sqrt{M_v^2 - 1}}$. The other variables have identical behaviors. Upstream of the characteristic line the perturbations are zero. Downstream of the characteristic line, they have a constant value. The solutions are summarized below:

$$u_1^{(o)}(X, Y) = u_0\Upsilon(X - Y\sqrt{M_v^2 - 1}), \tag{4.24}$$

$$v_1^{(o)}(X, Y) = -u_0\Upsilon(X - Y\sqrt{M_v^2 - 1}), \tag{4.25}$$

$$\rho_1^{(o)}(X, Y) = -M_v^2\rho_0\Upsilon(X - Y\sqrt{M_v^2 - 1}), \tag{4.26}$$

$$b_1^{(o)}(X, Y) = -M_v^2 b_0\Upsilon(X - Y\sqrt{M_v^2 - 1}). \tag{4.27}$$

4.4.2 Asymptotic Solutions at Large Distances

Transition Layer along the Characteristic Line

Along the characteristic line, the "far field solution" has a discontinuity. Therefore the right hand side of the complete operator cannot be neglected in this region. One can expect some type of inner-layer to appear along that line, which will smooth out the sharp discontinuity. In order to find this correction let us consider the following inner expansion valid in the region of the characteristic line:

$$v_1(X,Y;\epsilon') = V_0(\tilde{X},\tilde{Y}) + \epsilon' V_1(\tilde{X},\tilde{Y}) + \cdots \tag{4.28}$$

with the following coordinate "contractions":

$$\tilde{X} = \epsilon' X, \tag{4.29}$$

$$\tilde{Y} = \epsilon'^{1/2}(Y - \frac{X}{\beta_v}), \tag{4.30}$$

where ϵ' is a small number which goes to zero, and $\beta_v = \sqrt{M_v^2 - 1}$. This inner expansion will be matched to the outer expansion; in this case the solution is:

$$v_1^{(o)}(X,Y) = -u_0 \Upsilon(X - Y\sqrt{M_v^2 - 1}). \tag{4.31}$$

To simplify the notation it is convenient to define the parameters:

$$\beta_v^2 = M_v^2 - 1, \tag{4.32}$$

$$\beta_a^2 = M_a^2 - 1, \tag{4.33}$$

After substituting in the equation 4.19 and collecting the terms of higher order, one obtains the parabolic equation:

$$2u_0 \frac{\partial V_0}{\partial \tilde{X}} = \frac{M_v^2}{M_a^2}\left(\frac{\beta_a^2}{\beta_v^4} + \frac{\beta_a^2 - 1}{\beta_v^2} - 1\right)\frac{\partial^2 V_0}{\partial \tilde{Y}^2}, \tag{4.34}$$

with the boundary conditions (see figure 4-2):

$V_0(\tilde{X}, -\infty) = -u_0$ (downstream matching);

$V_0(\tilde{X}, \infty) = 0$ (upstream matching);

$V_0(0, \tilde{Y}) = -u_0\ \Upsilon(-\tilde{Y})$ (matching along the electrode).

The downstream boundary condition ($V_1 = -u_o$) should be imposed on the line $Y = 0$ (that is $\tilde{X} = -\epsilon'^{1/2}\beta_v \tilde{Y}$). But in order to simplify the analysis it is convenient to impose it instead on the line $\tilde{X} = 0$. The equation then becomes,

$$\frac{\partial V_0}{\partial \tilde{X}} = K \frac{\partial^2 V_0}{\partial \tilde{Y}^2}, \tag{4.35}$$

with

$$K = \frac{1}{2u_0} \frac{M_v^2}{M_a^2} \left(\frac{\beta_a^2}{\beta_v^4} + \frac{\beta_a^2 - 1}{\beta_v^2} - 1 \right) \tag{4.36}$$

completed by the boundary conditions mentioned above.

It can be shown that the solution for this problem is:

$$V_0(\tilde{X}, \tilde{Y}) = -\frac{u_0}{2} \mathrm{erfc} \left(\frac{\tilde{Y}}{2\sqrt{K\tilde{X}}} \right), \tag{4.37}$$

where

$$\mathrm{erfc}(z) = \frac{2}{\sqrt{\pi}} \int_z^\infty e^{-t^2} dt. \tag{4.38}$$

This can also be expressed it in terms of the variables X, Y leading to:

$$V_0(X, Y) = -\frac{u_o}{2} \mathrm{erfc} \left(\frac{(Y - \frac{X}{\beta_v})}{2\sqrt{KX}} \right). \tag{4.39}$$

This solution shows that the far field transition is smoothed out in the region along the characteristic leaving the corner. The profile of this inner-layer is shown in figure 4-3. The thickness of this layer increases as the square root of the distance to the corner. As a result the layer thickness grows, but its width relative to the distance decreases as one over the square root of the distance, turning it into a sharp line at infinity.

Notice that for this analysis to be valid, the thickness of the transition layer, which is proportional to $\sqrt{R}$, where $R = \sqrt{X^2 + Y^2}$, must be larger than the width of the nonlinear "far field fan", which is itself of order αR. This limits the validity of the linear analysis to $R < 1/\alpha^2$. (For $\alpha = 0.1$ this radius is of order 100 Λ_m, which is larger than the size of practical thruster). At greater distances the width of the nonlinear "far field fan" would be larger than the transition layer, and it would be necessary to include the nonlinear effects. The transition layer would then separate in two parts: one along the leading characteristic of the fan, the other along the trailing characteristic, leaving a portion of the original non-linear fan between them. These transition layers would be somewhat different since the discontinuities in the outer solution (the non-linear far field solution) would be less severe.[3]

Magnetic Wake along the Downstream Wall

One can expect some type of wake layer to appear along the downstream wall. This wake corresponds to the relaxation of the magnetic field perturbation created by the corner. Unlike the velocity perturbations which adjust fairly rapidly to their asymptotic value over a length scale of order Λ_m, the magnetic field perturbation takes a much longer distance to adjust to the asymptotic value. This is due to the different natures of the boundary conditions. For both velocities, the boundary conditions impose a quick transition right after the corner. For the magnetic field, the boundary condition, which states that the normal derivative must be zero, allows for a more gradual adjustment under the influence of the diffusion (transverse to the flow) and the convection of the magnetic field.

In order to find the asymptotic solution it is convenient to take a perturbation method approach, looking for an inner expansion valid in a boundary-layer located along the downstream wall. Using the coordinate transformation:

$$\tilde{X} = \epsilon' \frac{M_v^2}{u_o M_a^2} X, \tag{4.40}$$

$$\tilde{Y} = \epsilon'^{1/2} Y, \tag{4.41}$$

and an expansion of the form:

$$b_1(X, Y; \epsilon') = b_{1\infty} + \epsilon' \tilde{b}_1(\tilde{X}, \tilde{Y}) + \cdots \tag{4.42}$$

After substitutions and elimination of the higher order terms, the fourth order oper-

---

[3] The function is continuous, but the derivatives are discontinuous. It is the linearization process which creates the first order discontinuity in the solution

ator of equation (4.19) reduces to:

$$\frac{\partial^2 \tilde{b}_1}{\partial \tilde{Y}^2} = \frac{\partial \tilde{b}_1}{\partial \tilde{X}}, \tag{4.43}$$

with the boundary conditions: $\tilde{b}_1(\tilde{X}, \infty) = 0$, $\frac{\partial \tilde{b}_1}{\partial \tilde{Y}}(\tilde{X}, 0) = 0$, $\tilde{b}_1(0, \tilde{Y}) = C\delta(\tilde{Y})$, where $\delta(\tilde{Y})$ is the Dirac "delta-function". This problem is similar to the problem of the fully developed laminar wake. (See White in [64].) It has the following solution:

$$\tilde{b}_1 = C\tilde{X}^{-1/2} \exp\left(-\frac{\tilde{Y}^2}{4\tilde{X}}\right). \tag{4.44}$$

The constant C is still an unknown at this point and can only be determined by a more complicated matching with the solution near the corner.

This section will be concluded by observing that the variables ρ_1 and p_1 have similar behaviors. This means that the assumption that there cannot be a magnetic boundary layer along a conducting wall is somewhat simplistic, as this analysis has shown, but the assumption that the corner is isolated makes this case somewhat contrived. In reality the presence of the opposite electrode will make this second order effect negligible relative to other stronger first order effects.

4.5 Numerical Solution by a Fourier Transformation

Since the domain of definition for the small-angle/weak disturbance problem is the *upper half plane*, $Y > 0$, the Fourier transformation with respect to the X variable can be used in order to solve equation 4.19. The variable v_1 is related to its Fourier transform along the X direction by:

$$v_1(X, Y) = \frac{1}{2\pi} \int_{-\infty}^{\infty} \tilde{v}_1(k, Y) e^{ikX} dk, \tag{4.45}$$

with

$$\tilde{v}_1(k,Y) = \int_{-\infty}^{\infty} v_1(X,Y)e^{-ikX}dX. \tag{4.46}$$

The equation becomes:[4] so that $u_0 = 1$, and the expansions are then

$$u = 1 + \epsilon u_1(X,Y) + \cdots$$

$$v = \epsilon v_1(X,Y) + \cdots$$

$$\frac{\partial}{\partial X}\left(\beta_v^2\frac{\partial^2}{\partial X^2} - \frac{\partial^2}{\partial Y^2}\right)v_1 = \frac{M_v^2}{M_a^2}\nabla^2\left(\beta_a^2\frac{\partial^2}{\partial X^2} - \frac{\partial^2}{\partial Y^2}\right)v_1, \tag{4.47}$$

$$\beta_v^2\partial^3_{XXX}v_1 - \partial^3_{XYY}v_1 = \frac{M_v^2}{M_a^2}\left(\beta_a^2\partial^4_{XXXX} + (\beta_a^2 - 1)\partial^4_{XXYY} - \partial^4_{YYYY}\right)v_1. \tag{4.48}$$

Taking the Fourier transformation in X gives:

$$\left(\frac{M_v^2}{M_a^2}\right)\partial^4_{YYYY}\tilde{v}_1 + \left(-ik - k^2(1-\beta_a^2)\frac{M_v^2}{M_a^2}\right)\partial^2_{YY}\tilde{v}_1 + \left(-ik^3\beta_v^2 - \frac{M_v^2}{M_a^2}k^4\beta_a^2\right)\tilde{v}_1 = 0, \tag{4.49}$$

using $\delta = \frac{M_v^2}{M_a^2}$ it becomes:

$$\partial^4_{YYYY}\tilde{v}_1 + \left(-\frac{ik}{\delta} - k^2(1-\beta_a^2)\right)\partial^2_{YY}\tilde{v}_1 + \left(-ik^3\frac{\beta_v^2}{\delta} - \beta_a^2k^4\right)\tilde{v}_1 = 0. \tag{4.50}$$

This is an ordinary differential equation for $\tilde{v}_1(k,Y)$. The solutions are of the form:

$$\tilde{v}_1(k,Y) = u_o\sum_{j=1}^{4}\mu_j e^{-\nu_j(k)\,Y}, \tag{4.51}$$

---

[4] The coordinates and the reference variables are chosen such that the incoming flow velocity is equal to one ($u_0 = 1$) and such that the magnetic Reynolds number disappears from the equations. The coordinates X, Y are defined by

$$X = \mu_o\sigma\bar{u}_o\bar{x}$$

$$Y = \mu_o\sigma\bar{u}_o\bar{y}$$

where μ_o is the magnetic permeability of vacuum, σ is the conductivity, $\bar{u}_o$ is the unperturbed uniform velocity, and $\bar{x}, \bar{y}$ are the coordinates. All these quantities have their usual dimensions except X and Y which are dimensionless. The velocity is

$$\mathbf{u} = \frac{\bar{\mathbf{u}}}{\bar{u}_o}$$

where the ν_j are the roots of the equation:

$$\nu^4 + \nu^2 \left((\beta_a^2 - 1)k^2 - \frac{i\,k}{\delta} \right) + \left(-\beta_a^2 k^4 - \frac{i\,k^3\,\beta_v^2}{\delta} \right) = 0. \tag{4.52}$$

This is a biquadratic equation with four roots ν_1, ν_2, ν_3, ν_4 such that $\nu_3 = -\nu_1$ and $\nu_4 = -\nu_2$. The coefficients ν_1 and ν_2 are defined such that $\mathrm{Re}(\nu_1) > 0$ and $\mathrm{Re}(\nu_2) > 0$ by choosing an appropriate branch cut.

For $k \in \mathbf{R}$,

$$\nu_{1,2} = \left(\frac{1-\beta_a^2}{2} k^2 + \frac{i}{2}\frac{k}{\delta} \pm \frac{1}{2}|k| \sqrt{(\beta_a^2+1)^2 k^2 + 2\,i\,\frac{k}{\delta}\,(2\,\beta_v^2 - \beta_a^2 + 1) - \frac{1}{\delta^2}} \right)^{1/2}. \tag{4.53}$$

The asymptotic expansions at infinity for ν_1 and ν_2 are $\nu_1 \sim |k|$ and $\nu_2 \sim i\ \beta_a |k|$. Near zero the asymptotic expansions for ν_1 are:

$$\nu_1 \sim \sqrt{k} e^{i\pi/4}, \text{ for } k \in \mathbf{R}, k > 0,$$

$$\nu_1 \sim \sqrt{-k} e^{-i\pi/4}, \text{ for } k \in \mathbf{R}, k < 0,$$

and for ν_2:

$$\nu_2 \sim -ik\beta_v, \text{ for } k \in \mathbf{R}.$$

The coefficients μ_j of the expansion (4.51) can be calculated using the boundary conditions and our knowledge of the solution behavior at infinity. Two of the four modes can be eliminated by the requirements that the solution be bounded for $Y \to \infty$, and that the propagation vector for the wave-like perturbations be directed downstream. Thus only μ_1 and μ_2 are non-zero. The boundary conditions at $Y = 0$ impose the other two conditions needed to uniquely determine the μ_j. One of them is the condition that the velocity be tangent to the wall, $v_1(X, 0) = -u_0 \Upsilon(X)$ which implies

$$\tilde{v}_1(k, 0) = \frac{u_0}{ik}, \text{ for } \mathbf{Im}(k) < 0. \tag{4.54}$$

The other is the equipotential condition:

$$\beta_a^2 \frac{\partial^2 v_1}{\partial X^2} - \frac{\partial^2 v_1}{\partial Y^2} = 0, \quad \text{for } Y = 0. \tag{4.55}$$

One can then solve for the coefficients μ_1, μ_2, which turn out to be

$$\mu_1 = -\frac{i}{k} \frac{\beta_a^2 k^2 + \nu_2^2}{\nu_2^2 - \nu_1^2}, \tag{4.56}$$

$$\mu_2 = \frac{i}{k} \frac{\beta_a^2 k^2 + \nu_1^2}{\nu_2^2 - \nu_1^2}; \tag{4.57}$$

the expression for the Fourier transform of the normal velocity is then:

$$\tilde{v}_1(k, Y) = u_0(\mu_1 e^{-\nu_1 Y} + \mu_2 e^{-\nu_2 Y}), \tag{4.58}$$

$$\tilde{v}_1(k, Y) = \frac{u_0}{ik} \left(\frac{\beta_a^2 k^2 + \nu_2^2}{\nu_2^2 - \nu_1^2} e^{-\nu_1 Y} - \frac{\beta_a^2 k^2 + \nu_1^2}{\nu_2^2 - \nu_1^2} e^{-\nu_2 Y} \right), \tag{4.59}$$

and the velocity is then

$$v_1(X, Y) = \frac{1}{2\pi} \int_{-\infty}^{\infty} \tilde{v}_1(k, Y) e^{ikX} dk. \tag{4.60}$$

Note that $\tilde{v}_1(k, Y)$ is not defined for $k = 0$. This can be tracked back to the fact that the Fourier transform of the step function, $\Upsilon(X)$, is also singular at $k = 0$. In fact the Fourier integral is only defined for $\mathbf{Im}(k) < 0$, and consequently the integration path for the inverse Fourier transformation should be defined by $k = k_r + i\ k_i$; with k_r going from $-\infty \rightarrow +\infty$ and $k_i = -\tau$; where $0 < \tau$ so that it lies within the domain of definition of the transform of $\Upsilon(X)$. In fact the constraint on k is more severe. It can be shown [5] that the integration path must lie in the strip defined by $-\tau_- < \mathbf{Im}(k) < 0$,

---

[5] The condition $\mathbf{Im}(k) < 0$ is not mathematically correct. The real condition is that $-\tau_- < \mathbf{Im}(k) < 0$, where τ_- is determined by the requirement that the inverse Fourier integral (4.60), which defines v_1, converges for the negative values of X.

The function $\Upsilon(X)$ has a Fourier transform: $\int_{-\infty}^{\infty} \Upsilon(X) e^{-ikX} dk$ for all k with $k_i < 0$. Moreover this Fourier transform is equal to $\frac{1}{ik}$ for all k in the domain of definition. The fact that the domain of definition is the half plane $\mathbf{Im}(k) < 0$ is a consequence of the fact that the function $\Upsilon(X)$ is equal to zero for negative X.

However the function $v_1(X)$ has non-zero values for large negative X, and one must pay some where τ_- is a small positive number determined by the asymptotic properties of $v_1(X)$ near $-\infty$ in order to guarantee the convergence of the inverse Fourier integral. The integration path can be defined by: $k = k_r + i\,k_i$; $k_r \in]-\infty, \infty[$; $k_i = -\tau$; $0 < \tau < \tau_-$. The expression for $v_1(X,Y)$ is then:

$$v_1(X,Y) = \frac{u_0}{2\pi} \int_{-\infty-i\tau}^{+\infty-i\tau} \frac{1}{ik} \left\{ \left(\frac{\beta_a^2 k^2 + \nu_2^2}{\nu_2^2 - \nu_1^2} \right) e^{-\nu_1 Y + ikX} - \left(\frac{\beta_a^2 k^2 + \nu_1^2}{\nu_2^2 - \nu_1^2} \right) e^{-\nu_2 Y + ikX} \right\} dk. \tag{4.61}$$

Similarly one can find expressions for the remaining variables:

$$u_1(X,Y) = u_o \frac{1}{2\pi} \int_{-\infty}^{+\infty} \left(-\frac{ik}{\nu_1} \mu_1 e^{-\nu_1 Y} - \frac{ik}{\nu_2} \mu_2 e^{-\nu_2 Y} \right) e^{ikx} dk, \tag{4.62}$$

$$b_1(X,Y) = b_o \left(\frac{\gamma p_o}{2b_o^2} \right) \frac{1}{2\pi} \int_{-\infty}^{+\infty} \left(i \frac{\nu_1^2 + \beta_a^2 k^2}{\nu_1 k} \mu_1 e^{-\nu_1 Y} + i \frac{\nu_2^2 + \beta_a^2 k^2}{\nu_2 k} \mu_2 e^{-\nu_2 Y} \right) e^{ikx} dk, \tag{4.63}$$

$$\rho_1(X,Y) = \rho_o \frac{1}{2\pi} \int_{-\infty}^{+\infty} \left(-i \frac{\nu_1^2 - k^2}{\nu_1 k} \mu_1 e^{-\nu_1 Y} - i \frac{\nu_2^2 - k^2}{\nu_2 k} \mu_2 e^{-\nu_2 Y} \right) e^{ikx} dk. \tag{4.64}$$

If one attempts to invert the Fourier transformation analytically, one is confronted to a difficult problem: the functions ν_1, ν_2 are two of the roots of a biquadratic equations. The fourier transform of v_1 has several singularities which are not necessary poles.

4.5.1 Numerical Inversion

In order to invert the Fourier transformation, it is convenient to use a numerical method based on the Fast Fourier Transformation algorithm which will be justified now. Starting from the expression of the inverse Fourier transform of a function:

$$f(x) = \frac{1}{2\pi} \int_{-\infty}^{\infty} \tilde{f}(k) e^{ikx} dk, \tag{4.65}$$

---

attention to the convergence of the integral $\tilde{v}_1(k) = \int_{-\infty}^{\infty} v_1(X) e^{-ikX} dk$ which defines the Fourier transform of v_1. For large negative X, the exponent is: $-ikX = -i\,(k_r + i\,k_i)\,X = k_i\,X - i\,k_r\,X$. The exponential term will only converge to zero if k_i is positive. But this is not possible, since the integral would otherwise diverge for the positive values of X. It is the fact that the function $v_1(X)$ decays to zero faster than $e^{\tau - X}$ for large negative values of X which allows the integral to converge despite the growing factor in the exponential kernel.

k can be replaced by $2\pi\xi$:

$$f(x) = \int_{-\infty}^{\infty} \tilde{f}(2\pi\xi) e^{2\pi i \xi x} d\xi, \tag{4.66}$$

The equation is evaluated at the discrete points $x = m\Delta x$:

$$f(x_m) = \int_{-\infty}^{\infty} \tilde{f}(2\pi\xi) e^{2\pi m i \xi \Delta x} d\xi. \tag{4.67}$$

The integral is discretized by sampling at the points $\xi_j = \frac{j}{N\Delta x}$:

$$f(x_m) \simeq \sum_{j=-\infty}^{\infty} \tilde{f}(2\pi\xi_j) e^{2\pi i \; m\xi_j \Delta x} \Delta\xi, \tag{4.68}$$

$$f(x_m) \simeq \sum_{j=-\infty}^{\infty} \frac{1}{N\Delta x} \tilde{f}(\frac{2\pi j}{N\Delta x}) \; e^{2\pi i \frac{j\, m}{N}}. \tag{4.69}$$

The FFT algorithm is used to calculate the sum.[6] In the process the sum is truncated to $j \in [-\frac{N}{2} + 1, \frac{N}{2}]$. Finally:

$$f(x_m) \simeq \frac{1}{\Delta x} \left\{ \frac{1}{N} \sum_{j=-\frac{N}{2}+1}^{\frac{N}{2}} \tilde{f}(2\pi \frac{j}{N\Delta x}) e^{2\pi m i \frac{jm}{N}} \right\}, \tag{4.70}$$

where the expression in the curly bracket on the right hand side is the result of the Fast Fourier Transformation algorithm applied to the values taken by the Fourier transform $\tilde{f}$ at the discrete points $k = 2\pi\xi_j$, with $\xi_j = \frac{j}{N\Delta x}$.

Since the FFT algorithm assumes that one deals with $k \in \mathbf{R}$, something needs to be done about the singularity at $k = 0$, in the integral which defines v_1 (equation 4.61). For instance, one choice is to invert the partial derivative of v_1 with respect to X, which does not have a singularity at $k = 0$, and to integrate the result again after the

---

[6] This implies that $\tilde{f}(2\pi\xi_j)$ is a periodic function of ξ, however this constraint is neglected, since the function is assumed to decay fast enough at both ends of the interval of definition of k

numerical inversion.

$$\frac{\partial v_1}{\partial X}(X,Y) = \frac{\partial}{\partial X}\left\{\frac{u_0}{2\pi}\int_{-\infty}^{+\infty}\frac{1}{ik}\left\{\left(\frac{\beta_a^2k^2+\nu_2^2}{\nu_2^2-\nu_1^2}\right)e^{-\nu_1Y+ikX} - \left(\frac{\beta_a^2k^2+\nu_1^2}{\nu_2^2-\nu_1^2}\right)e^{-\nu_2Y+ikX}\right\}dk\right\} \tag{4.71}$$

$$\frac{\partial v_1}{\partial X}(X,Y) = \frac{u_0}{2\pi}\int_{-\infty}^{+\infty}\left\{\left(\frac{\beta_a^2k^2+\nu_2^2}{\nu_2^2-\nu_1^2}\right)e^{-\nu_1Y+ikX} - \left(\frac{\beta_a^2k^2+\nu_1^2}{\nu_2^2-\nu_1^2}\right)e^{-\nu_2Y+ikX}\right\}dk \tag{4.72}$$

Similar methods can be used in order to invert the other variables, u_1 b_1, etc... The expressions for the variables $\frac{\partial u_1}{\partial X}$, and $\frac{\partial^2 b_1}{\partial X^2}$ are given below. Notice that the magnetic field b_1 must be differentiated twice, since the singularity for b_1 is in $\frac{1}{k^2}$.

$$\frac{\partial u_1}{\partial X}(X,Y) = -\frac{u_0}{2\pi}\int_{-\infty}^{+\infty}\left\{\left(\frac{\beta_a^2k^2+\nu_2^2}{\nu_2^2-\nu_1^2}\right)\frac{ik}{\nu_1}e^{-\nu_1Y+ikX} - \left(\frac{\beta_a^2k^2+\nu_1^2}{\nu_2^2-\nu_1^2}\right)\frac{ik}{\nu_2}e^{-\nu_2Y+ikX}\right\}dk, \tag{4.73}$$

$$\begin{aligned}\frac{\partial^2 b_1}{\partial X^2}(X,Y) = \left(\frac{\gamma p_0}{2b_0^2}\right)\frac{b_0}{2\pi}\int_{-\infty}^{+\infty}\{&\left(\frac{\beta_a^2k^2+\nu_2^2}{\nu_2^2-\nu_1^2}\right)\left(-\frac{\beta_a^2k^2}{\nu_1}-\nu_1\right)e^{-\nu_1Y+ikX}\\ &+\left(\frac{\beta_a^2k^2+\nu_1^2}{\nu_2^2-\nu_1^2}\right)\left(\frac{\beta_a^2k^2}{\nu_2}+\nu_2\right)e^{-\nu_2Y+ikX}\}dk.\end{aligned} \tag{4.74}$$

4.5.2 Discussion of the Results

It has been shown in the previous chapter that in the far-field, where the effect of magnetic diffusion can be neglected, the flow undergoes an adiabatic magneto-acoustic expansion comparable to a Prandtl-Meyer expansion. Similarly it can be shown that in the near-field, the flow undergoes an isentropic purely acoustic Prandtl-Meyer expansion. The small disturbance analysis shows the transition between these two expansions, from the near-field to the far-field. Here an expansion fan (which has an extent proportional to the small deflection angle ϵ) appears as a discontinuity (as would a weak compression shock too). The smooth blending between the near and far-field behaviors happens by a gradual weakening of the discontinuity strength as the distance increases away from the corner. Similarly information propagates ahead (upstream) of the discontinuity, as a result of the partially "elliptic" character of the operator.

Cross-sections of the density and the magnetic field for several values of the distance Y are shown in figures 4-4 and 4-5. In the density plot, the sonic fan appears as a sharp discontinuity, whereas the magneto-sonic fan is smeared considerably under the effect of the magnetic diffusion. As the distance Y increases, the sonic fan becomes weaker, moves towards the right, and eventually merges into the flow. A plot of the density contours is shown in figure 4-6.

In the magnetic field cross sections, the sonic fan appears as a discontinuity in the *derivative*, but b itself is continuous. The corresponding contour plots are shown in figure 4-7. In the density plots, the density undershoots its asymptotic value along the downstream electrodes. This implies that the cavitation effects of the expansion will be felt most strongly in the immediate vicinity of the corner, on its downstream side. In the magnetic field plot, the contours of constant magnetic field are also current lines. These lines broadly follow the direction of the magneto-sonic fan, as they converge toward the corner. Those which reach the edge of the sonic fan turn around and reattach downstream of the corner's edge, reaching the wall with a zero normal derivative in the absence of the Hall effect. The slow adjustment of the magnetic field to its asymptotic value, is spread over a large distance, as discussed in the section concerning the magnetic wake along the downstream wall.

The unexpected refraction of the current lines across the expansion fan can be justified in the following way. The Ohm's law for the one-fluid plasma can be written (in *dimensional* units) as:

$$\mathbf{E} + \mathbf{u} \times \mathbf{B} = \frac{\mathbf{J}}{\sigma} + \frac{\mathbf{J} \times \mathbf{B}}{\mathbf{e}\ \mathbf{n_e}}. \tag{4.75}$$

As the fluid expands across the sonic expansion fan, the normal component of the velocity vector $\mathbf{u}$ changes abruptly (at least in the first order term). However $\mathbf{B}$ is continuous across the fan, leaving only $\mathbf{J}$ and $\mathbf{E}$ to balance this increase. In fact the increase is balanced by a discontinuous change in the current vector $\mathbf{J}$, as will be shown below.

The Ohm's law is projected on the directions normal and parallel to the sonic fan, giving the equations:

$$E_{||} - u_{\perp}B = \frac{J_{||}}{\sigma} - \frac{J_{\perp}B}{e\,n_e}, \tag{4.76}$$

$$E_{\perp} + u_{||}B = \frac{J_{\perp}}{\sigma} + \frac{J_{||}B}{e\,n_e}. \tag{4.77}$$

From the condition: div $\mathbf{J} = 0$ one can derive the jump condition $[J_{\perp}] = 0$. Similarly, from the condition: $\nabla \times \mathbf{E}$ one can derive the jump condition: $[E_{||}] = 0$. From the mass conservation equation: div $\rho\mathbf{u} = 0$ one can derive: $[\rho\ u_{\perp}] = 0$, and from the conservation equation for the momentum in the direction parallel to the fan one can derive $[\rho\ u_{\perp}\ u_{||}] = 0$, which leads to: $[u_{||}] = 0$. Using these relations one can reduce the above equations to:

$$-\,[u_{\perp}]\ B = \frac{[J_{||}]}{\sigma}, \tag{4.78}$$

$$[E_{\perp}] = \frac{[J_{||}]\ B}{e\,n_e}. \tag{4.79}$$

The former equation gives a relation between the change in velocity across the fan and the corresponding change in current. The second equation gives the change in the normal electric field. This analysis assumes that the expansion fan reduces to a discontinuity. In reality the fan has a finite thickness, and the current refraction will be spread across the thickness of the fan.

Experimental confirmations of this phenomenon were found in several reports. Some examples are given in figure 4-13 and 5-9. Notice that these phenomena are observed near the anode, and not around the cathode. This is a consequence of the Hall effect, which introduces a distinction between the electrodes. This will be considered now in more detail.

4.6 Addition of the Hall Effect

As mentioned in the introduction, the Hall conductivity modifies the solution, and it is desirable to study how this effect modifies the previous results. If one neglects the variations of the conductivity σ and of the Hall parameter H_a, the Hall effect does not appear explicitly in the differential equations. It only appears in the boundary condition related to the magnetic field (the equipotential condition). The small disturbance approximation can therefore be used with little modification.

The linear problem can be reformulated as:

$$u_0 \frac{\partial}{\partial X}\left((1-M_v^2)\frac{\partial^2}{\partial X^2}+\frac{\partial^2}{\partial Y^2}\right)v_1 = \frac{M_v^2}{M_a^2}\nabla^2\left((1-M_a^2)\frac{\partial^2}{\partial X^2}+\frac{\partial^2}{\partial Y^2}\right)v_1, \tag{4.80}$$

$$v_1(X,0) = -u_0\Upsilon(X) \quad \text{for } Y=0, \tag{4.81}$$

$$\frac{\partial b_1}{\partial Y} + \beta_e\frac{\partial b_1}{\partial Y} = 0 \quad \text{for } Y=0, \tag{4.82}$$

where β_e is the Hall coefficient. The Fourier transformation can be used as well, provided that the coefficients (μ_1,μ_2) of the modal decomposition are modified to reflect the new boundary conditions. The method to calculate the new values of μ_1,μ_2 will now be detailed. From equations (4.8-4.12) it is possible to construct the equation:

$$\left(\frac{2b_o^2}{\gamma p_o}\right)\frac{u_o}{b_o}\frac{\partial^2 b_1}{\partial X^2} = -\beta_a^2 u_{1XX} + v_{1XY}. \tag{4.83}$$

From:

$$v_1 = u_o\frac{1}{2\pi}\int_{\mathbf{R}}(\mu_1 e^{-\nu_1 Y} + \mu_2 e^{-\nu_2 Y})e^{ikX}dk, \tag{4.84}$$

$$u_1 = u_o\frac{1}{2\pi}\int_{\mathbf{R}}(-\frac{ik}{\nu_1}\mu_1 e^{-\nu_1 Y} - \frac{ik}{\nu_2}\mu_2 e^{-\nu_2 Y})e^{ikX}dk, \tag{4.85}$$

one can derive the expression of b_1:

$$b_1 = \left(\frac{2b_o^2}{\gamma p_o}\right)b_o\frac{1}{2\pi}\int_{\mathbf{R}}(\frac{\nu_1^2+\beta_a^2k^2}{i\nu_1 k}\mu_1 e^{-\nu_1 Y} + \frac{\nu_2^2+\beta_a^2k^2}{i\nu_2 k}\mu_2 e^{-\nu_2 Y})e^{ikX}dk. \tag{4.86}$$

The equipotential boundary condition, $\frac{\partial b_1}{\partial Y} + \beta_e\frac{\partial b_1}{\partial Y} = 0$ for $Y = 0$, leads to the equation,

$$\mu_1(\nu_1^2+\beta_a^2k^2)\left(1-\frac{ik\beta_e}{\nu_1}\right) + \mu_2(\nu_2^2+\beta_a^2k^2)\left(1-\frac{ik\beta_e}{\nu_2}\right) = 0. \tag{4.87}$$

Similarly the tangency condition $v_1 = -u_0 \Upsilon(X)$ leads to the condition,

$$\mu_1 + \mu_2 = -\frac{1}{ik}. \tag{4.88}$$

These two equations form a linear system which yields the following solutions:

$$\mu_1 = \frac{1}{ik} \frac{\left(\nu_2^2 + \beta_a^2 k^2\right)\left(1 - \frac{ik\beta_e}{\nu_2}\right)}{\left(\nu_1^2 + \beta_a^2 k^2\right)\left(1 - \frac{ik\beta_e}{\nu_1}\right) - \left(\nu_2^2 + \beta_a^2 k^2\right)\left(1 - \frac{ik\beta_e}{\nu_2}\right)}, \tag{4.89}$$

$$\mu_2 = -\frac{1}{ik} \frac{\left(\nu_1^2 + \beta_a^2 k^2\right)\left(1 - \frac{ik\beta_e}{\nu_1}\right)}{\left(\nu_1^2 + \beta_a^2 k^2\right)\left(1 - \frac{ik\beta_e}{\nu_1}\right) - \left(\nu_2^2 + \beta_a^2 k^2\right)\left(1 - \frac{ik\beta_e}{\nu_2}\right)}. \tag{4.90}$$

The Fourier transform of v_1 is inverted by the Fast Fourier Transformation (FFT) algorithm as before.

4.7 Discussion of the Results

Some interesting changes can be seen in the density contour plots shown in figures 4-8 and 4-9. The density perturbations anticipate the corner's presence along the cathode surface, whereas they lag behind along the anode. The expected mass depletion along the anode is also visible. However it appears in a way which was not fully expected: it occurs *downstream* of the corner. The asymptotic value downstream of the corner for the density and the magnetic field is given by:

$$b_\infty / b_0 = 1 - \epsilon M_v^2 + O(\epsilon^2) \tag{4.91}$$

$$\rho_\infty / \rho_0 = 1 - \epsilon M_v^2 + O(\epsilon^2) \tag{4.92}$$

For both quantities, and with the conditions considered in the calculations, these asymptotic values are equal to 0.8. A plot of the density along the line $Y = 0$, both for an anode and for a cathode is shown in figure 4-10.

The fluid anticipates the presence of the corner through its interaction with the magnetic field. In fact one can give a hierarchy of interactions: At short distances from the corner the flow is independent from the magnetic field which reacts locally to the boundary conditions along the electrodes, including the constraints imposed by the Hall effect. Over larger distances, both upstream and downstream of the corner, the perturbation on the magnetic field is compensated by a modification in the gas flow.

It has been previously recognized [4] that the Hall effect was responsible for the anodic mass depletion. This analysis confirms this fact but suggests that part of this depletion is intrinsically related to the presence of the corner. It suggests that the depleted region occurs outside the channel, on the side of the anode located downstream from the corner, and over a region of a finite length. Similarly it appears that the mass concentration along the cathode is due to the Hall effect and to the presence of the corner.

Since for an isentropic flow the temperature variations are proportional to the density variations, these conclusions are also valid for the temperature. This suggests a possible explanation for the high temperatures and the luminosity often observed near the cathode: the adiabatic compression just ahead of the cathode corner increases the gas temperature to a level where the gas becomes luminous. In most experimental designs the thruster geometry is axisymmetrical. One of the effects of the cylindrical geometry is to create a density gradient due to the pinching effect of the Lorentz force. So far the luminosity has been attributed to axisymmetrical effects, but this analysis predicts that it should also be observed in thrusters with a "two-dimensional" or "slab" geometry.

The results for the magnetic field are displayed in figures 4-11 and 4-12. As stated above, the Hall conductivity changes the boundary conditions along the electrodes. The equipotential condition implies that the current no longer penetrates the electrode perpendicular to the surface but instead is deflected from the perpendicular by an angle θ such that $\tan\theta$ is equal to the Hall parameter β_e. An important difference appears in the distribution of the current between the anode and cathode cases. For the cathode, the current lines strike the electrode *ahead* of the corner. For the anode, the opposite phenomenon occurs. The majority of the current lines strike the electrode on the downstream side of the corner. This confirms the theory that some of the current lines tend to reattach outside the thruster channel. However it should be kept in mind that this analysis does not account for the other electrode. This limitation will be lifted in the next section, and it will be shown that the effect of the other electrode is to limit the extent to which the current lines move outside the thruster channel. Finally the current refraction is more visible near the anode than the cathode. This is a consequence of the equipotential boundary condition, namely that the current lines must reach the electrode with the appropriate angle.

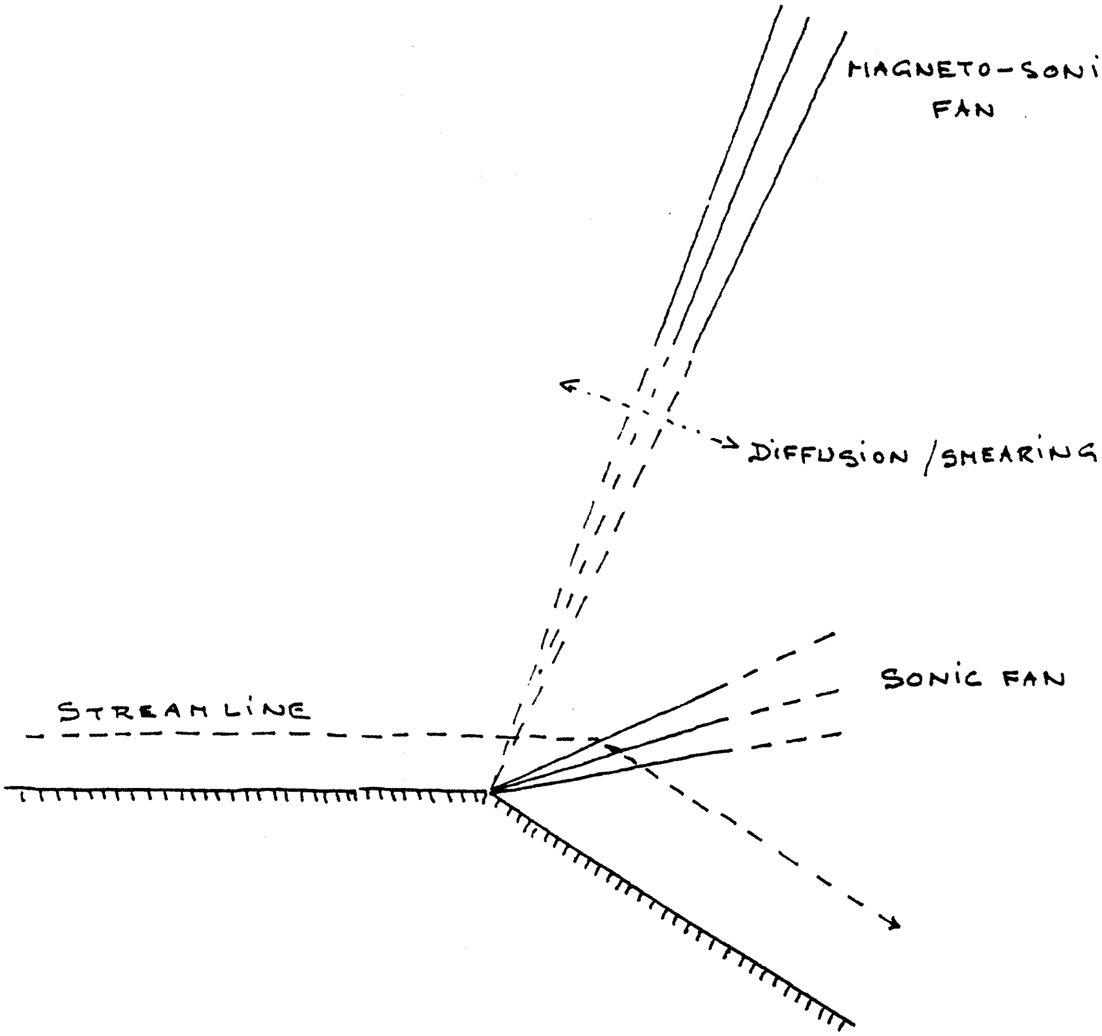

Figure 4-1: Structure of the flow around a weak corner. The drawing shows the existence of a magneto-sonic expansion fan at a large distance from the corner and a sonic expansion fan near the corner. The magnetosonic fan is smeared out by the effect of the magnetic field diffusion associated with the finite resistivity of the medium.

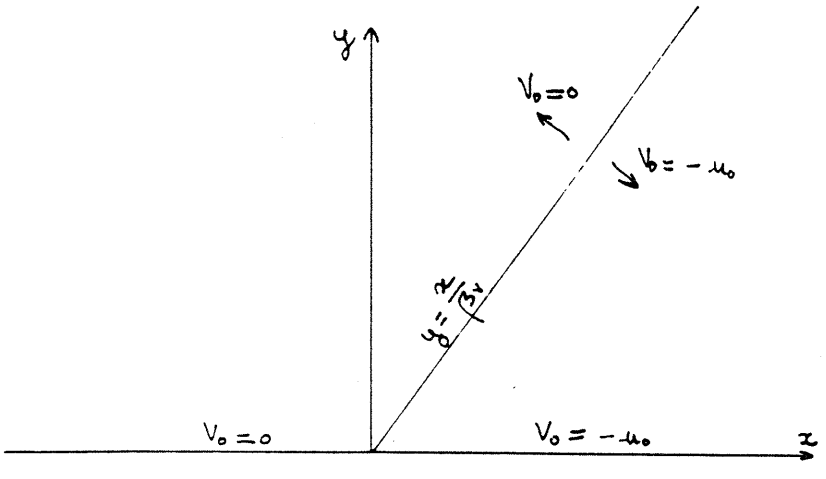

IN THE (x, y) PLANE

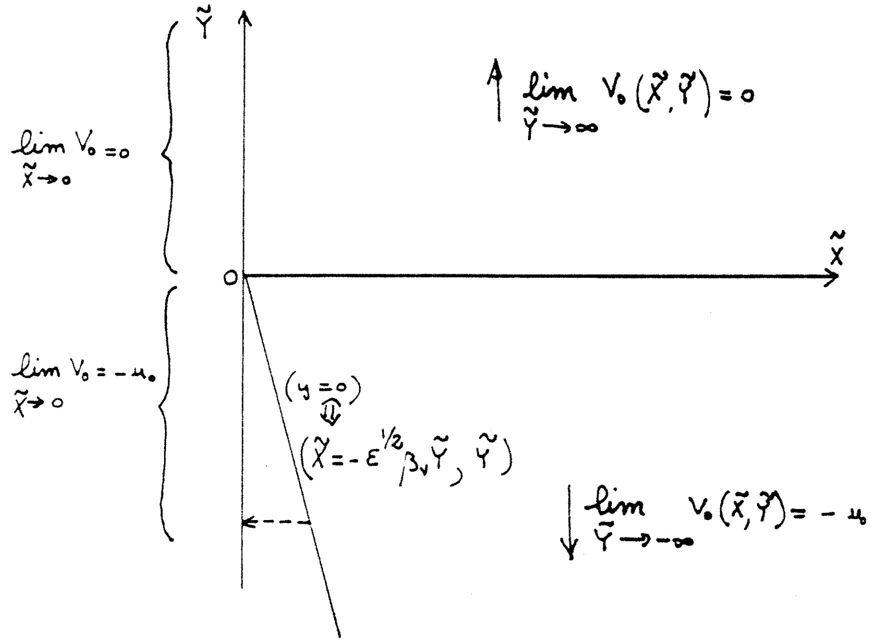

IN THE $(\tilde{X}, \tilde{Y})$ PLANE

Figure 4-2: Boundary conditions for the asymptotic solution at large distance from the corner.

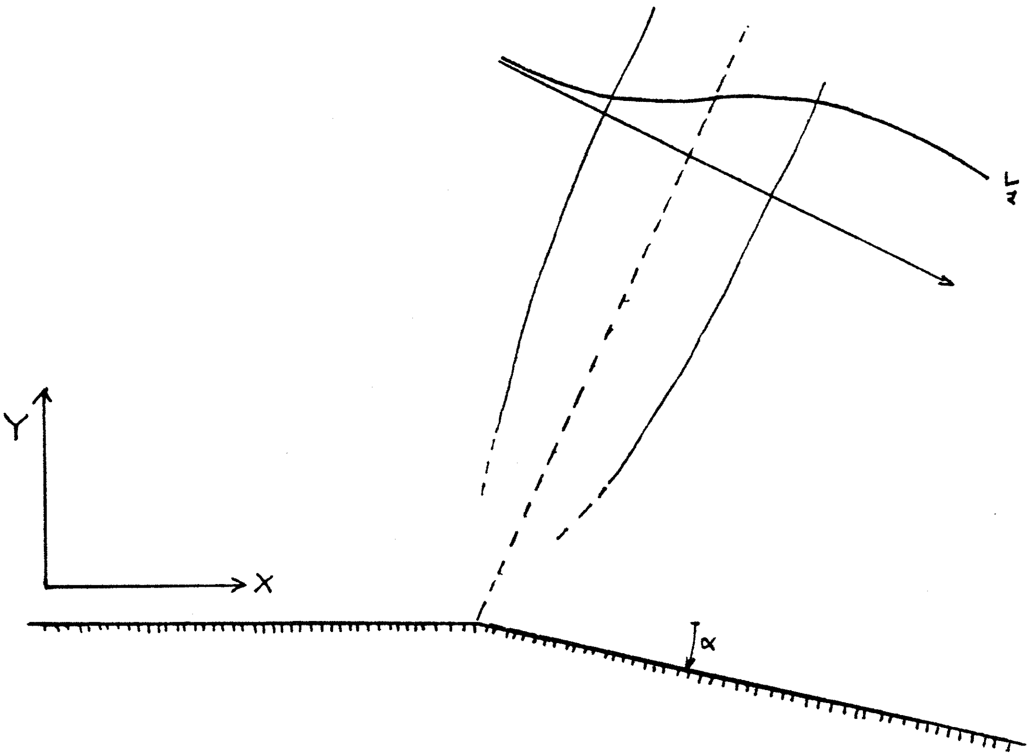

Figure 4-3: Asymptotic Structure of the transition layer across the characteristic leaving the corner. The transverse velocity v_1 is plotted against the coordinate: $(Y - \frac{X}{\beta_*})$. The velocity exhibits a smooth transition from $v_1 = 0$ to $v_1 = u_o$.

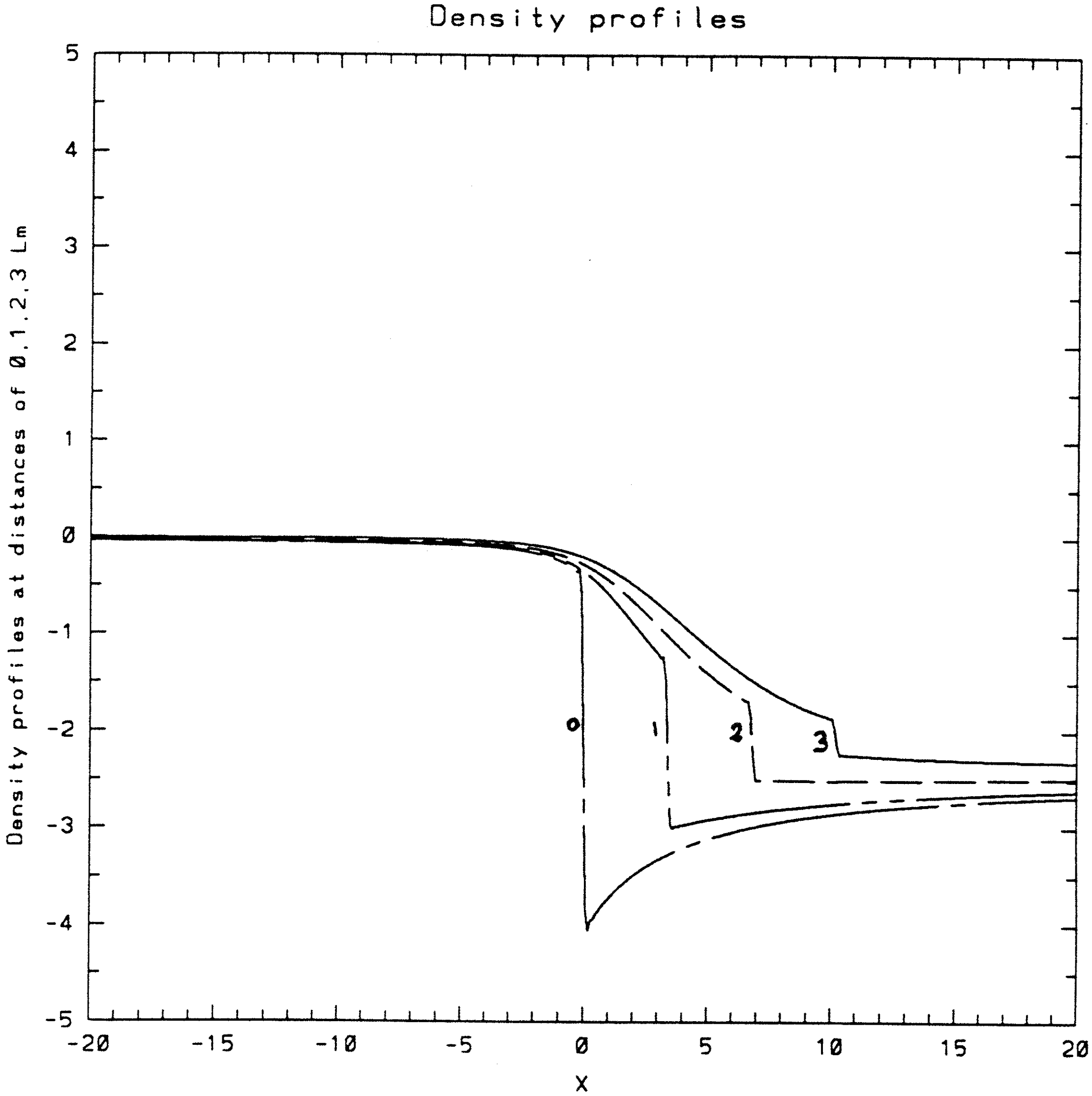

Figure 4-4: Flow above a weak corner. Profiles of the density perturbation $\rho_1(X,Y)/\rho_0$ at various distance from the electrode: $Y = 0,1,2,3\Lambda_m$, with $M_v = 1.414$, $M_a = 3.544$. The sharp discontinuity is due to the passage through the sonic expansion fan. (In the small perturbation method, the sonic expansion fan reduces to a discontinuity.)

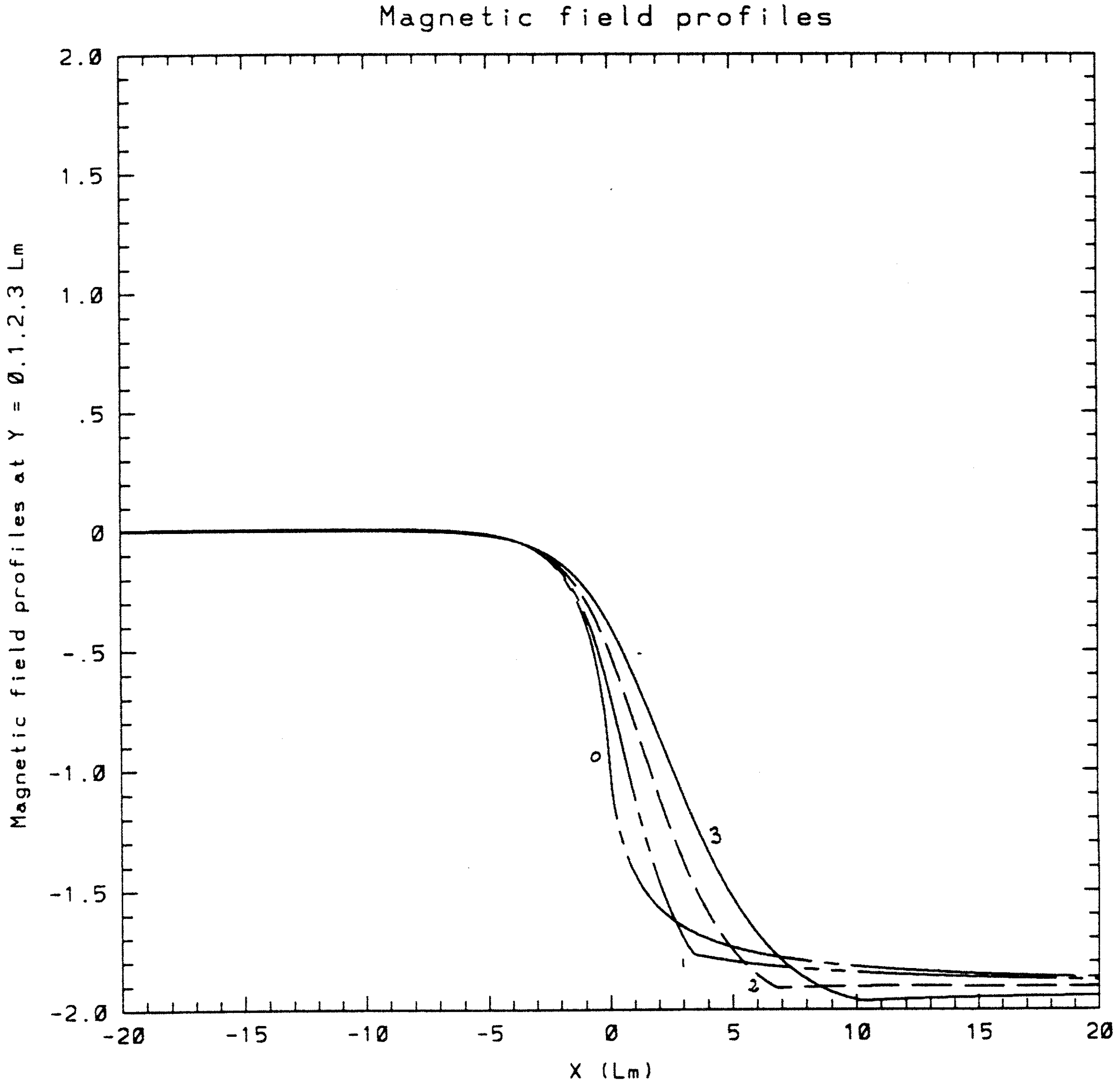

Figure 4-5: Flow above a weak corner. Profiles of the magnetic field perturbation $b_1(X,Y)/b_0$ at various distance from the electrode: $Y = 0, 1, 2, 3\Lambda_m$, with $M_v = 1.414$, $M_a = 3.544$. The Magnetic field is continuous across the sonic expansion fan.

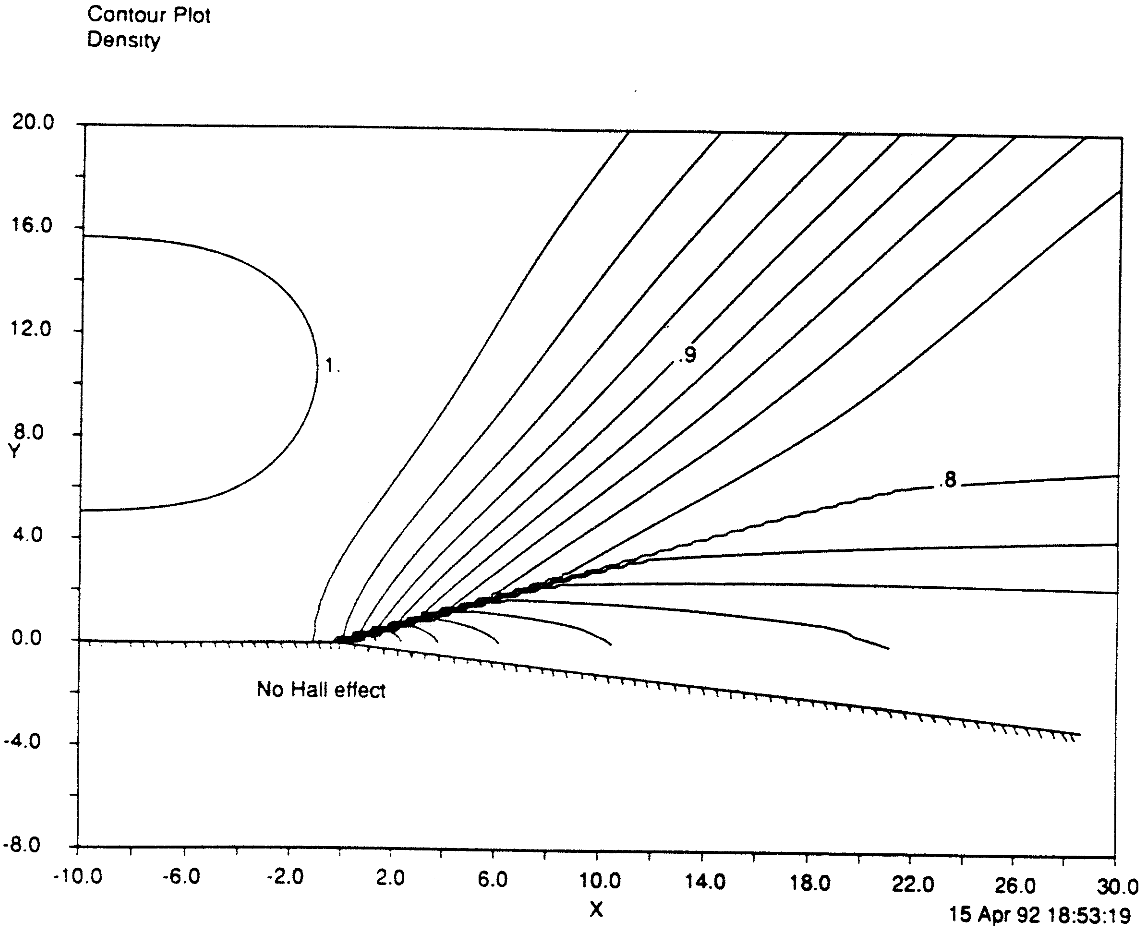

Figure 4-6: Flow above a weak corner. Contour plot of the density $\rho = \rho_0 + \epsilon\, \rho_1$, with $M_v = 1.414$, $M_a = 3.544$, $\epsilon = 0.1$. The density changes abruptly across the sharp sonic expansion fan.

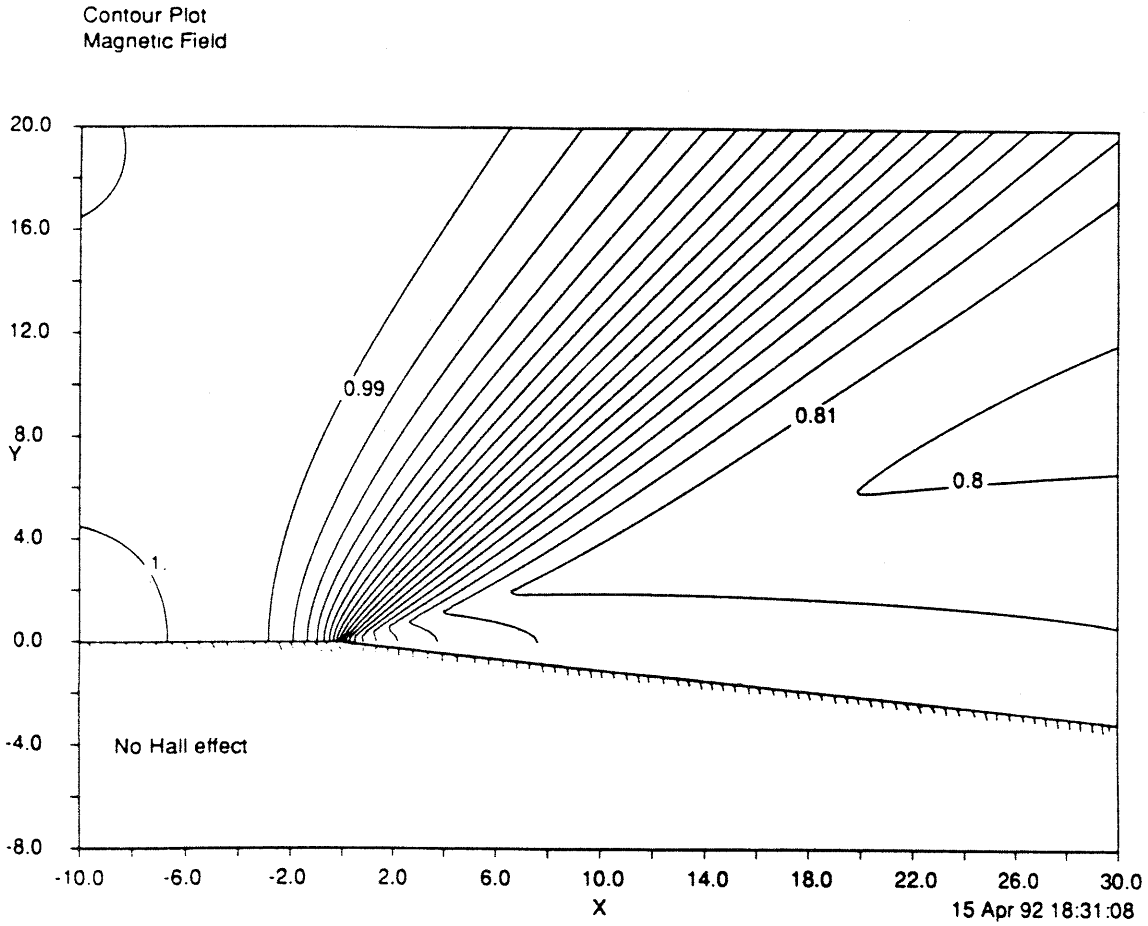

Figure 4-7: Flow above a weak corner. Contour plot of the magnetic field $b = b_0 + \epsilon\, b_1$, with $M_v = 1.414$, $M_a = 3.544$, $\epsilon = 0.1$. The magnetic field is continuous across the sharp expansion fan, but the current lines are refracted by the sonic fan.

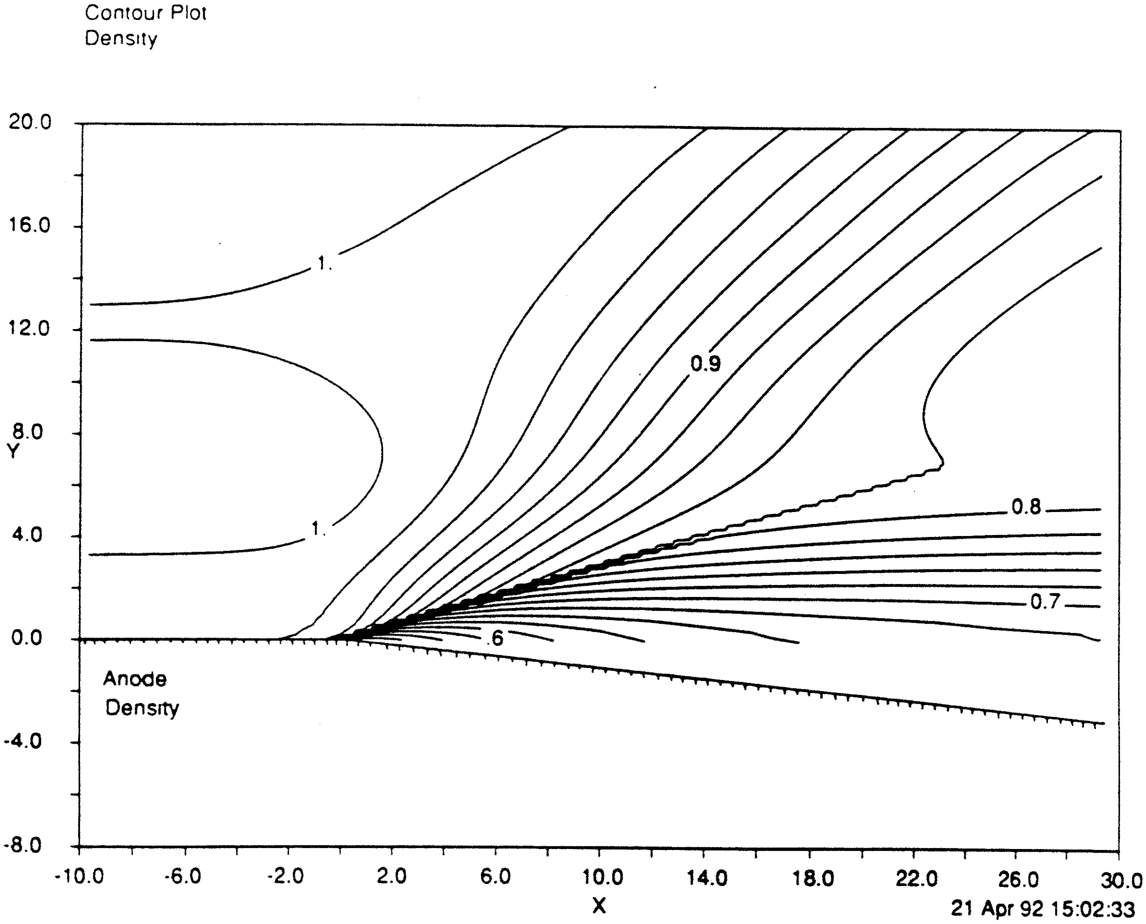

Figure 4-8: Flow above a weak corner in the presence of the Hall effect. Contour plot of the density $\rho = \rho_0 + \epsilon\ \rho_1$, with $M_v = 1.414$, $M_a = 3.544$, $\beta_e = 1$, $\epsilon = 0.1$. The situation corresponds to an anode.

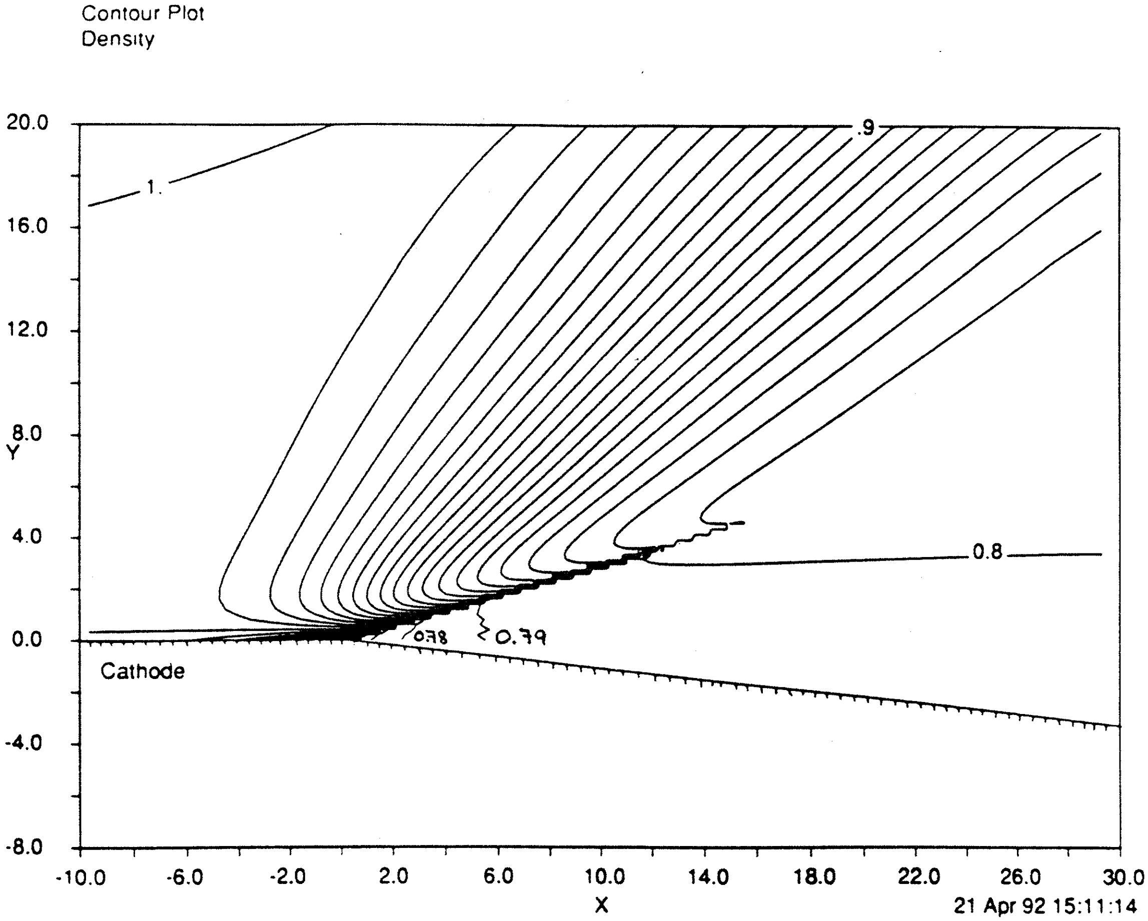

Figure 4-9: Flow above a weak corner in the presence of the Hall effect. Contour plot of the density $\rho = \rho_0 + \epsilon\, \rho_1$, with $M_v = 1.414$, $M_a = 3.544$, $\beta_e = 1$, $\epsilon = 0.1$. The situation corresponds to a cathode.

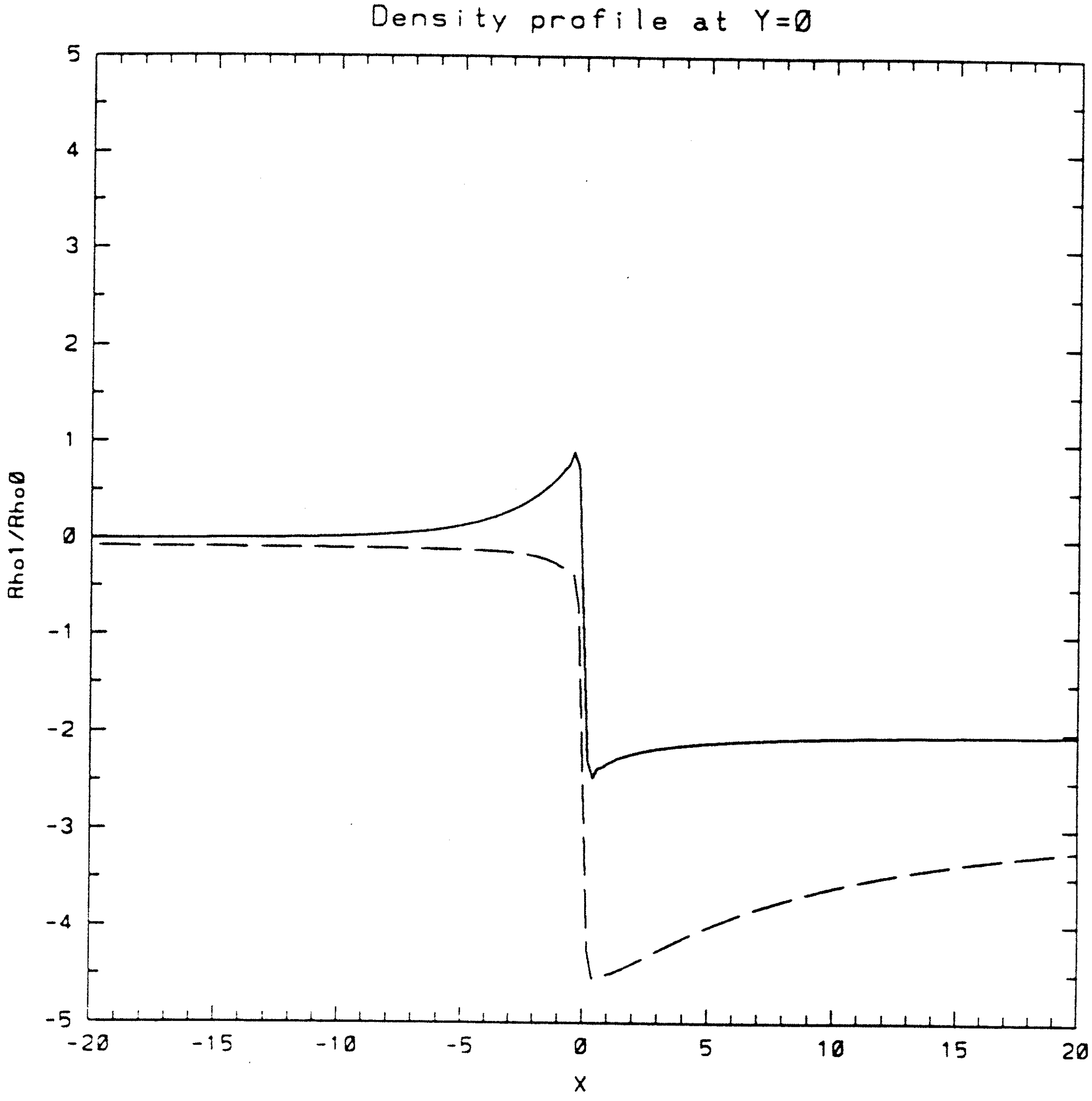

Figure 4-10: Density profiles for ρ_1 along $Y = 0$, with $M_v = 1.414$, $M_a = 3.544$, $\beta_e = 1$. The solid line corresponds to a cathode, the broken line corresponds to an anode.

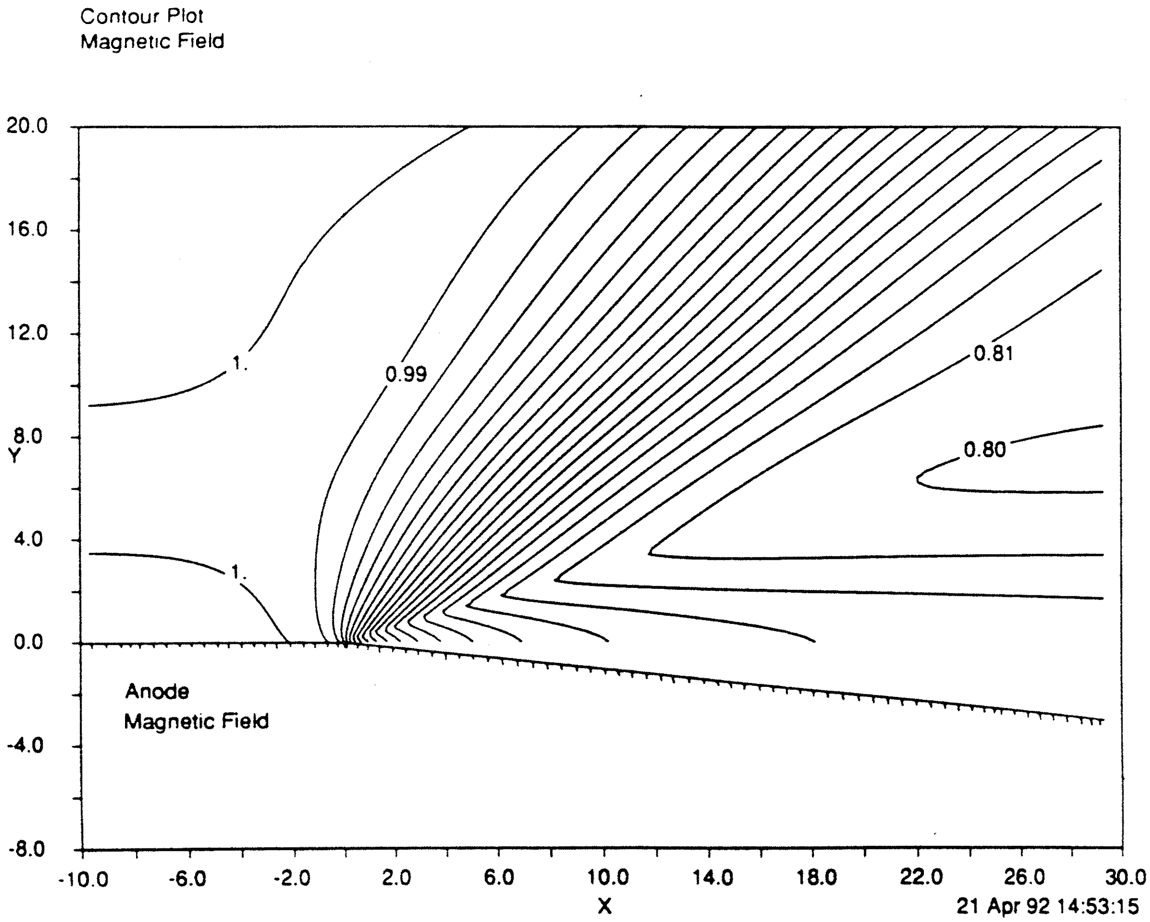

Figure 4-11: Flow above a weak corner in the presence of the Hall effect. Contour plot of the magnetic field $b = b_0 + \epsilon\, b_1$, with $M_v = 1.414$, $M_a = 3.544$, $\beta_e = 1$, $\epsilon = 0.1$. The situation corresponds to an anode.

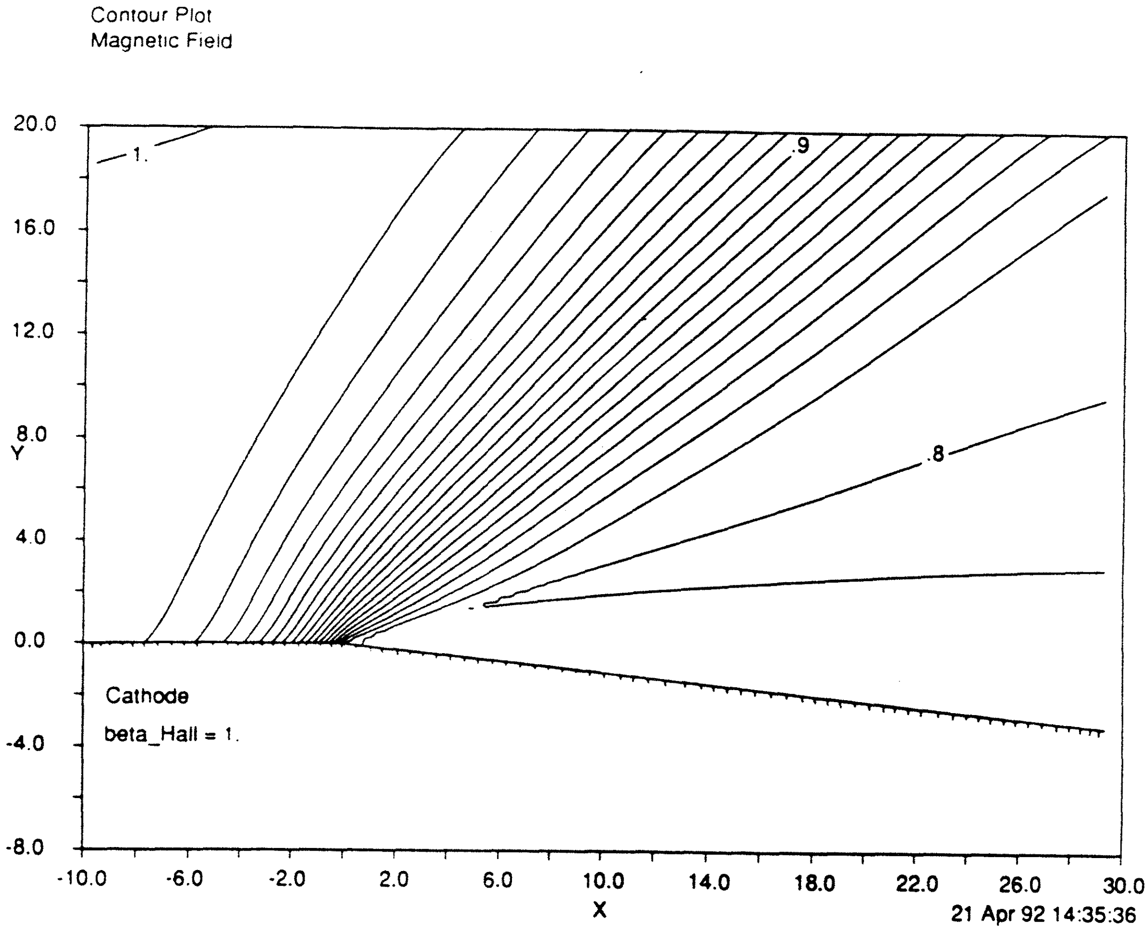

Figure 4-12: Flow above a weak corner in the presence of the Hall effect. Contour plot of the magnetic field $b = b_0 + \epsilon\, b_1$, with $M_v = 1.414$, $M_a = 3.544$, $\beta_e = 1$, $\epsilon = 0.1$. The situation corresponds to a cathode.

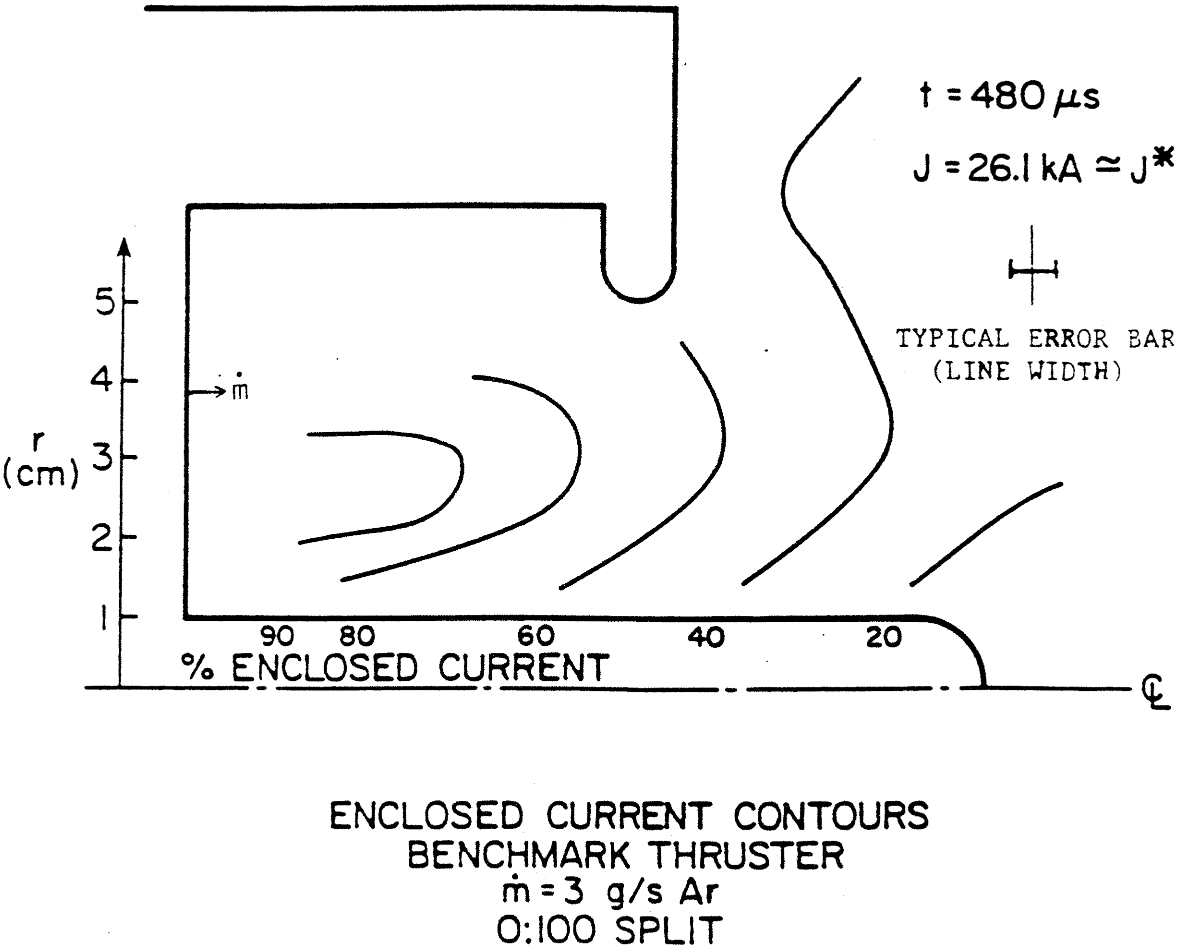

Figure 4-13: Enclosed current contours in a Princeton "benchmark" thruster . (From [Barnett J.W., 1985]) Near the anode the contour line corresponding to 40% of the total current shows a deflection similar to that predicted by the linear model.

Chapter 5

Resistive Solution for a Slightly Divergent Channel

5.1 Statement of the Problem

The linear analysis of Chapter 4 can be extended to cover the case of a two-dimensional channel whose boundaries are slightly different from the two flat planes which define a constant area channel. A logical extension of Chapter 4 is to consider a symmetrical channel whose boundaries are shown in figure 5-1.

The solution is no longer limited by the assumption that $\Lambda_m \ll H$, but includes the cases $\Lambda_m \sim H$. The case without the Hall effect, whose solution can be written as an integral, will be considered first. Then, the case which includes the Hall effect will be considered. It will be shown that the Hall effect modifies the solution in a considerable way. Some of the effects that have been observed experimentally will be seen in the linear solution when the Hall effect is included, namely the gas compression along the cathode and a rather strong depletion along the anode, near the exit.

As for the case of the weak corner, the major application for this analysis lies in the insight into the *structure* of the flow: the main features include the regions of strong variations of density, temperature, pressure, and velocity near the exit, the influence of the flow expansion, and the gradients created by the Hall effect.

However the non-linear effects are still not considered by this model. There are two conditions which limit the validity of the linear analysis for the *corner* flow. First, the deflection angle must be small, and second, the solution is not valid far from the corner because non-linear effects become dominant. (The abrupt transition turns into a fan.) There are two similar limits of validity for the linear *channel* analysis: first the deflection angle must be small, and second, the solution loses its validity at a large distance downstream of the point where the channel's diameter starts growing, as non-linear effects become dominant.

In addition the analysis assumes a uniform incoming flow. From the asymptotic matching of the inlet layer to the outer solution in the main part of the channel one can see that the inlet plays a critical role in the distribution of the density, temperature and velocity in the incoming flow. In the absence of the Hall effect, and for a sufficiently long channel, the symmetry of the problem at the inlet dictates that the flow be uniform. However this uniformity is broken when the Hall effect is taken into account. If the channel is sufficiently long the problem can still be separated into two problems, one dealing with the calculation of the inlet acceleration layer, the other dealing with the corner flow. The effect of the non-uniform distribution could, in theory, be accounted for in the linearized model by assuming an artificial relation between the small parameter (the deflection angle ϵ) and the strength of the non-uniformity. Since the author of this thesis was not able to solve the two-dimensional inlet problem in the presence of the Hall effect, it was not possible to account for the flow non-uniformity either. A qualitative comparison with some experimental results is shown at the end of the chapter for a realistic set of parameters.

5.2 Formulation of the Linearized Problem

The results of the inlet inner-solution and of the mid-channel outer-solution are used to determine the upstream boundary condition. The upstream flow is assumed to be constant and can be defined by the Mach and Mach-Alfven number M_a and M_v. The channel height introduces a non-dimensional parameter: the ratio $\frac{H}{\Lambda_m}$ which can be considered as a magnetic Reynolds number based on the channel height (equivalent to the inter-electrode gap). If we consider the Hall effect, this introduces a second non-dimensional parameter, H_a or β_e (depending on whether the strength of the local magnetic field is included in the parameter definition).

The equations of the weak corner analysis are still valid, and the linearized problem gives the same fourth order differential operator. The only change is in the boundary conditions. The assumption of vanishing modes as $Y \to \infty$ and the causality condition are replaced by two boundary conditions at the upper electrode. These two conditions are of the same type as those defined on the lower electrode (at $Y = 0$) namely the tangential velocity and the equipotential condition. The linearized problem can therefore be expressed by the following operator and boundary conditions:

$$u_0 \frac{\partial}{\partial X}\left((1 - M_v^2)\frac{\partial^2}{\partial X^2} + \frac{\partial^2}{\partial Y^2}\right) v_1 = \frac{M_v^2}{M_a^2}\nabla^2\left((1 - M_a^2)\frac{\partial^2}{\partial X^2} + \frac{\partial^2}{\partial Y^2}\right) v_1, \qquad (5.1)$$

$$v_1(X, 0) = -u_0 \Upsilon(X) \quad \text{at } Y = 0, \qquad (5.2)$$

$$v_1(X, H) = u_0 \Upsilon(X) \quad \text{at } Y = H, \qquad (5.3)$$

$$\frac{\partial b_1}{\partial Y} + \beta_e \frac{\partial b_1}{\partial X} = 0 \quad \text{at } Y = 0, \qquad (5.4)$$

$$\frac{\partial b_1}{\partial Y} - \beta_e \frac{\partial b_1}{\partial X} = 0 \quad \text{at } Y = H. \qquad (5.5)$$

where H is the channel height and $\Upsilon(X)$ is the step function.

5.3 Method of Solution

The Fourier transformation in X can be used to calculate the solution in the strip defined by $X \in \mathbf{R}$; $Y \in [0, H]$. The transformation of equation (5.1) is a fourth-order constant-coefficient ordinary differential equation in Y, which can be integrated easily. The solution can be expressed as a linear combination of four modes:

$$v_1(X, Y) = u_o \frac{1}{2\pi}\int_{\mathbf{R}} \left(\mu_1 e^{-\nu_1 Y} + \mu_2 e^{-\nu_2 Y} + \mu_3 e^{\nu_1 Y} + \mu_4 e^{\nu_2 Y}\right) e^{ikX} dk. \qquad (5.6)$$

The μ_j are complex functions of $k, Y, H, \beta_a^2, \beta_v^2, \beta_e$. They are defined by the four boundary conditions described above. Similarly the expressions for the other variables are:

$$\begin{aligned} \rho_1(X,Y) &= \rho_o \frac{1}{2\pi}\int_{\mathbf{R}} \Bigg(-i\frac{\nu_1^2 - k^2}{k\nu_1}\mu_1 e^{-\nu_1 Y} - i\frac{\nu_2^2 - k^2}{k\nu_2}\mu_2 e^{-\nu_2 Y} + \\ & \qquad i\frac{\nu_1^2 - k^2}{k\nu_1}\mu_3 e^{\nu_1 Y} + i\frac{\nu_2^2 - k^2}{k\nu_2}\mu_4 e^{\nu_2 Y} \Bigg) e^{ikX} dk, \end{aligned} \tag{5.7}$$

$$\begin{aligned} u_1(X,Y) &= u_o \frac{1}{2\pi}\int_{\mathbf{R}} \Bigg(-\frac{ik}{\nu_1}\mu_1 e^{-\nu_1 Y} - \frac{ik}{\nu_2}\mu_2 e^{-\nu_2 Y} + \\ & \qquad \frac{ik}{\nu_1}\mu_3 e^{\nu_1 Y} + \frac{ik}{\nu_2}\mu_4 e^{\nu_2 Y} \Bigg) e^{ikX} dk, \end{aligned} \tag{5.8}$$

$$\begin{aligned} b_1(X,Y) &= b_o \frac{1}{2\pi}\int_{\mathbf{R}} \Bigg(i\frac{\nu_1^2 + \beta_a^2 k^2}{k\nu_1}\mu_1 e^{-\nu_1 Y} + i\frac{\nu_2^2 + \beta_a^2 k^2}{k\nu_2}\mu_2 e^{-\nu_2 Y} - \\ & \qquad i\frac{\nu_1^2 + \beta_a^2 k^2}{k\nu_1}\mu_3 e^{\nu_1 Y} - i\frac{\nu_2^2 + \beta_a^2 k^2}{k\nu_2}\mu_4 e^{\nu_2 Y} \Bigg) e^{ikX} dk. \end{aligned} \tag{5.9}$$

After taking the Fourier transform of the boundary conditions one obtains the following conditions, respectively:

$$\mu_1 + \mu_2 + \mu_3 + \mu_4 = \frac{i}{k}, \tag{5.10}$$

$$\mu_1 e^{-\nu_1 H} + \mu_2 e^{-\nu_2 H} + \mu_3 e^{\nu_1 H} + \mu_4 e^{\nu_2 H} = -\frac{i}{k}, \tag{5.11}$$

$$\begin{aligned} &\mu_1(\nu_1^2 + \beta_a^2 k^2)(1 - \beta_e \frac{ik}{\nu_1}) + \mu_2(\nu_2^2 + \beta_a^2 k^2)(1 - \beta_e \frac{ik}{\nu_2}) \\ &\quad + \mu_3(\nu_1^2 + \beta_a^2 k^2)(1 + \beta_e \frac{ik}{\nu_1}) + \mu_4(\nu_2^2 + \beta_a^2 k^2)(1 + \beta_e \frac{ik}{\nu_2}) = 0, \end{aligned} \tag{5.12}$$

$$\mu_1(\nu_1^2 + \beta_a^2 k^2)(1 - \beta_e \frac{ik}{\nu_1}) e^{-\nu_1 H} + \mu_2(\nu_2^2 + \beta_a^2 k^2)(1 - \beta_e \frac{ik}{\nu_2}) e^{-\nu_2 H}$$

$$+\mu_3(\nu_1^2+\beta_a^2k^2)(1+\beta_e\frac{ik}{\nu_1})e^{\nu_1 H}+\mu_4(\nu_2^2+\beta_a^2k^2)(1+\beta_e\frac{ik}{\nu_2})e^{\nu_2 H}=0. \quad (5.13)$$

If the Hall effect is neglected, it is possible to find closed form expressions for the μ_j which are given below:

$$\mu_1=\frac{i}{k}\frac{\nu_2^2+\beta_a^2k^2}{\nu_2^2-\nu_1^2}\frac{1}{1-e^{-\nu_1 H}}, \quad (5.14)$$

$$\mu_2=-\frac{i}{k}\frac{\nu_1^2+\beta_a^2k^2}{\nu_2^2-\nu_1^2}\frac{1}{1-e^{-\nu_2 H}}, \quad (5.15)$$

$$\mu_3=-\frac{i}{k}\frac{\nu_2^2+\beta_a^2k^2}{\nu_2^2-\nu_1^2}\frac{e^{-\nu_1 H}}{1-e^{-\nu_1 H}}, \quad (5.16)$$

$$\mu_4=\frac{i}{k}\frac{\nu_1^2+\beta_a^2k^2}{\nu_2^2-\nu_1^2}\frac{e^{-\nu_2 H}}{1-e^{-\nu_2 H}}, \quad (5.17)$$

And the expression for $\tilde{v}_1(k,Y)$ is then:

$$\tilde{v}_1(k,Y)=\frac{i}{k}\frac{\nu_2^2+\beta_a^2k^2}{\nu_2^2-\nu_1^2}\frac{e^{-\nu_1 Y}-e^{-\nu_1(H-Y)}}{1-e^{-\nu_1 H}}-\frac{i}{k}\frac{\nu_1^2+\beta_a^2k^2}{\nu_2^2-\nu_1^2}\frac{e^{-\nu_2 Y}-e^{-\nu_2(H-Y)}}{1-e^{-\nu_2 H}}. \quad (5.18)$$

The velocity $\tilde{v}_1(k,Y)$ can be inverted using a Fast Fourier Transformation algorithm as before. The caveat about the pole at $k=0$ still applies, and one can use the techniques described above (integration below the real axis or inversion of $\frac{\partial\tilde{v}_1}{\partial X}$ followed by integration in X.) Notice, in the case of the channel flow, that $\tilde{u}_1(k,Y)$ must be differentiated twice, like $\tilde{b}_1$ and $\tilde{\rho}_1$, in order to remove the singularity at $k=0$.

When the Hall effect is included, there is no simple closed form solution. It is however possible to solve for the μ_j numerically as functions of k. This can be done after rescaling of the unknowns. A closed form solution for the μ_j was found using the MACSYMA package. Although this solution was too complicated to use, it showed the asymptotic behavior of the solution for $\nu_1 Y \gg 1$ and for $\nu_1(H-Y)\gg 1$. The solution includes exponential terms like $e^{-\nu_1 Y}$ and $e^{-\nu_1(H-Y)}$ (similar to equations (5.14) to (5.17)) which can change by many orders of magnitude. When the exponential part of the μ_j are factored out, the solutions are well-behaved, and the fourth order linear system is well-conditioned.

The results for $H = 30$ are shown in figures 5-2, 5-3. Notice that ρ_1 and b_1 become unbounded in the far downstream region as a result of the expansion through an ever increasing channel area. This is also true for the variable u_1, however v_1 stays bounded.

5.4 Discussion

5.4.1 Wide Channels

An example of the results for a wide channel ($h = 30\Lambda_m$) is shown in figures 5-2 and 5-3. The properties of the weak corner solution discussed in section 4.7 (compression and expansion along the electrodes) apply to the channel as well. The current refraction is visible near both electrodes. This analysis confirms that the depletion region near the anode appears downstream from the origin of the divergent section, suggesting that the anode depletion is not only related to the presence of the Lorentz "pumping force", but also the channel divergence. It also appears that there is a small compression zone along the cathode, ahead of the origin of the divergent section (difficult to see in the plots). All these effects would disappear in the absence of divergence in the channel, and conversely the compression and depletion regions would be exchanged if the channel were convergent instead of divergent. A transverse cross section of the density downstream of the corner is shown in figure 5-4. This figure shows that the density is not monotonic but has an alternation of maxima and minima (+ - + -). Thus a local maximum exits between the core of the flow and the near-anode depletion region, and conversely a local minimum exits between the core of the flow and the near-cathode high-density region. The effects of the Hall conductivity are thus local effects, which is consistent with the fact that they appear in second order derivatives. They are confined in boundary layers which appear near the surface of the electrodes. An increase of the Hall parameter results in an increase of the gradients near the electrodes, in particular for the density.

It must be kept in mind that this analysis assumes a uniform incoming flow calculated from the one-dimensional inlet layer without the Hall effect, and that the inclusion of the Hall effect in the inlet region would most likely create transverse gradients, in particular for the temperature, density, and velocity.

5.4.2 Narrow Channels

When the height of the channel is decreased the results are modified significantly. The major effect is that the longitudinal variations in the divergent section are much stronger for the narrow channel. In addition a decrease of the channel height results in the displacement of the current lines towards the inlet. The retrograde displacement of the current lines along the cathode is depicted in figure 5-5, where the attachment point of an arbitrary current line (defined by $b_1/b_0 = -1$) is plotted as a function of the channel height. The geometry is that of figure 5-1 (a symmetrical divergent channel). When the channel height is larger than about $20\Lambda_m$, most of the current attachment is confined to the exit area, and when the channel height is lower than about $10\Lambda_m$, the attachment point moves upstream proportionally to $\log h$.[1]

This property invalidates the intuitive concept that the one-dimensional model becomes more accurate as the channel height is decreased. One must distinguish here between two different phenomena. On one hand it can be shown, by considering a limiting process where the channel height tends to zero, that some of the variables (namely b and p) will have a one-dimensional distribution within the channel. This can be stated more formally by writing that, in the limit when the thickness h tends to zero, the first term b_0 of the perturbation expansion $b(X,Y;h) = b_0(X) + h\, b_1(X,Y) + h^2\, b_2(X,Y) + \dots$ does not depend on the transverse coordinate Y and similarly for p. Notice that the variables ρ and u_x do not have this property, and therefore do not, in general, tend to a one-dimensional distribution.

The second effect to consider is the fact that the inter-electrode gap h replaces Λ_m as the scale length for the plasma expansion, and consequently the results change

---

[1] It can be approximated by $X^* \simeq -34 + 30 \log h_1 0$.

on a smaller scale. However the diffusive effects still change on the same length scale, Λ_m. Consequently there is a balance between a source term whose "strength" is proportional to $1/h$ and a damping factor whose "strength" is constant.

An analogy can be drawn with the interaction between a supersonic shock and a laminar boundary layer. Under certain conditions the boundary layer separates from the wall, and the separation occurs upstream of the point where the shock reaches the boundary layer. The elliptic properties of the differential operator associated with the viscosity are responsible for the upstream separation under the influence of the shock.

The previously accepted condition for the thruster to work in the magnetosonic regime, (*i.e.* that the direct electromagnetic acceleration will dominate over the electrothermal acceleration mechanism), is that the magnetic Reynolds number based on the channel length be large compared to one: $R_{m(L)} \gg 1$. The author suggests that the condition[2]: $R_{m(h)} \gg 1$, should be added to the first, in order to prevent current attachment close to the inlet, to guarantee a quasi one-dimensional behavior for the thruster and to increase the effective magnetic Reynolds number for the flow. Using a different approach Schoenberg *et al.* [52] have proposed a similar criterion.

The linearized calculation does not include the effect of the variation of the transport coefficients, namely the electrical conductivity and the Hall parameter. However these parameters vary in space, and are essentially functions of the electron temperature, electron density and the magnetic field. The Hall parameter is proportional to the magnetic field, and is therefore higher near the inlet than near the exit, in addition it is inversely proportional to the electron density, and will therefore be higher near the anode than the cathode. An increase of the Hall effect can decrease the local electron density near the anode, which in turn may increases the Hall effect locally. This type of positive feedback can rapidly create a complete starvation of charge carrier along the anode. Therefore it is possible that the upstream influence could be stronger along the anode in a non-linear model.

Although it was difficult to find experimental results for quasi one-dimensional

---

[2] That the magnetic Reynolds number based on the channel height be large compared to one.

thruster geometries, some qualitative comparison can be made between experimental results and the present theory based on the measurements of Wolff [65]. Figure 5-9 shows the measured current distribution inside a flared thruster. The corresponding calculations appear in figures 5-7 and 5-8. The calculations are based on a channel geometry which is derived from the experimental geometry and which appears in figure 5-6. The major differences are that: the real channel is finite whereas the channel used in the calculation is infinite; at the exit plane the anode ends abruptly and the deflection angle is 90 degrees, whereas in the calculation the deflection angle is small; the conical section in the middle of the channel has an angle whose tangent is about 0.22, whereas the calculation uses an angle whose tangent is about 0.1; the real problem is axisymmetrical whereas the calculation ignores all axisymmetrical effects; finally the electrical conductivity and the Hall effect are variable, whereas in the calculation they are constant. Despite these limitations one can observe the same qualitative features. These include the tilting of the current lines under the Hall effect, with the current attaching towards the upstream section of the cathode and toward the downstream section of the anode. The current line refraction across the expansion fan originating from the start of the divergent section can also be seen in the calculation as well as in the experimental results. Similarly, an opposite refraction occurs across the weak shock originating from the end of the divergent section. The plot of the density distribution inside the thruster suggests that there is a strong density gradient in the transverse direction, with a maximum along the cathode. This maximum appears to be a consequence of the expansion due to the conical anode section. Similarly the density drops to very low values near the anode surface as a consequence of this expansion.

If one compares both cases to the one-dimensional model it appears that the current distribution is more spread-out than what the one-dimensional theory would predict (given that the magnetic Reynolds number based on the thruster length is about 20.) The experimental results and the theory thus confirm the fact that the current lines attach far inside the thruster when the channel height is decreased.

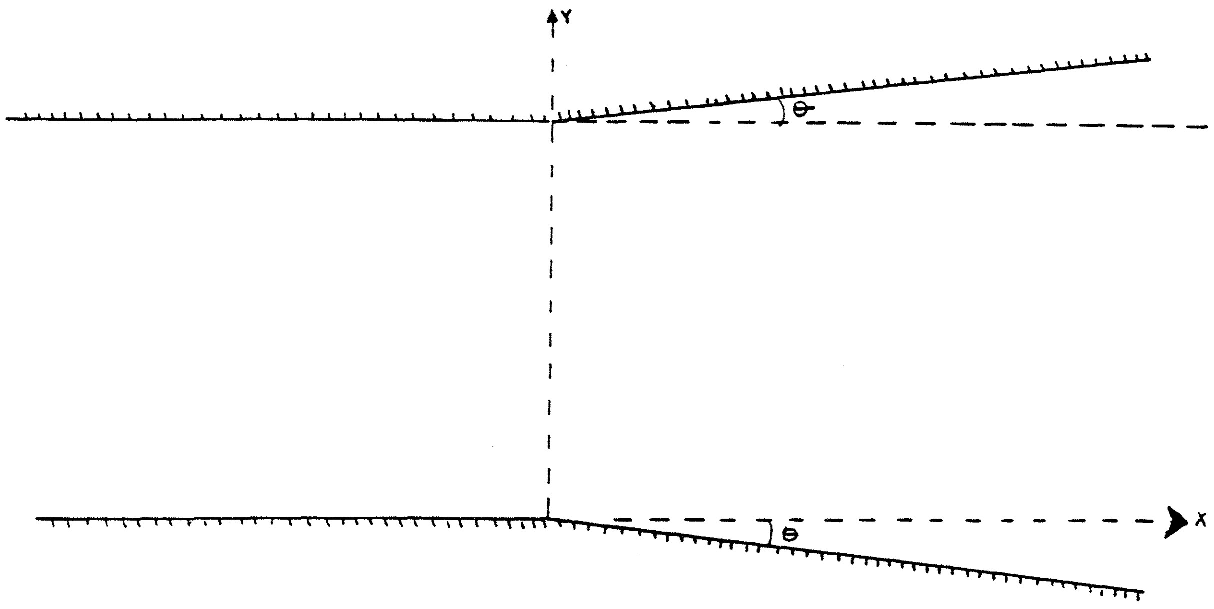

Figure 5-1: Geometry of a symmetric channel with a slight divergence.

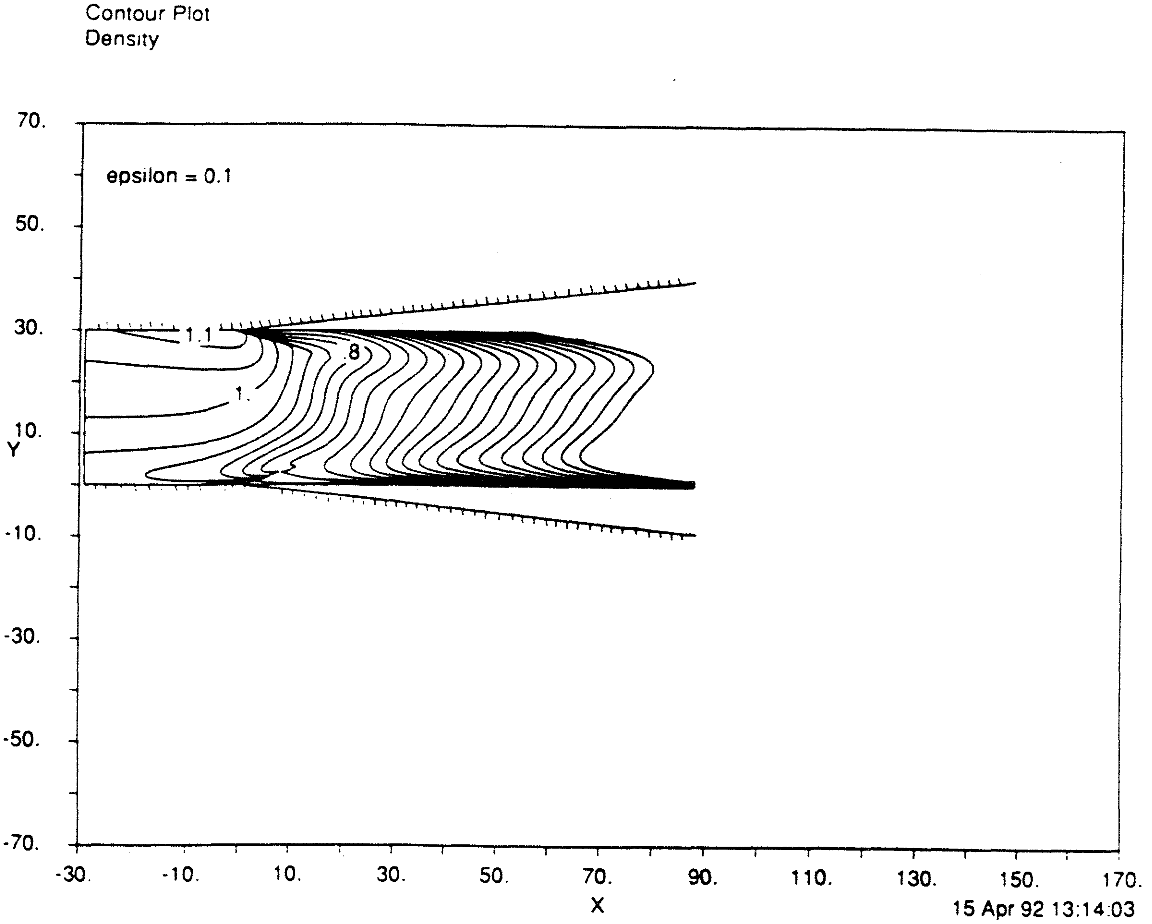

Figure 5-2: Flow in a channel with a slight divergence. Contour plot of the density $\rho = \rho_0 + \epsilon \; \rho_1$, with $M_v = 1.414$, $M_a = 3.544$, $\epsilon = 0.1$. The Hall parameter is $\beta_e = 2$. The channel height is $H = 30\Lambda_m$

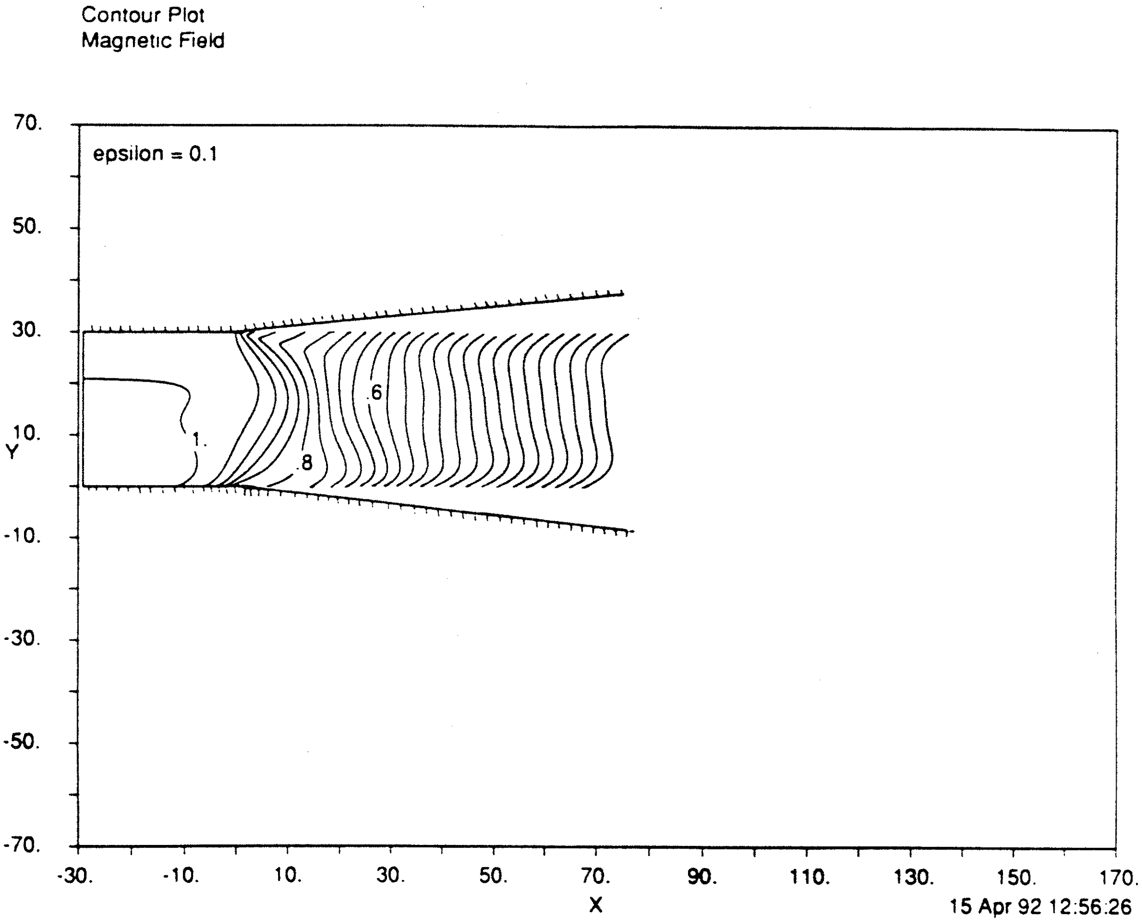

Figure 5-3: Flow in a channel with a slight divergence. Contour plot of the magnetic field $b = b_0 + \epsilon b_1$, with $M_v = 1.414$, $M_a = 3.544$, $\epsilon = 0.1$. The Hall parameter is $\beta_e = 2$. The channel height is $H = 30\Lambda_m$

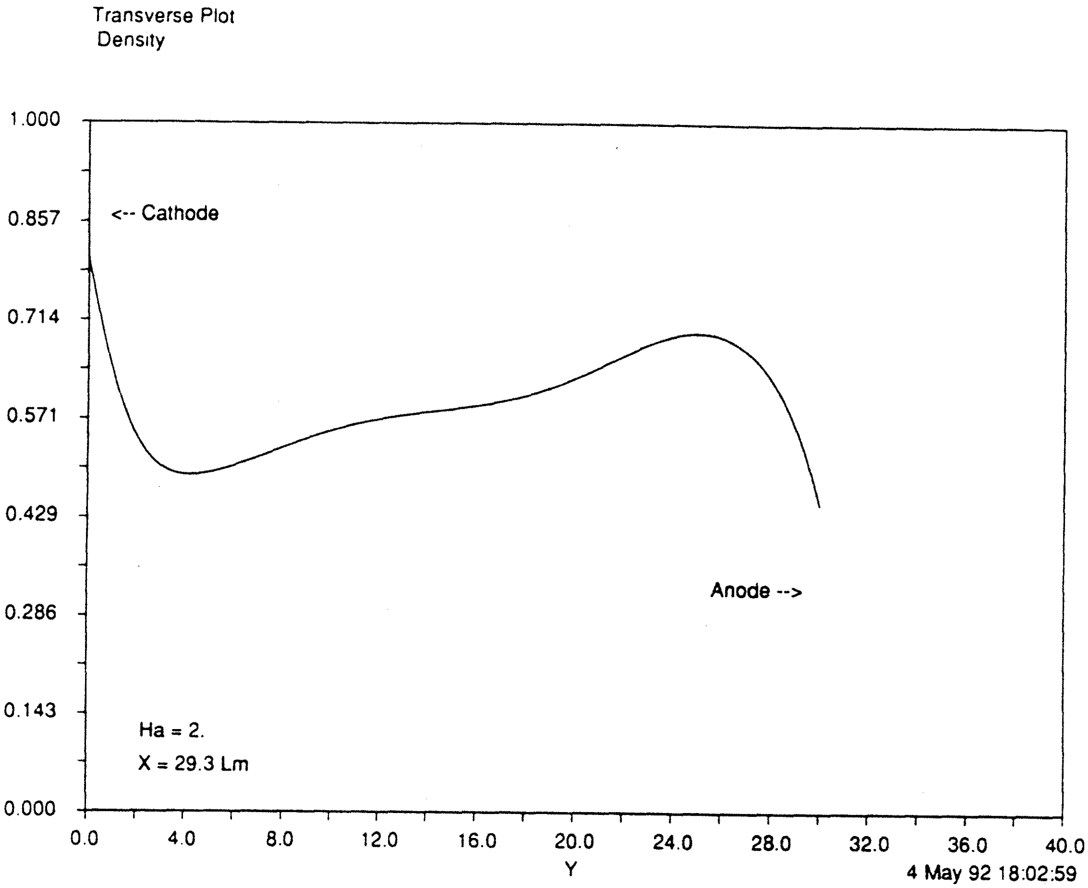

Figure 5-4: Flow in a channel with a slight divergence. Plot of the transverse density profile downstream of the corners, at a distance of $X = 29.3\Lambda_m$. $\rho = \rho_0 + \epsilon\ rho_1$, with $M_v = 1.414$, $M_a = 3.544$, $\epsilon = 0.1$. The Hall parameter is $\beta_e = 2$. The channel height is $H = 30\Lambda_m$

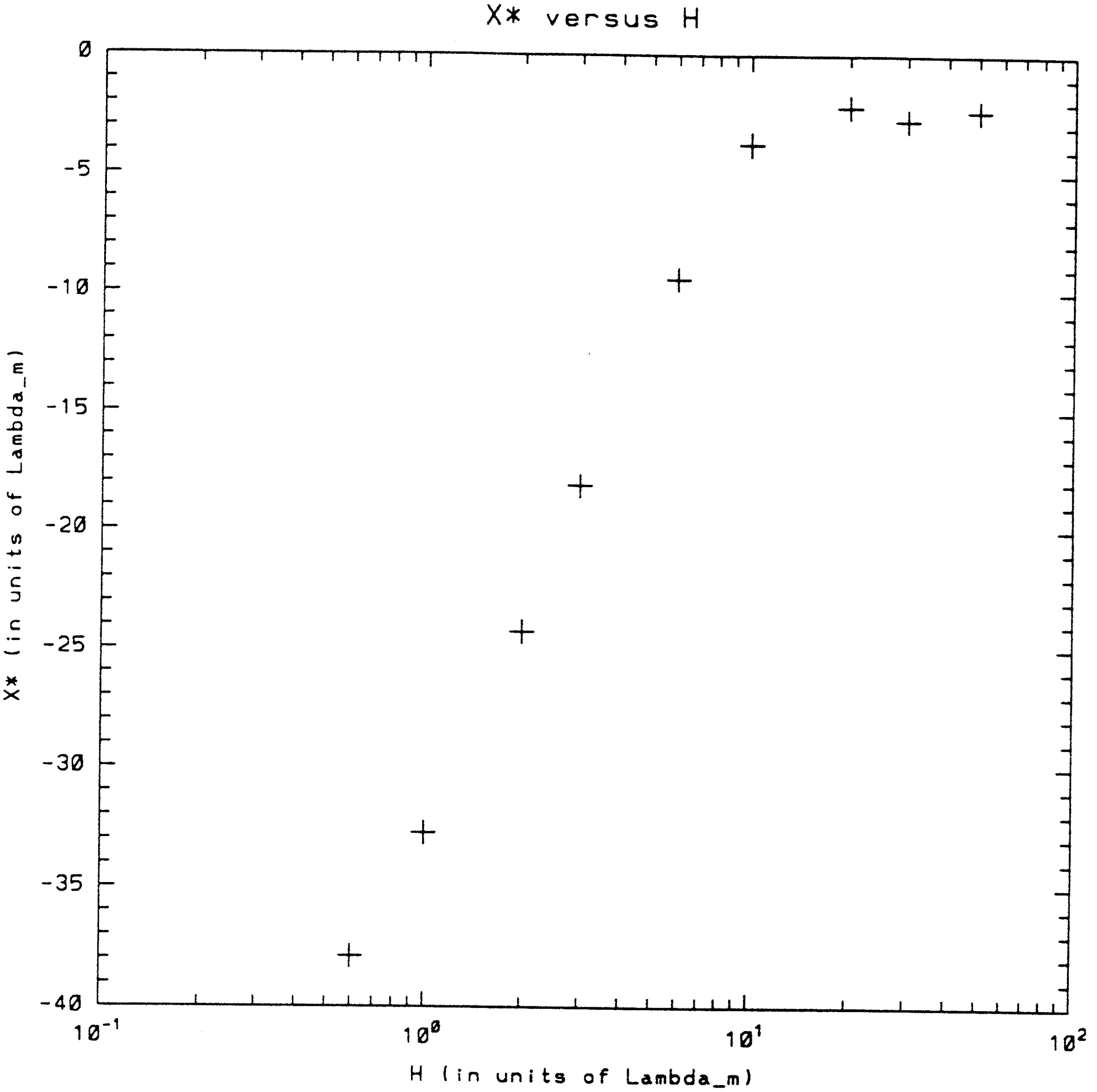

Figure 5-5: Plot of the position at the point at which $b_1/b_0 = -1$ along the cathode surface. The geometry corresponds to the symmetric divergent channel of figure 5.1. The distance is computed from the origin of the divergent section. The point moves back upstream as the channel height is decreased, indicating that the influence of the exit on the inlet region becomes stronger when the channel height is decreased. The conditions are: $M_v = 1.414, M_a = 3.544$, and the Hall parameter is $\beta_e = 2$.

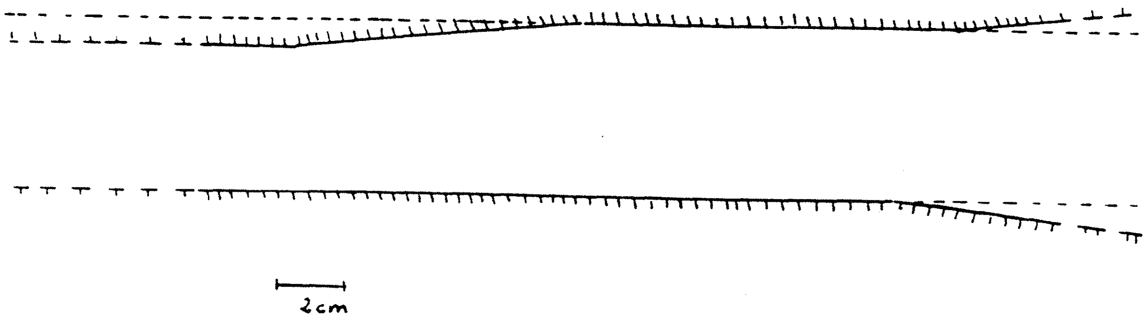

Figure 5-6: Geometry similar to the flared thruster of Wolff *et al.* used for the narrow channel calculations.

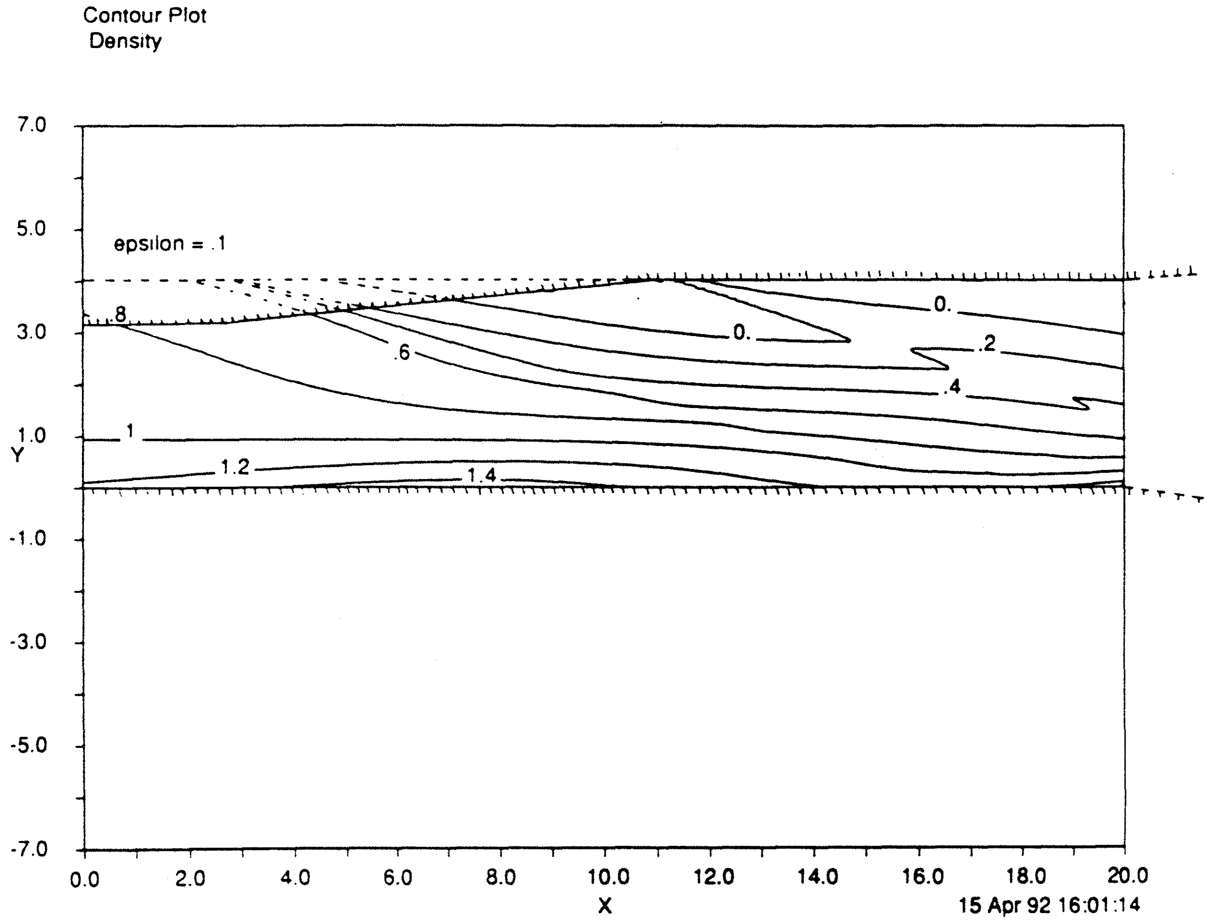

Figure 5-7: Flow in a narrow channel with a slight divergence. The channel is similar to the flared thruster of Wolff *et al.* Contour plot of the density $\rho = \rho_0 + \epsilon\ \rho_1$, with $M_v = 1.414$, $M_a = 3.544$ $\epsilon = 0.1$ and the Hall parameter is $\beta_e = 2$.

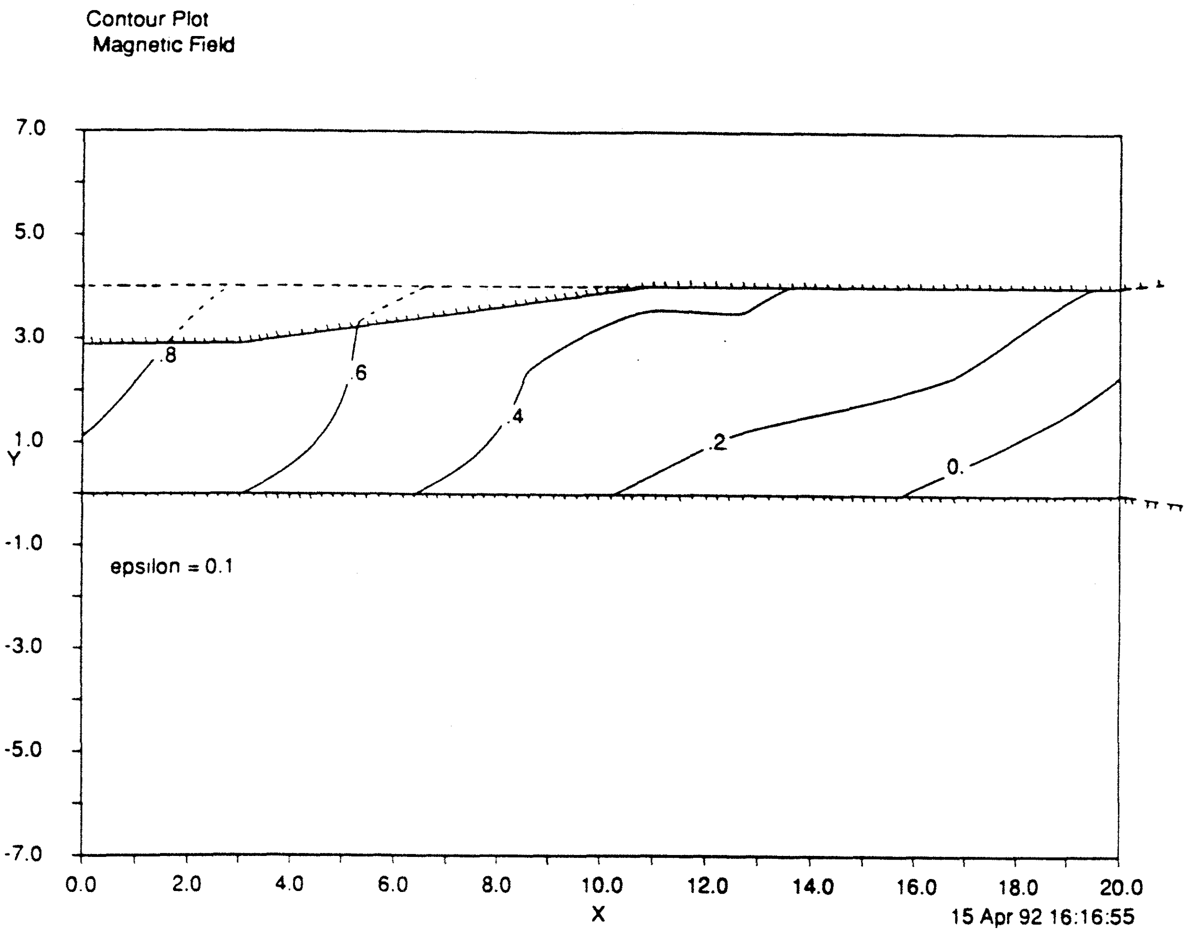

Figure 5-8: Flow in a narrow channel with a slight divergence. The channel is similar to the flared thruster of Wolff *et al.* Contour plot of the magnetic field $b = b_0 + \epsilon\, b_1$, with $M_v = 1.414$, $M_a = 3.544$, $\epsilon = 0.1$ and the Hall parameter is $\beta_e = 2.$.

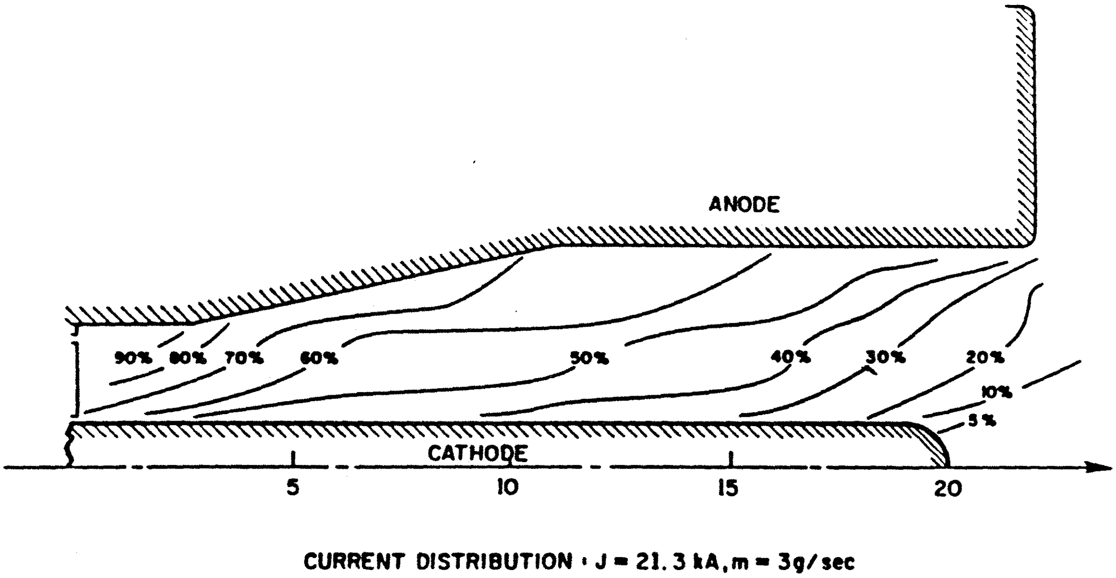

Figure 5-9: Experimental results for the geometry studied by Wolff *et al.*

Chapter 6

Flow along a Flat Insulator

When the plasma leaves the central region of the discharge it can be characterized by the following properties: It has a high velocity, of the order of the magneto-acoustic velocity, a low density, a low temperature, and a residual magnetic field. The level of this residual magnetic field depends on the degree of completeness of the plasma expansion. In some thruster geometries, such as that considered by Di Capua *et al.* [16], the electrodes are extended by insulators which are used as nozzle walls. (See figure 1-4.) Since no current can flow through these insulators all current lines are forced to attach at the end of the electrode, just ahead of the insulated section. Thus the magnetic field is suddenly forced to go to zero at the surface of the insulator. This forced transition will release some of the electromagnetic energy convected by the plasma. This release will be confined to a region in the neighborhood of the insulator, and will take the form of Ohmic heating. The plasma will see its temperature increased on a length scale corresponding to the decrease of the magnetic field. In the region near the transition from the conductor to the insulator, the flow has a complex structure which most likely cannot be reduced to a self-similar solution. In a classical boundary layer this region would be the region near the leading edge of a flat plate. Downstream of this transition region the flow relaxes to a self-similar structure which is a boundary layer. This structure is the object of this chapter. In a classical boundary layer this structure would be called the Prandtl boundary layer. Here the problem is complicated by the presence of the magnetic field, the electrical conductivity, and the gas compressibility.

6.1 Self-Similar Solution without Heat and Momentum Transport

6.1.1 Formulation

For an insulating wall the outer solution does not satisfy the boundary condition $B = 0$ at the surface of the insulator, and a boundary layer appears along the wall. Since the magnetic boundary layer is located in a narrow region adjacent to the wall it appears justified to stretch the coordinate which is normal to the boundary. This will introduce what can be called the boundary layer equations, which can then be solved by a self-similar transformation.

The equations can be written in cartesian coordinates as follow:

$$\frac{\partial}{\partial x}(\rho\, u) + \frac{\partial}{\partial y}(\rho\, v) = 0, \tag{6.1}$$

$$\rho\, u \frac{\partial u}{\partial x} + \rho\, v \frac{\partial u}{\partial y} + \frac{\partial}{\partial x}(p + b^2) = 0, \tag{6.2}$$

$$\rho\, u \frac{\partial v}{\partial x} + \rho\, v \frac{\partial v}{\partial y} + \frac{\partial}{\partial y}\left(p + b^2\right) = 0, \tag{6.3}$$

$$\rho^\gamma\, u \frac{\partial}{\partial x}(\frac{p}{\rho^\gamma}) + \rho^\gamma\, v \frac{\partial}{\partial y}(\frac{p}{\rho^\gamma}) = \frac{2\,(\gamma - 1)}{R_m} \left\{(\frac{\partial b}{\partial x})^2 + (\frac{\partial b}{\partial y})^2\right\}, \tag{6.4}$$

$$\rho\, u \frac{\partial}{\partial x}(\frac{b}{\rho}) + \rho\, v \frac{\partial}{\partial y}(\frac{b}{\rho}) = \frac{1}{R_m}\left(\frac{\partial^2 b}{\partial x^2} + \frac{\partial^2 b}{\partial y^2}\right). \tag{6.5}$$

The normal coordinate can be stretched the following way: $Y = y/\sqrt{\epsilon}$, $\epsilon = \frac{1}{R_m}$, while keeping the other coordinate constant: $X = x$. After substituting the inner variables expansions,

$$(\rho, u_x, u_y, p, b) = (R, U, \epsilon^{1/2} V, P, B) + \cdots, \tag{6.6}$$

inside the partial differential equations, and neglecting the higher orders in ϵ one obtains the following *boundary layer equations*:

$$\frac{\partial}{\partial X}(RU) + \frac{\partial}{\partial y}(RV) = 0, \tag{6.7}$$

$$R(U\frac{\partial}{\partial X} + V\frac{\partial}{\partial Y})U + \frac{\partial}{\partial X}(P + B^2) = 0, \tag{6.8}$$

$$\frac{\partial}{\partial Y}(P + B^2) = 0, \tag{6.9}$$

$$\frac{1}{\gamma - 1}R^\gamma(U\frac{\partial}{\partial X} + V\frac{\partial}{\partial Y})\left(\frac{P}{R^\gamma}\right) = 2\left(\frac{\partial B}{\partial Y}\right)^2, \tag{6.10}$$

$$R(U\frac{\partial}{\partial X} + V\frac{\partial}{\partial Y})\left(\frac{B}{R}\right) = \frac{\partial^2 B}{\partial Y^2}. \tag{6.11}$$

Using a method proposed by Hansen [22] it is possible to find a similarity transformation which turns the system of partial differential equations into a system of ordinary differential equations. This transformation is a generalization of the flat plate compressible boundary layer transformation to the case of a compressible flow with a transverse magnetic field. The transformation is also valid when viscosity and heat diffusion are included in the equations.[1]

In the case of a flat plate, the transformation has the form: $\eta = \frac{Y}{\sqrt{X}}, \xi = X$, and the variables take the form:

$$R = R(\eta),\ U = U(\eta),\ V = \xi^{-1/2}\tilde{V}(\eta),\ P = P(\eta),\ B = B(\eta).$$

After substituting in the system of partial differential equations and keeping the terms

---

[1] The compressible boundary-layer is usually calculated using the Illingworth-Stewartson transformation, which converts the parabolic system of partial differential equations of the compressible boundary layer into a system of two ordinary differential equations, one for the momentum equation, and one for the energy equation. The mass conservation equation (continuity equation) is satisfied by expressing the velocities in term of the derivative of a streamfunction. It can be shown that the Illingworth-Stewartson is actually equivalent to the transformation considered in this chapter. The choice of one versus the other is mostly a question of taste. The Illingworth-Stewartson leads to a smaller number of equations and it can take a form similar to that of the incompressible boundary layer, but the algebra is fairly complicated; the method presented here leads to a larger number of equations but the algebra is considerably easier, in particular for the magnetic field equation.

of dominant order in x, one obtains the system of ordinary differential equations:

$$-\frac{1}{2}\eta\frac{\partial}{\partial\eta}(RU)+\frac{\partial}{\partial\eta}(R\tilde{V})=0, \tag{6.12}$$

$$R(\tilde{V}-\frac{1}{2}\eta U)\frac{\partial U}{\partial\eta}-\frac{1}{2}\eta\frac{\partial}{\partial\eta}(P+B^2)=0, \tag{6.13}$$

$$\frac{\partial}{\partial\eta}(P+B^2)=0, \tag{6.14}$$

$$R^{\gamma}(\tilde{V}-\frac{1}{2}\eta U)\frac{\partial}{\partial\eta}(\frac{P}{R^{\gamma}})=2\,(\gamma-1)\,(\frac{\partial B}{\partial\eta})^2, \tag{6.15}$$

$$R\,(\tilde{V}-\frac{1}{2}\eta U)\frac{\partial}{\partial\eta}(\frac{B}{R})=\frac{\partial^2 B}{\partial\eta^2}. \tag{6.16}$$

After simplifications and assuming that $\tilde{V}\neq\frac{1}{2}\eta U$ one obtains the system,

$$\frac{\partial U}{\partial\eta}=0, \tag{6.17}$$

$$\frac{\partial}{\partial\eta}(P+B^2)=0, \tag{6.18}$$

$$\frac{\partial R}{\partial\eta}=\frac{R}{\gamma P}\left(2BJ-2(\gamma-1)\frac{J^2}{\tilde{V}-\frac{1}{2}\eta U}\right), \tag{6.19}$$

$$\frac{\partial\tilde{V}}{\partial\eta}=\frac{1}{\gamma P}\left(2(\gamma-1)J^2-2BJ(\tilde{V}-\frac{1}{2}\eta U)\right), \tag{6.20}$$

$$\frac{\partial J}{\partial\eta}=J(\tilde{V}-\frac{1}{2}\eta U)+\frac{B}{\gamma P}\left(2(\gamma-1)J^2-2BJ(\tilde{V}-\frac{1}{2}\eta U)\right), \tag{6.21}$$

$$\frac{\partial B}{\partial\eta}=J, \tag{6.22}$$

with the boundary conditions given by the matching conditions with the outer flow,

$$R(\delta_e)=\rho_e, \tag{6.23}$$

$$P(\delta_e)=p_e, \tag{6.24}$$

$$B(\delta_e)=b_e, \tag{6.25}$$

and at the wall,

$$\tilde{V}(0) = 0, \tag{6.26}$$

$$B(0) = 0. \tag{6.27}$$

where δ_e is a finite distance which is large compared to the thickness of the boundary layer.

6.1.2 Method of Solution

The system of ordinary differential equations can be integrated numerically. The integration was done with the package called COLNEW written by Ascher, Cristiansen, and Russel, and available from NETLIB. This package is a general purpose collocation code which requires, as input, the description of the differential equations and of the boundary conditions. The package handles automatically the mesh generation, and the successive mesh refinements. The algorithm was able to converge to a close approximation of the solution despite the presence of an unforeseen singularity at the origin, where the density goes to zero.

6.1.3 Results

The results of the model are shown in figure 6-1. The values at the edge of the boundary layer correspond to the zeroth-order solution of the constant area channel, and are therefore indicative of the values taken by the variables inside the channel.

The most significant result of this analysis is the presence of a singularity near the wall, where the density goes to zero. Simultaneously the temperature reaches $+\infty$ in order to maintain a finite pressure at the wall. This singular behavior is the consequence of the model. In the entropy equation, the convection of entropy balances the dissipation due to the Joule effect. As the distance d to the wall decreases, the convective term scales as d^{-1}, whereas the dissipative term scales as d^{-2}. In order to maintain the balance, the entropy has to go to infinity, and since the pressure near the wall is constant, the density must go to zero. In the next section it will be shown that the addition of a small amount of viscosity and heat conduction to the model eliminates the singularity. These effects, which include second order derivatives, end up balancing the Joule dissipation near the wall.

In addition the results show an inversion in the velocity component normal to the wall. At large distances the normal velocity is directed towards the wall. Close to the wall the normal component is directed away from the wall. This creates a "convergent streamline", with streamlines converging towards it from both sides, as shown in figure 6-2.

The density shows a maximum in the middle of the boundary layer, and this maximum is attributed to the conflicting effects of the boundary layer compression under the influence of the Lorentz force, and the requirement that the density decrease near the wall as a result of the balance between entropy convection and entropy creation within the boundary layer.

Experimental results that could be used to check the conclusions of this analysis are difficult to find. The current distribution for the parallel-plate thruster experimented by Di Capua [16] is shown in figure 1-4. The small size of the thruster barely allows the magnetic boundary-layers to develop into a self-similar structure. The two boundary layers, which grow on the upper and lower walls, merge in the middle of the channel.

6.2 Self-Similar Solution with Momentum and Heat Transport

The singularity at the wall in the solution described above can be eliminated by allowing heat and momentum conduction to balance the Ohmic heating.

η	$\tilde{\rho}$	$\tilde{v}$	$\tilde{B}$	$\tilde{P}$	$\tilde{T}$
0.000	0.000	0.000	0.000	0.387	∞
0.202	0.429	0.0364	0.0598	0.384	0.895
0.404	0.794	0.0725	0.119	0.374	0.470
0.606	1.130	0.108	0.179	0.356	0.315
0.808	1.436	0.142	0.238	0.331	0.230
1.010	1.709	0.175	0.297	0.299	0.175
1.212	1.934	0.203	0.356	0.261	0.135
1.414	2.095	0.226	0.413	0.217	0.104
1.616	2.156	0.236	0.468	0.169	0.0783
1.818	2.065	0.216	0.519	0.119	0.0576
2.020	1.776	0.132	0.560	0.0747	0.0421
2.222	1.445	-0.022	0.582	0.0489	0.0338
2.424	1.329	-0.100	0.587	0.0423	0.0318
2.626	1.314	-0.112	0.589	0.0414	0.0316
2.828	1.313	-0.113	0.589	0.0414	0.0315
3.030	1.312	-0.114	0.589	0.0414	0.0315
3.232	1.312	-0.114	0.589	0.0414	0.0315
∞	1.312	-0.114	0.589	0.0414	0.0315

Table 6.1: Magnetic Boundary Layer over a Flat Insulator. $\tilde{\rho}_\infty = 1.312$, $\tilde{u}_\infty = 0.762$, $\tilde{P}_\infty = 0.0414$, $\tilde{B}_\infty = 0.589$

6.2.1 Formulation

Using the same "stretched" coordinates: $Y = y/\sqrt{\epsilon}$, $\epsilon = \frac{1}{R_m}$ and $X = x$, and the expansions:

$$(\rho, u_x, u_y, T, p, b) = (R, U, \epsilon^{1/2}V, T, P, B) + \cdots, \tag{6.28}$$

a new set of "boundary-layer equations" similar to those presented above, but including the transport terms, can be written as:

$$\frac{\partial}{\partial X}(RU) + \frac{\partial}{\partial Y}(RV) = 0, \tag{6.29}$$

$$R(U\frac{\partial}{\partial X} + V\frac{\partial}{\partial Y})U + \frac{\partial}{\partial X}(P + B^2) = \frac{R_m}{R_e}\frac{\partial^2 U}{\partial Y^2}, \tag{6.30}$$

$$\frac{\partial}{\partial Y}(P + B^2) = 0, \tag{6.31}$$

$$\frac{1}{\gamma-1}R^{\gamma}(U\frac{\partial}{\partial X}+V\frac{\partial}{\partial Y})\left(\frac{T}{R^{\gamma-1}}\right)=2\left(\frac{\partial B}{\partial Y}\right)^2+\frac{R_m}{R_e}\left(\frac{\gamma}{\gamma-1}\frac{1}{Pr}\frac{\partial^2 T}{\partial Y^2}+\left(\frac{\partial U}{\partial Y}\right)^2\right), \tag{6.32}$$

$$R(U\frac{\partial}{\partial X}+V\frac{\partial}{\partial Y})\left(\frac{B}{R}\right)=\frac{\partial^2 B}{\partial Y^2}, \tag{6.33}$$

$$P=RT. \tag{6.34}$$

The same similarity transformation, defined by: $\eta=\frac{Y}{\sqrt{X}}$, $\xi=X$, $R=R(\eta)$, $U=U(\eta)$, $V=\sqrt{\xi}\,\tilde{V}(\eta)$, $P=P(\eta)$, $B=B(\eta)$ leads, after substitution in the system of partial differential equations, to the following set of ordinary differential equations:

$$-\frac{1}{2}\eta\frac{\partial}{\partial\eta}(RU)+\frac{\partial}{\partial\eta}(R\tilde{V})=0, \tag{6.35}$$

$$R(\tilde{V}-\frac{1}{2}\eta U)\frac{\partial U}{\partial\eta}-\frac{1}{2}\eta\frac{\partial}{\partial\eta}(RT+B^2)=\frac{R_m}{R_e}\frac{\partial^2 U}{\partial\eta^2}, \tag{6.36}$$

$$\frac{\partial}{\partial\eta}(RT+B^2)=0, \tag{6.37}$$

$$\frac{1}{\gamma-1}R^{\gamma}(\tilde{V}-\frac{1}{2}\eta U)\frac{\partial}{\partial\eta}(\frac{T}{R^{\gamma-1}})=2(\frac{\partial B}{\partial\eta})^2+\frac{R_m}{R_e}\left(\frac{\gamma}{\gamma-1}\frac{1}{P_r}\frac{\partial^2 T}{\partial\eta^2}+\left(\frac{\partial U}{\partial\eta}\right)^2\right), \tag{6.38}$$

$$R(\tilde{V}-\frac{1}{2}\eta U)\frac{\partial}{\partial\eta}(\frac{B}{R})=\frac{\partial^2 B}{\partial\eta^2}, \tag{6.39}$$

with boundary conditions at a large distance:

$$R(\delta_e)=\rho_e, \tag{6.40}$$

$$U(\delta_e)=u_e, \tag{6.41}$$

$$P(\delta_e)=p_e, \tag{6.42}$$

$$B(\delta_e)=b_e, \tag{6.43}$$

and at the wall,

$$U(0)=0, \tag{6.44}$$

$$\tilde{V}(0)=0, \tag{6.45}$$

$$B(0) = 0. \tag{6.46}$$

For the temperature condition at the wall, one can define either a "cold" wall condition:

$$T(0) = T_o, \tag{6.47}$$

or an insulated wall condition:

$$\frac{\partial T}{\partial Y} = 0. \tag{6.48}$$

This gives a system of 4 equations, with a total order of 7.

6.2.2 Method of Solution

The same package (COLNEW) was used successfully to solve the system of ordinary differential equations for various ratios of R_e/R_m. It was necessary to start with a value of R_e close to R_m, and to increase R_e progressively, using one solution as a starting point for the next.

6.2.3 Results and Conclusion

As expected the model shows that the wall singularity is eliminated. The density no longer goes to zero at the wall, and in the case of a thermally insulated wall, the wall temperature is finite. However this temperature is high, as is the heat flux to the wall in the case of a wall whose temperature is maintained constant ("cold" wall condition). In the case of an insulated wall, and in the limit where $\frac{R_e}{R_m} \rightarrow \infty$, the ratio of wall-to-plasma temperatures, T_w/T_e, and the ratio of plasma-to-wall densities, R_w/R_e, is proportional to the ratio $\sqrt{R_e/R_m}$.

Some examples of profiles are shown in figures 6-3 to 6-5. When the Reynolds number becomes large the magnetic boundary layer can be separated into two distinct regions: (i) the main magnetic boundary layer where the dominant terms are those described in the previous section and where the effects of momentum and heat transport are negligible, and (ii) an inner layer, close to the wall, where the heat and momentum transfer are significant. There the Ohmic heating and the viscous friction are balanced by the heat conduction. The size of this layer is small and the ratio of its width to the main magnetic boundary layer width is proportional to the square root of R_e/R_m.

The velocity inversion predicted in the previous section is sensitive to the presence of viscosity and heat conduction within the boundary layer. It is easily eliminated by even small amounts of viscosity. The critical value of $\frac{R_e}{R_m}$, for which the inversion disappears, falls in the interval [200,500].

In conclusion it has been shown that the presence of insulating surfaces downstream of a plasma containing a residual magnetic field will give rise to very intense local heating along the surface of the insulator. This heating is the result of the recovery of both the kinetic energy of the gas which is released by the mechanism of viscous friction and heat conduction, as well as the recovery of the residual electromagnetic energy, which is released by the mechanism of Ohmic heating. As a practical result, the designer should avoid placing insulating surfaces downstream of the electrodes or should attempt to reduce the residual electromagnetic field convected by the plasma so that it does not represent a significant part of the plasma kinetic energy at the point when it comes in contact with the insulator. Such an adiabatic expansion could be done by using divergent electrodes, in the manner suggested by [29] and [40].

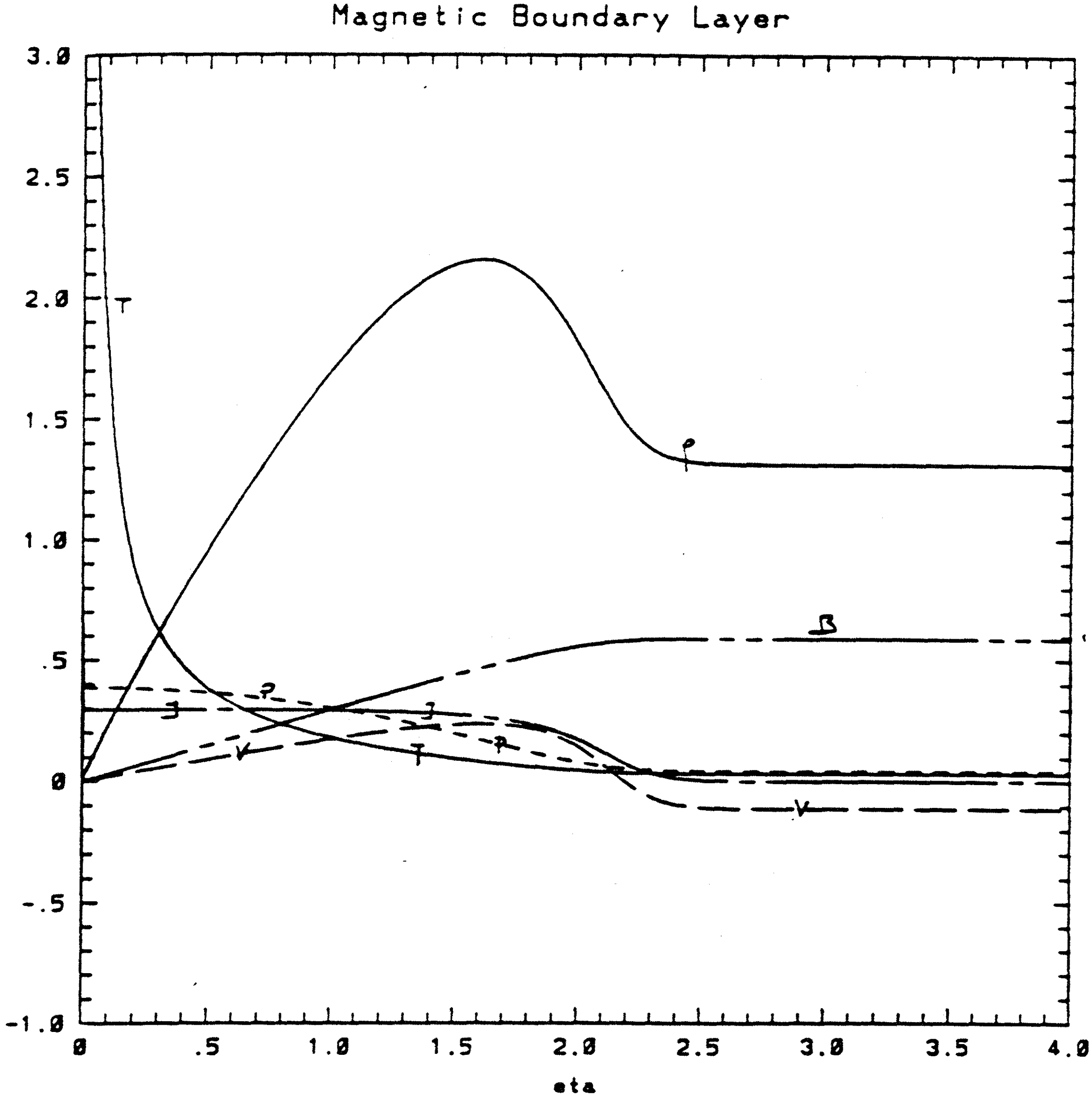

Figure 6-1: Magnetic boundary layer over a flat insulator for the conditions of table 6.1. The horizontal coordinate is η, the vertical coordinate indicates the values of R, the density; B, the magnetic field; P, the pressure; $\tilde{V}$, the normal velocity and T, the temperature.

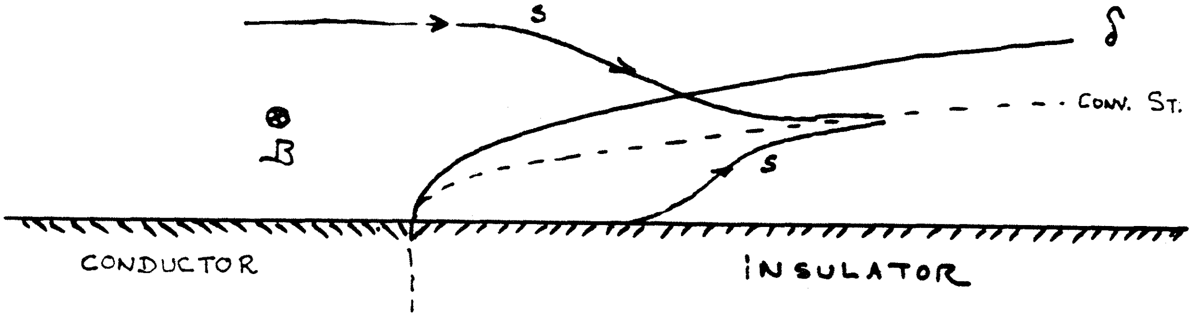

Figure 6-2: Structure of the magnetic boundary layer over a flat insulator showing the existence of a converging streamline.

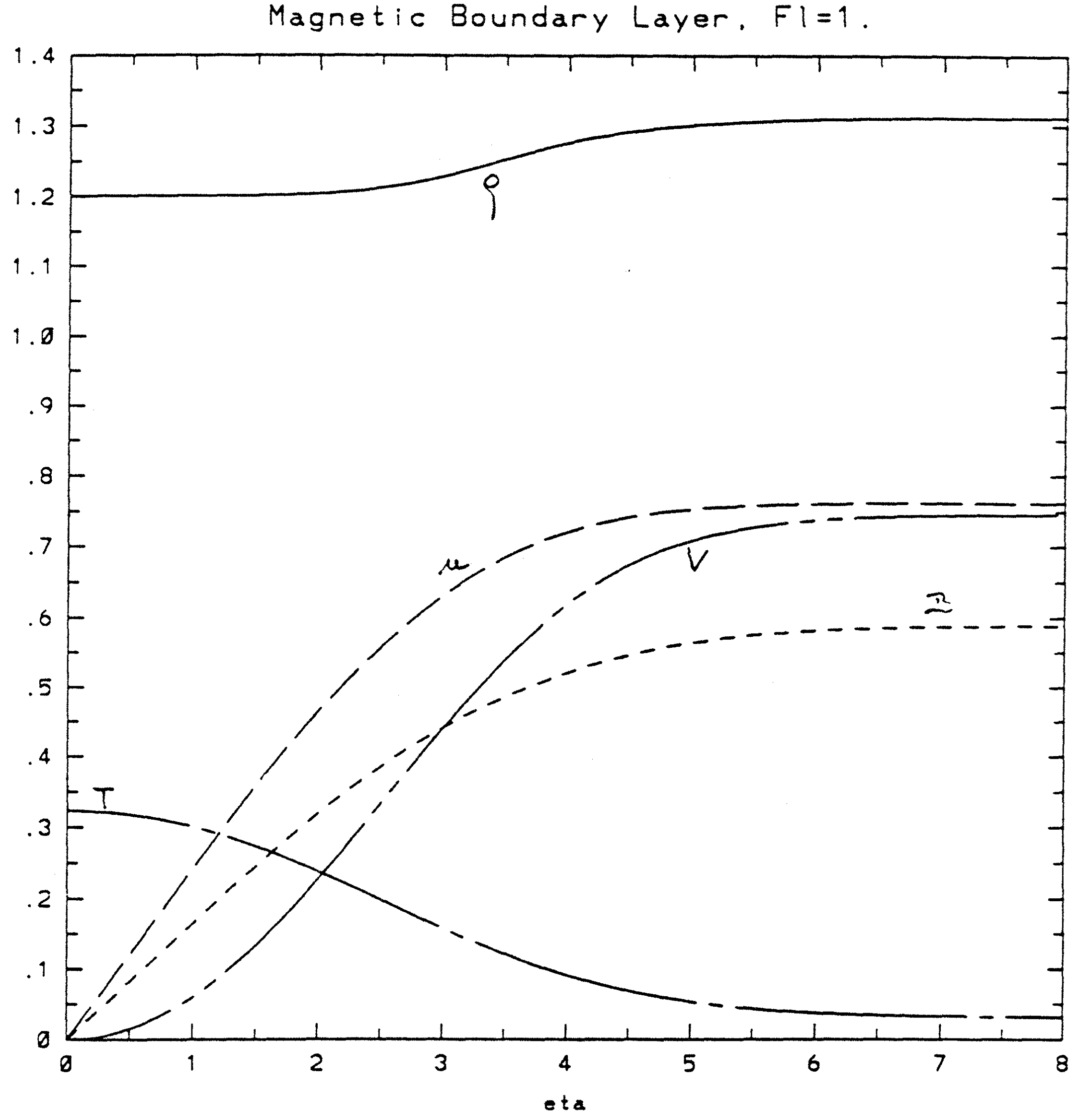

Figure 6-3: Magnetic boundary layer over a flat insulator in the presence of momentum and heat transport. $R_e/R_m = P_r = 1$. The magnetic boundary layer and the viscous layer are of the same scale. They cannot be distinguished.

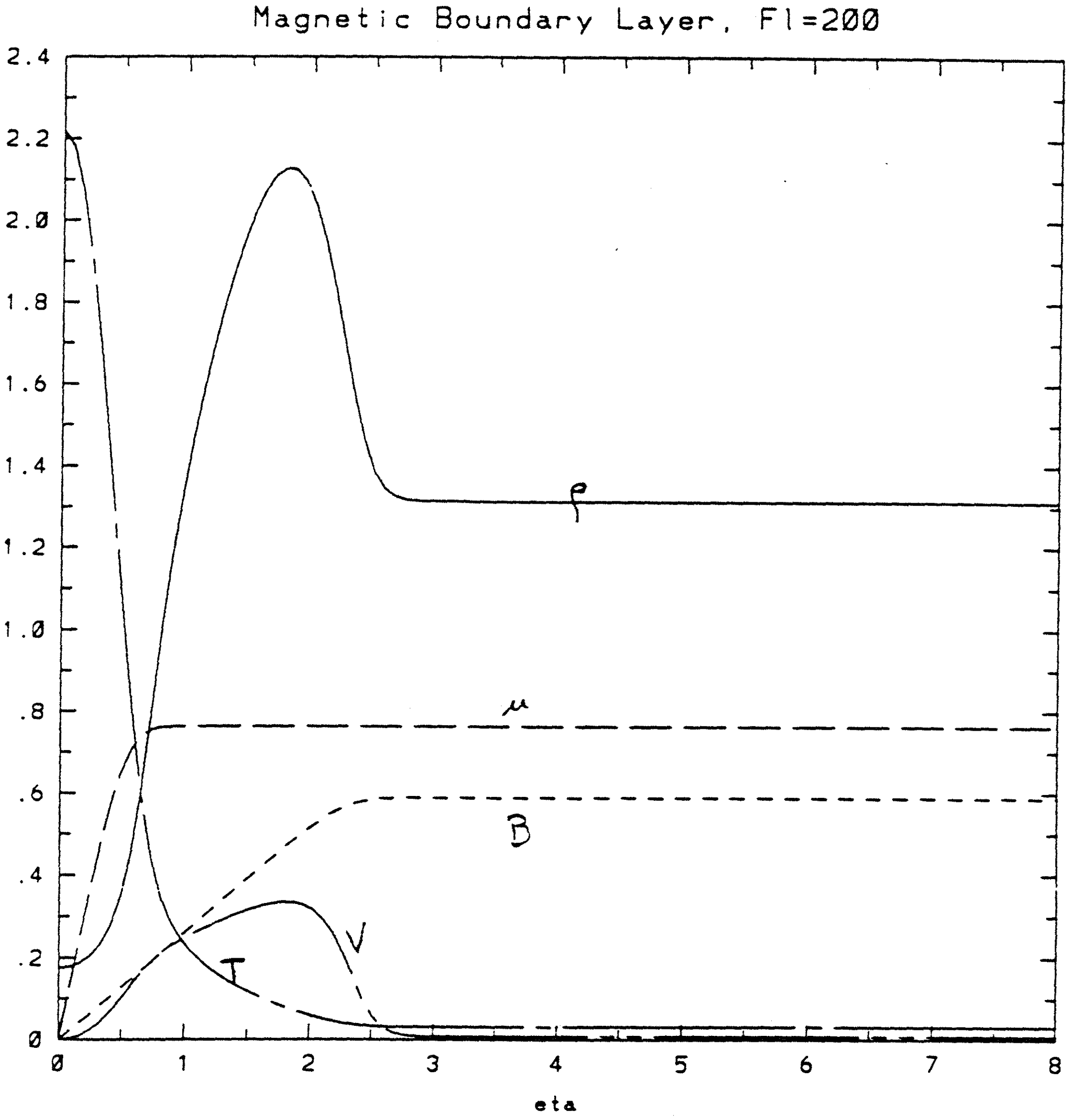

Figure 6-4: Magnetic boundary layer over a flat insulator in the presence of momentum and heat transport. $R_e/R_m = 200$, $P_r = 1$. The viscous sublayer is smaller than the magnetic layer and can be observed near the wall. The viscosity is too large for the normal-velocity inversion to appear.

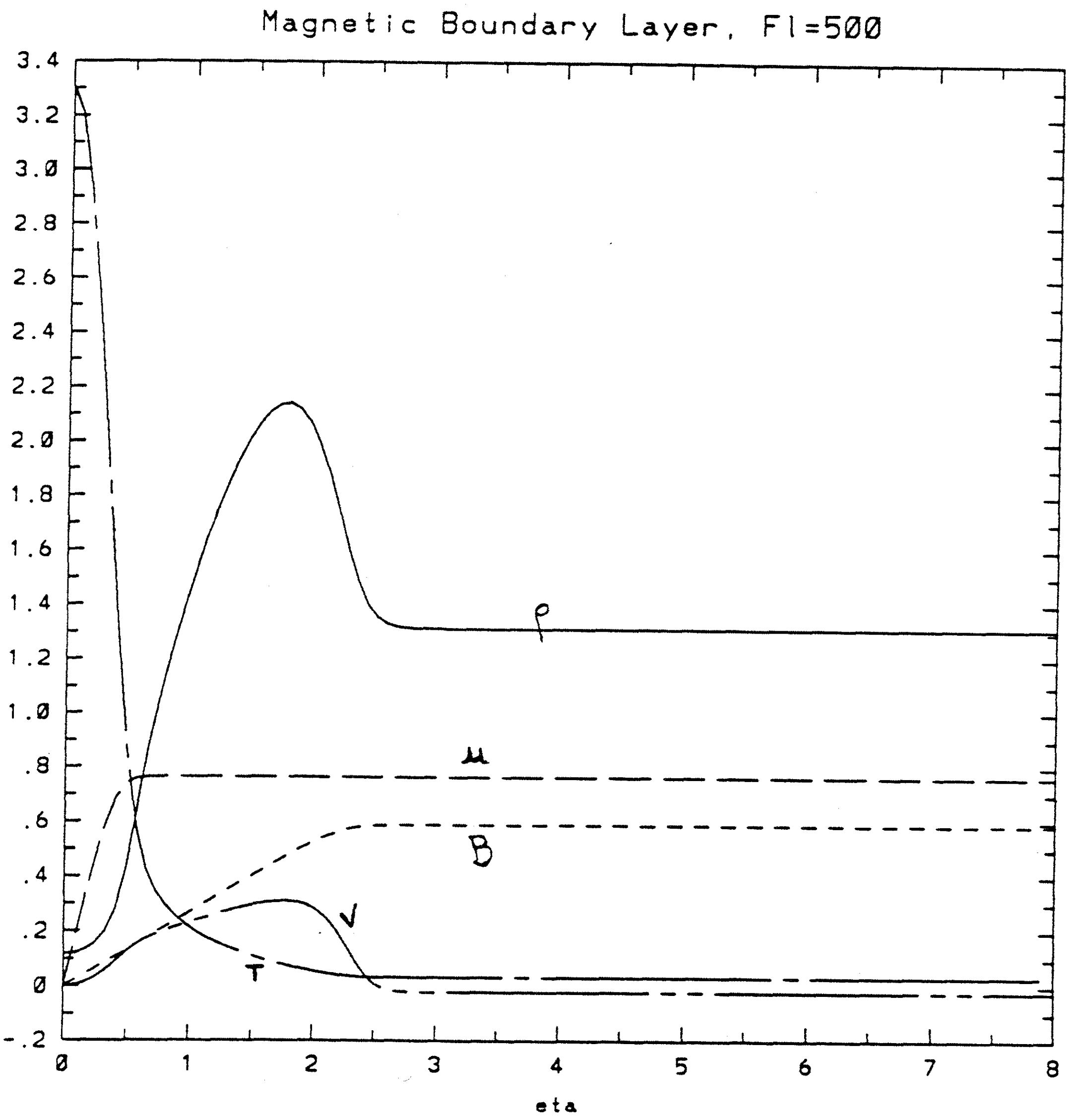

Figure 6-5: Magnetic boundary layer over a flat insulator in the presence of momentum and heat transport. $R_e/R_m = 500$, $P_r = 1$. The viscous sublayer is smaller than the magnetic layer and can be observed near the wall. The normal-velocity changes sign near $\eta = 2.5$ and $\tilde{V}(\infty) < 0$.

Chapter 7

General Conclusion and Achievements of this Research

This dissertation will be concluded by a summary of the principal results that have been found and by a series of suggestions for those who will attempt to further the theoretical study of Magneto-Dynamic thrusters.

7.1 Achievements of this Research

The object of this dissertation was to develop analytical tools for the understanding of the gas flow in magneto-dynamic thrusters. A magneto-hydro-dynamic model was chosen to describe the physical behavior of the thruster. From an analysis of previous work on one-dimensional models, the author found several questions which had remained unanswered, and which could not be answered by the simple one-dimensional model. These questions concerned the structure of the flow near the exit, the applicability of the one-dimensional model, and the effect of the Hall conductivity. Experiments have shown the existence of strong transverse gradients and there is a practical advantage in understanding their cause and consequences. More generally, very little is known of the distribution of density, velocity and temperature.

Although the complexity of the system of equations did not allow the author to give a comprehensive answer to these questions in the form of a general solution to the non-linear, two-dimensional problem, it was possible to find approximate solutions valid in the regime of high magnetic Reynolds numbers.

First, the inverse of the magnetic Reynolds number was used to define a singular perturbation. This method, which was used previously by Martinez-Sanchez [40] for the one-dimensional model, was extended to the case of two-dimensional flows. This method made it possible to separate the problem into several simpler problems, which interact by an appropriate matching process. A finite element code was written for the purpose of solving the outer problem describing the bulk of the plasma flow, based on an ideal magneto-hydrodynamic model. The results showed that a piecewise-linear triangulation was ill-suited to solve the problem which is strongly non-linear in the expansion region near the end of the thruster.

Second, a regular perturbation was used to obtain an idea of the flow structure both inside the thruster and in the region near the exit. This perturbation method has the advantage of being valid for any value of the magnetic Reynolds number. Its primary success is in providing a qualitative description of the features of the flow within the channel and around the exit.

The results of this research suggest that the principal difficulty of this magneto-hydro-dynamic model is the coupling between the magnetic field and the fluid dynamics. This can be expressed mathematically by a non-linear operator of fourth order (not given here). It is however possible to have an idea of the structure of this operator by looking at its linearized version around a constant background. The first implication of this analysis is that the usual mental concepts of fluid dynamics, intrinsically determined by a second order partial differential equation, are insufficient to encompass the behavior of the plasma, in particular the influence of the boundary conditions and the magnetic field diffusivity.

An important result of this research on the linearized flow approximation is that the effect of dissipation in the energy equation (Joule heating) disappears but the effect of magnetic diffusion is retained by the linearized operator. A practical consequence of this phenomenon is that when the linearized flow approximation is valid, the flow is nearly isentropic, despite the Joule heating and despite the theoretical suggestion of the non-resistive model that there is an infinite current concentration on the lips of the accelerator, and therefore, an infinite source of heat and of entropy.

An interesting property of the flow is the existence of nearly-isentropic expansion fans in the vicinity of the lips (corners) of the electrodes even when the conditions of linearized flow are not valid, that is when the non-linearities are included. This is however a local result, as the flow loses its isentropicity away from the corners.

This research confirmed the importance of the tensorial electric conductivity on the plasma behavior. In this model the Hall effect appears only through the boundary conditions applied to the problem. This does not prevent its effects from being felt rather drastically in regions of significant current flow, in particular near the exit. The results show the presence of strong density gradients in the direction perpendicular to the flow. The expected region of mass depletion near the anode was observed in the results. This analysis also suggests that the mass depletion, which appears along the anode, is in part a consequence of the intrinsic divergence of the channel. It also shows that the influence of the exit expansion is felt at large distances upstream of the exit plane, in particular in narrow channels. Therefore the author suggests that the condition[1]: $R_{m(h)} \gg 1$ should be used as a way to reach higher efficiencies. This points to designs of the type presented by Schoenberg *et al.* [52].

The phenomenon of current refraction in the expansion fans, which had not received much attention so far, was first noticed in the results of the linear analysis. It was explained as a consequence of the increase in the electromotive field across the expansion fan, and was later observed in many experimental reports.

Finally this research has shown that when the plasma flows along a flat insulator extending the length of the electrode, one should expect a high temperature near the insulator surface, as well as a high rate of heat transfer to the wall. Simultaneously the plasma density becomes very small near the insulator surface in order to maintain a finite pressure at the insulator surface despite the high temperature. It was noticed that the magnetic boundary layer is the seat of an uncommon phenomenon: an inversion of the normal velocity in the middle of the boundary layer. This inversion

---

[1] *i.e.* The magnetic Reynolds number based on the thruster height is large compared to one.

disappears when a small amount of viscosity is present in the fluid.

7.2 Suggestions for Future Work

A logical extension of this research would be to undertake the experimental verification of some of the phenomena predicted by this theory. Quantitative maps of the density and of the magnetic field in the exit region could be constructed using, respectively, interferometric techniques and Rogowski coils. The results could be used to verify the presence of the sonic fans and of the current refraction near the anode corner. In addition it would be useful to investigate the presence of expansion and compression patterns in the plume, including the presence of current loops. Finally a systematic series of tests with different inter-electrode distances should be undertaken in order to verify the effect of narrowing the channel height.

In addition several extensions to the theory can be undertaken. The linear analysis shows that, under the influence of the Hall effect, the transverse gradients are considerable, even when the incoming flow is assumed to be uniform. But the Hall effect also has an influence on the inlet acceleration layer. Unfortunately this problem cannot be solved by the regular perturbation method used for the divergent section since it is fully non-linear and two-dimensional. The interaction between the Hall effect and the acceleration layer is expected to create a density stratification parallel to the electrode surface, and this will reinforce the species depletion along the anode. In order to solve this problem a non-linear solution must be found. Such an analysis should be based on the magneto-hydro-dynamic model including the Hall effect. The author suggests attempting to solve the problem using the method of integral relations, which reduces the two-dimensional problem to a small number of one-dimensional problems which could be integrated numerically.

The next step should be to incorporate the viscosity in the model. This would give a better estimate of the overall efficiency of the thruster, since as Niewood and Martinez-Sanchez pointed out in [47], it is a significant loss factor. Finally, when these problems are solved reliably, it will then be possible to proceed to the next logical step, namely the study of the dynamic stability of the flow, which is of importance for both the practical applications and the numerical simulation of these devices.

Appendix A

Derivation of the Model Equations

A.1 Generalities

The equations describing the model are derived from the general magneto-hydrodynamic approximation which includes the following equations: conservation of mass, momentum, and energy in the inviscid fluid, the Ohm's law (derived from the electron momentum conservation), and the quasi-static Maxwell's equations. These equations can be written[1]:

$$\partial_t(\rho) + \nabla(\rho \mathbf{u}) = 0, \tag{A.1}$$

$$\partial_t(\rho \mathbf{u}) + \mathbf{Div}(\rho \overline{\overline{\mathbf{u}\mathbf{u}}} + \overline{\overline{\mathbf{P}}}) = \mathbf{J} \times \mathbf{B}, \tag{A.2}$$

$$\partial_t(\frac{1}{2}\rho u^2 + \frac{P}{\gamma - 1}) + \nabla \cdot \left(\mathbf{u}(\frac{1}{2}\rho u^2 + \frac{\gamma}{\gamma - 1}P)\right) = \mathbf{J} \cdot \mathbf{E}, \tag{A.3}$$

$$\nabla \times \mathbf{E} + \partial_t \mathbf{B} = 0, \tag{A.4}$$

$$\nabla \cdot \mathbf{B} = 0, \tag{A.5}$$

$$\nabla \times \mathbf{B} = \mu_o \mathbf{J}, \tag{A.6}$$

$$\mathbf{E} + \mathbf{u} \times \mathbf{B} = \frac{\mathbf{J}}{\sigma} + \frac{\mathbf{J} \times \mathbf{B}}{e n_e}. \tag{A.7}$$

---

[1] In this appendix all the variables have their usual dimensions. The dimensionless quantities are introduced in the next appendix.

We will now go through them more systematically and carry out simplifications, finally obtaining the equations of our model.

A.2 Momentum Conservation

The momentum conservation equation,

$$\partial_t(\rho \mathbf{u}) + \mathbf{Div}(\rho\overline{\overline{\mathbf{u}\mathbf{u}}} + \overline{\overline{\mathbf{P}}}) = \mathbf{F}, \tag{A.8}$$

includes the effect of the electromagnetic body force **F** (in Newtons per meter cubed) on the fluid. On a microscopic scale the force on the particle (j) is:

$$\mathbf{f}_j = q_j(\mathbf{E} + \mathbf{v}_j \times \mathbf{B}). \tag{A.9}$$

On a macroscopic scale the force per unit volume is then:

$$\mathbf{F} = \Sigma_s n_s q_s(\mathbf{E} + \mathbf{v}_s \times \mathbf{B}), \tag{A.10}$$

$$\mathbf{F} = (\Sigma_s n_s q_s)\mathbf{E} + (\Sigma_s n_s q_s \mathbf{v}_s) \times \mathbf{B}. \tag{A.11}$$

If one assumes quasi-neutrality of the plasma, $\Sigma_s n_s q_s = 0$, then:

$$\mathbf{F} = (n_e q_e \mathbf{v}_e + n_i q_i \mathbf{v}_i) \times \mathbf{B}, \tag{A.12}$$

$$\mathbf{F} = \mathbf{J} \times \mathbf{B}. \tag{A.13}$$

Using Maxwell's equation, $\nabla \times \mathbf{B} = \mu_0 \mathbf{J}$, we have:

$$\mathbf{F} = \frac{1}{\mu_0}(\nabla \times \mathbf{B}) \times \mathbf{B}. \tag{A.14}$$

Using cartesian tensor notation this becomes:

$$F_i = \frac{1}{\mu_0}\epsilon_{ijk}\epsilon_{jlm}\nabla_l(B_m)B_k,$$

$$F_i = \frac{1}{\mu_0}(\delta_{kl}\delta_{im} - \delta_{km}\delta_{li})\nabla_l(B_m)B_k,$$

$$F_i = \frac{1}{\mu_0}(\nabla_k(B_i)B_k - \nabla_l(B_k)B_k),$$

$$F_i = \frac{1}{\mu_0}\nabla_j(B_iB_j - \frac{1}{2}\delta_{ij}B_kB_k),$$

$$F_i = \frac{\partial T_{ij}}{\partial x_j}, \tag{A.15}$$

with:

$$T_{ij} = \frac{1}{\mu_0}(B_iB_j - \frac{1}{2}\delta_{ij}B_kB_k). \tag{A.16}$$

In conclusion we observe that the body force $\mathbf{F} = \mathbf{J} \times \mathbf{B}$ can be expressed as the divergence of the Maxwell stress tensor. For a one-fluid MHD model the momentum equation:

$$\frac{\partial}{\partial t}\rho u_i + \frac{\partial}{\partial x_j}(\rho u_i u_j + \delta_{ij}P) = (J \times B)_i, \tag{A.17}$$

can be transformed into a conservative equation. In cartesian tensor notation it takes the following form:

$$\frac{\partial}{\partial t}\rho u_i + \frac{\partial}{\partial x_j}(\rho u_i u_j + \delta_{ij}P + \frac{1}{2\mu_o}\delta_{ij}B_kB_k - \frac{1}{\mu_o}B_iB_j) = 0. \tag{A.18}$$

Since the body force disappears from the momentum equation, we can use the momentum theorem [7] to calculate the thrust. The force exerted by the fluid on the thruster is (neglecting the fluid viscosity):

$$F_i = -\iint_{S_o}(\rho\, u_i\, u_j + \delta_{ij}P + \frac{1}{2\mu_o}\delta_{ij}B_kB_k - \frac{1}{\mu_o}B_iB_j)n_j dS, \tag{A.19}$$

where S_o is any surface completely surrounding the thruster.

In cartesian tensor notation, using the simplifications proper to our geometry, we have the following physical components for the generalized momentum tensor:

$$\Pi = \begin{pmatrix} \Pi_{xx} & \Pi_{xy} & \Pi_{xz} \\ \Pi_{yx} & \Pi_{yy} & \Pi_{yz} \\ \Pi_{zx} & \Pi_{zy} & \Pi_{zz} \end{pmatrix} = \begin{pmatrix} \rho u_x^2 + P + \frac{B_z^2}{2\mu_o} & \rho u_x u_y & 0 \\ \rho u_x u_y & \rho u_y^2 + P + \frac{B_z^2}{2\mu_o} & 0 \\ 0 & 0 & P - \frac{B_z^2}{2\mu_o} \end{pmatrix}, \tag{A.20}$$

and the momentum equation becomes:

$$\partial_t(\rho \mathbf{u}) + \mathbf{Div}(\mathbf{\Pi}) = \mathbf{F}, \tag{A.21}$$

that is:

$$\frac{\partial}{\partial t}(\rho u_x) + \frac{\partial}{\partial x}(\Pi_{xx}) + \frac{\partial}{\partial y}(\Pi_{xy}) = 0, \tag{A.22}$$

$$\frac{\partial}{\partial t}(\rho u_y) + \frac{\partial}{\partial x}(\Pi_{yx}) + \frac{\partial}{\partial y}(\Pi_{yy}) = 0. \tag{A.23}$$

In this case, the x-component of the thrust is then:

$$F_x = -\iint_{S_o} (\Pi_{xx} n_x + \Pi_{xy} n_y) dS, \tag{A.24}$$

where S_o is a closed surface surrounding the thruster, and $\mathbf{n} = (n_x, n_y, 0)$ is the local normal to S_o. If S_o is a plane surface, normal to the x-axis and located downstream from the thruster exit, the x-component of the thrust becomes:

$$F_x = -\int\int_{S_o} (\Pi_{xx}) n_x dS. \tag{A.25}$$

A.3 Energy Conservation

The energy conservation for the plasma can be written as:

$$\partial_t(E_i + E_k) + \nabla \cdot (\mathbf{u}(E_i + E_k + P)) = S, \tag{A.26}$$

where S is the electric energy per unit volume, where $\overline{\overline{\overline{P}}} = m_s n_s < \mathbf{c_s c_s} >$ is the pressure stress tensor, $E_i = \rho e_i$ is the internal energy per unit volume, $E_k = \frac{1}{2}\rho u^2$ is the kinetic energy per unit volume and P is the pressure.

The energy transferred to each particle per unit time by the magnetic field is

$$\mathbf{f}_j \cdot \mathbf{v}_j = q_j(\mathbf{E} + \mathbf{v}_j \times \mathbf{B}) \cdot \mathbf{v}_j = q_j\mathbf{v}_j \cdot \mathbf{E} + [\mathbf{v}_j, \mathbf{B}, \mathbf{v}_j] = q_j\mathbf{v}_j \cdot \mathbf{E}. \tag{A.27}$$

On a macroscopic scale the energy per unit volume is then:

$$S = \Sigma_s n_s q_s \mathbf{v}_s \cdot \mathbf{E} = \mathbf{J} \cdot \mathbf{E}. \tag{A.28}$$

Assuming a one-fluid Ohm's law of the form:

$$\mathbf{E} + \mathbf{u} \times \mathbf{B} = \frac{\mathbf{J}}{\sigma} + \frac{\mathbf{J} \times \mathbf{B}}{en_e}, \tag{A.29}$$

the $\mathbf{J} \cdot \mathbf{E}$ term can be written as,

$$\mathbf{J} \cdot \mathbf{E} = \mathbf{J} \cdot (\frac{\mathbf{J}}{\sigma} + \frac{\mathbf{J} \times B}{en_e} - \mathbf{u} \times \mathbf{B}) = \frac{\mathbf{J}^2}{\sigma} + [\mathbf{u}, \mathbf{J}, \mathbf{B}]. \tag{A.30}$$

The terms on the right are respectively: Ohmic heating and the electro-magnetic power. The $\mathbf{J} \cdot \mathbf{E}$ term can also be written in a conservative form using the Poynting equation,

$$\mathbf{J} \cdot \mathbf{E} = \frac{1}{\mu_o}\nabla(\mathbf{E} \times \mathbf{B}) - \frac{\partial}{\partial t}(\frac{B^2}{2\mu_o} + \frac{\epsilon_o E^2}{2}). \tag{A.31}$$

In our case we can use the magneto-quasi-static approximation where $\frac{B^2}{2\mu_o} \gg \frac{\epsilon_o E^2}{2}$, and we can incorporate $\mathbf{J} \cdot \mathbf{E}$ into the left hand side of the equation:

$$\partial_t(E_{em} + E_i + E_k) + \nabla \cdot \left((E_i + E_k + P)\mathbf{u} + \frac{\mathbf{E} \times \mathbf{B}}{\mu_o}\right) = 0, \tag{A.32}$$

where $E_{em} = \frac{B^2}{2\mu_o}$ is the electromagnetic energy per unit volume and $\frac{\mathbf{E} \times \mathbf{B}}{\mu_o}$ is the Poynting vector. The energy equation is completed by a state equation relating the pressure to the internal energy. For instance for a perfect gas we would have,

$$P = (\gamma - 1)\rho e_i. \tag{A.33}$$

For a perfect gas the energy equation becomes, with the Poynting transformation:

$$\partial_t(\frac{1}{2}\rho u^2 + \frac{P}{\gamma-1} + \frac{B^2}{2\mu_o}) + \nabla \cdot \left(\mathbf{u}(\frac{1}{2}\rho u^2 + \frac{\gamma}{\gamma-1}P) + \frac{\mathbf{E}\times\mathbf{B}}{\mu_o}\right) = 0. \tag{A.34}$$

Without the Poynting transformation one obtains a non-conservative form:

$$\partial_t(\frac{1}{2}\rho u^2 + \frac{P}{\gamma-1}) + \nabla \cdot \left(\mathbf{u}(\frac{1}{2}\rho u^2 + \frac{\gamma}{\gamma-1}P)\right) = \mathbf{J}\cdot\mathbf{E}. \tag{A.35}$$

Using Ohm's law (A.29) the Poynting vector $\frac{\mathbf{E}\times\mathbf{B}}{\mu_o}$ can be separated into a convective and a dissipative part:

$$\frac{\mathbf{E}\times\mathbf{B}}{\mu_o} = (-\mathbf{u}\times\mathbf{B} + \frac{\mathbf{J}}{\sigma} + \frac{\mathbf{J}\times\mathbf{B}}{e\,n_e}) \times \frac{\mathbf{B}}{\mu_o}. \tag{A.36}$$

The energy equation can then be written in conservative form. If σ and n_e are constant then:

$$\partial_t(\frac{1}{2}\rho u^2 + \frac{P}{\gamma-1} + \frac{B^2}{2\mu_o}) + \nabla \cdot \left(\mathbf{u}(\frac{1}{2}\rho u^2 + \frac{\gamma}{\gamma-1}P + \frac{B^2}{\mu_o})\right) = \frac{1}{\sigma\mu_0^2}\nabla\cdot(B\times(\nabla\times B)). \tag{A.37}$$

Similarly the non-conservative form for the energy equation can be broken into a convective and a dissipative part:

$$\partial_t(\frac{1}{2}\rho u^2 + \frac{P}{\gamma-1}) + \nabla \cdot \left(\mathbf{u}(\frac{1}{2}\rho u^2 + \frac{\gamma}{\gamma-1}P)\right) + \frac{1}{\mu_o}(\mathbf{u}\times\mathbf{B})\cdot(\nabla\times\mathbf{B}) = \frac{1}{\mu_o^2\sigma}(\nabla\times\mathbf{B})^2. \tag{A.38}$$

For a cartesian geometry with $\mathbf{B} = B\mathbf{e_z}$ we have:

$$\partial_t(\frac{1}{2}\rho u^2 + \frac{P}{\gamma-1}) + \nabla \cdot \left(\mathbf{u}(\frac{1}{2}\rho u^2 + \frac{\gamma}{\gamma-1}P)\right) + \frac{1}{\mu_o}(\mathbf{u}\cdot\nabla)\frac{B^2}{2} = \frac{1}{\mu_o^2\sigma}(\nabla B)^2. \tag{A.39}$$

For a real gas we would need to account for the effect of ionization. At equilibrium the ionization fractions can be calculated by the Saha equation. However the gas does not reach equilibrium and the ionization level departs significantly from the level predicted by Saha's equilibrium. The full set of equations is difficult to solve and some very crude assumptions need to be made in order to carry the calculations through.

A.4 Magnetic Field

In the magneto-quasi-static limit Maxwell's equations reduce to:

$$\begin{aligned} \nabla \times \mathbf{E} + \partial_t \mathbf{B} &= 0, \qquad \nabla \cdot \mathbf{B} = 0, \\ \nabla \times \mathbf{B} &= \mu_o \mathbf{J}. \end{aligned} \tag{A.40}$$

We have assumed that the field is quasi-static and that the plasma is approximately neutral. The equations are combined with the Ohm's law A.29 in order to eliminate **E** and **J**. We obtain an equation for **B** which describes the diffusion and convection of the magnetic field in a conducting medium:

$$\partial_t \mathbf{B} + \nabla \times \left(-\mathbf{u} \times \mathbf{B} + \frac{\nabla \times \mathbf{B}}{\mu_o \sigma} + \frac{(\nabla \times \mathbf{B}) \times \mathbf{B}}{\mu_o e n_e} \right) = 0. \tag{A.41}$$

We neglect the last two terms of the equation, which represent the Hall effect and the electron diffusion terms. In a self-field accelerator there is no externally imposed magnetic field. The magnetic field is only generated by the current flowing through the medium. As a result there is only one component for the magnetic field.

If we consider a two-dimensional cartesian flow in the plane (x, y), this non-zero component of the magnetic field is in the direction z.

A.5 Summary of the Equations

A.5.1 Conservative Forms

We have written below the final equation set after taking into account the simplifications mentioned above. The equations are in cartesian coordinates. The magnetic field is $\mathbf{B} = (0, 0, b)$.

Mass Conservation:

$$\frac{\partial}{\partial t}(\rho)+\frac{\partial}{\partial x}(\rho u_x)+\frac{\partial}{\partial y}(\rho u_y)=0. \tag{A.42}$$

Momentum Conservation:

$$\frac{\partial}{\partial t}(\rho u_x)+\frac{\partial}{\partial x}\left(\rho u_x u_x+P+\frac{B^2}{2\mu_o}\right)+\frac{\partial}{\partial y}(\rho u_x u_y)=0. \tag{A.43}$$

$$\frac{\partial}{\partial t}(\rho u_y)+\frac{\partial}{\partial x}(\rho u_x u_y)+\frac{\partial}{\partial y}\left(\rho u_y u_y+P+\frac{B^2}{2\mu_o}\right)=0. \tag{A.44}$$

Energy Conservation:

$$\frac{\partial}{\partial t}\left(\frac{1}{\gamma-1}P+\frac{1}{2}\rho u^2+\frac{B^2}{2\mu_o}\right)$$

$$+\frac{\partial}{\partial x}\left(u_x\left(\frac{\gamma}{\gamma-1}P+\frac{1}{2}\rho u^2+\frac{B^2}{\mu_o}\right)\right)+\frac{\partial}{\partial y}\left(u_y\left(\frac{\gamma}{\gamma-1}P+\frac{1}{2}\rho u^2+\frac{B^2}{\mu_o}\right)\right)=$$

$$\frac{1}{2\mu_o^2\sigma}\left(\frac{\partial^2 B^2}{\partial x^2}+\frac{\partial^2 B^2}{\partial y^2}\right). \tag{A.45}$$

Magnetic Field Conservation:

$$\frac{\partial B}{\partial t}+\frac{\partial}{\partial x}(u_x B)+\frac{\partial}{\partial y}(u_y B)=\frac{1}{\mu_o\sigma}\left(\frac{\partial^2 B}{\partial x^2}+\frac{\partial^2 B}{\partial y^2}\right). \tag{A.46}$$

Electric Field Equation:

$$\mathbf{E}=-\mathbf{u}\times\mathbf{B}+\frac{\nabla\times\mathbf{B}}{\mu_o\sigma}+\frac{(\nabla\times\mathbf{B})\times\mathbf{B}}{\mu_o e n_e}. \tag{A.47}$$

A.5.2 Non-Conservative forms

We can still simplify these equations, at the expense of losing their conservative form. They can be written, neglecting the Hall effect as:

Mass Conservation:

$$\frac{\partial}{\partial x}(\rho u_x)+\frac{\partial}{\partial y}(\rho u_y)=0. \tag{A.48}$$

Momentum Conservation:

$$\rho u_x \frac{\partial u_x}{\partial x} + \rho u_y \frac{\partial u_x}{\partial y} + \frac{\partial}{\partial x}(P + \frac{B^2}{2\mu_o}) = 0, \tag{A.49}$$

$$\rho u_x \frac{\partial u_y}{\partial x} + \rho u_y \frac{\partial u_y}{\partial y} + \frac{\partial}{\partial y}(P + \frac{B^2}{2\mu_o}) = 0. \tag{A.50}$$

Energy Conservation:

$$\rho^\gamma u_x \frac{\partial}{\partial x}(\frac{P}{\rho^\gamma}) + \rho^\gamma u_y \frac{\partial}{\partial y}(\frac{P}{\rho^\gamma}) = \frac{\gamma - 1}{\mu_o^2 \sigma}\{(\frac{\partial B}{\partial x})^2 + (\frac{\partial B}{\partial y})^2\}. \tag{A.51}$$

Magnetic Field Conservation:

$$\rho u_x \frac{\partial}{\partial x}(\frac{B}{\rho}) + \rho u_y \frac{\partial}{\partial y}(\frac{B}{\rho}) = \frac{1}{\mu_o \sigma}\{\frac{\partial^2 B}{\partial x^2} + \frac{\partial^2 B}{\partial y^2}\}. \tag{A.52}$$

Electric Field Equations:

$$E_x = -u_y B + \frac{1}{\sigma\ \mu_0}\frac{\partial B}{\partial y} - \frac{1}{\mu_0\ e\ n_e} B \frac{\partial B}{\partial x}, \tag{A.53}$$

$$E_y = u_x B - \frac{1}{\sigma\ \mu_0}\frac{\partial B}{\partial x} - \frac{1}{\mu_0\ e\ n_e} B \frac{\partial B}{\partial y}. \tag{A.54}$$

A.6 Equations Including Heat and Momentum Transport

The expression of the equations with heat and momentum transport included are given here.

Mass Conservation:

$$\frac{\partial}{\partial x}(\rho u_x) + \frac{\partial}{\partial y}(\rho u_y) = 0. \tag{A.55}$$

Momentum Conservation:

$$\rho u_x \frac{\partial u_x}{\partial x} + \rho u_y \frac{\partial u_x}{\partial y} + \frac{\partial}{\partial x}(P + \frac{B^2}{2\mu_o}) = \mu \left(2\frac{\partial^2 u_x}{\partial x^2} + \frac{\partial^2 u_x}{\partial y^2} + \frac{\partial^2 u_y}{\partial x \partial y} + \frac{\lambda}{\mu}\frac{\partial}{\partial x}\ \mathrm{div}\ \mathbf{u} \right), \tag{A.56}$$

$$\rho u_x \frac{\partial u_y}{\partial x} + \rho u_y \frac{\partial u_y}{\partial y} + \frac{\partial}{\partial y}(P + \frac{B^2}{2\mu_o}) = \mu \left(2\frac{\partial^2 u_y}{\partial y^2} + \frac{\partial^2 u_y}{\partial x^2} + \frac{\partial^2 u_x}{\partial x \partial y} + \frac{\lambda}{\mu}\frac{\partial}{\partial y}\,\mathbf{div\ u} \right). \tag{A.57}$$

Energy Conservation:

$$\frac{1}{\gamma - 1}\left\{ \rho^\gamma u_x \frac{\partial}{\partial x}(\frac{P}{\rho^\gamma}) + \rho^\gamma u_y \frac{\partial}{\partial y}(\frac{P}{\rho^\gamma}) \right\} = \tag{A.58}$$

$$\frac{1}{\sigma \mu_o^2}\left\{ \left(\frac{\partial B}{\partial x}\right)^2 + \left(\frac{\partial B}{\partial y}\right)^2 \right\} + k\left\{ \frac{\partial^2 T}{\partial x^2} + \frac{\partial^2 T}{\partial y^2} \right\} \tag{A.59}$$

$$+\mu \left\{ 2\left(\frac{\partial u_x}{\partial x}\right)^2 + 2\left(\frac{\partial u_y}{\partial y}\right)^2 + \left(\frac{\partial u_x}{\partial y} + \frac{\partial u_y}{\partial x}\right)^2 + \frac{\lambda}{\mu}\left(\frac{\partial u_x}{\partial x} + \frac{\partial u_y}{\partial y}\right)^2 \right\}. \tag{A.60}$$

Magnetic Field Conservation:

$$\rho u_x \frac{\partial}{\partial x}(\frac{B}{\rho}) + \rho u_y \frac{\partial}{\partial y}(\frac{B}{\rho}) = \frac{1}{\mu_o \sigma}\{ \frac{\partial^2 B}{\partial x^2} + \frac{\partial^2 B}{\partial y^2} \}. \tag{A.61}$$

Electric Field Equations:

$$E_x = -u_y B + \frac{1}{\sigma\ \mu_0}\frac{\partial B}{\partial y} - \frac{1}{\mu_0\ e\ n_e} B \frac{\partial B}{\partial x}, \tag{A.62}$$

$$E_y = u_x B - \frac{1}{\sigma\ \mu_0}\frac{\partial B}{\partial x} - \frac{1}{\mu_0\ e\ n_e} B \frac{\partial B}{\partial y}. \tag{A.63}$$

Appendix B

Non-Dimensional Forms

B.1 Non-Dimensional Parameters

Starting from the equations in non-conservative form:

$$\partial_t \rho + \mathrm{div}(\rho \mathbf{u}) = 0, \tag{B.1}$$

$$\rho(\partial_t + \mathbf{u} \cdot \nabla)\mathbf{u} + \nabla(P + \frac{B^2}{2\mu_o}) = 0, \tag{B.2}$$

$$\frac{1}{\gamma - 1}\rho^\gamma(\partial_t + \mathbf{u} \cdot \nabla)\left(\frac{P}{\rho^\gamma}\right) = \frac{1}{\mu_o \sigma}(\nabla B)^2, \tag{B.3}$$

$$\partial_t B - \nabla \times (\mathbf{u} \times B) = \frac{1}{\mu_o \sigma}\nabla \times (\nabla \times B), \tag{B.4}$$

$$\mathbf{E} = -\mathbf{u} \times \mathbf{B} + \frac{\nabla \times \mathbf{B}}{\mu_o \sigma} + \frac{(\nabla \times \mathbf{B}) \times \mathbf{B}}{\mu_o e n_e}, \tag{B.5}$$

we introduce the following non-dimensional variables:

$$\rho^* = \frac{\rho}{\rho_{ref}}, \tag{B.6}$$

$$u^* = \frac{u}{u_{ref}}, \tag{B.7}$$

$$p^* = \frac{P}{P_{ref}}, \tag{B.8}$$

$$b^* = \frac{B}{B_{ref}}, \tag{B.9}$$

$$t^* = \frac{t\ u_{ref}}{L_{ref}}, \tag{B.10}$$

$$x^* = \frac{x}{L_{ref}}, \tag{B.11}$$

$$e^* = \frac{E}{u_{ref} B_{ref}}. \tag{B.12}$$

After substitution in the system we obtain:

$$\partial_t^* \rho^* + \operatorname{div}^*(\rho^* \mathbf{u}^*) = 0, \tag{B.13}$$

$$\rho^*(\partial_t^* + \mathbf{u}^* \cdot \nabla^*)\mathbf{u}^* + \left(\frac{p_{ref}}{\rho_{ref} u_{ref}^2}\right) \nabla^*(p^*) + \left(\frac{b_{ref}^2}{2\rho_{ref} u_{ref}^2 \mu_o}\right) \nabla^*(b^{*2}) = 0, \tag{B.14}$$

$$\frac{1}{\gamma - 1}\rho^{*\gamma}(\partial_t^* + \mathbf{u}^* \cdot \nabla^*)\left(\frac{p^*}{\rho^{*\gamma}}\right) = \left(\frac{b_{ref}^2}{\mu_o^2 \sigma p_{ref} u_{ref}}\right)(\nabla^* b^*)^2, \tag{B.15}$$

$$\rho^*(\partial_t^* + \mathbf{u}^* \cdot \nabla^*)\left(\frac{b^*}{\rho^*}\right) = \left(\frac{1}{\mu_o \sigma u_{ref} L_{ref}}\right) \nabla^{*2} b^*, \tag{B.16}$$

$$\mathbf{e}^* = -\mathbf{u}^* \times \mathbf{b}^* + \frac{1}{\mu_o \sigma u_{ref} L_{ref}} \nabla \times \mathbf{b}^* + \frac{\frac{B_{ref}}{e\ n_e},}{\mu_o u_{ref} L_{ref}}(\nabla \times \mathbf{b}^*) \times \mathbf{b}^*. \tag{B.17}$$

Using the reference parameters:

$$M_{a_{ref}}^2 = \frac{\rho_{ref} u_{ref}^2}{\gamma P_{ref}}, \tag{B.18}$$

$$\beta_{ref} = \frac{2\mu_o P_{ref}}{B_{ref}^2}, \tag{B.19}$$

$$R_m = \mu_o \sigma u_{ref} L_{ref}, \tag{B.20}$$

$$H_a = \omega_{ce}\ \tau_e = \frac{\sigma B_{ref}}{e\ n_e}, \tag{B.21}$$

where M_a is the Mach number, β is the plasma-β, R_m is the magnetic Reynolds number and H_a is the Hall parameter, we can rewrite the equations the following way:

$$\partial_{t^*} \rho^* + \operatorname{div}^*(\rho^* \mathbf{u}^*) = 0, \tag{B.22}$$

$$\rho^*(\partial_t^* + \mathbf{u}^* \cdot \nabla^*)\mathbf{u}^* + \left(\frac{1}{\gamma M_{a_{ref}}^2}\right) \nabla^*(p^*) + \left(\frac{1}{\beta\gamma M_{a_{ref}}^2}\right) \nabla^*(b^{*2}) = 0, \tag{B.23}$$

$$\frac{1}{\gamma - 1}\rho^{*\gamma}(\partial_t^* + \mathbf{u}^* \cdot \nabla^*) \left(\frac{p^*}{\rho^{*\gamma}}\right) = \left(\frac{1}{R_m\beta\gamma M_{a_{ref}}^2}\right) (\nabla^* b^*)^2, \tag{B.24}$$

$$\rho^*(\partial_t^* + \mathbf{u}^* \cdot \nabla^*) \left(\frac{b^*}{\rho^*}\right) = \frac{1}{R_m}\nabla^{*2} b^*, \tag{B.25}$$

$$\mathbf{e}^* = -\mathbf{u}^* \times \mathbf{b}^* + \frac{1}{R_m}\nabla \times \mathbf{b}^* + \frac{H_a}{R_m}(\nabla \times \mathbf{b}^*) \times \mathbf{b}^*. \tag{B.26}$$

We can justify the existence of two modes of acceleration with an argument based on the ordering of the various terms which appear in these equations.

B.2 Electrothermal Regime

In the electrothermal regime we expect the gas to be heated by the current and then go through a pressure-driven expansion. In the momentum equation we expect the kinetic term $\rho(\mathbf{u} \cdot \nabla)\mathbf{u}$ to balance the pressure term $\frac{1}{\gamma M_a^2}\nabla p$, so that $\frac{1}{\gamma M_a^2}$ must be of order one. We also expect the magnetic term to be negligible, that is: $\frac{1}{\beta\gamma M_a^2} \ll 1$, which implies that $\beta \gg 1$.

In the entropy equation, the Joule heating is strong, and must be balanced by the convection of entropy. We expect $\frac{1}{R_m\beta\gamma M_a^2}$ to be of order one. Consequently $R_m \sim \frac{1}{\beta} \ll 1$. The electrothermal regime is therefore a regime of low magnetic Reynolds numbers.

B.3 Magnetodynamic Regime

In the magneto-dynamic regime we expect the flow to be driven by the magnetic pressure gradient, so that

$$\frac{1}{\beta\gamma M_a^2} \sim 1.$$

In the entropy equation we neglect the dissipation relative to the convection, which implies

$$\frac{1}{R_m \beta \gamma M_a^2} \ll 1.$$

Consequently,

$$R_m \gg 1. \tag{B.27}$$

The magneto-dynamic regime is therefore the regime of high magnetic Reynolds numbers.

B.4 Choice of the Reference Variables

Since we are chiefly interested in the magneto-dynamic regime, we choose the reference variables in the following way, using A_{ref} (the cross sectional area), $\dot{m}$ (the mass flow rate) and B_{ref} (the inlet magnetic field) as primary variables and we choose:

$$P_{ref} = \rho_{ref} u_{ref}^2, \tag{B.28}$$

$$\rho_{ref} u_{ref} = \frac{\dot{m}}{A_{ref}}, \tag{B.29}$$

$$\rho_{ref} u_{ref}^2 = \frac{B_{ref}^2}{2\mu_o}. \tag{B.30}$$

This implies

$$\rho_{ref} = \frac{2\mu_o \dot{m}^2}{A_{ref}^2 B_{ref}^2}, \tag{B.31}$$

$$u_{ref} = \frac{A_{ref} B_{ref}^2}{2\mu_o \dot{m}}, \tag{B.32}$$

$$P_{ref} = \frac{B_{ref}^2}{2\mu_o}, \tag{B.33}$$

$$\gamma M_{a_{ref}}^2 = 1, \tag{B.34}$$

$$\gamma \beta_{ref} M_{a_{ref}}^2 = \frac{1}{2}. \tag{B.35}$$

This implies that $\beta_{ref} = \frac{1}{2}$. The equations then reduce to the following expressions:

$$\partial_t^* \rho^* + \mathrm{div}^*(\rho^* \mathbf{u}^*) = 0, \tag{B.36}$$

$$\rho^*(\partial_t^* + \mathbf{u}^* \cdot \nabla^*)\mathbf{u}^* + \nabla^*(p^* + b^{*2}) = 0, \tag{B.37}$$

$$\frac{1}{\gamma - 1}\rho^{*\gamma}(\partial_t^* + \mathbf{u}^* \cdot \nabla^*)\left(\frac{p^*}{\rho^{*\gamma}}\right) = \frac{2}{R_m}(\nabla^* b^*)^2, \tag{B.38}$$

$$\rho^*(\partial_t^* + \mathbf{u}^* \cdot \nabla^*)\left(\frac{b^*}{\rho^*}\right) = \frac{1}{R_m}\nabla^{*2} b^*, \tag{B.39}$$

$$\mathbf{e}^* = -\mathbf{u}^* \times \mathbf{b}^* + \frac{1}{R_m}\nabla \times \mathbf{b}^* + \frac{H_a}{R_m}(\nabla \times \mathbf{b}^*) \times \mathbf{b}^*. \tag{B.40}$$

Throughout the thesis, except when otherwise indicated, the non-dimensional variables are normalized by the reference variables defined above. In addition the stars will be omitted in the rest of the thesis.

Appendix C

Proposal for the Numerical Simulation of the Non-Linear Two-Dimensional Flow

The analysis of the flow in the exit region presented in Chapter 4 was limited to the case of a corner with a small deflection angle. The more general problem of the flow around a sharp corner was not considered in that analysis, despite the obvious benefits that its solution would provide. In this section the problem of the flow around a sharp isolated corner will be described in more detail. The problem will be stated from the point of view of a numerical analysis, paying attention to its eventual resolution by a numerical method.

A similar description will be made of the problem of the flow at the end of the channel, taking into consideration the influence of both corners. A final section will generalize the problem to that of the simulation of the flow through the whole device.

C.1 Definition of the Numerical Problem for the Isolated Corner

The plasma flows along a conducting corner whose geometry is that of Chapter 4, but with a large deflection angle, typically equal to $\pi/2$. The incoming flow is assumed to be uniform ahead of the corner. The flow is assumed to be super magneto-sonic($M_v >$ 1). This condition will be verified in most experimental thrusters designed to work in the magneto dynamic regime. In addition the incoming Mach number is assumed to be of the order of 3, so that the flow is also supersonic at small scale length.

The system of equations which describes the problem is given in the sections above. The equations can be expressed in conservative or non-conservative form. The choice of the expression has several implications. First the majority of algorithms developed by fluid dynamicists, like the Finite Volume or the Galerkin Finite Element methods, require that the equations be expressed in conservative form. The conservative form has the benefit of conserving the right quantities across discontinuities like shocks, whereas a non-conservative method would give incorrect results across discontinuities.

A drawback of the conservative formulation is that it is ill-conditioned for typical flows in magneto-dynamic thrusters. In the magneto-dynamic regime the plasma's thermal energy is small compared to either the kinetic or the magnetic energy. As a result, small errors in the value of either the kinetic or the magnetic energy will result in large errors in the internal (thermal) energy of the fluid.

After the choice of the formulation, the next step is to consider the boundary conditions. Along the conductor surface, two conditions can be written. First, the velocity must be tangent to the surface of the conductor. Second, the electric field must be normal to the conductor, since it is an equipotential surface.

The other boundary conditions are slightly more difficult to establish. By considering the far field is is possible to show that, in the limit where the distance from the corner goes to infinity, the solution of the resistive non-linear problem tends almost everywhere to the solution of the non-resistive non-linear problem. The solution to the non-resistive problem can easily be calculated (see the section 3.4.2). From the hyperbolic nature of the non-resistive operator follows the fact that the boundary conditions of the problem must be compatible in order to insure that the problem is well-posed. The conditions in the fan region (ii) and in the downstream region (iii) of figure 3-16 or 3-17 are consequences of, and cannot be specified independently from those of region (i). Five independent boundary conditions must be specified to uniquely determine the it uniform incoming plasma. These conditions can be for instance taken as: the incoming density, longitudinal and transverse velocities, the incoming pressure, and the incoming magnetic field. Some of these conditions can be replaced by either the Mach number, the Mach-Alfven number, the plasma-β, or the temperature. The problem is then well-posed and the solution can theoretically be obtained from these boundary conditions.

In practice one has to deal with the additional constraints of the numerical process. One must choose the method of discretization and the type of algorithm. Since the solution is usually represented by the values taken by the approximation on a finite number of points, the domain of validity of the approximation, also called the computational domain, has a finite size. The boundary conditions must therefore be extrapolated from infinity to the edge of this finite domain.

Two methods can be considered. In the first, one can use as much knowledge of the actual solution as possible to extrapolate analytically the solution to a finite distance and impose the result as fixed boundary conditions on the numerical solution. In order to do so, one must know an analytic expression for the asymptotic solution in the far field. In other words, it is not sufficient to know the limit at infinity, but one must know the next term (a function of the coordinates) of the solution's asymptotic expansion near infinity. Although it is usually possible to derive the *form* that this asymptotic solution must take, there is often an unknown multiplicative constant involved in the expression of this solution. The value of this multiplicative constant cannot be found from the boundary conditions at infinity, but the asymptotic limit can be used to impose a relationship between the gradient at a finite distance and the difference between the value at that point and the asymptotic limit.

Another possible method for determining the boundary condition is to estimate these conditions based on the knowledge of the differential equations and the data available locally near the boundary. This method is commonly used in computational fluid dynamics, both for subsonic and for supersonic problems. It is particularly well adapted to time-marching algorithms where the solution is relaxed to a steady state solution by simulating the dynamical behavior of the system, and where the boundary conditions on the computational domain are iterated as well. However the relaxation method for the boundary conditions is necessarily more complicated than the relaxation method of the main part of the computational domain, since information from both the outside and the inside of the computational domain must be taken into consideration. Here the problem is complicated by the fact that the behavior of the differential operator depends on the scale length which is considered. This research has shown that the large scale behavior is nearly hyperbolic, whereas the small scale behavior is both elliptic and hyperbolic. If one considers the steady state behavior of the flow, one can define for each boundary-point two characteristic lines (similar to the characteristic lines of a classical gas) along which some information is propagated. These lines define a "wedge" of dependence, which delineates the limited range of space from which there is an influence on the solution at the point considered. Simultaneously the equations have an elliptic behavior which means that the value at the point considered will depend on information coming from all possible directions. The task of the numerical analyst is then to decide what should be updated elliptically and what should be updated hyperbolically, what information should be extrapolated from inside the computational domain and what information should be extrapolated from the outside.

It seems that the choice of an algorithm for relaxing the boundary conditions which is consistent with the steady state solution is difficult. In addition there is the difficulty of maintaining the stability of the calculation during the iterative process. It is probably hopeless to expect that one could prove in the general (non-linear) case that stability will be guaranteed by a particular algorithm. This leaves the algorithm designer with the empirical method as his only option. To the knowledge of the author of this dissertation there is no systematic way to approach this problem. The author's experience leads him to believe that solving resistive magneto-dynamic flow is considerably more difficult than solving normal fluid dynamic flows. The author has tried to solve the problem with a time marching algorithm but was unable to find a algorithm for the boundary conditions which maintains stability throughout the computational domain without radically changing the nature of the problem by adding too much artificial damping.

C.2 Definition of the Numerical Problem for the Exit Region of a Symmetric Channel

The numerical solution for the flow in the exit region differs from solution for the corner flow only because the boundary conditions are different. In this case the difficulties are limited to the far field on the exit side. If the fluid expands in perfect vacuum, the magnetic field, the pressure and the density decay to zero in the far field, whereas the velocity tends to a constant value reflecting the residual kinetic energy left in the fluid at the end of the expansion. If there is some residual pressure in the medium into which the plume expands, the flow will not be purely radial, but will have a more complex structure which includes a series of shocks like a classical exhaust plume. The structure of this plume is difficult to calculate. In addition it is a somewhat academic exercise, since the flow quickly becomes a rarefied flow, and the collision-dominated MHD model becomes invalid.

C.3 Definition of the Numerical Problem for the Whole Thruster

If one adds the initial section of the thruster to the problem, one now faces an additional difficulty: the singularity where the Mach number equals one, also called the sonic passage. If one chooses to start the calculation with a uniform flow at a subsonic velocity, one of the initial boundary conditions must be left free so that this extra degree of freedom will be used to remove the singularity at the sonic point. In the case of a time marching algorithm, this implies that one of the boundary conditions should be extrapolated at each time step from the inside of the channel, according to a method of characteristics similar to what is used in computational fluid dynamics. But an algorithm to do this calculation cannot be found easily.

If one looks at a scale length at which the gradients of density, velocity, pressure...etc. are small, the non-linear operator can be approximated by the linearized fourth order operator which has the hyper-elliptic properties mentioned above. Even if one could find an algorithm based on the known properties of the linear operator, this algorithm would probably require a very high grid definition near the inlet, since the gradients are very strong there, and the relevance of the linear operator would be limited to extremely short scale lengths.

In conclusion the task of calculating the solution of the problem using a numerical method based on either a finite volume or a finite element method is considerable. The author's experience is that the strong gradients encountered near the inlet and near the exit are the source of violent instabilities which can only be damped at the cost of completely changing the nature of the problem and smearing out all the small scale features of the solution.

Appendix D

Comparison Between Momentum and Resistive Transport

D.1 Estimates of Resistivity and Viscosity

In most of this dissertation the only transport process considered is the electrical resistivity. The other processes were neglected for essentially two reasons: first, they add significant mathematical difficulties, and second, their effect is believed to be less important than the effects of the electrical resistivity. Based on a one-dimensional model Niewood and Martinez-Sanchez [47] have shown that, among several of the other transport phenomena, the viscosity had the second most important effect on the decrease of the overall efficiency of slender thrusters. In this section the relative scales of these two transport phenomena (resistivity and viscosity,) will be estimated, based on the classical theory, (*i.e.* on the kinetic theory of conductive gases,) while ignoring the effects of turbulence.

The electrical conductivity can be estimated by the Spitzer-Härm formula

$$\sigma = 1.53\ 10^{-2}\, \frac{T_e^{3/2}}{\ln \Lambda}, \tag{D.1}$$

where $\ln \Lambda$ is the Coulomb logarithm, T_e is the electron temperature in Kelvin, and σ is the conductivity in Si/m. For $T_e = 12500$K, and $\ln \Lambda = 7$ the conductivity is about

$\sigma = 3000$ Si/m.

Figure D-1 shows an estimate of the viscosity calculated by Miller [43] for argon in thermodynamic equilibrium. The viscosity is strongly affected by the ionization level. The viscosity is proportional to the mean-free-path of the heavy particles. Because of the strong effect of Coulomb collisions, the mean free path of ions is much shorter than that of neutral atoms. Therefore the gas viscosity decreases by several orders of magnitude as the gas ionization fraction goes from near zero, to near one. The electron temperature inside the discharge is estimated to be 12500K or above. This turns out to give a viscosity close to the minimum, of the order of $\mu_{min} \simeq 0.05\ 10^{-4}$ kg m^{-1} s^{-1}. However it may be that some part of the discharge will have a lower electron temperature, and consequently a much higher viscosity. In order to be on the safe side, one can estimate an upper bound for the viscosity. In this case a reasonable estimate for the worst case viscosity would be $\mu_{max} \simeq 2.4\ 10^{-4}$ kg/m/s.

D.2 Boundary Layer Size

The relative scale of the resistive and viscous effects is given by the ratio of the Reynolds number to the magnetic Reynolds number which are respectively defined by

$$R_e = \frac{\rho u L}{\mu},$$

$$R_m = \mu_0 \sigma u L.$$

Therefore

$$\frac{R_e}{R_m} = \frac{\rho}{\mu_0 \sigma \mu}. \tag{D.2}$$

Table D.1 shows the estimates for the ratio $\frac{R_e}{R_m}$, for each of the three thrusters considered. In the most likely case, the viscous scale is significantly smaller than the resistive scale. In the worst case the viscous scale length is of the same order as the resistive scale length, which suggests that it may be important to consider these two effect simultaneously.

The size of the viscous boundary layer along an electrode can be estimated using

	Flared	Gun	Parallel
$\left(\frac{R_e}{R_m}\right)$ max	833	24	1750
$\left(\frac{R_e}{R_m}\right)$ min	17	0.5	37

Table D.1: Estimates of the ratio $\frac{R_e}{R_m}$

the results of chapter 6. The similarity transformation is still valid in this case and the results for two arbitrary values of $\frac{R_e}{R_m}$ are shown in figures D-2 and D-3, where η is the non-dimensional similarity variable which can be expressed in terms of the dimensional variables $\bar{x}, \bar{y}$, and Λ_m by $\eta = \frac{\bar{y}}{\sqrt{\bar{x}\Lambda_m}}$. If one defines, somewhat arbitrarily, the edge of the boundary layer by the value of the similarity variable η^* where the local velocity reaches 90% of the free stream velocity (therefore η^* is a function of the ratio $\frac{R_e}{R_m}$), one can estimate the thickness of the boundary layer by

$$\bar{\delta} \simeq \eta^* \sqrt{\bar{x}\Lambda_m}. \tag{D.3}$$

The results at the end of the channel are displayed in table D.2. They indicate that the boundary layer can reach a significant fraction of the electrode gap near the exit.

D.3 Conclusion

The plasma resistivity and viscosity were calculated using classical transport theory. The scale length for the resistive effects is expected to be much larger than the scale length for the viscosity. This suggests that the resistivity should determine the main features of the flow, while the viscosity should play a secondary, but not negligible role. This conclusion is supported by the comparison between the viscous and inviscid solutions for the magnetic boundary layer flow presented in chapter 6.

	Flared	Gun	Parallel
$\bar{x} = L$ [cm]	22	112	13.3
Λ_m [cm]	1.1	0.32	0.28
$\sqrt{\bar{x}\Lambda_m}$ [cm]	4.9	6.0	1.9
η^* min	0.5	0.5	0.5
η^* max	0.5	4.	0.5
δ min. [cm]	2.5	6.	1.0
δ max. [cm]	4.9	36.	1.3
h [cm]	4.1	9.5	5.1

Table D.2: Estimates of the boundary layer size near the exit.

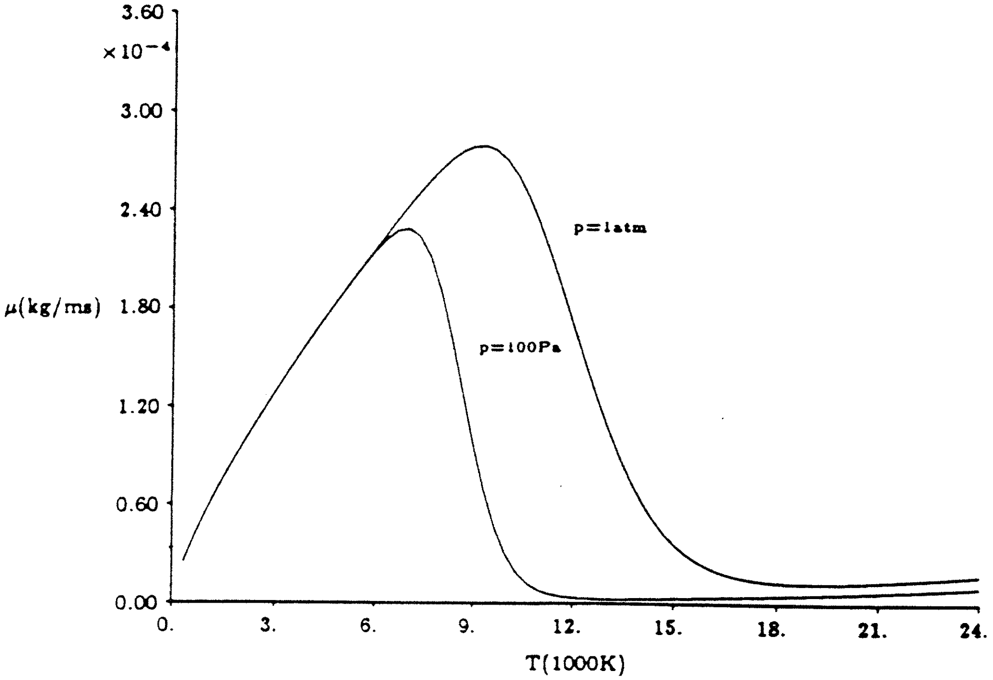

Figure D-1: Diagram of the total viscosity for argon in thermodynamic equilibrium, at 10^2 and at 10^5 Pascals

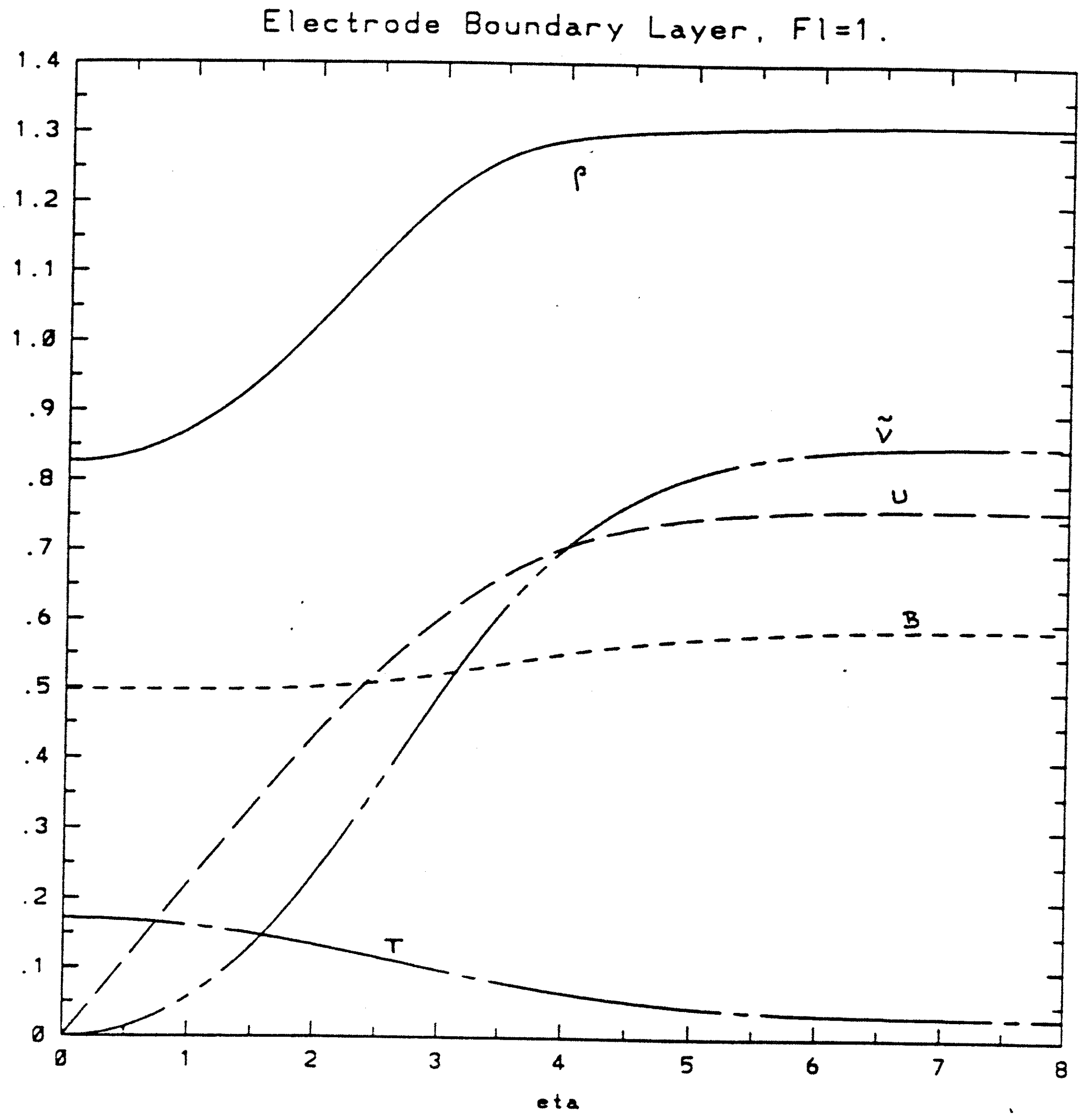

Figure D-2: Structure of the boundary layer along a flat electrode in the absence of the Hall effect for $R_e/R_m = 1$.

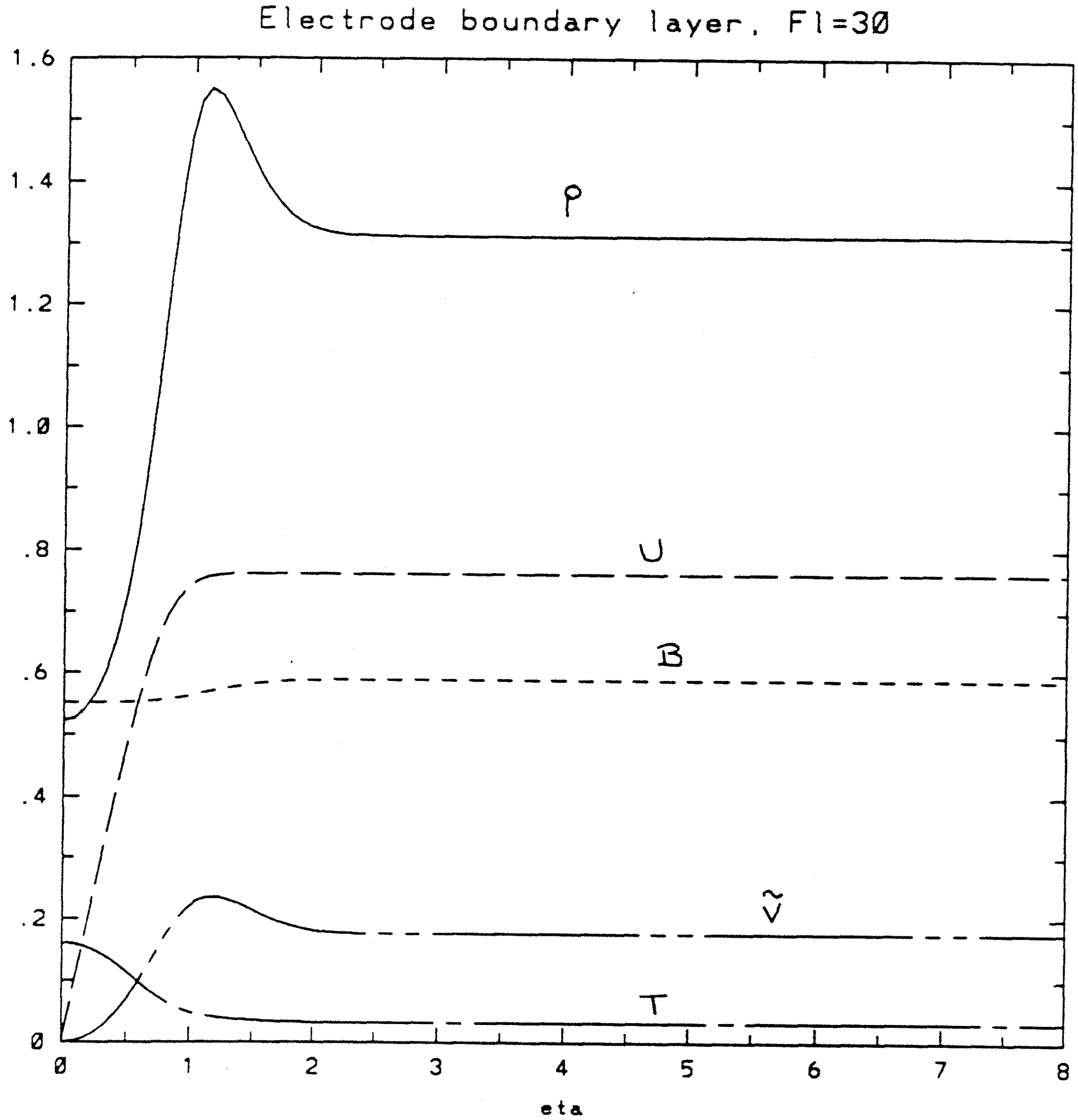

Figure D-3: Structure of the boundary layer along a flat electrode in the absence of the Hall effect for $R_e/R_m = 30$.

Bibliography

[1] Ackeret J., "Luftkräfte auf Flügel, die mit grösserer als Shallgeschwindigkeit bewegt werden," *Z. Flugtech. u. Motorluftschiffahrt* vol. 16, pp. 72-74, 1925. Translated in *NACA Technical Memorandum 317*, 1925.

[2] Ames, W. F., *Numerical Methods for Partial Differential Equations*, Second Edition, Academic Press, 1977.

[3] Auweter-Kurtz M., Glaser S.F., Kurtz H.L., Schrade H.O., Sleziona P.C., "An Improved Code for Nozzle-Type Steady State MPD Thrusters," AIAA Paper, No. AIAA-88-040, *20th International Electric Propulsion Conference*, 1988.

[4] Baksht F.G. and Moishes B.Ya. and Rybakov A. B., "Critical regime of a plasma accelerator", *Sov. Phys. Tech. Phys.*, Vol. 18, No. 12, June 1974.

[5] Bargman V., "On Nearly Glancing Reflection of Shocks," *Applied Mathematics Panel Report 108.2R (Applied Mathematics Group – Institute for Advanced Study)*, 1945.

[6] Barnett J.W., "Operation of the MPD Thruster with Stepped Current Input," Ph.D. Dissertation, Department of Mechanical and Aerospace Engineering, Princeton University, Princeton, New-Jersey, USA, 1985.

[7] Borisenko, A.I., Tarapov, I.E., *Vector and Tensor Analysis with Applications*, Dover Publications, pp. 209-210, 1968.

[8] Brackbill J.U., "FLIP-MHD: A Particle-in-Cell Method for Magnetohydrodynamics," *Journal of Computational Physics* Vol. 96, No. 1, pp. 163-192, September 1991.

[9] Brushlinskii K.V., Gerlakh N.I., and Morozov A.I., "Two-Dimensional Steady Flow of Highly Conducting Plasma in a Coaxial System," *Izvestiia Akademii Nauk SSSR: Mekhanika Zhidkostei i Gazov* Vol. 1, No. 2 pp. 189-192, 1966; translated in *Fluid Dynamics* 1966.

[10] Buff J., Frese M. H., Giancola A. J., Peterkin R. E. Jr., Roderick N. F., "Simulations of a Plasma Flow Switch," *IEEE Transactions on Plasma Science*, Vol. PS-15, No. 6, December 1987.

[11] Buff J., Peterkin R. E. Jr., Roderick N. F., Degnan J.H., Frese M. H., Turchi P. J., "Enhancement of the Radiation Yield in Plasma Flow Switch Experiments," *IEEE Transactions on Plasma Science*, Vol. 19, No. 3, June 1991.

[12] Chanty J.M.G., Martinez-Sanchez M., "Two-Dimensional Numerical Simulation of MPD Flows", AIAA Paper AIAA-87-1090, *AIAA/DGLR/JSASS 19th International Conference*, May 11-13, 1987, Colorado Springs, Colorado.

[13] Choueiri E. Y., "Electron-Ion Streaming Instsabilities of an Electromagnetically Accelerated Plasma," Ph.D. Thesis, Princeton University, October 1991.

[14] Clarke J.F., McChesney M., *The Dynamics of Real Gases,* Butterworths, Washington, 1964.

[15] Connolly, D.J., Sovie, R.J., Seikel,G.,R., "Performance and Diagnostics of a Water-Cooled Magnetoplasmadynamic Arc Thruster," NASA TN D-5836, 1970

[16] Di Capua M.S., Jahn R.G., "Energy Deposition in Parallel-Plate Plasma Accelerators," AIAA Paper No. 71-197, *AIAA 9th Aerospace Sciences Meeting*, New-York, January 1971.

[17] Drobot A.T., (Editor) *Computer Applications in Plasma Science and Engineering*, Springer Verlag, New-York, 1991.

[18] Fletcher C.A.J., "Computational Galerkin Methods," Springer Verlag, pp. 160-162, 1984.

[19] Gallimore A.D., Kelly A.J., and Jahn R.G., "Anode Power Deposition in MPD Thrusters," *AIDAA/AIAA/DGLR/JSASS 22nd International Electric Propulsion Conference*, 14-17 October 1991, Viareggio, Italy.

[20] Glauert H., "The Effect of Compressibility on the Lift of an Airfoil," *Proc. Roy. Soc. A118*, pp. 113-119, 1928.

[21] Gruber R., Rappaz J., *Finite Element Methods in Linear Ideal Magnetohydrodynamics*, Springer Verlag, Berlin, 1985.

[22] Hansen A. G., *Similarity Analysis of Boundary Value Problems in Engineering*, Prentice Hall, 1964.

[23] Hastings D.E., Niewood E., "Theory of the Modified Two-Stream Instability in Magnetoplasmadynamic Thruster," Journal of Propulsion of Power, Vol. 7, No. 2, March-April, pp. 258-268, 1991.

[24] Heimerdinger D. J., "Fluid Mechanics in a Magnetoplasmadynamic Thruster," Ph.D. Dissertation, Department of Aeronautics and Astronautics, Massachusetts Institute of Technology, Cambridge, Massachusetts, USA, 1988.

[25] Kevorkian, J. and Cole J.D., *Perturbation Methods in Applied Mathematics*, Springer Verlag, pp. 408-413, 1981.

[26] Kilfoyle, D.B. and Martinez-Sanchez, M. and Heimerdinger D.J., and Sheppard, E.J., "Spectroscopic Investigation of the Exit Plane of an MPD Thruster," Paper IEPC-88-027, *DGLR/AIAA/JSASS 20th International Electric Propulsion Conference*, October 3-6 1988, Garmisch-Partenkirchen. W. Germany.

[27] Kimura I., Toki K., Tanaka M., "Current Distribution on the Electrodes of MPD Arcjets," *AIAA Journal*, Vol. 20, No. 7, July 1982.

[28] Kunii Y., Shimizu Y. and Kuriki K., "Current Distribution in a Quasi-Steady MPD Arcjet," AIAA Paper AIAA-82-1917, *AIAA/JSASS/DGLR 16th. International Electric Propulsion Conference.*

[29] Kuriki K., Kunii Y., and Shimizu Y., "Current Distribution in Plasma Thruster," AIAA Paper AIAA-81-0685, *AIAA/JSASS/DGLR 15th. International Electric Propulsion Conference.*

[30] Kurtz, H.L., Auweter-Kurtz, M., and Schrade, H.O., "Self-Field MPD Thruster Design Experimental and Theoretical Investigations," AIAA Paper 85-2002, Sept. 1985.

[31] Kurtz H.L., Auweter-Kurtz M., Merke W., Schrade H.O., "Experimental MPD Thruster Investigations," AIAA paper 87-1019.

[32] Landau, L.D. and Lifshitz, E. M., *Fluid Mechanics*, Pergamon Press, Elmsford, NY,1960.

[33] Lary E. C., "A theory of thin airfoils and slender bodies in fluids of arbitrary electrical conductivity," Ph.D. Thesis, Cornell University 1959.

[34] "Theory of Onset in Magnetoplasmadynamic Thrusters," *AIAA Journal of Propulsion and Power*, vol. 3, no. 2, pp. 121-127, 1987.

[35] Leontovich, M.A. (ed.), *Reviews of Plasma Physics*, translation of *Voprosy teorii plasmy*, Consultant Bureau, Plenum Publishing, New-York, 1965.

[36] Lien H., Garrison, R.L., "System Trade-offs for Pulsed MPD Thrusters in Space Mission Application," AIAA-72-457.

[37] Liepmann H.W., Ashkenas, H., Cole J.D., *U.S. Air Force Technical Report 5667*; see also Hilton W.J., *High Speed Aerodynamics,* Longmans Green, New-York, 1952.

[38] Lighthill M.J., "The Diffraction of a Blast I," *Proc. Roy. Soc. A198,* pp. 454-470, 1949.

[39] Martinez-Sanchez, M., "The Structure of Self-Field Accelerated Plasma Flows," AIAA-87-1065, *AIAA/DGLR/JSASS, 19th. International Electric Propulsion Conference.*

[40] Martinez-Sanchez M., "Structure of Self-Field Accelerated Plasma Flows," *Journal of Propulsion and Power*, vol. 7, No. 1, Jan-Feb 1991, pp.56-64.

[41] Matsumoto H., Omura Y., "Particle Simulation of Electromagnetic Waves," in *Computer Simulation of Space Plasmas*, edited by Matsummoto H., and Sato T., D. Reidel Publishing Co., Dordrecht, 1984, pp. 43-102.

[42] McCune J. E., Resler E. L. Jr., "Compressibility Effects in Magnetoaerodynamic Flows Past Thin Bodies," *Journal of Aerospace Sciences* Vol. 27, pp. 493-503, 1960.

[43] Miller S. A., "Viscous and Diffusive Effects in Magnetoplasmadynamic Flows," Masters Thesis, Department of Aeronautics and Astronautics, Massachusetts Institute of Technology, 1990.

[44] Morozov A.I., Solovev L.S., "Axially Symmetric and Steady-State Plasma Flow across an Azimuthal Magnetic Field," *Soviet Physics–Technical Physics*, vol. 9, No. 3, September 1964.

[45] Morozov A.I., Solovev L.S., "Plane Flows of Ideally Conducting Compressible Fluids with Hall Effects Considered," *Soviet Physics–Technical Physics*, Vol. 9, No. 7, September 1965.

[46] Munk M.M., "Elements of the Wing Section Theory and of the Wing Theory," *NACA Technical note 1032,* 1946. Also *NACA Report 835*, 1946.

[47] Niewood E. H., Martinez-Sanchez M., "Quasi One-Dimensional Numerical Simulation of Magnetoplasmadynamic Thrusters," AIAA-paper 90-2604.

[48] Niewood E. H., Martinez-Sanchez M., "The Hall Effect in a Numerical Model of MPD Thrusters," *AIDAA/AIAA/DGLR/JSAJJ 22nd International Electric Propulsion Conference*, October 1991, Viareggio, Italy.

[49] Niewood E. H., Preble J., Hastings D. E. and Martinez-Sanchez M., "Electrothermal and Modified Two-Stream Instabilities in MPD Thrusters," AIAA Paper 90-2607, *21st International Elecric Propulsion Conference*, June 1990, Orlando, Florida, USA.

[50] Oswatitsch K., Berndt S. B., "Aerodynamic Similarity at axisymmetric Transonic Flow around Slender Bodies," *Kgl. Tek. Hogskol. Handl. Aero. Technical Note 15*, Royal Inst. Tech., Stockholm, Sweden, 1950.

[51] Sato, T., "Principles of Magnetohydrodynamic Simulation in Space Plasmas," in *Computer Simulation of Space Plasmas*, edited by Matsummoto H., and Sato T., D. Reidel Publishing Co., Dordrecht, 1984, pp. 133-153.

[52] Schoenberg K.F., Gerwin R.A., Barnes C.W., Henins I., Mayo R., Moses R. Jr., Scarberry R., and Wurden G., "Coaxial Plasma Thrusters for High Specific Impulse Propulsion," AIAA Paper 91-3570, *AIAA/NASA/OAI Conference on Advanced SEI Technologies*, September 1991, Cleveland Ohio, USA.

[53] Schrade H.O., Auweter-Kurtz M. and Kurtz H. L., "Stability Problems in Magneto-Plasmadynamic Arc Thrusters," AIAA Paper No. 85-1633, *AIAA 18th Fluid Dynamics and Plasmadynamics and Lasers Conference* July 16-18, 1985, Cincinnati Ohio.

[54] Sears W. R., Resler E. L., "Theory of thin airfoils in fluids of high electrical conductivity," *Journal of Fluid Mechanics,* vol. 5, pp. 257-273, 1959.

[55] Shapiro R. A., "An adaptive finite element solution algorithm for the Euler equations," PhD. Thesis, MIT, 1988.

[56] Sichel M., "Two-Dimensional Shock Structure in Transonic and Hypersonic Flow," *Advances in Applied Mechanics*, vol. 11, pp. 131-207, Academic Press, New-York, 1971.

[57] Sleziona P.C., Auweter-Kurtz M., Schrade H.O., "Numerical Codes for Cylindrical MPD Thrusters," AIAA Paper, No. AIAA-88-040, *20th International Electric Propulsion Conference.*

[58] Sovey J.S., Mantenieks M.A., "Performance and Lifetime Assessment of MPD Arc Thruster Technology," NASA Technical Memorandum 101293, 1988, AIAA-88-3211.

[59] Tanaka M., Kimura I., Arakawa Y., "Current Distribution on the Electrodes of MPD Arcjets with Applied Magnetic Field," AIAA Paper, No. AIAA-82-1918, 1982

[60] Tanaka M., Kimura I., "Theoretical Analysis of Current Distribution and Plasma Acceleration in MPD Arcjet," *Proceedings of the 17th International Electric Propulsion Conference* Tokyo 1984, IEPC 84-07.

[61] Tilley D.L., Choueiri E.Y., Kelly A.J., Jahn R.G., "An Investigation of Microinstabilities in a kW level Self-Field MPD Thruster," *AIDAA/AIAA/DGLR/JSASS 22nd International Electric Propulsion Conference*, 14-17 October 1991, Viareggio, Italy.

[62] Timman R, van de Vooren A.I., and Greidanus J.H., "Aerodynamic Coefficients of an Oscillating Airfoil in Two-Dimensional Subsonic Flow," *J. Aero. Sci.,* vol. 18, No. 12, pp. 797-802, 1951.

[63] Vainberg, L.I. and Lyubimov, G.A. and Smolin, G.G., "High current discharge effects and anode damage in an end-fire plasma accelerator," Translation published in: *Sov. Phys. Tech. Phys.* Vol. 23 (4), April 1978.

[64] White, F. M., *Viscous Fluid Flow*, McGraw Hill, 1974.

[65] Wolff M., Kelly A.J., Jahn R.G., "A High Performance Magnetoplasmadynamic Thruster," AIAA Paper 84-32.